Excited State Dynamics and Photophysics in Bulk, Confined and Bio-mimetic Systems

A Thesis

Submitted in Partial Fulfillment of the Requirements

for the Degree of

Doctor of Philosophy

by

Abhigyan Sengupta

ID: 20093039

Indian Institute of Science Education and Research (IISER), Pune

2014

Dedicated

to the sweet memories of my father

Indian Institute of Science Education and Research (IISER), Pune

Certificate

Certified that the work incorporated in this thesis entitled "*Excited State Dynamics and Photophysics in Bulk, Confined and Bio-mimetic Systems*" submitted by *Mr. Abhigyan Sengupta* was carried out by the candidate, under my supervision. The work presented here or any part of it has not been included in any other thesis submitted previously for the award of any degree or diploma from any other university or institution.

Date: 16th July 2014

Dr. Partha Hazra
Research Supervisor

Email: p.hazra@iiserpune.ac.in | Contact no: +91 (20) 25908077

Declaration

I declare that this written submission represents my ideas in my own words and wherever other's ideas have been included; I have adequately cited and referenced the original sources. I also declare that I have adhered to all principles of academic honesty and integrity and have not misrepresented or fabricated or falsified any idea/data/fact/source in my submission. I understand that violation of the above will cause for disciplinary action by the Institute and can also evoke penal action from the sources which have thus not been properly cited or from whom proper permission has not been taken when needed.

Date: 16th July 2014

Abhigyan Sengupta

ID: 20093039

Acknowledgement

I am deeply indebted to my research supervisor **Dr. Partha Hazra** who guided me and continuously encouraged me in last five years. With his efficient guidance I learnt designing and successful execution of research projects. Being the first PhD student of his research group I got the unique opportunity to learn how to set a new lab. His diligent effort and training was the reason behind every success I achieved and undoubtedly is the asset for my future research. I acknowledge Indian Institute of Science Education and Research (IISER), Pune for providing excellent research facilities and an outstanding research ambiance.

I am grateful to the Research Advisory Committee (RAC) members Dr. S. G. Srivatsan, Dr. Shouvik Datta and Dr. S. K. Asha (NCL Pune) for their guidance and invaluable advices at every step of my research work. The critical examination of my research work and valuable comments by all of the RAC members were always very useful. I specially thank Dr. S. G. Srivatsan for his countless efforts to make me perfect in terms of experiments, knowledge and presentations.

I am thankful to Dr. Arnab Mukherjee, Dr. Nirmalya Ballav, Dr. Pinaki Talukdar and Dr. Pankaj Mandal for giving me the opportunity to work with them in different collaborative research projects. Because of their guidance and suggestions I gained working experience in diverse fields of research which indeed is very helpful. I am also very thankful to Dr. Hosahudya N. Gopi and Dr. M. Jayakannan for their valuable suggestions. In fact I owe heartiest thank to every faculty of IISER-Pune who was always ready to share their knowledge and experience with me. It was indeed a pleasure to work in such an ambiance. I am indebted to Dr. B. S. M. Rao, dean of doctoral studies at IISER-Pune for his generous support and encouragement. I also thank Dr. V. S. Rao, registrar at IISER-Pune for his valuable support and help. I am also indebted to my teachers in masters (Scottish Church College, CU, Kolkata, especially Dr. Rana Sen) and in graduation (St. Paul's C. M. College, CU) for their excellent teaching and engraving the urge to pursue a career in research.

I thank Dr. Umeshareddy Kacherki (deputy librarian) and Anuradha for library support. I thank Sachin, Koushik and Abhijeet for IT support. I thank IISER, Pune administrative staff especially Mayuresh, Suvarna, Nayana, Tushar, Snehal and Prabhas for their kind support.

It's my pleasure to thank all the members of the team, I belong to; Krishna, Rajkumar, Sagar and Bibhisan as they always maintained a very lively environment in lab. An all time

running discussion and sharing of experiences helped me to expand the horizon of knowledge. I would also like to thank Mr. Rahul V. Khade (present PhD scholar in Pune University), Wilbee (from Dr. Arnab Mukherjee and group), Reman (from Dr. Arnab Mukherjee and group) and Sohini (Dr. Pankaj Mandal and group) for giving me the opportunity to work with and contributing significantly in several publications of mine.

I must thank my friends, seniors and juniors specially; Parthada (Dr. Partha Biswas, assistant professor Scottish Church College, CU), Anupamda, Sumit, Shukla, Ramya, Somu, Smita, Moumita, Biplab, Sohini, Tanmoy, Soumya, Sagar, Partha (Kalo), Arundhuti, Partho, Arindam, Abhishek, Sudeb, Manna, Mota, Maroti, Sandeep and Arvind.

No words can ever convey my sense of gratitude for my parents (my father; Mr. Jogabrata Sengupta and mother; Mrs. Kuntala Sengupta). It is due to their unconditional trust, timely encouragement, endless patience and unstinting sacrifice; I am able to reach this position. It is also a pleasure to acknowledge the best half of my life, Shree (Dr. Sreemoyee Mukherjee) for her inspiration and brace. I feel proud enough to know that she stood by my side against every odd in my life. I thank my sister (Mrs. Sayani Sengupta) and her husband Bubun (Mr. Amitava Sengupta) for their constant supports. I owe a very special thank to my father in law Mr. Kalyan Kumar Mukherjee, mother in law, Mrs. Alpana Mukherjee and brother in law Samrat da (Mr. Samrat Mukherjee) for their heartiest understanding and very caring attitude towards me. I am indebted to Koushikda (Dr. Koushik Mandal) for his unconditional stand by my side during the most crisis period of my life which can never be forgotten.

Finally, I am thankful to Council of Scientific and Industrial Research (CSIR), Department of Science and Technology (DST), Government of India, for my research scholarship (CSIR-SRF) the financial support during the course of PhD. Moreover, I like to thank American Chemical Society (ACS), Royal Society of Chemistry (RSC), John Wiley & Sons, Elsevier Science Ltd., for publishing several research articles produced during the course of my research as well as for giving the permission for reprint of copyrighted materials.

IISER Pune **Abhigyan Sengupta**

Preface

Present thesis deals with fluorescence spectroscopic studies of excited state dynamics and photophysics of biologically important fluorophores and drugs. It majorly contains three topics; (a) folding-unfolding dynamics of a flavo-enzyme cofactor named as flavin adenine dinucleotide or FAD, (b) environment sensitive emission of an anti-cancer drug and its respective color switch to probe non-specific protein-DNA interaction, and (c) dynamics of solvents over hydrophobic surface as well as hydrogen bonded solids in nano-cavity. The thesis is divided in six chapters.

Chapter 1 (***Fluorescence; the Principles and Applications***) gives a brief introduction to fluorescence spectroscopy and principles of fluorescence based techniques (like fluorescence quenching, lifetime, anisotropy and solvation dynamics), which are used to explore the research projects.

Chapter 2 (***Working Systems, Materials and Methods***) introduces the working systems, like, micelles, reverse micelles, carbon nanotubes (CNTs), serum albumin (SA) and RNA aptamer, as well as several photo-physically and biologically important fluorophores which are used during the research.

Chapter 3 (***Instrumentation, Technique and Analysis***) offers a detailing about instrumentations (absorption, steady state fluorescence, time correlated single photon counting (TCSPC), fluorescence up-conversion, circular dichroism (CD), isothermal titration Calorimetry (ITC) and field emission scanning electron microscopy (FE-SEM) etc.) and methods (detailed of sample preparation, experimental and theoretical procedures), which are majorly utilized in research.

Chapter 4 (***Modulation of Flavin Adenine Dinucleotide (FAD) Dynamics and Selective Detection of Flavins***) describes the folding-unfolding dynamics of an enzymatic cofactor; flavin adenine dinucleotide or FAD (one of the most known electron shuffling agent, ubiquitously present in living organisms) and its impact on its electron shuffling properties in presence of external stimuli like pH and urea. It also encircles the association behavior of flavins (namely FAD, flavin mononucleotide (FMN) and riboflavin (RF, also known as vitamin B_2)) with serum protein (human serum albumin, HSA) and RNA aptamer. This chapter is sub-divided in to 4 (4a to 4d) sections which are as follows;

4a. *pH Dependent Dynamics of Flavin Mononucleotide (FMN) and Flavin Adenine Dinucleotide (FAD): a Femtosecond to Nanosecond Study.*

4b. *Urea Induced Unfolding Dynamics of Flavin Adenine Dinucleotide (FAD): Spectroscopic and Molecular Dynamics Simulation Studies from Femtosecond to Nanosecond Regime.*

4c. *Comparative Study of Flavins Binding with Human Serum Albumin: A Fluorometric, Thermodynamic and Molecular Dynamics Approach.*

4d. *Role of Mg^{+2} Ions over Flavin Recognition by RNA Aptamer: Spectroscopic and Thermodynamic Glimpse.*

Chapter 5 (***An anticancer drug to probe non-specific protein-DNA interactions***) portraits that the visible fluorescence switch of an eminent anti-carcinogen; ellipticine has been used to probe non-specific protein-DNA interaction. The unique pattern of protein-DNA complexation is depicted for the first time through field emission scanning electron microscopy (FE-SEM) images and spectroscopic techniques.

Chapter 6 (***Solvation Dynamics in Heterogeneous and Confined Media***) deals with the two issues related to solvation dynamics; (a) Dynamics of water over a hydrophobic surface and (b) solvation dynamics of hydrogen bonded urea network confined inside reverse micelle cavity. This chapter is subdivided in two parts as follows;

6a. *Solvation Dynamics of Coumarin 153 in SDS Dispersed Single Walled Carbon Nanotubes (SWNTs).*

6b. *How does the urea dynamics differ from water dynamics inside the reverse micelle?*

Glossary of Acronyms

ADC	Analog to digital converter
AOM	Acousto-optic modulator
AOT	Aerosol-OT (dioctyl sodium sulfosuccinate)
4-AP	4-aminophtalimide
AuNP	Au (gold) nanoparticle
BIV	Bovine immunodeficiency virus
[bmim][BF_4]	1-butyl-3-methylimidazolium tetrafluoroborate
[bmim][PF6]	1-butyl-3-methyl imdazolium hexafluorophosphate
[bmpy][Tf_2N]	N-butyl-N-methylpyrrolidinium bis(trifluoromethanesulfonyl)imide
Brij	Polyoxyethylene glycol alkyl ethers, a nonionic surfactant
BSA	Bovine serum albumin
BSE	Back-scattered electrons
C-152	Coumarin 152
C-153	Coumarin 153
C-343	Coumarin 343
C-480	Coumarin 480
C-481	Coumarin 481
C-490	Coumarin 490
CD	Circular dichroism
CFD	Constant fraction discriminator
CHO	Chinese hamster overy
CLD	Cytoplasmic lipid droplet
CNM	Composite nano-material
CNT	Carbon nanotube
COM	Center of masses
CPM	7-(diethylamino)-3-(4-maleimidophenyl)-4-methylcoumarin
CT	Charge transfer / Calf thymus
CTAB	Cetyl trimethylammonium bromide
CTAC	Cetyl trimethylammonium chloride
CVD	Chemical vapor deposition
CW	Continues wave
DAPI	4',6-diamidino-2-phenylindole
DC	Dielectric constant
DCM	4-(dicyanomethylene)-2-methyl-6-(p-dimethylaminostryl) 4H-pyran
2DIRS	2 Dimensional infrared spectroscopy
DLA	Diffusion limited aggregation

DLC	Delocalized lipophilic cations
DLS	Dynamic light scattering
DMF	*N*,*N*-Dimethylformamide
DMSO	Dimethylsulfoxide
DOPC	1,2-di-(9Z-octadecenoyl)-*sn*-glycero-3-phosphocholine
DWNT	Double walled nanotube
EDTA	Ethylenediaminetetraacetic acid
[emim][BF_4]	1-ethyl-3-methylimidazolium tetrafluoroborate
FA	Formamide
FAD	Flavin Adenine Dinucleotide
FCS	Fluorescence correlation spectroscopy
FDA	Food and Drug Administration
FE	Field emission
FE-SEM	Field Emission Scanning Electron Microscopy
FFCF	Frequency frequency correlation function
FMN	Flavin mononucleotide
FRET	Fluorescence resonance energy transfer
FWHM	Full width half maximum
GAFF	General amber force field
GB1	B1 domain of streptococcal protein G
GFP	Green fluorescent protein
GO	Graphene oxide
GOD	Glucose oxidase
HA	Hyaluronic acid
HEPES	4-(2-hydroxyethyl)-1-piperazineethanesulfonic acid
HIV	Human immunodeficiency virus
[hmim][PF6]	1-hexyl-3-methyl imdazolium hexafluorophosphate
HNF	2-hydroxy-7-nitrofluorene
HSA	Human serum albumin
IC	Internal conversion
IET	Intra molecular electron transfer
IL	Ionic liquid
ISC	Inter system crossing
Iso	Isoalloxazine
ITC	Isothermal titration calorimetry
KSI	Δ^5-3-ketosteroid isomerase

LBO	Lithium triborate
LE	Locally excited
LED	Light emitting diode
MCAD	Medium-chain acyl Co-A dehydrogenase
MD	Molecular dynamics
Met	Metallic
MeCN	Acetonitrile
MEOH	Methanol
MG	Molten globule / Malachite green
MSA	Mean spherical approximation
MWNT	Multi walled nanotube
NaDC	Sodium deoxycholate
NaDDBS	Sodium dodecylbenzenesulfonate
NIH	National institute of health
NMRD	Nuclear magnetic relaxation dispersion
OLEDs	Organic light emitting diodes
ORD	Optical rotary dispersion
P-123	Pluronic-123 tri block copolymer
PET	Photo-induced electron transfer
PDB	Protein data bank
PEPS	Photon echo peak shift
PME	Particle Mesh Ewald
PRODAN	6-propionyl-2-dimethylaminonaphthalene
PSA	Prostate specific antigen
PSMA	Prostate specific membrane antigen
QCM	Quartz crystal microbalance
QD	Quantum dots
RBF	Riboflavin binding protein
RESP	Restrained electrostatic potential
RF	Riboflavin
RISM	Reference interaction site model
RM	Reverse micelle
RMSD	Root mean square deviation
RT	Reverse transcriptase
SAW	Surface acoustic wave
SA	Serum albumin

SANS	Small angle neutron scattering
SAXS	Small angle X-ray scattering
SC	Subtilisin Carlsberg / Semi conducting
SDS	Sodium dodecyl sulfate
SEM	Scanning electron microscopy
SHG	Second harmonic generation
SPT	Single photon timing
siRNAs	Small interfering RNAs
SS I/II	Sudlow's site I/II
SWNT	Single walled carbon nanotube
SYNC	Synchronizer
TAC	Time to amplitude converter
TAR	Trans activation responsive
TCSPC	Time correlated single photon counting
TDSS	Time dependent Stokes shift
TFTs	Thin-film transistors
TRES	Time-resolved emission spectra
TRFSS	Time resolved fluorescence Stokes shift
Trp	Tryptophan
TX-100	Triton X-100
VEGF	Vascular endothelial growth factor

Contents

Chapter 1

Fluorescence; the Principles and Applications

1.1. Introduction

"Light", the origin of life on earth, is able to distinguish objects that can respond to it (named as living) from those who do not (called dead). Not only the livings but the non-livings also offer finite response to light in several ways which are intriguing but not easy to detect. Being a practitioner of light, I am distinctly interested in such light induced changes in molecules. Molecules irradiated with photons of desirable energy, results electronic transitions. Sometimes during the return of molecules to the ground state, it is accompanied by colourful emission, known as luminescence (majorly of two kinds; fluorescence and phosphorescence). I majorly used fluorescence spectroscopy based techniques to probe diverse processes, like excited state folding-unfolding dynamics, intra- and inter-molecular proton transfer, electron shuffling, visible colour switching, solvation dynamics and binding interactions. The thesis consists of such intriguing events like, dynamics of flavo-protein chromophores (namely, flavin adenine dinucleotide or FAD, the most known electron shuffling agent in living world), environment sensitive emission switch of an anti-cancer drug ellipticine to probe non-specific protein-DNA interaction, and dynamics of solvents over hydrophobic surface as well as dynamics of hydrogen bonded solid in nano-confinement. The present chapter offers an insight about florescence principle and several fluorescence based techniques, which have been extensively used in this thesis. More precisely it details about the basic principle of fluorescence spectroscopy, fluorescence quenching, principles of steady state and time resolved fluorescence measurements, fluorescence anisotropy and solvation dynamics.

1.2. Fluorescence; When and How?

During last few decades' fluorescence has been pervasively used in the field of chemistry and biology. Fluorescence is a dominant methodology used extensively in material analysis, flow cytometry, DNA sequencing, biotechnology, medical diagnostics, forensics, and genetic analysis etc. The very basic advantage related to fluorescence detection is its high sensitivity due to which fluorescence easily substituted the complicacy of marking a molecule by radioactive tracers for most of the biochemical measurements. In recent days fluorescence imaging revealed the intracellular localization of molecules and even extended up to the level of single-molecule detection, which in term is a research focus of the present era.

The journey of fluorescence started at the year of 1845, when *Sir John Fredrich William Herschel* observed a beautiful celestial blue colour from quinine solution[1] after irradiation by sunlight. After seven years *Sir George Gabriel Stoke* first coined (in 1852) the term fluorescence.[2] Interesting to note that quinine, one of the oldest known fluorophore on earth was itself responsible for development of fluorescence spectroscopy. During World War-II malaria epidemic caused several lives in the war fronts and war department was interested to study anti-malaria drugs including quinine. At the year 1950 National Institute of Health (NIH) developed the first practical fluorescence spectrophotometer to study anti-malaria drug assays majorly focusing on quinine.[3] Due to high sensitivity and cost worthy nature gradually the fame of fluorescnece started grasping several fields of apllications including daily life techniques. In 1877 the sensitivity fluorescenec was practically used for first time out of a research lab to show the underground connection of Danube and Rhine river streams.[4] This was shown by placing a large amaunt of fluorescein (a green fluorescent dye) in Danube, and around sixty hours latter the characteristic fluorescence started appearing from a stream that led to Rhine river. From such daily life application to research labs, gradually fluorescence became an indispensable tool in the field of research.

1.3. Fluorescence; What and Why?

In spectroscopy we often come across the term photoluminescence, fluorescence, and phosphorescence etc. Luminescence is the emission of light from an electronically excited molecule. Depending over the nature of the excited state the process of emission is typically subdivided into two categories namely fluorescence and phosphorescence. The basic properties of any electronic transition are very well described from Jablonski diagram named after *Professor Alexander Jablonski*[5]. A typical Jablonski diagram is shown **Figure 1.1** where the singlet (unpaired spin) ground, first, and second excited electronic states are represented as S_0, S_1, and S_2, respectively. A number of vibrational states within each of the electronic states are shown by 0, 1, 2, 3 etc. The decreasing spacing between consecutive vibrational levels is trivial and are well known outcome of anharmonicity of vibrational states and hence not extended in detail. The electronic transitions are shown by vertical arrows (**Figure 1.1**). When a molecule is irradiated by the light electrons from different ground (S_0) vibrational energy states jump to higher vibrational states of higher electronic states (S_n, where $n \geq 0$). This transition due to absorption of energy occurs in ~10^{-15} seconds or femtosecond time-scale, a time period too short for significant displacement of nuclei, (known as Franck-Condon principle). The energy difference between the S_0 and S_n excited states is too high for any thermal population at S_n and hence, light energy is required to populate the higher singlet electronic states. Following light absorption, several energy dissipative processes take place. The thermal relaxation of molecules from higher vibrational levels to the lowest possible vibrational state of that corresponding electronic state is known as thermal or vibrational relaxation and is usually completed within ~10^{-14}-10^{-11} seconds. Excluding few rare exceptions, molecules in solution phase rapidly relax to the lowest vibrational state of S_1 within a time scale of ~10^{-12} seconds (picoseconds) or less. This phenomenon of molecular transition within electronic states is termed as internal conversion (IC). The electronic transition of a molecule form its lowest possible vibrational state of first electronic state (S_1) to the ground vibrational states is termed as "**Fluorescence**". Since fluorescence lifetimes are typically near 10^{-8} to 10^{-9} (nanosecond) seconds, all other energy dissipative processes complete prior to fluorescence emission. Hence, fluorescence results only from a thermally equilibrated excited state, that is, the lowest energy vibrational state of S_1. Moreover, molecules from S_1 state can also undergo a spin conversion to the first triplet state T_1. Conversion of S_1 to T_1 is called intersystem crossing (ISC). Emission from T_1 is termed

"**Phosphorescence**" which is designated as another kind of luminescence. Electronic transition from T_1 to the singlet ground state (S_1) being spin forbidden, phosphorescence results a rate constant several orders smaller in magnitude than those for fluorescence, and occurs within a time scale of 10^{-3}-10^{3} seconds. Heavy atoms like bromine and iodine are known to facilitate phosphorescence in a molecule; the detailed mechanism is avoided as it's not a topic of interest of the present thesis.

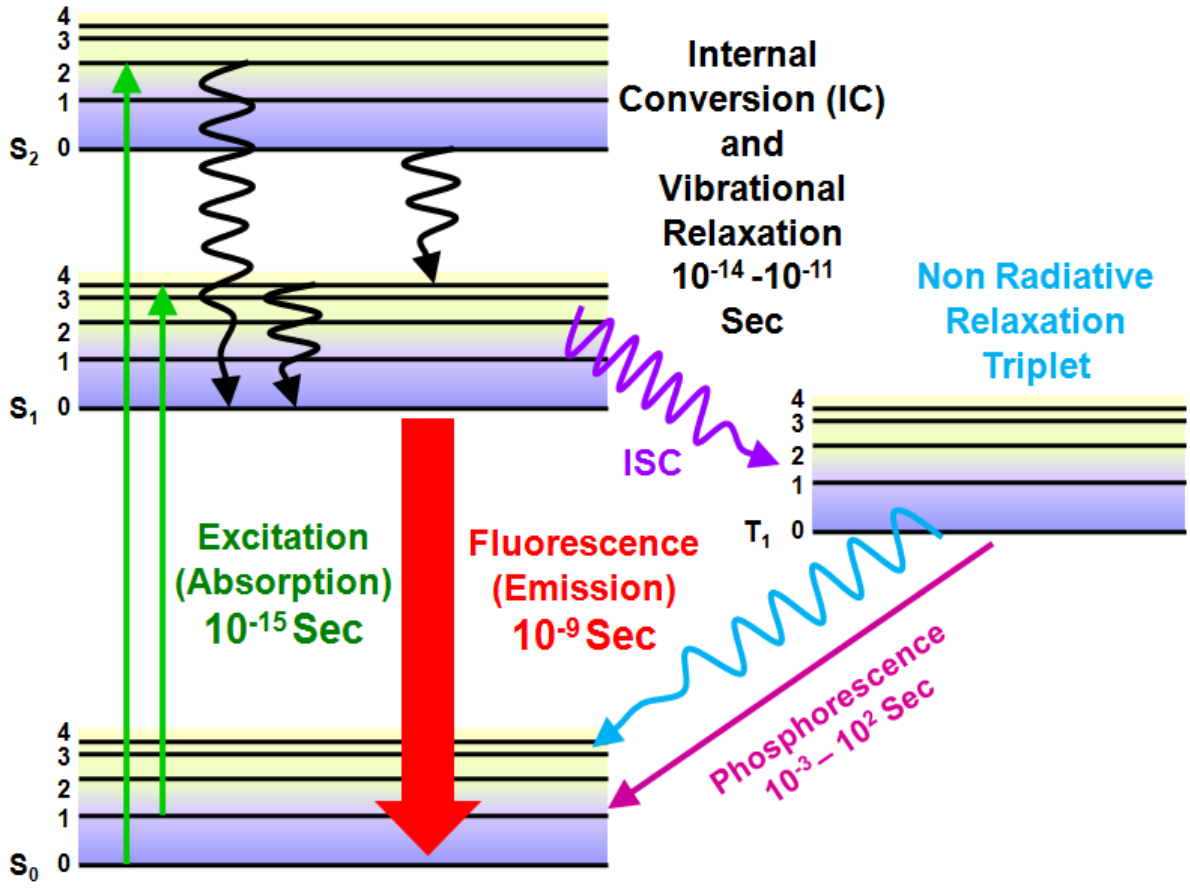

Figure 1.1. *Jablonski diagram showing different electronic and vibration transitions.*

When a fluorophore is excited and scanned the emission photons against wavelength, the resultant intensity/photon counts (in y axis) *vs*. wavelength (nm) or energy (cm^{-1}) spectrum is known as emission spectrum. As fluorescence emission is associated with lower energy gap compared to the absorption energy gap of the same molecule, hence fluorescence spectrum of a molecule always appears to be red shifted relative to its absorption. This shift of fluorescence spectrum compared to absorption spectrum is known as Stoke's shift (**Figure**

1.2) first observed by *G. G. Stokes* in 1852.[2] Moreover, fluorescence being a radiative transition from S_1 to S_0, emission maximum of a fluorophore mostly remains independent over its excitation. It is the emission intensity which alters with changing excitation wavelength. The very characteristic feature about the intensity of a fluorophore is usually

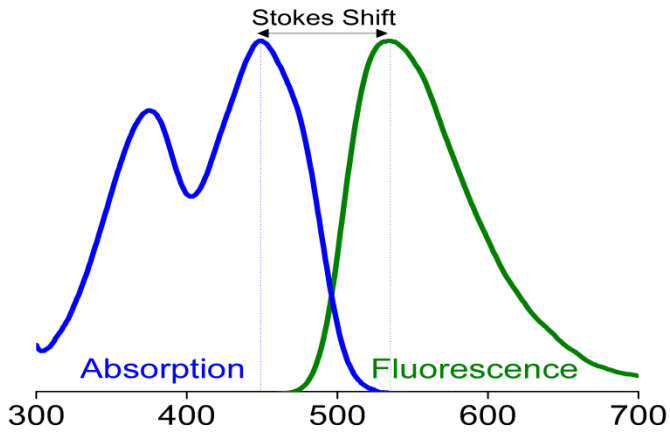

Figure 1.2. *Absorption and emission spectrum of FAD and respective Stokes shift shown.*

decided by the fluorescence quantum yield (Φ_f). Fluorescence quantum yield (Φ_f) for a molecule is defined as the ratio of number of emitted photons to the number photons absorbed by the molecule;

$$\Phi_f = \frac{Number\ of\ photons\ emitted}{Number\ of\ photon\ absopbred} \quad \ldots 1.1$$

Hence, the maximum fluorescence quantum yield can be 1.0 if the number of emission photons equal to the absorbed photons. However, this is an impossible situation as molecules have inherent non-radiative decay channels, like internal conversion(IC), intersystem crossing (ISC) etc. Another way to define the quantum yield of fluorescence is by the rate of excited state decays;

$$\Phi_f = \frac{k_f}{k_f + k_i} \quad \ldots 1.2$$

where, k_f is the rate of spontaneous emission and k_i is the sum of all non-radiative decay constants. Thus if the rate of any pathway changes both the excited state lifetime and the fluorescence quantum yield will be affected. The measurement of absolute quantum yield is a

tedious job, and, hence, mostly the relative fluorescence quantum is determined with respect to a fluorophore of known quantum yield with an identical experimental setup (excitation wavelength, slit widths, photomultiplier voltage etc.). The quantum yield is then calculated by;

$$\Phi_{sam} = \Phi_{ref} \times \frac{A_{sam}}{A_{ref}} \times \frac{Abs_{ref}}{Abs_{sam}} \times \frac{\eta_{sam}^2}{\eta_{ref}^2} \quad \ldots 1.3$$

where, Φ represents quantum yield, A represents area under the emission curve, *Abs* stands for fraction of light absorbed and η is the refractive index of the solvent. The subscript '*sam*' and '*ref*' is the abbreviated form of sample and reference, respectively.

1.4. Fluorescence Lifetime; the Time to Emit

Fluorescence lifetime measurement offers a dynamic (time dependent) feature of fluorescence. Moreover, it can correlate the impact of the surrounding factors (or environment) like ionic strength, hydrophobicity, quencher concentration, binding interaction to macromolecules, and the proximity of molecules to the excited state of the fluorophore in a time dependent manner. Hence, along with steady state measurements fluorescence lifetime measurements also appear as an incessant point of attention.

Before going to any detailing, it is important to know what exactly the word lifetime stands for. In simple words one can define lifetime as the time period up to which a photo-excited fluorophore resides in its excited state or the time required to relax back to its ground state. Mathematically lifetime can be defined as the time period within which $(1/e)^{th}$ of the excited state population returns to the ground state. Let us consider the extremely short laser pulse (δ pulse) is used to excite a fluorophore which results initial n_0 population in the excited state. After time t if n_t number of excited state molecules decay randomly which follows the resultant equation;

$$n_t = n_0 exp^{-\frac{t}{\tau}} \quad \ldots 1.4$$

As intensity is proportional to the number of molecules, hence equation 1.4 can be reformed in terms of intensity as;

$$I(t) = I_0 exp^{-\frac{t}{\tau}} \quad \ldots 1.5$$

Where, I (t) is the time dependent intensity collected from the fluorescence instrument, I_0 is the intensity at time t = 0. The I (t) vs. t plot results an exponential curve. By fitting the lifetime curve once can get the lifetime components along with its percentage contribution. Moreover, fluorescence lifetime also depends over the rate constants. The lifetime (τ) is the inverse of the total decay constant $\tau = (k_r + k_{nr})^{-1}$, where k_r and k_{nr} are the radiative and non-radiative rate constants, respectively. In case of multiple emitting species having different fluorescence lifetimes, the equation 1.5 looks like;

$$I(t) = \sum_{i=1}^{n} \alpha_i exp^{-\frac{t}{\tau_i}} \quad \ldots 1.6$$

where, τ_i represents the decay times, α_i represent the amplitudes of the components at t = 0, and n is the number of decay times.

1.5. Fluorescence Quenching; the Dumped Emission

Fluorescence quenching is a process by which the fluorescence intensity of a sample decreases. Various molecular interactions may lead to fluorescence quenching. These include ground state non-fluorescent complex formation, excited state reactions, energy transfer, electron transfer, collisional quenching etc. In broad sense, the quenching process is categorized by two major mechanisms, namely, dynamic (at excited state) or static (at ground state) quenching.

In case of dynamic or collisional quenching, the quencher and fluorophore diffuse during the excited state lifetime of fluorophore. Upon contact, the fluorophore returns to the ground state, without emission of a photon and without any permanent change in the molecule. O_2, I^-, Cs^+, acryl amide are few such quenchers known to actively participate in dynamic quenching process. The quantitative estimation of collisional quenching is done with the help of Stern-Volmer equation, as shown below;

$$\frac{I_0}{I} = 1 + K_{sv}[Q] \quad \ldots 1.7$$

where, I_0 and I represents the fluorescence intensity in absence and presence of quencher, K_{SV} is known as Stern-Volmer constant and Q is the concentration of the quencher. The plot of I_0/I against $[Q]$ (**Figure 1.3**) yields a straight line with intercept '1' and from the slope of the plot K_{SV} can be determined. Again it is already well known that;

$$K_{sv} = k_q \times \tau_0 \qquad \ldots 1.8$$

where, k_q is the bimolecular quenching rate constant and τ_0 is the lifetime of the fluorophore in absence of any quencher. It is quite evident that the value of bimolecular quenching constant is close to the diffusion controlled rate constant (k_d = 1×10^{10} M^{-1}). In case of a purely dynamic or collisional quenching I_0/I is equal to the τ_0/τ and hence the Stern-Volmer equation in terms of lifetime appears as;

$$\frac{\tau_0}{\tau} = 1 + k_q \tau_0 [Q] \qquad \ldots 1.9$$

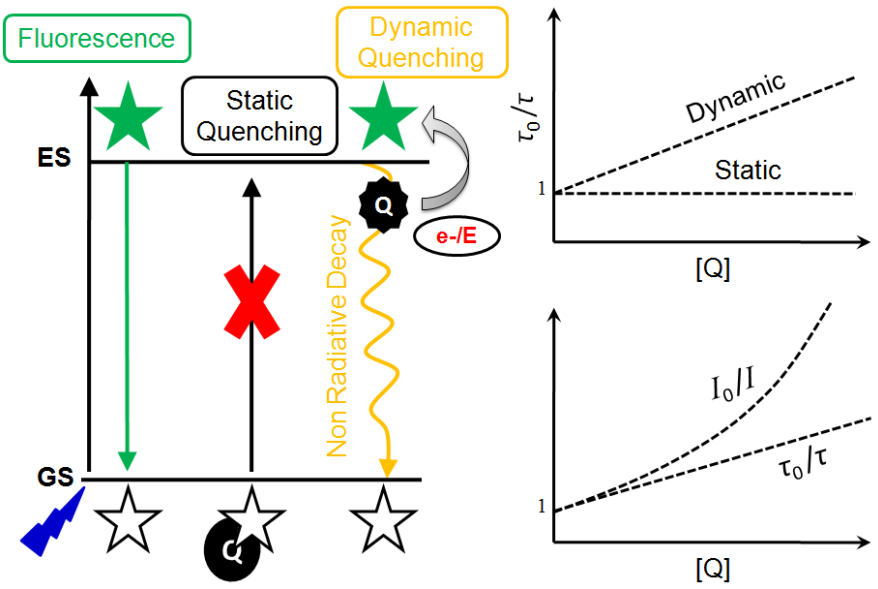

Figure 1.3. *A schematic representation of different kind of fluorescence quenching processes (static and dynamic. The plots at the right sides represents Stern-Volmer plot for different quenching processes like static, dynamic and static-dynamic combined.*

In certain cases, if the fluorophore forms a stable complex with another molecule in the ground state and the complex is non-fluorescent in nature, then the process of quenching is

known as static quenching. In such cases the dependence of fluorescence over the quencher concentration can be expressed by the following equation;

$$\frac{I_0}{I} = 1 + K_a[Q] \qquad \ldots 1.10$$

where, K_a stands for association constant. The static and dynamic quenching can be differentiated with the help of lifetime of the fluorophore. In case of static quenching lifetime will never change, as ground state complexation will decrease the number of freely fluorescing molecules in the ground state, but it cannot affect the lifetime of the fluorophore which are not complexed. It is the dynamic quenching, which directly affects the fluorescence lifetime. Hence, the lifetime results are the key factor to designate a process of quenching as static or dynamic. Interestingly possibilities may occur when both of static and dynamic quenching take place together and in such cases the fluorescence is governed by the following equation;

$$K_{app} = \left[\frac{I_0}{I} - 1\right]\frac{1}{[Q]} = (K_D + K_s) + K_D K_s[Q] \qquad \ldots 1.11$$

where, K_D and K_s are the dynamics and static quenching constants. A plot of K_{app} *vs.* [Q] provides the values of K_D and K_s from the slope and intercept.

1.6. Fluorescence Anisotropy; When Rotation Matters

When polarized light is applied to a bulk of randomly oriented fluorophores, those fluorophores whose transition moments are oriented in a direction close to that of the electric vector of the incident beam are preferentially excited. This phenomenon is called photo-selection (**Figure 1.4**). As the distribution of excited fluorophores is anisotropic, the resulted fluorescence will also be anisotropic. Any change in direction of the emission transition moment will induce a depolarization of fluorescence. Rotational diffusion changes the direction of transition moments and is one of the major causes of fluorescence depolarization. Anisotropy measures the extent of fluorescence depolarization, and indirectly provides the average angular displacement of the fluorophore that occurs between absorption and subsequent emission of a photon. The anisotropy value in absence of rotational diffusion of

fluorophore is termed as intrinsic anisotropy, denoted by r_0 and it arises when the absorption transition moment vector and emission transition moment vector are not collinear. This

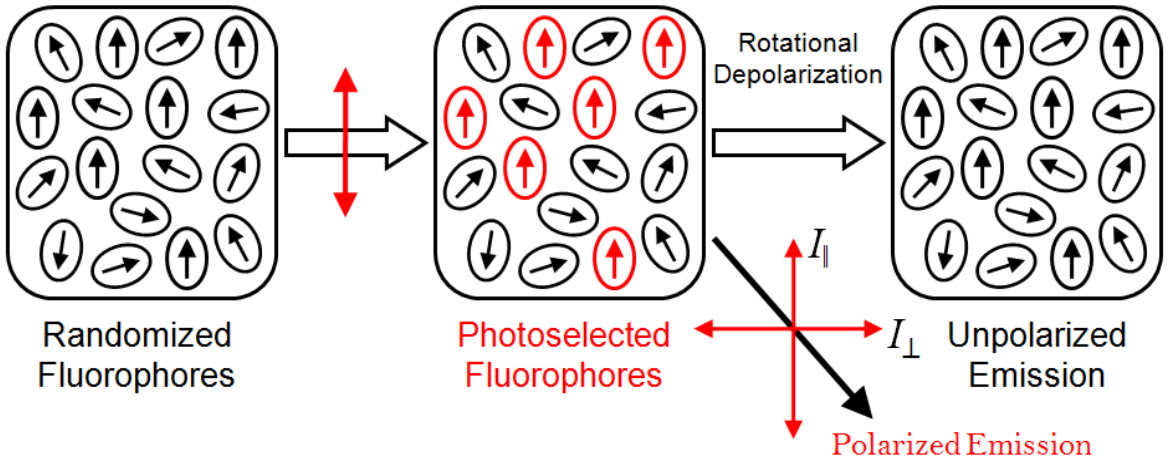

Figure 1.4. *Schematic representation of polarized excitation and de-excitation processes.*

intrinsic anisotropy (r_0) is usually measured by embedding the fluorophore in frozen poly alcohols.

The extent of depolarization depends on how quickly the fluorophore changes its orientation (the rotational relaxation time, τ_{rot}) compared to the fluorescence lifetime (τ).[6] The scrambling of orientations can occur by the whole molecule tumbling or by the rotation of only the fluorescent part. The rate of tumbling is related to the measured anisotropy by the Perrin's relationship[6, 7];

$$r = \frac{r_0}{1 + \frac{\tau}{\theta}} \qquad \ldots 1.12$$

Where r is the observed anisotropy, r_0 is the intrinsic anisotropy of the molecule, τ is the fluorescence lifetime and θ is the rotational time constant. This analogy is valid only when the fluorophores are relatively far apart.

Molecular depolarization or fluorescence anisotropy has been extensively used to measure the binding constants and kinetics of reactions that cause a change in the rotational time of the molecules. If the fluorophore is bound to a small molecule, the difference between bound and unbound state anisotropy will be small. If the fluorophore is attached to the bigger

protein through a stronger binding interaction, the difference in anisotropy between bound and unbound states will be reasonably large and easily distinguishable.

Fluorescence anisotropy is also applied to microscopy with use of polarizer in the path of the illuminating light and also before the camera. This can be used to study the local viscosity of the membranes, giving information about the membrane microstructure and the relative concentrations of various lipids. This technique has also been used to detect the binding of molecules to their partners. A very detailed description for instrumentation of anisotropy measurements, equations for anisotropy calculation and its respective data analysis have been discussed in **Chapter 3**.

1.7. Solvation Dynamics

1.7a. What is Solvation Dynamics?

Excluding the atmospheric part of the earth, most of the chemical reactions and biological processes occur in solution phase. This trivial fact spurred tremendous enthusiasm for a prolonged duration aimed in exploring the effect of solvents over chemical reactions and

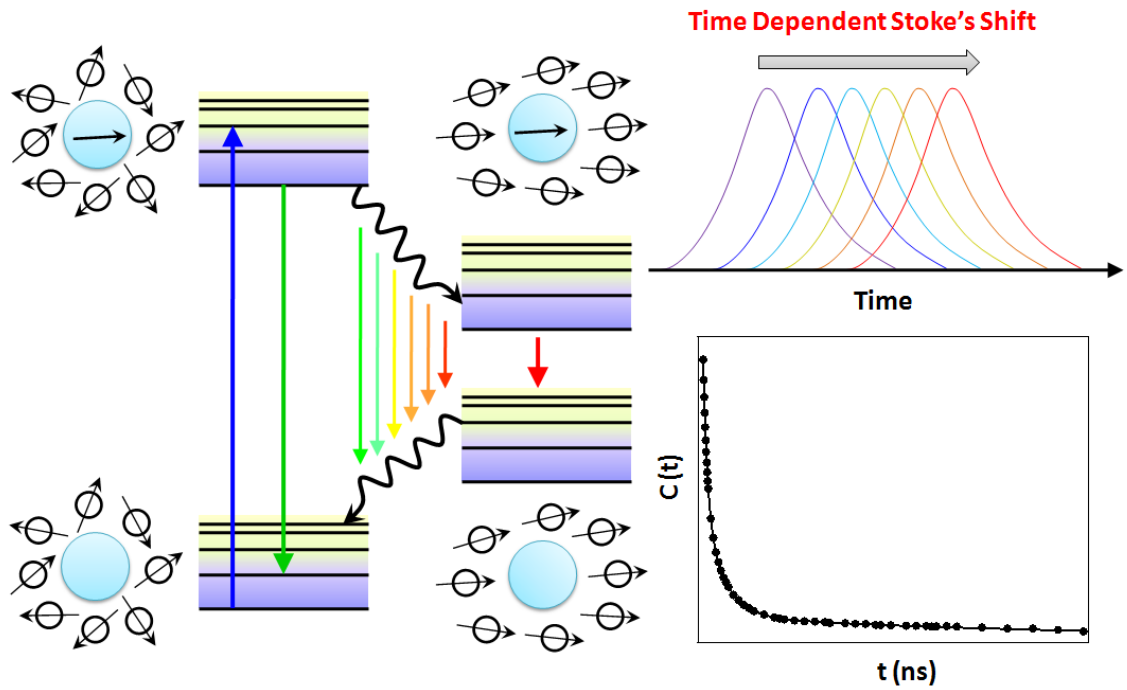

Figure 1.5. *Schematic representation of solvent reorientation around phtoto-excited dipole. Right side shows time dependent Stokes shift (TDSS) and respective solvation dynamics plot.*

biological processes. In an urge to develop a unified principle behind solvation of molecules experimentalists and theoreticians had invested a monumental effort till date. Still the dynamic nature of solvents complicates its effects over reaction dynamics and solvation dynamics remains as focus of research for a prolonged duration of time.

Light offers a very clean way to selectively excite molecules in terms of energy and time. Any chemical or photochemical reaction in condensed phase results redistribution of charge within the chromophores. If a chromophore is void of polarity in the ground state a photo excitation results an excited dipole due to charge redistribution in its excited state. Hence the first step of any photo induced process is a generation of an instantaneous dipole of the absorbing atom or molecule due to the modification of the field of forces within the molecule. The very next obvious outcome is the rearrangement of solvent molecules around the dipole. This rearrangement of the solvent molecules around an excited state molecular dipole has been termed "solvation dynamics" and is illustrated in **Figure 1.5**. As the solute is excited instantaneously, the solvent species find themselves at time t=0 in a relatively high energy random configuration due to the sudden change of field of forces. Subsequently, they begin to move and rearrange to reach their new equilibrium configuration (**Figure 1.5**). This nuclear motion mainly consist rotational and translational motions. Considering water as the solvent, rotational motion will include libration, while translations will further include the intermolecular vibrations due to extensive hydrogen bonding. The two specific motions, libration and intermolecular vibration are of relatively high frequency and play a dominant role in the initial part of the solvation. Librational (originated from Latin word *librare* which means "to balance") motion is a type of reciprocating motion in which an object with a nearly fixed orientation repeatedly moves back and forth. On the other hand vibration is any kind of oscillation which occurs about an equilibrium point. These oscillations may be periodic (e.g. pendulum) or random (movement of a tire on a rough road) depending over the external conditions. Due to time dependent reorientation of the solvent molecule around the excited state dipole a highly solvent equilibrated state results and the solvation completes. During this whole process the emission spectrum at each consecutive time gets more and more red shifted as it corresponds to energetically more stabilize state. This phenomenon of time resolved red shift of emission is known as time dependent Stokes' shift (TDSS).[8-12] The wavelength dependent temporal decays of emission and TDSS (**Figure 1.5**) are regarded as major evidences of solvation dynamics. The TDSS technique is the most popular method of

studying dynamics. The solvation dynamics is followed by the decay of the solvent response function, C(t), which is defined as;

$$C(t) = \frac{\nu(t) - \nu(\infty)}{\nu(0) - \nu(\infty)} \quad \ldots 1.13$$

Where, ν (0), ν (t) and ν (∞) are the energies in terms of emission frequencies at time zero, t and ∞, respectively. The solvation time, τ_s, is the time constant of the decay of the response function C(t), so that C(t) = exp (-t/τ_s). If the decay of C(t) is multi exponential, e.g. [a_1*exp (-t/τ_{s1}) + a_2*exp (-t/τ_{s2})+…+ a_n*exp (-t/τ_{sn})], one considers the average solvation time, $\langle\tau_s\rangle$ = ($a_1\tau_{s1}$ + $a_2\tau_{s2}$+…+ $a_1\tau_{sn}$). The solvation time τ_s is also known as longitudinal relaxation time of the solvent. According to simple continuum theory, the solvation time is related to the dielectric relaxation time, τ_D [13-15] as;

$$\tau_s = \frac{\varepsilon_\infty}{\varepsilon_0}\tau_D \quad \ldots 1.14$$

For most polar liquids, $\frac{\varepsilon_\infty}{\varepsilon_0} < 1$. As a result, the solvation time, τ_s, is shorter than the dielectric relaxation time, τ_D. Thus the solvation is inevitably related to dielectric relaxation of the solvent. Hereafter we considered the models describing solvation and avoided the detailing about the measurements and analysis of solvation data, as very extensive description for the same is given in **Chapter 3**.

1.7b. Theoretical Aspects of Solvation Dynamics

1.7b.1. Continuum Model Theories

(i) Homogeneous Dielectric Models

This is a generalization of the equilibrium solvation models of Born and Onsager[16] to the time domain. In this model the solvent has been considered as a continuous medium instead of individual solvent molecules. In this case, the frequency (ω) dependent dielectric continuum, ε(ω) is given by;

$$\varepsilon(\omega) = \varepsilon_\infty \frac{\varepsilon_0 - \varepsilon_\infty}{1 + i\omega\tau_D} \quad \ldots 1.15$$

where, ε_0 and ε_∞ are the static and infinite frequency dielectric constant of the solvent and τ_D is the Debye relaxation time of the dipolar solvent.[13, 14] The solvation energy is obtained by evaluating the reaction field of the polar solute molecule inside the molecular cavity. The predictions of homogeneous continuum theories[13, 15, 17] are most simply expressed in terms of solvation time correlation function defined by;

$$C_S(t) = \frac{E_{sol}(t) - E_{sol}(\infty)}{E_{sol}(0) - E_{sol}(\infty)} \quad \ldots 1.16$$

where, E_{sol} (t) is the time dependent solvation energy. If the dipolar molecule is assumed to be a spherical cavity with a point dipole at its center and the solvent is approximated by a dielectric continuum with a single relaxation time, then the continuum model predicts that the solvation time correlation function is a single exponential with a time constant given by;

$$\tau_L^D = \frac{2\varepsilon_\infty + \varepsilon_C}{2\varepsilon_0 + \varepsilon_C} \times \tau_D \quad \ldots 1.17$$

where, ε_c is the static dielectric constant of the cavity. In the case of an ion the continuum model predicts slightly faster solvation, and the time constant is given by;

$$\tau_L = \frac{\varepsilon_\infty}{\varepsilon_0} \times \tau_D \quad \ldots 1.18$$

Where, τ_L is the longitudinal polarization relaxation time of the unperturbed solvent. For typical values of ε_0, ε_∞, and ε_c, the difference between τ_L^D and τ_L is unimportant and one can simply state that homogeneous continuum models predict that the solvation correlation function should relax exponentially with a time constant given by τ_L. For most polar solvent, τ_L is the order of magnitude smaller than τ_D as $\varepsilon_0 > \varepsilon_\infty$.

According to simple homogeneous continuum model, a single solvent relaxation time should be observed. However, experimentally observed $C_s(t)$, is generally non-exponential in nature and non-exponentially increases with the polarity of the solvent. Hence, experimental $C_s(t)$ cannot be fitted to the simple homogeneous continuum model. Moreover, experimentally measured solvation times are generally larger than the predicted τ_L values and usually vary between τ_L and τ_D. In some cases, solvation times were measured to be more

than an order of magnitude longer than τ_L.[18] The assumptions that the molecular cavity is spherical and the solvent dielectric response is of simple Debye form are the possible reasons for the lack of quantitative success of the continuum models.[15, 17] Both the assumptions are relaxed in later studies[19] that investigated consequences of an ellipsoidal cavity and a non-Debye dielectric response. It was noticed that if the molecular cavity is ellipsoidal, the decay is bi-exponential even with a Debye form of $\varepsilon(\omega)$; however, the relaxation times differ at most 30% to 40% under extreme conditions. The effect of the non-Debye form was studied by the Davidson-Cole [14, 20] and Cole-Cole[14, 21] form;

$$\varepsilon_{DC}(\omega) = \varepsilon_\infty + [\frac{\varepsilon_0 - \varepsilon_\infty}{1 + i\omega\tau_0}]^\beta, 0 < \beta \leq 1 \quad \ldots 1.19$$

$$\varepsilon_{CC}(\omega) = \varepsilon_\infty + \frac{\varepsilon_0 - \varepsilon_\infty}{1 + (i\omega\tau_0)^\delta}, 0 < \delta \leq 1 \quad \ldots 1.20$$

Both forms have a distribution of relaxation times about ε_0 which contributes to ε_∞. The Laplace transform can be obtained numerically and C(t) can be fitted well by a stretched exponential function.[9, 13, 19]

$$C(t) = \exp[-(t/\tau)_\alpha], 0<\alpha<1 \quad \ldots 1.21$$

It was observed that short time dynamics were significantly affected even when the deviation from Debye behavior was small. The agreement between the predicted and observed C(t) is good for the polar aprotic solvents, when one considers appropriate dielectric parameters for the solvents.

(ii) Inhomogeneous Dielectric Models

The homogeneous continuum model of solvation dynamics ignores the details of solute-solvent interaction, and the spatial and orientational order, which are present in a dense dipolar liquid. Bagchi *et al.*[22] and Castner *et al.*[23] proposed an inhomogeneous dielectric continuum model to rectify some of these shortcomings. The basic idea is the differential response of solvent molecules that are very close to the polar solute molecule responses differently than those are located distantly. This difference may arise from the strong electric field of the ion or the dipole, or from some specific solute-solvent interactions, such as

hydrogen bonding. In this model[22, 23] a distance dependent dielectric constant, $\varepsilon(r,\omega)$ was proposed. According to this model,

$$\varepsilon(r,\omega) = \varepsilon_\infty + \frac{\varepsilon_0(r) - \varepsilon_\infty}{1 - i\omega\tau_D} \quad \ldots 1.22$$

with the boundary condition, $lim_{r\to\infty}\, \mathcal{E}_0(r) \to \mathcal{E}_0$, where ε_0 is the bulk dielectric constant. The merits of these models are the intuitive picture of solvation dynamics and incorporation of some aspects of solute dynamics and solute-solvent interactions. The inhomogeneous continuum models exhibited many differences from simple continuum models, such as non-exponential $C_s(t)$ response and solute size sensitivity. Many of the predictions of the inhomogeneous continuum models are in good agreement with experiments[9, 18, 24] and microscopic theories.[25, 26] However, since $\varepsilon_0(r)$ is not an observable quantity, this model could only help rationalize experimental results rather actually predict them.

1.7b.2. Microscopic Theories of Solvation Dynamics

The molecular insight of solute-solvent interactions is necessary in order to understand the dynamics of solvation. Nichols *et al.*[25] and Rips *et al.*[26] derived analytic expression for ion and dipole solvation dynamics within a non-equilibrium mean spherical approximation (MSA) model, which was first proposed by Wolynes[27]. MSA theory is helpful to predict longer relaxation time from experimental results. However, this theory considers only the rotational relaxation of the solvent molecules, and is devoid of other solvent relaxation modes, among which translational modes of relaxation is most prominent. Later on Bagchi and coworkers[28-31] have focused on the role of translational diffusion in the dynamics of solvation by employing Smoluchowski-Vlasov equation. Experimentally, the role of translational mechanism was also noted by Su and Simon.[32, 33] They showed that translational motion significantly accelerates near the solvation probe. Bagchi and co-workers has developed self-consistent microscopic treatment to study the effects of self-motion of the polar solute on solvation dynamics.[34, 35] Several statistical mechanical theories of non-polar solvation have been proposed, such as viscoelastic continuum model of Berg[36], the molecular theory of Skinner and co-workers[37, 38] based on the Smouluchowski equation and linearized solvation theories, including the surrogate Hamiltonian method of Friedman and co-workers[39, 40].

Microscopic calculation of the solvation dynamics of ion in liquid water is presented by Roy and Bagchi.[41] The calculated solvation time correlation function shows an ultrafast Gaussian decay, ~70-90% of the total solvation completed <50 fs, followed by an exponential decay with time constant equal to 250 fs and 1 ps. These results are in excellent agreement with experimental findings of Barbara and Jarzeba.[24] They reported that the rotational, librations and the intermolecular translational modes of water contribute significantly to the initial Gaussian decay, whereas O-O stretching of O-H-O vibrational stretching modes are considered as under damped. In a later study, they concluded that the initial part of ultrafast solvation in water is essentially controlled by the macroscopic polarization modes of the solvent arises from the intermolecular vibrational and librational modes.[42] They also studied the effect of isotope substitution of solvation dynamics and found that a significant isotopic effect may contribute in long time solvation dynamics results. A simple molecular hydrodynamic theory has been used to calculate both the initial Gaussian and the long time exponential decays in the solvation of a rigid ion in methanol.[43] The theory predicts that non-linear response in the solvation dynamics of a single rigid ion in water and acetonitrile appears only after 70-80% of the relaxation, whereas for methanol nonlinearity may appear somewhat earlier.[43]

The effort was also given to understand the origin of basic of solvent response and the mechanism in non-hydrogen bonded solvents.[44] A theoretical study on ionic solvation in acetonitrile was carried out by Roy *et al.*,[45] which was in close but not perfect agreement with experimental observations.[24] Later Bagchi *et al.*[46] carried out ultrafast solvation dynamics in three non-associated polar solvents, namely, acetonitrile, DMSO and acetone using molecular hydrodynamic theory. For acetonitrile dielectric data gives excellent agreement with experimental results, whereas for DMSO and acetone, the present theory predicts slower decay than the experimental observation.

1.7c. Literature Reports of Solvation Dynamics Studies

1.7c.1. Solvation Dynamics in Pure and Mixed Solvents

Molecular dynamics (MD) simulation played a pivotal role to envisage solvation responses and determining the molecular origin of the solvent dynamics.[47-57] Most of the simulation studies relate solvation of pure water molecules.[23, 48, 50, 51, 57] Although a wide range of solutes and a variety of water potentials have been employed, the observed dynamic exhibits many

similarities. The most common feature is the bimodal nature of solvation dynamics. Water exhibits a very rapid initial relaxation (20-50 fs), followed by a much slower (1-2 ps) long time trail. In most cases over 50% the solvation energy relaxation takes place via fast part of the solvation response.[57] The librational motions of water molecules are believed to be responsible for this ultrafast relaxation.[57] Simulation studies indicate that the solvation response in acetonitrile is also bimodal in nature consisting of initial Gaussian components (~100 fs) and a slow exponential decay; however the librational component is not prominent like water.[52-55] Notably MD simulations predicted that solvation dynamics in methanol also has almost similar feature as that of water and acetonitrile.[53, 56, 58] But the short time Gaussian contribution is much smaller, accounting for only 10-20% of the solvation response.[53, 56, 58] Thus, the solvation dynamics in methanol is slowest compared to water and acetonitrile. This is because there are three distinct ways of performing the rotational motion (with nearly equal moments of inertia) in water, whereas in methanol there is only single way. Therefore, the effectiveness of free hydrogen bond rotation in relaxing C(t) is much lesser in water than methanol[56, 58]

Solvation dynamics various bulk liquids have been extensively studied using time-domain techniques such as fluorescence up-conversion,[9, 59-61] Optical Kerr effect[62, 63] three photon echo peak shift (3PEPS)[64-66], ultrafast fluorescence depletion spectroscopy[67], inelastic X-ray scattering[68] and polarization damping method[69]. Among others fluorescence up-conversion appeared as the most popular technique to study solvation dynamics in polar and non-polar liquids. Jarzeba *et al.*[60] first reported solvation dynamics of *7-(dimethylamino)coumarin-4-acetate* ion in water on femtosecond time scale using up-conversion technique. Later on using the up-conversion technique, Vajda *et al.*[61] reported that solvation of pure water occurs with the time constants of <50 fs (26%) and 310 fs (74%). Huppert and co-workers[62] resolved the bimodal behavior by time resolved heterodyne optical kerr effect, in water, with an ultrafast component of less than 100 fs. Lang *et al.* employed three pulse photo echo peak shift (3PEPS) measurement to study aqueous solvation dynamics and showed that the majority (~60%) of the aqueous solvation response occurred on an ultrafast time scale of ~30 fs.[64] Horng *et al.*[70] reported methanol solvation through fluorescence upconversion technique by using C-153 as the solvation probe. They concluded that vibrational relaxation has a very negligible role (even up to a very short time regime within ~100 fs) in time dependent shift of methanol. Joo *et al.*[65] studied the solvation dynamics of alcohols with variable alkyl chain length by third-order nonlinear time-resolved

spectroscopic techniques and theoretical measurements. They reported a common initial solvation response of ~100 fs in methanol, ethanol and butanol for which the amplitude decreased with increasing alkyl chain length. Cho *et al.*[63] have used vibrational characteristics of liquid dynamics to describe heterodyne detected optical Kerr effect measurements on acetonitrile, via a Brownian oscillator model. Fleming and co-workers[71] measured the solvation time of LDS-750 in acetonitrile and predicted the average Debye relaxation time ~4.3 ps. Solvation dynamics of bulk formamide have also been explored thoroughly and measurements show that the extensive hydrogen bonding results reasonably slower solvation dynamics in formamide.[70, 72, 73] The inertial component of the solvation dynamics, which comprises more than 50% of the response in water, is represented by a mere 10% of relaxation in formamide.[70] The diffusive components of the formamide solvation dynamics are also slower than those of water. Solvation dynamics in many other polar solvents, like ethylene glycol[70], dimethylsulfoxide[9, 74, 75], ethyl acetate[10] etc also have been studied. Notably the solvation dynamics in these polar solvents also proceeds with bimodal time scales: an ultrafast (~200 fs) and slower (1-100 ps) components. Solvation dynamics of non-polar solvents (dioxane and benzene) also exhibit time dependent Stokes' shift.[70, 76] The fact that these non-polar solvents do solvate probe solute is a consequence of the large quadruple and high order electrostatic moments of these molecules.[70, 76]

1.7c.2. Solvation Dynamics in Ion-Solvent Mixture and Ionic liquids

Not only solvents but the effect of ion atmosphere is also essential to understand dynamics of chemical reaction in electrolyte solution. Fist time Van der Zwan and Hynes theoretically calculated the time of ion atmosphere relaxation around a solute dipole which included only diffusional motion of ion but not the contribution of inertial motion of ions.[77] Later Chandra and Patey presented the molecular theory of ion solvation dynamics in electrolyte solvation. Their calculations predicted a very fast inertial relaxation time followed by a slow long time decay associated with the organization of ion atmosphere around the solute ion.[78] Chandra *et al.* also presented a theoretical analysis regarding salt concentration effect on solvation dynamics in electrolyte solvation.[79] This theory predicts that when solvent molecules are characterized by the large moment of inertia the initial Gaussian decay is governed by ion motions and depends strongly over salt concentration. Chandra and Mahajan presented a molecular theory of ions-solvent dynamics in electrolyte solution including both diffusive

and non-diffusive (such as inertial) modes of relaxation.[80] Using computer simulation Neria and Nitzan have shown that ionic solution solvation is basically biphasic in nature, comprising a fast Gaussian time constant and a slow exponential decay time constant. Among these, the Gaussian time constant is independent on salt concentration whereas the slow exponential time constant strongly depends on the electrolyte concentration and it decreases when the electrolyte concentration decreases.[81] Later Zhang *et al.* reported LiF ionic pair solvation dynamics through Ab-initio molecular dynamics simulations for two different spin states namely singlet (S) and triplet (T) states, and found that the singlet state solvation occurs very fast (within ~50 fs).[82] Later on Yamazaki *et al.* studied ion solvation in water-urea mixture through molecular dynamics simulations and the reference interaction site model (RISM) integral equation theory. They reported that urea preferentially solvates positively charged species and the solvation free energies indicating that larger solutes favor the transfer from water to a water−urea mixture.[83] Recently Criscenti *et al.* have compared the solvation of alkali-earth metal ions in carbon dioxide and water using molecular dynamics simulation. They suggested that solvation energies of these cations are larger in water than in carbon dioxide which results preferential solvation into water. For both aqueous and CO_2 solutions, the solvation energies decreased with cation size and increased with cation charge.[84] Most recently absolute solvation free energy of the lithium cation in methanol is calculated by the cluster-continuum quasi-chemical theory of solvation.[85] The obtained solvation free energy of the proton was -253.6 kcal mol^{-1}.[85] Several experimental results have been reported exploring the ion solvation effect.[86-91] Huppert and co-workers measured the static and dynamic solvation in molten tetraalkylammonium salts by several Coumarin dyes using time resolved fluorescence technique and reported a biphasic solvation within picoseconds-nanosecond time scale.[86-88] Chapman and Maroncelli also investigated solvation of polar and aromatic solute in ionic solutions. The ionic solvation occurs on 1-10 ns time scale which corresponds to the ion/solvent rearrangement in the first solvation shell of the probe.[89] Palit *et al.* compared the solvation dynamics of directly injected electrons and fluorenone anion in 4 different primary alcohols through picosecond pulse radiolysis and they observed non-exponential dynamics for both. For electron solvation out of 3 different solvation components, <15 ps represents the initial time scale of the dynamics, ~80 ps corresponds to translational motion leading to structural changes of the hydrogen bonding network of inner solvation shell. The ~1800 ps component of electron solvation represents restructuring of the hydrogen bond network of the solvent in the outside region of the

solvation shell. For fluorenone ion solvation the contribution of the shortest component (15 ps) in all four alcohols appeared much longer than the electron solvation time in the corresponding solvents. This component is assigned to the restructuring of first solvation shell by breaking the solvent-fluorenone hydrogen bonds.[90] Most recently Zeng *et al.* performed the solvation dynamics of Li^+ ions in water, methanol and ethanol. According to their observation Li^+ forms stable tetrahedral coordination in water and methanol than that in ethanol, and results slower diffusion of water in its first solvation shell.[91]

It has been ~15 years since the field of ionic liquid (IL) research appeared in feature. Since then ILs are extensively used in chemistry as a green solvent and hence the solvation behavior of ILs[92-105] are becoming the burgeoning point of interest. Samanta and co-researchers[92-94] have extensively studied the solvation dynamics of several imidazolium ionic liquids and reported a biphasic dynamics occurring in picosecond and nanosecond time scales. This dynamics of ILs are attributed to smaller anions and the collective diffusional motion of the cations and anions, respectively. Later Samanta and coworkers studied the solvation dynamics using coumarin-153 (C-153), 4-aminophthalimide (AP), and 6-propionyl-2-dimethylaminonaphthalene (PRODAN) probes in pyrrolidinium ionic liquid *N-butyl-N-methylpyrrolidinium bis(trifluoromethanesulfonyl)imide* ([bmpy][Tf_2N]) which has a comparable polarity with imidazolium ionic liquids. They also observed biphasic solvation containing a 115−440 ps component, and a very long solvation component of 610−1395 ps.[98] Maroncelli and co-workers measured the solvation dynamics in *1-butyl-3-methyl imdazolium hexafluorophosphate* ([bmim][PF6]) within the temperature range 298-355 K using 4-aminophthalimide (4-AP) as a probe. They reported a biphasic solvation markedly different in time scale which are <5 ps and ~1 ns. The fast component (<5 ps) arises due to the translational adjustment of the ions within the solvation structure present at the time of solute excitation. The slow component (~ 1 ns) is linked to solvent viscosity and presumably involves large-scale rearrangement of solvation structure.[99] Chakrabarty *et al.* reported solvation dynamics using two Coumarins (C-153 and C-152) in two room temperature ionic liquids (*[bmim][PF6] and 1-hexyl-3-methyl imdazolium hexafluorophosphate, [hmim][PF6]*). They also found biphasic as well as drastically retarded solvent relaxation in these ionic liquids. The ionic motions are found to be responsible for solvation in these ionic liquids.[100] Petrich *et al.* experimentally and theoretical investigated the role of dielectric constant (DC) in solvation for non-glassy and non-supercooled ILs. A relative comparison between comparison of imidazolium liquids with their pure organic counterpart butyl

imidazole suggested that not the translational motion of ions but the DC may be the predominant factor in short-time solvation of ionic fluids.[101] More recently Zhang *et al.* has designed simple qualitative scale which correlates the conductance and solvation time of 34 different room temperature ionic liquids using a simple mathematical formula $\ln(\langle\tau_{solv}\rangle/ps) = 4.37 - 0.92 \ln(\sigma_0/S\ m^{-1})$.[102] Terranova *et al.* have explored the mechanism of complex solvation kinetics over a broad range of time scale from femto- to nano-second in *1-ethyl-3-methylimidazolium tetrafluoroborate* [emim][BF_4] using Coumarin 153 (C-153). They revealed preferential solvation by the emim cations along with translational and rotational motions BF_4 anions as dominant contributor to solvation dynamics.[103] Shim *et al.* studied temperature dependent solvation dynamics of *1-butyl-3-methylimidazolium hexafluorophosphate* ([bmim][PF_6]). Although the ultrafast inertial component of solvation dynamics remained unchanged with the increase in temperature, the dissipative relaxation components become faster as the temperature increases.[104] Very recently Zhang *et al.* studied solvation dynamics in *1-butyl-3-methylimidazolium tetrafluoroborate* ([bmim][BF_4]) in water through dielectric relaxation method using coumarin 153 (C153).[105] They predicted the solvation response functions by a simple dielectric continuum model, and observed that the solvation here is also biphasic like neat ILs. They observed a fast solvation component (0.2 ps) over wide range of water mole-fraction ($0.1 \leq$ water mole fraction ≤ 1), along with a long component extending over picosecond to nanosecond range, which decreases with addition of water in IL.[105]

1.7c.3. Solvation Dynamics in Micelles and Mixed Micelles

Dynamics of water in confinement environment is always expected to be retarded. While solvation is probed in micelles, the probe may reside in three possible locations, namely, the bulk water, the dry micelle core and the Stern layer. Probe in bulk water offers sub-picosecond solvation time whereas in core (which resembles with aliphatic hydrocarbons) shows no solvation or Stokes' shift. If the probe stays in the Stern layer, the solvation dynamics may be quite different from that in the bulk water because the mobility of water molecules may be considerably constrained in the Stern layer. Sarkar *et al.*[106] and Datta *et al.*[107] studied solvation dynamics of C-480 and 4-aminophthalimide (4-AP) in neutral (TX-100), cationic (CTAB), and anionic (SDS) micelles. It was shown that for SDS, CTAB, and TX-100 give average solvation times 180 ps, 470 ps and 1450 ps, respectively for C-480[106]

and 80 ps, 270 ps, and 720 ps for 4-AP respectively, [106, 107]. The observed solvation time is ~3 orders magnitude slower than the bulk water.[106, 107] Later on Hara *et al.* studied the effect of high pressure effect on the solvation dynamics of C-153 in TX-100 micelle.[108] With increase in pressure, the solvation dynamics became faster and it was attributed to the weakening of hydrogen bond with pressure. The ultrafast components of the solvation dynamics in micelles were detected by femtosecond upconversion study.[109] The measured solvation dynamics consists of components of 2.1, 165, and 2050 ps for TX-100 and 0.23, 6.5 (average 1.75 ps), and 350 ps for CTAB using 4-(dicyanomethylene)-2-methyl-6-(p-dimethylaminostryl) 4H-pyran (DCM) as a probe.[109] Sen *et al.* [110] reported the solvation dynamics of DCM in secondary aggregates of bile salt (sodium deoxycholate, NaDC) and observed tri-exponential components with time constants of 110, 700, 2750 ps.[110] These components were significantly slower than those in bulk water. The observed slow dynamics in all these micelle systems was attributed to trapped water and ions present at the central region of the bile salt aggregate. Chakrabarty *et al.*[111] reported solvation dynamics of C-480 in pure TX-100, pure NaDC and mixed micelles of TX-100 and NaDC. Results showed that solvation time in pure NaDC and TX-100 were 3.35 ns and 1.51 ns respectively, but in mixed micelles, it is 2.27-3.26 ns. The relatively slow dynamics in the Stern layer of the NaDC micelles was appearing due to the motion of the Na^+ ions and the water molecules confined in the micellar cavity. In the mixed micelles, the solvation dynamics becomes relatively faster because of the removal of Na^+ ion from the Stern layer. They have also studied the solvation dynamics of Coumarin 480 (C-480) and Coumarin 490 (C-490) in neutral polyoxyethylene lauryl ether (Brij-35) and polyoxyethylene cetyl ether (Brij-58) micelles respectively.[112] The average solvation time of C-480 in Brij-35 micelle was 949 ps whereas in Brij-58 it time was 960 ps. The average solvation time of C-490 in Brij-35 and Brij-58 were 439 and 545 ps, respectively. The fast component of the micelle solvation was attributed to the water molecules present at the palisade layer of the micelle whereas, the slow solvation component was attributed to the hydrogen bonded water molecules to the polar heads of the micelle.[112] Later on Chakrabarty *et al.* studied alkyl chain length and head group size dependent solvation dynamics of C-480 CTAB micelle and mixed micelle.[113] The average solvation was found retarded from CTAB micelle (812 ps) to CTAB+CDAB mixed micelle (980 ps). The sluggish solvation was attributed to increased alkyl chain length and head group size which resulted a more closed packed micelle and hence restricted water motion.[113] Balasubramanian and Bagchi carried out a computer simulation of the hydrogen bond

dynamics,[114] and solvation,[115] at the surface of micelle. The decay of C(t) at the micellar surface[115] was fitted to a triexponential function having components, 1.6 ps, 4.3 ps, and 30 ps which appeared close to the experimental observations.[109] Kumbhakar studied the influence of ionic surfactants (CTAC and SDS) over the solvation dynamics of C-153 in tri block copolymer (P123 and F127) micelle and detected a biphasic solvation with increasing surfactant concentration.[116] Distinctly two different water solvation times ~0.5 ns and ~2.5 ns were attributed to the mechanically (non specifically trapped water molecules) trapped and thermodynamically (hydrogen bonded water molecules with oxygen atoms of the head group) bound water molecules respectively.[116] Later on Dey *et al.* reported the P123-CTAC mixed micellar solvation dynamics by C-480.[117] In contrary to Kumbhakar's results, Dey *et al.* reported a tri-phasic solvation dynamics with three distinct decay components of 2 ps, 60 ps and 4000 ps. They assigned the 60 ps component (which was mostly varying with surfactant concentration) to the polymer chin dynamics whereas the shortest and longest decay components were attributed to the free water and bound water in the micellar corona region, whereas the 2 ps was attributed to the bulk motion of water.[117] Recently Das *et al.* studied the solvation dynamics of C-151, C-152, C-153, C-480 and C-481 in [pmim][BF_4]-P123 mixed micelle and detected three distinct solvation components of ~5 ps, 350 ps and 4000 ps.[118] The very fast component was attributed to the ultrafast electron transfer dynamics whereas the other two corresponds to mechanically and thermodynamically trapped water molecules.[118] Very Recently, Tiwari *et al.*[119] demonstrated the effect of hydroxyl substituted spacer group of gemini surfactants on the bimodal behavior of solvation dynamics. The solvation dynamics is found to be slower on hydroxyl substitution of spacer group due to the formation of hydrogen bonds between water molecules and hydroxyl group(s) of spacer group. Such kind of hydrogen bonding protects the probe molecule from its contact with water molecules and also results in restricted mobility of water molecules.[119]

1.7c.4. Solvation Dynamics in Reverse Micelle

Reverse micelle (RM) is defined as surfactant coated polar droplets dispersed in non-polar media, which is mainly characterized by *w* (where, *w* = [polar solvent]/[surfactant]). In this section we will introduce reports related to solvation dynamics inside RM and hence skipeed a very descriptive discussion about RM and its researches is given in chapter 2. Solvation dynamics in confined solvent pool reverse micelles and microemulsions has been the subject

of many investigations.[73, 120-134] Sarkar *et al.*[120] studied the solvation dynamics of C-480 in n-heptane/ AOT/water reverse micelle. They reported solvation time of ~8 ns for smaller water pool (w_0=4, r_w=8 Å), while for very large water pool (w_0=32, r_w=64 Å) the response is bimodal with a fast component of 1.7 ns and a slower component of 12 ns. Zhang *et al.*[131] determined the nanosecond reorganization rates within the interior of AOT reverse micelles as a function of water content and temperature with a average solvation time ~8 ns for a small water pool (w_0=2) and ~2 ns for a large water pool (w_0=8). Das *et al.* showed that in AOT reverse micelle the solvation time of 4-AP increases from 1.9 ns in H_2O to 2.3 ns in D_2O, displaying almost 20% isotope effect.[121] Mandal *et al.* studied solvation dynamics of 4-AP in a reverse micelle containing neutral surfactant, TX-100, where no ions are present in the water pool[123] and observed nanosecond solvation dynamics with a major (65%) component of 0.74 ns along with a very long (nano-second) component.[123] Therefore, it was believed that the long component observed in almost all previous measurements were not due to slow Na^+ ion solvation. Hazra *et al.* also probed the solvation dynamics of water molecules inside the RM using C-152 as a probe, and found that solvation dynamics is drastically retarded compared to pure water.[135] The observed bimodal nature of solvation dynamics was attributed to the presence of different types of water molecules inside RM. The 'bound water' molecules, which are strongly attached to the polar head groups of the surfactant molecules by Coulombic attraction, are responsible for the slow component in the solvation dynamics measurement, whereas the relatively faster component corresponds to 'free water' in the water pool of the reverse micelle. Riter *et al.* studied the mobility of water in water/Aerosol OT (AOT)/isooctane reverse micelles via polar solvation dynamics measurements using ultrafast fluorescence-upconversion technique.[125] They observed with increasing w_0 time-correlation functions exhibit multi exponential decays suggesting increased mobility of water inside RM. They have also studied the solvation dynamics of C343 in lecithin and AOT microemulsions using femtosecond upconversion.[124] At hydration levels $w_0 \leq 4.8$ they observed a single relaxation time much longer than the response of bulk water, whereas at $w_0 \geq 5.8$ three distinct relaxation times were observed (0.5 ps, 15 ps and 200 ps) among which the shortest one correlates to 'free water' motion. Moilanen *et al.* have reported a comparative solvation dynamics of two different kinds of reverse micelles formed by Aerosol-OT (ionic head group) and Igepal CO 520 (non-ionic head group) using ultrafast infrared pump-probe spectroscopy. They used the OD stretch of HOD and showed that the hydrogen bonding network remains unaltered for both the reverse micelles irrespective to the

surfactant head group charge. Therefore, they concluded that it is the effect of confinement given by the interface resulting a nanoscopic 'water pool' is the primary factor governing the dynamics of nanoscopic water.[136] Moilanen *et al.* have also compared the water dynamics in AOT Lamellar Structures and reverse micelles through ultrafast infrared spectroscopy.[137] They found that vibrational relaxation time of water molecules in lamellar (4.2 ps) and RM (4.3 ps) structures is almost similar and hence does not depends over the length of confinement but depends over the type of water-interface interaction. Recently Costard *et al.* studied the ultrafast dynamics of OH stretching excitations (vibrations) of H_2O confined in dioleoylphosphatidylcholine (DOPC) reverse micelles studied in femtosecond pump–probe experiments. Interestingly the -OH stretching lifetime (500 fs) at $w_0 = 1$ decreases to 300 fs for large water pools formed at $w_0 = 16$.[138] Simorellis *et al.* measured low temperature induced water dynamics in AOT-RM by one-dimensional ^1H solution NMR spectroscopy and they found water displayed fine structures at −20°C and −30°C indicating the presence of multiple transient water populations in RM.[139] Fenn *et al.* characterized the solvation of water in RM using two-dimensional infrared (2DIR) vibrational echo spectroscopy and pump–probe experiments.[140] They characterized the frequency-frequency correlation function (FFCF) for each small reverse micelle, and found ~1 ps decay time attributing to the local hydrogen bond fluctuations and a slower ~6–10 ps decay time due to slow hydrogen bond rearrangements for non-interfacial water molecules. Very recently Bakulin *et al.* explored the water dynamics inside reverse micelle using multidimensional vibrational spectroscopy and molecular dynamics simulation study and re-explored the existence of 'free' and 'bound' waters.[141] They showed that these two groups of water distribution never correlate each other. Costard *et al.* have reported femtosecond -OH bending dynamics of water nanopools confined three different RMs; dioctyl sodium sulfosuccinate (AOT) and dioleoylphosphatidylcholine (DOPC) and nonionic tetraethylene glycol dodecyl ether (Brij-30).[142] They concluded though in ionic AOT/DOPC RMs, the OH bending lifetime $T_1 > 615$ fs at $w_0 = 3$ decreases to $T_1 = 345$ fs at $w_0 = 16$, H_2O in Brij-30 RMs shows a much shorter lifetime ($T_1 = 400$ fs at $w_0 = 2$ to 250 fs at $w_0 = 8$). Recently, several groups studied solvation dynamics of nonaqueous solvents, such as formamide (FA)[73, 143], *N*,*N*-Dimethylformamide (DMF)[143], acetonitrile[144-146], and methanol[144-146] in AOT microemulsions. Using a picosecond setup Shirota[144] and Hazra[145, 146] *et al.* have reported that the solvation dynamics of acetonitrile and methanol is nonexponential and 1000 times slower as compared to those in the pure solvents. Another important feature observed in their solvation dynamics results is

that solvation dynamics depends on *w* values in case of MeOH RM, whereas there is no *w* dependency observed in case of acetonitrile RM. The various *w* dependencies of solvation dynamics in water, methanol, and acetonitrile reverse micelles are explained on the basis of the presence and the absence of hydrogen bonding networks in water, methanol, and acetonitrile, respectively.[144-146] On the other hand solvation dynamics of FA and DMF in AOT-RM is found extremely slow in comparison to the bulk FA and DMF. Although the solvation dynamics of aprotic DMF in reverse micelles shows a small *w* dependency but solvation dynamics of FA in RM depends strongly on the *w*.[73, 143]

The dynamics of water in reverse micelles has also been investigated using computer simulation.[127, 130] In an interesting MD simulation, Senapati and Chandra modeled the water pool of a RM as a Stockmeyer liquid confined in a smooth spherical cavity[127] where the dielectric constant found to increase with the cavity size. Faeder and Ladayni[130] clearly showed that at small w_0 value (w_0=1) nearly all the counter ions remain bound to the surfactant. They identified three types of water molecules namely, the trapped, bound and free, proposed earlier to explain the IR spectra of RM. The translational and rotational mobility of the trapped and bound water were found to be slower than that of free water. Abel and fellow researchers studied the effect of surfactant conformation on the structures of small nonionic (poly(ethylene glycol) alkyl ether (C_mE_n) surfactants) RMs at constant pressure (P = 0.1 MPa) and temperature (T = 298 K) by molecular dynamics simulation.[147] They concluded that the surfactant head group conformation affects mainly the water core size, the area per surfactant head group, the head group hydration, and the water core translational diffusion. Later Rosenfeld *et al.* reported molecular dynamics simulation based dynamical properties of water confined within reverse micelles (RMs) ranging in size from R = 10 Å to R = 23 Å.[148] The low-frequency infrared spectra showed linear dependency on the fraction of bulk like water within the RMs. Moreover these spectra show nearly isosbestic behavior in the region near 660 cm^{-1}. Later Pieniazek *et al.* used combined atomistic molecular dynamics simulations and theoretical vibrational spectroscopy to study water dynamics confined in AOT RM and successfully reproduced the experimental spectra, rotational anisotropy decays, and spectral diffusion time-correlation functions as a function of RM size.[149] Recently Rosenfeld *et al.* analyzed dynamics of the water hydrogen bond network at ionic, nonionic, and hydrophobic interfaces of RMs by molecular dynamics simulations and resulted universal slowdown in rotational and hydrogen bond dynamics at the RM interface relative to bulk water.[150] Most Recently Martinez *et al.*

probed the dynamics of water in AOT RM by MD simulation study and explored the dependence over system density, reverse micelle structure, and water configurational relaxation times as a function of reverse micelle composition.[151] In all unrestrained simulations they reported substantial deviations from spherical reverse micelle geometries. Rotational anisotropy decay times and water residence times are found strongly dependant on force field and water model used whereas power-law relaxation in time found no dependency over the force field. [151]

1.7c.5. Solvation Dynamics in Different Bio-Macromolecular Confinements like Protein, DNA and Inside Cells

The behavior of water molecules in the immediate vicinity of biomolecules such as proteins and DNA is a consistent point of attention in chemistry and biology. Pierce and Boxer[152] and Bashkin *et al.*[153] studied solvation dynamics in protein environments using dynamic Stokes shift and reported a 10 ns component of protein dynamics. Jordanides *et al.*[154] employed three photon echo peak shift (3PEPS) spectroscopy to study the dynamic properties of the protein environment and reported 530 ps component which is absent for free eosin in bulk water. Pal *et al.*[155] studied solvation dynamics in human serum albumin (HSA) using non-covalently bound probe, DCM and observed two components of 600 ps and 10 ns. Denisov *et al.*[156] studied water relaxation in the denatured and molten globule state of α-lactalbumin, lysozyme, ribonuclease A, apomyoglobin and carbonic anhydrase by probing water ^{17}O relaxation dispersion. For the first time Zewail and co-researchers[157-159] used the solvation dynamics of the intrinsic probe tryptophan (Trp) in different proteins to study the protein solvation. They described how the hydration dynamics at the surface of single-Trp protein Subtilisin Carlsberg (SC) occurs with two well separated time scales; 800 fs and 38 ps.[157, 158] The 800 fs time constant was attributed to 'free' or 'quasifree' water and the slower time constant was assigned to those water molecules that interact strongly with hydration site.[157, 158] Later they also investigated the hydration dynamics at the surface of sweet protein Monellin by probing the single tryptophan residue at the protein surface.[159] They reported a "bimodal" solvation with 1.3 and 16 ps time constants of the surface water for native Monellin. The fast component is ascribed to the 'free' or 'quasi free' water molecules and the longer component is assigned for restricted water molecules that interact strongly with the hydration site. In contrary, denatured Monellin showed increased fast (3.5 ps, along with

doubled contribution for this component) and slow (56 ps) components. The 3.5 ps component is attributed to the bulk type solvation around Trp site of denatured protein, whereas 56 ps is assigned to the ion solvation in collapsed protein pocket.[159] Nitrile probe tagged site specific solvation dynamics of *Δ^5-3-ketosteroid isomerase* (KSI) enzyme has been explore by Jha *et al.* using time-resolved vibrational spectroscopy and the results showed that rigid water at the enzyme active site may help to maintain the organized electrostatic environment required for efficient catalysis.[160] Sushko *el al.* [161] have extensively described the terahertz spectral domain computational analysis of hydration shell of small structure peptide (TRP-cage$_{13\text{-}20}$ peptide, TRP-cage, BPTI) as well as lysozyme. They predicted water molecules at the protein surface (hydration shell depth extended up to ~10 Å) show similar dynamics and does not depend on protein size; rather it depends over the water molecules present at the Trp solvation cage. The average number of buried water molecules are 41 and 95 for BPTI and lysozyme, respectively, and these water molecules are tightly bound to protein and exhibits retarded dynamics.[161] Li *et al.* reported site specific solvation dynamics around tryptophan of apomyoglobin with a biphasic distribution of time scales, 5 ps and 87 ps, where initial dynamics represents fast local motions, such as reorientations and translations of hydrating water molecules, whereas the slow relaxation involving strongly coupled water-protein motions.[162] Abbyad *et al.* reported solvation dynamics at the B1 domain of a small globular protein streptococcal protein G (GB1), using the synthetic fluorescent amino acid Aladan by fluorescence upconversion and time-correlated single photon counting techniques. They suggested as the probe is moved from the surface to more buried sites, the dynamics of the solvation response become slower.[163] Similarly Halle *et al.* in their perspective write up concluded that the decay times from 10 ps to several nanoseconds appears due to differential position dependent hydration motions of water molecules in protein solvation.[164] Later on Chang *et al.* measured the solvation dynamics at the functional site of Flavodoxin in its three different redox states and detected three different solvation components. The initial ultrafast component of 1-2.6 ps reflects the local water-network relaxation around the shallow, solvent-exposed function site; whereas 20-40 ps component results from the coupled local water-protein fluctuation, and finally, the hundreds of picoseconds dynamics is from the intrinsic fluctuation of the loose loops flanking the cofactor at the function site.[165] Recently Jha *et al.* used fluorescence upconversion and anisotropy techniques for an acrylodan labeled protein and verified that solvation and protein internal dynamics is a correlated phenomenon. They found both the motions are dependent

upon the location of the probe as well as on the structural form of the protein. The internal dynamics of the fluorophore completes 0.1-3 ns time, whereas the mean solvent relaxation occurs within 20−300 ps.[166] Later on Mazur *et al.* using ultrafast optical Kerr effect showed that water dynamics in the first solvation layer of bovine serum albumin occurs 8 times slower than bulk, whereas the most hydrophobic protein trypsin had a slightly smaller effect in comparison to bulk water.[167] Not only experiments, but a countless theoretical efforts have been invested to explain water dynamics in various protein surfaces and cores. Bagchi and co-researchers[10, 168-170] proposed a dynamic exchange between 'bound' and 'free' water molecules in aqueous protein solution. They explained the bimodal dynamics of water in biomolecules in terms of concept of "bound" water (the water molecules which are involved in hydrogen bonding interaction or electrostatic interactions with the macromolecular surface) and "free" water (which are not involved with the biomolecules by any kind of interactions) molecules. In general, the bound water molecules results the long time solvation component, whereas free water contributes towards the faster solvation component. Few other computer simulation studies related to dielectric relaxation or solvation dynamics at the protein surface[171-174] indicate that the rotational relaxation of water molecules in the close proximity of the protein surface is significantly slower compared to bulk. By using a model protein, HP36 Bandyopadhyay *et al.* reported that a higher surface exposure of the solvation probe results in a faster solvation dynamics of the water in protein pockets.[175] They have also shown that the time dependent fluorescence Stokes shift of the chromophore in a molten globule (MG) state of the protein is substantially different when from the native state.[176] Golosov *et al.* have done similar kind of work for 11 different residues of the immunoglobulin binding domain B1 of protein G and they have concluded that solvation dynamics are position-dependent, highly heterogeneous, and found to span from a few picoseconds to hundreds of picoseconds. The slower solvation component was attributed to coupled hydration and protein conformational dynamics.[177] Very recently Fogarty *et al.* compared the reorientation dynamics of individual water molecules within the hydration shell of a series of globular proteins; acetylcholinesterase, subtilisin Carlsberg, lysozyme, and ubiquitin. Despite of their wide range of sizes, functions, and different secondary structures all four proteins showed a very similar hydration shell dynamics.[178] Very recently Pal *et al.* used molecular dynamics simulation to characterize the residence time of water molecules in solvation shell of different helical part of globular protein barstar. They showed domains with stronger water electrostatic anchoring sites (e.g. helix 1) results

biphasic water residence times of 16.03 ps and 44.26 ps due to strong electrostatic interactions and hydrogen bonding with protein surface.[179]

The behavior of water around DNA helixes always remained the central point of attention. Long back Saif *et al.*[180] attributed the slow dynamics inside the DNA to the counter ion motion. Halle and co-researchers[181, 182] studied water dynamics in DNA using nuclear magnetic relaxation dispersion (NMRD) and found that the high residence time in the minor grooves of DNA. First time Berg and co-researchers used base-stacked Coumarin (abasic-site pair replacing a natural base pair) and showed that DNA dynamics extend into the nanosecond regime[183] and later concluded that the time resolved fluorescence Stokes shift (TRFSS) dynamics follow a single power law from 40 fs to 40 ns[184, 185]. Zewail and co-workers used both of a base-stacked and a groove-bound probe to measure time dependent fluorescence Stokes shift (TRFSS) in DNA.[186, 187] They reported a bimodal response of 1 ps (60%) and 20 ps (40%), which originate from bulk like labile water and weakly bound ordered water in the groove, respectively.[186] Moreover, in case of site (major and minor groove) and sequence (different DNA lengths) selective solvation dynamics study[187] they detected no significant different of solvation, as in both cases ~1.5 ps and ~12 ps components persist. Their results corroborated well with the previous molecular dynamics simulation of ultrafast hydration in 16-mer DNA duplex by Bonvin *et al.*[188] where they have reported no significant difference in minor and major groove solvation of the DNA. Later on Dallmann *et al.* introduced 2-hydroxy-7-nitrofluorene (HNF) into ds-DNA opposite an abasic site as a base pair surrogate and probed the time resolved Stokes emission using femtosecond optical pump-probe experiment.[189] They reported a bimodal solvation comprising 0.3 ps and 8.3 ps which corresponds to the free water and weakly bound ordered water molecules. Banerjee *et al.* reported bi-exponential nanosecond dynamics of 0.130 ns (75%) and 2.35 ns (25%) using DNA groove-bound DAPI.[190] Pal *el al.* used DAPI to probe groove dynamics over a vast time scale of 100 fs to 100 ps and proposed that DNA with base stacked probe generally retains the spine of hydration with a set of structured water in the groove.[191] They have also showed that the dynamics measured with either the groove-bound or the base-stacked probe are similar in the time span of 100 fs to ~100 ps but differ substantially from ~100 ps to 10 ns.[191] Sen *et al.* carried out fluorescence TRSS experiment followed by long (46 ns) simulation of 17-mer native DNA. They found excellent agreement between the experiments with a base-stacked probe and the simulated electric field in the base stack of native DNA and detected that smaller, but non-negligible impact from counter ion perturbed DNA solvation with a

time constant of 220 ps. [192] Earlier using a base-stacked probe (a native base), Hynes and Bagchi reported a slow (250 ps) component in DNA assigned to water and ions using a long simulation up to 15 ns.[193] On the other hand, Furse and Corcelli simulated DNA with an very high time scale (770 ns) using Hoechst-33258 bound to DNA groove[194] and reported a relaxation up to 350 ps. This slowest dynamics were attributed to DNA motion, but not water or ion motions. Later on Furse *el al.* theoretically explored the power law solvation dynamics of DNA groove water monitored by Hoechst 3258 bound to DNA and found to be ~19 ps.[195] Very recently Bagchi reported that the dynamics, which is predicted to be the water dynamics in the DNA groove by several experiments, may not be true. Solvated ions around DNA molecules may be the possible reason for slow power law decay dynamics in DNA grove.[196]

Batabyal *el al.*[197] have explored ultrafast interfacial water (at the DNA protein interface) dynamics in specific protein-DNA (lambda repressor protein-operator DNA) interactions using minor groove binder dye, Hoechst. The solvation time scale corresponding to the minor groove water molecules (~50 ps) and DNA side chain flexibility (~10 ns) appeared completely unchanged in protein-DNA complex compared to free DNA.[197] Goel *et al.*'s[198] reported solvation dynamics for trans-activation responsive (TAR) bovine immunodeficiency virus (BIV) RNA and Tat peptide interaction. Solvation dynamics of BIV TAR RNA having 2-AP located at the bulge region have been carried out in the absence and presence of the Tat peptide. BIV TAR RNA-Tat complex offered a bimodal solvation response with 0.80 and 5.4 ns components. The fast component is attributed to the faster diffusion between the bound water layer and trapped water layer. On the other hand the slower solvation correlation time (5.4 ns) originated from restricted motion of the water molecules hydrogen bonded to the RNA in the presence of the peptide (i.e. thermodynamically bound water).[198]

Not only in vitro solvation of DNA and protein, the application of solvation dynamics has been extended up to cellular environment. Confocal microscopy based site specific solvation dynamics in living Chinese hamster ovary (CHO) has been reported by Ghosh *et al.* The average solvation time detected in the nucleus is ~750 ps and in cytoplasm it is ~1100 ps.[199, 200] Chowdhury *et al.* reported that cytoplasmic lipid droplets (CLDs) in live cells exhibit slower solvation dynamics than the cytoplasm using confocal microscopy.[201] They reported that CLDs of a live lung cancer cell (using C-153 stain) offers the average solvation time of 3750 ps, which is ~2 times sluggish compared to the solvation in CLDs of live non-cancer lung cell (1700 ps). This implies that the cancer cells are more active in terms

of membrane trafficking. [201] Ghosh *et al*[202] also probed the dynamics of the exofacial thiols (cell surface thiol contaning membrane protein) of a live Chinese hamster ovary (CHO) cell through fluorescence confocal microscopy. To get the specific solvation response from the membrane of living cell they have covalently attached *7-(diethylamino)-3-(4-maleimidophenyl)-4-methylcoumarin* (CPM) with membrane thiols. They observed ultraslow response with average solvation time ~475 ps and attributed to reversible, intermittent changes in the structure and conformation of the membrane proteins.

1.8. Reference

1. Sir J. F. W Herschel. On a case of superficial colour presented by a homogeneous liquid internally colourless. *Phil. Trans. Roy. Soc. (London)* **135**, 143-145 (1845).
2. Stokes, G.G. On the Change of refrangibility of Light. *Phil. Trans. Roy. Soc. (London)* **142**, 463-562 (1852).
3. Udenfriend, S. Development of the spectrophotofluorometer and its commercialization. *Protein Sci.* **4**, 542-551 (1995).
4. Berlman, I.B. Handbook of fluorescence spectra of aromatic molecules (Academic Press, 1965).
5. Jablonski, A. Über den mechanisms des photolumineszenz von farbstoffphosphoren. *Z. Phys.* **94**, 38–46 (1935).
6. Valeur, B. Molecular fluorescence; principles and applications (Wiley VCH, NY, 2001).
7. Lakowicz, J.R. Principles of fluorescence spectroscopy (Springer, 2006).
8. Simon, J.D. Time-resolved studies of solvation in polar media. *Acc. Chem. Res.* **21**, 128-134 (1988).
9. Maroncelli, M. The dynamics of solvation in polar liquids. *J. Mol. Liq.* **57**, 1-37 (1993).
10. Nandi, N., Bhattacharyya, K. & Bagchi, B. Dielectric relaxation and solvation dynamics of water in complex chemical and biological systems. *Chem. Rev.* **100**, 2013-2046 (2000).
11. Bhattacharyya, K. & Bagchi, B. Slow dynamics of constrained water in complex geometries. *J. Phys. Chem. A* **104**, 10603-10613 (2000).
12. Bhattacharyya, K. Solvation dynamics and proton transfer in supramolecular assemblies. *Acc. Chem. Res.* **36**, 95-101 (2002).
13. Bagchi, B. Dynamics of solvation and charge transfer reactions in dipolar liquids. *Annu. Rev. Phys. Chem.* **40**, 115-141 (1989).
14. C. J. F. Böttcher, P.B. Theory of electric polarization (Elesvier, Amesterdam, 1978).
15. Bagchi, B., Oxtoby, D.W. & Fleming, G.R. Theory of the time development of the stokes shift in polar media. *Chem. Phys.* **86**, 257-267 (1984).
16. Onsager, L. Electric moments of molecules in liquids. *J. Am. Chem. Soc.* **58**, 1486-1493 (1936).
17. Van der Zwan, G. & Hynes, J.T. Time-dependent fluorescence solvent shifts, dielectric friction, and nonequilibrium solvation in polar solvents. *J. Phys. Chem.* **89**, 4181-4188 (1985).
18. Maroncelli, M. & Fleming, G.R. Picosecond solvation dynamics of coumarin 153: The importance of molecular aspects of solvation. *J. Chem. Phys.* **86**, 6221-6239 (1987).
19. W. Castner Jr, E., R. Fleming, G. & Bagchi, B. Influence of non-Debye relaxation and of molecular shape on the time dependence of the stokes shift in polar media. *Chem. Phys. Lett.* **143**, 270-276 (1988).

20. Davidson, D.W. & Cole, R.H. Dielectric relaxation in glycerol, propylene glycol, and n-propanol. *J. Chem. Phys.* **19**, 1484-1490 (1951).
21. Cole, K.S. & Cole, R.H. Dispersion and absorption in dielectrics I. alternating current characteristics. *J. Chem. Phys.* **9**, 341-351 (1941).
22. Bagchi, B., Castner, E.W. & Fleming, G.R. On the generalized continuum model of dipolar solvation dynamics. *J. Mol. Struct.* **194**, 171-181 (1989).
23. Castner, E.W., Fleming, G.R., Bagchi, B. & Maroncelli, M. The dynamics of polar solvation: Inhomogeneous dielectric continuum models. *J. Chem. Phys.* **89**, 3519-3534 (1988).
24. Barbara, P.F. & Jarzeba, W. in Advances in photochemistry 1-68 (John Wiley & Sons, Inc., 2007).
25. Nichols, A.L. & Calef, D.F. Polar solvent relaxation: The mean spherical approximation approach. *J. Chem. Phys.* **89**, 3783-3788 (1988).
26. Rips, I., Klafter, J. & Jortner, J. Dynamics of ionic solvation. *J. Chem. Phys.* **88**, 3246-3252 (1988).
27. Wolynes, P.G. Linearized microscopic theories of nonequilibrium solvation. *J. Chem. Phys.* **86**, 5133-5136 (1987).
28. Chandra, A. & Bagchi, B. The role of translational diffusion in the polarization relaxation in dense polar liquids. *Chem. Phys. Lett.* **151**, 47-53 (1988).
29. Bagchi, B. & Chandra, A. Polarization relaxation, dielectric dispersion, and solvation dynamics in dense dipolar liquid. *J. Chem. Phys.* **90**, 7338-7345 (1989).
30. Chandra, A. & Bagchi, B. Microscopic expression for frequency and wave vector dependent dielectric constant of a dipolar liquid. *J. Chem. Phys.* **90**, 1832-1840 (1989).
31. Chandra, A. & Bagchi, B. Effects of molecular size in solvation dynamics. *J. Phys. Chem.* **94**, 1874-1876 (1990).
32. Simon, J.D. & Su, S.G. Intramolecular electron transfer and solvation. *J. Chem. Phys.* **87**, 7016-7023 (1987).
33. Su, S.G. & Simon, J.D. Solvation dynamics in ethanol. *J. Phys. Chem.* **91**, 2693-2696 (1987).
34. Roy, S. & Bagchi, B. Solvation dynamics, energy distribution and trapping of a light solute ion. *Chem. Phys.* **183**, 207-216 (1994).
35. Biswas, R. & Bagchi, B. Self-consistent microscopic treatment of the effects of self-motion of the probe on ionic and dipolar solvation dynamics. *J. Phys. Chem.* **100**, 4261-4268 (1996).
36. Berg, M. Viscoelastic Continuum Model of Nonpolar Solvation. 1. Implications for multiple time scales in liquid dynamics. *J. Phys. Chem. A* **102**, 17-30 (1998).
37. Saven, J.G. & Skinner, J.L. A molecular theory of the line shape: Inhomogeneous and homogeneous electronic spectra of dilute chromophores in nonpolar fluids. *J. Chem. Phys.* **99**, 4391-4402 (1993).
38. Stephens, M.D., Saven, J.G. & Skinner, J.L. Molecular theory of electronic spectroscopy in nonpolar fluids: Ultrafast solvation dynamics and absorption and emission line shapes. *J. Chem. Phys.* **106**, 2129-2144 (1997).

39. Raineri, F.O., Resat, H., Perng, B.C., Hirata, F. & Friedman, H.L. A molecular theory of solvation dynamics. *J. Chem. Phys.* **100**, 1477-1491 (1994).
40. Friedman, H.L., Raineri, F.O., Perng, B.-C. & Newton, M.D. Molecular theory of solvation processes in dipolar and non-dipolar solvents. *J. Mol. Liq.* **65–66**, 7-14 (1995).
41. Roy, S. & Bagchi, B. Solvation dynamics in liquid water. A novel interplay between librational and diffusive modes. *J. Chem. Phys.* **99**, 9938-9943 (1993).
42. Nandi, N., Roy, S. & Bagchi, B. Ultrafast solvation dynamics in water: Isotope effects and comparison with experimental results. *J. Chem. Phys.* **102**, 1390-1397 (1995).
43. Roy, S. & Bagchi, B. Microscopic theory of ion solvation dynamics in liquid methanol. *J. Chem. Phys.* **101**, 4150-4155 (1994).
44. Rosenthal, S.J., Xie, X., Du, M. & Fleming, G.R. Femtosecond solvation dynamics in acetonitrile: Observation of the inertial contribution to the solvent response. *J. Chem. Phys.* **95**, 4715-4718 (1991).
45. Roy, S., Komath, S. & Bagchi, B. Molecular theory of ultrafast solvation in liquid acetonitrile. *J. Chem. Phys.* **99**, 3139-3142 (1993).
46. Biswas, R. & Bagchi, B. Solvation Dynamics in nonassociated polar solvents. *J. Phys. Chem. A* **103**, 2495-2500 (1999).
47. Maroncelli, M. & Fleming, G.R. Computer simulation of the dynamics of aqueous solvation. *J. Chem. Phys.* **89**, 5044-5069 (1988).
48. Karim, O.A., Haymet, A.D.J., Banet, M.J. & Simon, J.D. Molecular aspects of nonequilibrium solvation: a simulation of dipole relaxation. *J. Phys. Chem.* **92**, 3391-3394 (1988).
49. Barnett, R.B., Landman, U. & Nitzan, A. Relaxation dynamics following transition of solvated electrons. *J. Chem. Phys.* **90**, 4413-4422 (1989).
50. Bader, J.S. & Chandler, D. Computer simulation of photochemically induced electron transfer. *Chem. Phys. Lett.* **157**, 501-504 (1989).
51. Bagchi, B. & Chandra, A. Ultrafast solvation dynamics: Molecular explanation of computer simulation results in a simple dipolar solvent. *J. Chem. Phys.* **97**, 5126-5131 (1992).
52. Maroncelli, M. Computer simulations of solvation dynamics in acetonitrile. *J. Chem. Phys.* **94**, 2084-2103 (1991).
53. Kumar, P.V. & Maroncelli, M. Polar solvation dynamics of polyatomic solutes: Simulation studies in acetonitrile and methanol. *J. Chem. Phys.* **103**, 3038-3060 (1995).
54. Ladanyi, B.M. & Maroncelli, M. Mechanisms of solvation dynamics of polyatomic solutes in polar and nondipolar solvents: A simulation study. *J. Chem. Phys.* **109**, 3204-3221 (1998).
55. Ladanyi, B.M. & Stratt, R.M. Short-time dynamics of solvation: Linear solvation theory for polar solvents. *J. Phys. Chem.* **99**, 2502-2511 (1995).
56. Fonseca, T. & Ladanyi, B.M. Solvation dynamics in methanol: Solute and perturbation dependence. *J. Mol. Liq.* **60**, 1-24 (1994).

57. Ralph Jimenez, Graham R.Fleming, P. V. Kumar & M. Maroncelli. Femtosecond solvation dynamics of water. *Nature* **369**, 471-473 (1994).
58. Fonseca, T. & Ladanyi, B.M. Breakdown of linear response for solvation dynamics in methanol. *J. Phys. Chem.* **95**, 2116-2119 (1991).
59. Ralph Jimenez, Graham R. Fleming, P. V. Kumar & Maroncelli, M. Femtosecond solvation dynamics of water. *Nature* **369**, 471-473 (1994).
60. Jarzeba, W., Walker, G.C., Johnson, A.E., Kahlow, M.A. & Barbara, P.F. Femtosecond microscopic solvation dynamics of aqueous solutions. *J. Phys. Chem.* **92**, 7039-7041 (1988).
61. Vajda, S., Jimenez, R., Rosenthal, S.J., Fidler, V., Fleming, G.R. & Castner, E.W. Femtosecond to nanosecond solvation dynamics in pure water and inside the [gamma]-cyclodextrin cavity. *J. Chem. Soc., Faraday Trans.* **91**, 867-873 (1995).
62. Zolotov, B., Gan, A., Fainberg, B.D. & Huppert, D. Resonance heterodyne optical Kerr spectroscopy of solvation dynamics in water and D_2O. *Chem. Phys. Lett.* **265**, 418-426 (1997).
63. Cho, M., Rosenthal, S.J., Scherer, N.F., Ziegler, L.D. & Fleming, G.R. Ultrafast solvent dynamics: Connection between time resolved fluorescence and optical Kerr measurements. *J. Chem. Phys.* **96**, 5033-5038 (1992).
64. Lang, M.J., Jordanides, X.J., Song, X. & Fleming, G.R. Aqueous solvation dynamics studied by photon echo spectroscopy. *J. Chem. Phys.* **110**, 5884-5892 (1999).
65. Joo, T., Jia, Y., Yu, J.Y., Lang, M.J. & Fleming, G.R. Third-order nonlinear time domain probes of solvation dynamics. *J. Chem. Phys.* **104**, 6089-6108 (1996).
66. Ohta, K., Tayama, J., Saito, S. & Tominaga, K. 149-167 (CRC Press, 2013).
67. Yang, S., Liu, J., Zhou, P., Chen, J., Han, K. & He, G. Mechanisms of ultrafast fluorescence depletion spectroscopy and applications to measure solvation dynamics of coumarin 153 in methanol. *J. Lumin.* **132**, 2275-2280 (2012).
68. Coridan, R.H. & Wong, G.C.L. Molecular solvation dynamics from inelastic X-ray scattering measurements. *Adv. Chem. Phys.* **149**, 83-127 (2012).
69. Guardia, E., Calvo, A.M. & Masia, M. How polarization damping affects ion solvation dynamics. *Theor. Chem. Acc.* **131**, 1-8 (2012).
70. Horng, M.L., Gardecki, J.A., Papazyan, A. & Maroncelli, M. Subpicosecond measurements of polar solvation dynamics: Coumarin 153 revisited. *J. Phys. Chem.* **99**, 17311-17337 (1995).
71. Castner, E.W., Maroncelli, M. & Fleming, G.R. Subpicosecond resolution studies of solvation dynamics in polar aprotic and alcohol solvents. *J. Chem. Phys.* **86**, 1090-1097 (1987).
72. Chang, Y.J. & Castner, E.W. Deuterium isotope effects on the ultrafast solvent relaxation of formamide and N,N-dimethylformamide. *J. Phys. Chem.* **98**, 9712-9722 (1994).
73. Riter, R.E., Undiks, E.P., Kimmel, J.R. & Levinger, N.E. Formamide in reverse micelles: Restricted environment effects on molecular motion. *J. Phys. Chem. B* **102**, 7931-7938 (1998).

74. Kato, S. & Amatatsu, Y. A theoretical study on the mechanism of charge transfer state formation of 4-(N,N-dimethylamino)benzonitrile in an aqueous solution. *J. Chem. Phys.* **92**, 7241-7257 (1990).
75. Chaban, V.V., Maciel, C. & Fileti, E.E. Solvent polarity considerations are unable to describe fullerene solvation behavior. *J. Phys. Chem. B* **118**, 3378-3384 (2014).
76. Gardecki, J., Horng, M.L., Papazyan, A. & Maroncelli, M. Ultrafast measurements of the dynamics of solvation in polar and non-dipolar solvents. *J. Mol. Liq.* **65–66**, 49-57 (1995).
77. van der Zwan, G. & Hynes, J.T. Chemical reaction rates and solvation dynamics in electrolyte solutions: ion atmosphere friction. *Chem. Phys.* **152**, 169-183 (1991).
78. Chandra, A. & Patey, G.N. Solvation dynamics in electrolyte solutions. *J. Chem. Phys.* **100**, 1552-1558 (1994).
79. Chandra, A. Dynamics of ion solvation in electrolyte solutions: dependence on salt concentration. *Chem. Phys. Lett.* **244**, 314-320 (1995).
80. Mahajan, K. & Chandra, A. Dynamics of electrolyte solutions at finite wave vectors: Theoretical results for ions in a molecular solvent. *J. Chem. Phys.* **106**, 2360-2371 (1997).
81. Neria, E. & Nitzan, A. Numerical simulations of solvation dynamics in electrolyte solutions. *J. Chem. Phys.* **100**, 3855-3868 (1994).
82. Zhang, L., Yan, S., Cukier, R.I. & Bu, Y. Solvation of excess electrons in LiF ionic pair matrix: Evidence for a solvated dielectron from ab initio molecular dynamics simulations and calculations. *J. Phys. Chem. B* **112**, 3767-3772 (2008).
83. Yamazaki, T., Kovalenko, A., Murashov, V.V. & Patey, G.N. Ion solvation in a water-urea mixture. *J. Phys. Chem. B* **114**, 613-619 (2009).
84. Criscenti, L.J. & Cygan, R.T. Molecular simulations of carbon dioxide and water: Cation solvation. *Environ. Sci. Technol.* **47**, 87-94 (2012).
85. Pliego, J.R. & Miguel, E.L.M. Absolute single-ion solvation free energy scale in methanol determined by the lithium cluster-continuum approach. *J. Phys. Chem. B* **117**, 5129-5135 (2013).
86. Bart, E., Meltsin, A. & Huppert, D. Static and dynamic solvation measurements of excited large dipole in molten salt. *Chem. Phys. Lett.* **200**, 592-596 (1992).
87. Bart, E., Meltsin, A. & Huppert, D. Solvation dynamics of coumarin 153 in molten salts. *J. Phys. Chem.* **98**, 3295-3299 (1994).
88. Bart, E., Meltsin, A. & Huppert, D. Solvation dynamics in molten salts. *J. Phys. Chem.* **98**, 10819-10823 (1994).
89. Chapman, C.F. & Maroncelli, M. Fluorescence studies of solvation and solvation dynamics in ionic solutions. *J. Phys. Chem.* **95**, 9095-9114 (1991).
90. Palit, D.K., Torche, F. & Marignier, J.-L. Picosecond pulse radiolysis study of dynamics of solvation of electron and fluorenone anion in primary alcohols. *J. Phys. Chem. B* **118**, 287-296 (2013).
91. Zeng, Y., Wang, C., Zhang, X. & Ju, S. Solvation structure and dynamics of Li^+ ion in liquid water, methanol and ethanol: A comparison study. *Chem. Phys.* **433**, 89-97 (2014).

92. Karmakar, R. & Samanta, A. Solvation dynamics of coumarin-153 in a room-temperature ionic liquid. *J. Phys. Chem. A* **106**, 4447-4452 (2002).
93. Karmakar, R. & Samanta, A. Steady-state and time-resolved fluorescence behavior of C153 and PRODAN in room-temperature ionic liquids. *J. Phys. Chem. A* **106**, 6670-6675 (2002).
94. Karmakar, R. & Samanta, A. Dynamics of solvation of the fluorescent state of some electron donor-acceptor molecules in room temperature ionic liquids, [BMIM][(CF3SO2)2N] and [EMIM][(CF3SO2)2N]. *J. Phys. Chem. A* **107**, 7340-7346 (2003).
95. Kumar Das, S. & Sarkar, M. Studies on the solvation dynamics of coumarin 153 in 1-ethyl-3-methylimidazolium alkylsulfate ionic liquids: Dependence on alkyl chain length. *ChemPhysChem* **13**, 2761-2768 (2012).
96. Castner, E.W., Wishart, J.F. & Shirota, H. Intermolecular dynamics, interactions, and solvation in Ionic Liquids. *Acc. Chem. Res.* **40**, 1217-1227 (2007).
97. Samanta, A. Solvation dynamics in ionic liquids: What we have learned from the dynamic fluorescence stokes shift studies. *J Phys. Chem. Lett.* **1**, 1557-1562 (2010).
98. Mandal, P.K. & Samanta, A. Fluorescence studies in a pyrrolidinium ionic liquid: Polarity of the medium and solvation dynamics. *J. Phys. Chem. B* **109**, 15172-15177 (2005).
99. Ingram, J.A., Moog, R.S., Ito, N., Biswas, R. & Maroncelli, M. Solute rotation and solvation dynamics in a room-temperature ionic liquid. *J. Phys. Chem. B* **107**, 5926-5932 (2003).
100. Chakrabarty, D., Hazra, P., Chakraborty, A., Seth, D. & Sarkar, N. Dynamics of solvent relaxation in room temperature ionic liquids. *Chem. Phys. Lett.* **381**, 697-704 (2003).
101. Halder, M., Headley, L.S., Mukherjee, P., Song, X. & Petrich, J.W. Experimental and theoretical investigations of solvation dynamics of ionic fluids: Appropriateness of dielectric theory and the role of DC conductivity. *J. Phys. Chem. A* **110**, 8623-8626 (2006).
102. Zhang, X.-X., Liang, M., Ernsting, N.P. & Maroncelli, M. Conductivity and solvation dynamics in ionic liquids. *J. Phys. Chem. Lett.* **4**, 1205-1210 (2013).
103. Terranova, Z.L. & Corcelli, S.A. On the Mechanism of solvation dynamics in imidazolium-based ionic liquids. *J. Phys. Chem. B* **117**, 15659-15666 (2013).
104. Shim, Y. & Kim, H.J. Dielectric relaxation and solvation dynamics in a room-temperature ionic liquid: Temperature dependence. *J. Phys. Chem. B* **117**, 11743-11752 (2013).
105. Zhang, X.-X., Liang, M., Hunger, J., Buchner, R. & Maroncelli, M. Dielectric relaxation and solvation dynamics in a prototypical ionic liquid + dipolar protic liquid mixture: 1-butyl-3-methylimidazolium tetrafluoroborate + water. *J. Phys. Chem. B* **117**, 15356-15368 (2013).
106. Sarkar, N., Datta, A., Das, S. & Bhattacharyya, K. Solvation dynamics of coumarin 480 in micelles. *J. Phys. Chem.* **100**, 15483-15486 (1996).

107. Datta, A., Mandal, D., Pal, S.K., Das, S. & Bhattacharyya, K. Solvation dynamics in organized assemblies, 4-aminophthalimide in micelles. *J. Mol. Liq.* **77**, 121-129 (1998).
108. Hara, K., Kuwabara, H. & Kajimoto, O. Pressure Effect on Solvation dynamics in micellar environment. *J. Phys. Chem. A* **105**, 7174-7179 (2001).
109. Mandal, D., Sen, S., Bhattacharyya, K. & Tahara, T. Femtosecond study of solvation dynamics of DCM in micelles. *Chem. Phys. Lett.* **359**, 77-82 (2002).
110. Sen, S., Dutta, P., Mukherjee, S. & Bhattacharyya, K. Solvation synamics in bile salt aggregates. *J. Phys. Chem. B* **106**, 7745-7750 (2002).
111. Chakrabarty, D., Hazra, P. & Sarkar, N. Solvation dynamics of coumarin 480 in tritonX-100 (TX-100) and bile salt mixed micelles. *J. Phys. Chem. A* **107**, 5887-5893 (2003).
112. Chakrabarty, D., Hazra, P., Chakraborty, A. & Sarkar, N. Dynamics of solvation and rotational relaxation in neutral Brij 35 and Brij 58 micelles. *Chem. Phys. Lett.* **392**, 340-347 (2004).
113. Chakrabarty, D., Chakraborty, A., Seth, D., Hazra, P. & Sarkar, N. Effect of alkyl chain length and size of the headgroups of the surfactant on solvent and rotational relaxation of Coumarin 480 in micelles and mixed micelles. *J. Chem. Phys.* **122**, - (2005).
114. Balasubramanian, S., Pal, S. & Bagchi, B. Hydrogen-bond dynamics near a micellar surface: Origin of the universal slow relaxation at complex aqueous interfaces. *Phys. Rev. Lett.* **89**, 115505 (2002).
115. Balasubramanian, S. & Bagchi, B. Slow solvation dynamics near an aqueous micellar surface. *J. Phys. Chem. B* **105**, 12529-12533 (2001).
116. Kumbhakar, M. Effect of ionic surfactants on the hydration behavior of triblock copolymer micelles: A solvation dynamics study of coumarin 153. *J. Phys. Chem. B* **111**, 12154-12161 (2007).
117. Dey, S., Adhikari, A., Mandal, U., Ghosh, S. & Bhattacharyya, K. A Femtosecond study of excitation wavelength dependence of a triblock copolymer-surfactant supramolecular assembly: (PEO)20−(PPO)70−(PEO)20 and CTAC. *J. Phys. Chem. B* **112**, 5020-5026 (2008).
118. Das, A.K., Mondal, T., Sen Mojumdar, S. & Bhattacharyya, K. Marcus-like inversion in electron transfer in neat ionic liquid and ionic liquid-mixed micelles. *J. Phys. Chem. B* **115**, 4680-4688 (2011).
119. Tiwari, A.K., Sonu & Saha, S.K. Effect of hydroxyl group substituted spacer group of cationic gemini surfactants on solvation dynamics and rotational relaxation of coumarin-480 in aqueous micelles. *J. Phys. Chem. B* **118**, 3582-3592 (2014).
120. Sarkar, N., Das, K., Datta, A., Das, S. & Bhattacharyya, K. Solvation dynamics of coumarin 480 in reverse micelles. Slow relaxation of water molecules. *J. Phys. Chem.* **100**, 10523-10527 (1996).
121. Das, S., Datta, A. & Bhattacharyya, K. Deuterium isotope effect on 4-aminophthalimide in neat water and reverse micelles. *J. Phys. Chem. A* **101**, 3299-3304 (1997).

122. Lundgren, J.S., Heitz, M.P. & Bright, F.V. Dynamics of acrylodan-labeled bovine and human serum albumin sequestered within aerosol-OT reverse micelles. *Anal. Chem.* **67**, 3775-3781 (1995).
123. Mandal, D., Datta, A., Pal, S.K. & Bhattacharyya, K. Solvation dynamics of 4-aminophthalimide in water-in-oil microemulsion of triton X-100 in mixed solvents. *J. Phys. Chem. B* **102**, 9070-9073 (1998).
124. Willard, D.M., Riter, R.E. & Levinger, N.E. Dynamics of polar solvation in lecithin/water/cyclohexane Reverse Micelles. *J. Am. Chem. Soc.* **120**, 4151-4160 (1998).
125. Riter, R.E., Willard, D.M. & Levinger, N.E. Water immobilization at surfactant interfaces in reverse micelles. *J. Phys. Chem. B* **102**, 2705-2714 (1998).
126. Fee, R.S. & Maroncelli, M. Estimating the time-zero spectrum in time-resolved emmsion measurements of solvation dynamics. *Chem. Phys.* **183**, 235-247 (1994).
127. Senapati, S. & Chandra, A. Molecular dynamics simulations of simple dipolar liquids in spherical cavity: Effects of confinement on structural, dielectric, and dynamical properties. *J. Chem. Phys.* **111**, 1223-1230 (1999).
128. Riter, R.E., Undiks, E.P. & Levinger, N.E. Impact of Counterion on water motion in aerosol OT reverse micelles. *J. Am. Chem. Soc.* **120**, 6062-6067 (1998).
129. Bhattacharyya, K., Hara, K., Kometani, N., Uozu, Y. & Kajimoto, O. Solvation dynamics in a microemulsion in near-critical propane. *Chem. Phys. Lett.* **361**, 136-142 (2002).
130. Faeder, J. & Ladanyi, B.M. Molecular Dynamics Simulations of the interior of aqueous reverse micelles. *J. Phys. Chem. B* **104**, 1033-1046 (2000).
131. Zhang, J. & Bright, F.V. Probing the internal dynamics of reverse micelles formed in highly compressible solvents: aerosol-OT in near-critical propane. *J. Phys. Chem.* **96**, 9068-9073 (1992).
132. Sen, S., Dutta, P., Sukul, D. & Bhattacharyya, K. Solvation Dynamics in the water pool of aerosol sodium dioctylsulfosuccinate microemulsion: Effect of polymer. *J. Phys. Chem. A* **106**, 6017-6023 (2002).
133. Mandal, D., Sen, S., Sukul, D., Bhattacharyya, K., Mandal, A.K., Banerjee, R. & Roy, S. Solvation dynamics of a probe covalently bound to a protein and in an AOT microemulsion: 4-(N-bromoacetylamino)-phthalimide. *J. Phys. Chem. B* **106**, 10741-10747 (2002).
134. Dutta, P., Sen, P., Mukherjee, S., Halder, A. & Bhattacharyya, K. Solvation dynamics in the water pool of an aerosol-OT microemulsion. Effect of sodium salicylate and sodium cholate. *J. Phys. Chem. B* **107**, 10815-10822 (2003).
135. Hazra, P., Chakrabarty, D. & Sarkar, N. Intramolecular charge transfer and solvation dynamics of coumarin 152 in aerosol-OT, water-solubilizing reverse micelles, and polar organic solvent solubilizing reverse micelles. *Langmuir* **18**, 7872-7879 (2002).
136. Moilanen, D.E., Levinger, N.E., Spry, D.B. & Fayer, M.D. Confinement or the nature of the interface? Dynamics of nanoscopic water. *J. Am. Chem. Soc.* **129**, 14311-14318 (2007).

137. Moilanen, D.E., Fenn, E.E., Wong, D. & Fayer, M.D. Geometry and nanolength scales versus interface interactions: Water dynamics in AOT lamellar structures and reverse micelles. *J. Am. Chem. Soc.* **131**, 8318-8328 (2009).
138. Costard, R., Levinger, N.E., Nibbering, E.T.J. & Elsaesser, T. Ultrafast vibrational dynamics of water confined in phospholipid reverse micelles. *J. Phys. Chem. B* **116**, 5752-5759 (2012).
139. Simorellis, A.K., Van Horn, W.D. & Flynn, P.F. Dynamics of low temperature induced water shedding from AOT reverse micelles. *J. Am. Chem. Soc.* **128**, 5082-5090 (2006).
140. Fenn, E.E., Wong, D.B., Giammanco, C.H. & Fayer, M.D. Dynamics of water at the interface in reverse micelles: Measurements of spectral diffusion with two-dimensional infrared vibrational echoes. *J. Phys. Chem. B* **115**, 11658-11670 (2011).
141. Bakulin, A.A., Cringus, D., Pieniazek, P.A., Skinner, J.L., Jansen, T.L.C. & Pshenichnikov, M.S. Dynamics of water confined in reversed micelles: Multidimensional vibrational spectroscopy study. *J. Phys. Chem. B* **117**, 15545-15558 (2013).
142. Costard, R. & Elsaesser, T. Femtosecond OH bending dynamics of water nanopools confined in reverse micelles. *J. Phys. Chem. B* **117**, 15338-15345 (2013).
143. Shirota, H. & Segawa, H. Solvation dynamics of formamide and N,N-dimethylformamide in aerosol OT reverse micelles. *Langmuir* **20**, 329-335 (2003).
144. Shirota, H. & Horie, K. Solvation dynamics in nonaqueous reverse micelles. *J. Phys. Chem. B* **103**, 1437-1443 (1999).
145. Hazra, P., Chakrabarty, D. & Sarkar, N. Solvation dynamics of coumarin 152A in methanol and acetonitrile reverse micelles. *Chem. Phys. Lett.* **358**, 523-530 (2002).
146. Hazra, P. & Sarkar, N. Solvation dynamics of coumarin 490 in methanol and acetonitrile reverse micelles. *PCCP* **4**, 1040-1045 (2002).
147. Abel, S., Waks, M., Marchi, M. & Urbach, W. Effect of surfactant conformation on the structures of small size nonionic reverse micelles: A molecular dynamics simulation study. *Langmuir* **22**, 9112-9120 (2006).
148. Rosenfeld, D.E. & Schmuttenmaer, C.A. Dynamics of water confined within reverse micelles. *J. Phys. Chem. B* **110**, 14304-14312 (2006).
149. Pieniazek, P.A., Lin, Y.-S., Chowdhary, J., Ladanyi, B.M. & Skinner, J.L. Vibrational spectroscopy and dynamics of water confined inside reverse micelles. *J. Phys. Chem. B* **113**, 15017-15028 (2009).
150. Rosenfeld, D.E. & Schmuttenmaer, C.A. Dynamics of the water hydrogen bond network at ionic, nonionic, and hydrophobic interfaces in nanopores and reverse micelles. *J. Phys. Chem. B* **115**, 1021-1031 (2010).
151. Martinez, A.V., Dominguez, L., Małolepsza, E., Moser, A., Ziegler, Z. & Straub, J.E. Probing the structure and dynamics of confined water in AOT reverse micelles. *J. Phys. Chem. B* **117**, 7345-7351 (2013).
152. Pierce, D.W. & Boxer, S.G. Dielectric relaxation in a protein matrix. *J. Phys. Chem.* **96**, 5560-5566 (1992).

153. Bashkin, J.S., McLendon, G., Mukamel, S. & Marohn, J. Influence of medium dynamics on solvation and charge separation reactions: comparison of a simple alcohol and a protein "solvent". *J. Phys. Chem.* **94**, 4757-4761 (1990).
154. Jordanides, X.J., Lang, M.J., Song, X. & Fleming, G.R. Solvation Dynamics in protein environments studied by photon echo spectroscopy. *J. Phys. Chem. B* **103**, 7995-8005 (1999).
155. Pal, S.K., Mandal, D., Sukul, D., Sen, S. & Bhattacharyya, K. Solvation dynamics of DCM in human serum albumin. *J. Phys. Chem. B* **105**, 1438-1441 (2001).
156. Denisov, V.P., Jonsson, B.-H. & Halle, B. Hydration of denatured and molten globule proteins. *Nat. Struct. Mol. Biol.* **6**, 253-260 (1999).
157. Pal, S.K., Peon, J. & Zewail, A.H. Biological water at the protein surface: Dynamical solvation probed directly with femtosecond resolution. *Proc. Natl. Acad. Aci. U.S.A.* **99**, 1763-1768 (2002).
158. Pal, S.K., Peon, J., Bagchi, B. & Zewail, A.H. Biological water: Femtosecond dynamics of macromolecular hydration. *J. Phys. Chem. B* **106**, 12376-12395 (2002).
159. Peon, J., Pal, S.K. & Zewail, A.H. Hydration at the surface of the protein Monellin: Dynamics with femtosecond resolution. *Proc. Natl. Acad. Aci. U.S.A.* **99**, 10964-10969 (2002).
160. Jha, S.K., Ji, M., Gaffney, K.J. & Boxer, S.G. Site-specific measurement of water dynamics in the substrate pocket of ketosteroid isomerase using time-resolved vibrational spectroscopy. *J. Phys. Chem. B* **116**, 11414-11421 (2012).
161. Sushko, O., Dubrovka, R. & Donnan, R.S. Terahertz spectral domain computational analysis of hydration shell of proteins with increasingly complex tertiary structure. *J. Phys. Chem. B* **117**, 16486-16492 (2013).
162. Li, T., Hassanali, A.A., Kao, Y.-T., Zhong, D. & Singer, S.J. Hydration dynamics and time scales of coupled water-protein fluctuations. *J. Am. Chem. Soc.* **129**, 3376-3382 (2007).
163. Abbyad, P., Shi, X., Childs, W., McAnaney, T.B., Cohen, B.E. & Boxer, S.G. Measurement of solvation responses at multiple sites in a globular Protein. *J. Phys. Chem. B* **111**, 8269-8276 (2007).
164. Halle, B. & Nilsson, L. Does the Dynamic stokes shift report on slow protein hydration dynamics? *J. Phys. Chem. B* **113**, 8210-8213 (2009).
165. Chang, C.-W., He, T.-F., Guo, L., Stevens, J.A., Li, T., Wang, L. & Zhong, D. Mapping solvation dynamics at the function site of flavodoxin in three redox states. *J. Am. Chem. Soc.* **132**, 12741-12747 (2010).
166. Jha, A., Ishii, K., Udgaonkar, J.B., Tahara, T. & Krishnamoorthy, G. Exploration of the correlation between solvation dynamics and internal dynamics of a protein. *Biochemistry* **50**, 397-408 (2010).
167. Mazur, K., Heisler, I.A. & Meech, S.R. Water dynamics at protein interfaces: Ultrafast optical kerr effect Study. *J. Phys. Chem. A* **116**, 2678-2685 (2011).
168. Nandi, N. & Bagchi, B. Dielectric relaxation of biological water. *J. Phys. Chem. B* **101**, 10954-10961 (1997).

169. Nandi, N. & Bagchi, B. Anomalous dielectric relaxation of aqueous protein solutions. *J. Phys. Chem. A* **102**, 8217-8221 (1998).
170. Bagchi, B. Water dynamics in the hydration layer around proteins and micelles. *Chem. Rev.* **105**, 3197-3219 (2005).
171. Simonson, T. & Brooks, C.L. Charge screening and the dielectric constant of proteins: Insights from molecular dynamics. *J. Am. Chem. Soc.* **118**, 8452-8458 (1996).
172. Rocchi, C., Bizzarri, A.R. & Cannistraro, S. Water dynamical anomalies evidenced by molecular-dynamics simulations at the solvent-protein interface. *Phys. Rev. E* **57**, 3315-3325 (1998).
173. Bizzarri, A.R. & Cannistraro, S. Molecular dynamics of water at the protein-solvent interface. *J. Phys. Chem. B* **106**, 6617-6633 (2002).
174. Marchi, M., Sterpone, F. & Ceccarelli, M. Water rotational relaxation and diffusion in hydrated lysozyme. *J. Am. Chem. Soc.* **124**, 6787-6791 (2002).
175. Bandyopadhyay, S., Chakraborty, S., Balasubramanian, S. & Bagchi, B. Sensitivity of polar solvation dynamics to the secondary structures of aqueous proteins and the role of surface exposure of the probe. *J. Am. Chem. Soc.* **127**, 4071-4075 (2005).
176. Bandyopadhyay, S., Chakraborty, S. & Bagchi, B. Exploration of the secondary structure specific differential solvation dynamics between the native and molten globule states of the protein HP-36. *J. Phys. Chem. B* **110**, 20629-20634 (2006).
177. Golosov, A.A. & Karplus, M. Probing polar solvation dynamics in proteins: A molecular dynamics simulation analysis. *J. Phys. Chem. B* **111**, 1482-1490 (2007).
178. Fogarty, A.C. & Laage, D. Water dynamics in protein hydration shells: The molecular origins of the dynamical perturbation. *J. Phys. Chem. B* (2014). Ahead of Print **DOI:** 10.1021/jp409805p.
179. Pal, S. & Bandyopadhyay, S. Importance of protein conformational motions and electrostatic anchoring sites on the dynamics and hydrogen bond properties of hydration water. *Langmuir* **29**, 1162-1173 (2013).
180. Saif, B., Mohr, R.K., Montrose, C.J. & Litovitz, T.A. On the mechanism of dielectric relaxation in aqueous DNA solutions. *Biopolymers* **31**, 1171-1180 (1991).
181. Denisov, V.P., Carlström, G., Venu, K. & Halle, B. Kinetics of DNA hydration. *J. Mol. Biol.* **268**, 118-136 (1997).
182. Sunnerhagen, M., Denisov, V.P., Venu, K., Bonvin, A.M.J.J., Carey, J., Halle, B. & Otting, G. Water molecules in DNA recognition I: hydration lifetimes of trp operator DNA in solution measured by NMR spectroscopy. *J. Mol. Biol.* **282**, 847-858 (1998).
183. Brauns, E.B., Madaras, M.L., Coleman, R.S., Murphy, C.J. & Berg, M.A. Measurement of local DNA reorganization on the picosecond and nanosecond time scales. *J. Am. Chem. Soc.* **121**, 11644-11649 (1999).
184. Andreatta, D., Pérez Lustres, J.L., Kovalenko, S.A., Ernsting, N.P., Murphy, C.J., Coleman, R.S. & Berg, M.A. Power-law solvation dynamics in DNA over six decades in time. *J. Am. Chem. Soc.* **127**, 7270-7271 (2005).

185. Andreatta, D., Sen, S., Pérez Lustres, J.L., Kovalenko, S.A., Ernsting, N.P., Murphy, C.J., Coleman, R.S. & Berg, M.A. Ultrafast dynamics in DNA: "Fraying" at the end of the helix. *J. Am. Chem. Soc.* **128**, 6885-6892 (2006).
186. Pal, S.K., Zhao, L. & Zewail, A.H. Water at DNA surfaces: Ultrafast dynamics in minor groove recognition. *Proc. Natl. Acad. Aci. U.S.A.* **100**, 8113-8118 (2003).
187. Pal, S.K., Zhao, L., Xia, T. & Zewail, A.H. Site- and sequence-selective ultrafast hydration of DNA. *Proc. Natl. Acad. Aci. U.S.A.* **100**, 13746-13751 (2003).
188. Bonvin, A.M.J.J., Sunnerhagen, M., Otting, G. & van Gunsteren, W.F. Water molecules in DNA recognition II: a molecular dynamics view of the structure and hydration of the trp operator. *J. Mol. Biol.* **282**, 859-873 (1998).
189. Dallmann, A., Pfaffe, M., Mügge, C., Mahrwald, R., Kovalenko, S.A. & Ernsting, N.P. Local THz time domain spectroscopy of duplex DNA via fluorescence of an embedded probe. *J. Phys. Chem. B* **113**, 15619-15628 (2009).
190. Banerjee, D. & Pal, S.K. Dynamics in the DNA recognition by DAPI: Exploration of the various binding modes. *J. Phys. Chem. B* **112**, 1016-1021 (2008).
191. Pal, N., Verma, S.D. & Sen, S. Probe position dependence of DNA dynamics: Comparison of the time-resolved Stokes shift of groove-bound to base-stacked probes. *J. Am. Chem. Soc.* **132**, 9277-9279 (2010).
192. Sen, S., Andreatta, D., Ponomarev, S.Y., Beveridge, D.L. & Berg, M.A. Dynamics of water and ions near DNA: Comparison of simulation to time-resolved Stokes-shift experiments. *J. Am. Chem. Soc.* **131**, 1724-1735 (2009).
193. Pal, S., Maiti, P.K., Bagchi, B. & Hynes, J.T. Multiple time scales in solvation dynamics of DNA in aqueous solution: The role of water, counterions, and cross-correlations. *J. Phys. Chem. B* **110**, 26396-26402 (2006).
194. Furse, K.E. & Corcelli, S.A. The dynamics of water at DNA interfaces: Computational studies of Hoechst 33258 bound to DNA. *J. Am. Chem. Soc.* **130**, 13103-13109 (2008).
195. Furse, K.E. & Corcelli, S.A. Molecular dynamics simulations of DNA solvation dynamics. *J Phys. Chem. Lett.* **1**, 1813-1820 (2010).
196. Bagchi, B. Anomalous power law decay in solvation dynamics of DNA: a mode coupling theory analysis of ion contribution. *Mol. Phys.*, Ahead of Print (2014).
197. Batabyal, S., Mondol, T., Choudhury, S., Mazumder, A. & Pal, S.K. Ultrafast interfacial solvation dynamics in specific protein DNA recognition. *Biochimie* **95**, 2168-2176 (2013).
198. Goel, T., Kumar, S. & Maiti, S. Thermodynamics and solvation dynamics of BIV TAR RNA-Tat peptide interaction. *Mol. BioSyst.* **9**, 88-98 (2013).
199. Sasmal, D.K., Ghosh, S., Das, A.K. & Bhattacharyya, K. Solvation Dynamics of biological water in a single live cell under a confocal microscope. *Langmuir* **29**, 2289-2298 (2013).
200. Ghosh, S., Chattoraj, S., Mondal, T. & Bhattacharyya, K. Dynamics in cytoplasm, nucleus, and lipid droplet of a live CHO cell: Time-resolved confocal microscopy. *Langmuir* **29**, 7975-7982 (2013).

201. Chowdhury, R., Jana, B., Saha, A., Ghosh, S. & Bhattacharyya, K. Confocal microscopy of cytoplasmic lipid droplets in a live cancer cell: number, polarity, diffusion and solvation dynamics. *Med. Chem. Commun.* **5**, 536-539 (2014).
202. Ghosh, S., Chattoraj, S. & Bhattacharyya, K. Solvation dynamics and intermittent oscillation of cell membrane: Live chinese hamster ovary cell. *J. Phys. Chem. B* **118**, 2949-2956 (2014).

End of Chapter 1

Chapter 2

Working Systems, Materials and Methods

This chapter describes about different working systems, fluorescent probes (drugs) and several other materials including non fluorescent molecules and solvents which are used in different projects depicted in the thesis. The major systems under consideration are reverse micelle (RM), carbon nanotube (CNT), serum protein (SA) and RNA aptamer. The present chapter also encompasses detailing about the experimental methods, sample preparations, molecular modeling and molecular dynamics simulations.

2.1. Working Systems

2.1a. Reverse Micelle

Reverse micelles (RM) are surfactant coated polar droplets considered as an *in-vitro* mimic of cells.[1-6] The interior diameter of reverse micelle matches well with the size of confinement observed in biological cavities, which also justifies the cell mimetic ability of RM.[1-5] The uniqueness of reverse micelles mainly belongs to the unidirectional trapping of water (polar solvents), which makes RM stable and tuneable, hence a persistent centre of attention to researchers. RM formed by a ternary mixture of polar-solvent, surfactant and non-polar solvent consists of a nanometre-sized water/polar solvent droplets or central 'nano-pool' surrounded by surfactant molecules in such a way that the polar head groups are oriented toward the surface of the 'nano-pool' and non-polar tails are projected out toward the bulk non-polar organic phase (**Scheme 2.1**). One of the well characterized RM-forming surfactants, AOT (aerosol OT, dioctyl sodium sulfosuccinate, **Scheme 2.1**), has the ability to solubilise substantial amounts of water or other polar solvent in a non-polar solvents.[5-9] RM is characterized by 'w_s', defined as the molarity ratio of polar solvent to surfactant. The definition of 'w_s' is as follows;

$$w_s = \frac{[Polar\ solvent]}{[surfactant]} \qquad \ldots 2.1$$

AOT molecules dissolved in a long chain alkane above a particular concentration (~0.1 mM) forms reverse micelle. Properties of the reverse micelles depend over factors like non-polar phase, temperature, and the presence of a co-surfactant, etc.[7] Although AOT is in lead role in RM formation but many other amphiphiles (such as SDS, TX-100, Brij) have also been extensively used to form reverse micelles in pure and mixed hydrocarbon solvents.[10] The stability of the reverse micelle in a non-polar solvent is mainly governed by four factors;

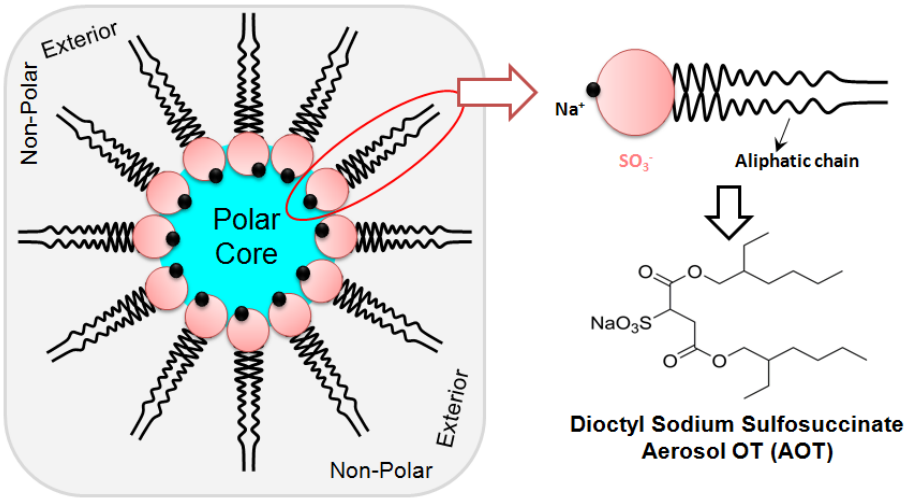

Scheme 2.1. *Schematic representation of reverse micelle.*

hydrogen bonding, dipole-dipole, dipole-induced dipole and dispersion interactions.[1-6] The nature of the surfactant head groups and counter ions are also known as governing factor for RM stability. Not only the formation but also an extensive effort has been invested till date for the determination of appropriate structure of the reverse micelles. To confirm the presence of RM in a solution one must be able to detect the individual particles in solution. One can do it in a best way through scattering methods. A number of scattering based methods namely, dynamic light scattering (DLS),[7, 11-15] small angle neutron scattering (SANS),[16-18] and small angle X-ray scattering (SAXS)[19-21] have been extensively used to monitor the formation and characterizations in solution phase. It is the DLS which have been considered as the premiere method to uncover details about the structures in microemulsions due to its easy access and user friendly nature of use.[16, 22] In recent days attention has been given also for other non-

scattering techniques (such as viscosity and diffusion based methods) to measure the formation of RM in solution. Interestingly, formation of RM will lead to the retardation of diffusion compared to the individual surfactant unit in the solvent. Depending over this principle one can determine the RM size using fluorescence correlation spectroscopy (FCS).[23-26] Moreover, conductometric as well as viscometric measurements have also been utilized to infer the formation and properties of RMs diffusing in non-polar solvent.[12, 27-29] A generalization of several characterization methods show that the size of a water reverse micelle is usually governed by the following equation;

$$R_H(nm) = 0.175w_0 + 1.5 \quad \ldots 2.2$$

where, R_H is the hydrodynamic radius of the water RM, and W_0 stand for water to surfactant concentration ratio. The irreversible trapping of polar solvents along with the size tuning ability enhanced the importance of the RM as a burgeoning topic of interest. Not only experimentalists but theoreticians have also shown their interest to explore the RM structures.[30-33] The effort has been extended by Senapati *et al.* and many others who explored various reverse micelles through coarse grain models.[34-41] Among various kinds, the water reverse micelle is the centre of attention as only water comprises the bio systems. A reverse micelle indeed can encapsulate a fairly large amount of water (50 water molecules per molecule of surfactant) to form RM. Such nanometre sized water droplet dispersed in a non-polar liquid is called "water pool".[42] The water molecules confined inside reverse micelle pool of are vastly different in terms of several physical properties (like polarity and viscosity) from the bulk water. All the water molecules except the six most tightly held ones freeze at -50ºC.[1-6] Existence of three distinct kinds of water molecules has been established inside RM using different techniques.[7, 43-45] The water molecules residing close to the polar head groups of the surfactant are held tightly and known as "bound water".[7, 43-45] Water molecules residing near to the central region of the water pool is labile in nature and termed as "free water".[7, 43-45] Waters which are entrapped in between the surfactant molecules are defined as "trapped water".[7, 43-45] Extensive efforts have been employed to differentiate the water molecules trapped inside RM with that of bulk water.[44, 46-52] To explore the behaviour of RM water, Fayer[51, 53-61] and Bakker[42, 62, 63] group followed the time-resolved vibrational spectroscopic technique by probing isotopically labelled water molecules (HOD) and detected a *w* dependent dynamics of water where as layer of water forms hydrogen bonds with the AOT

heads and the rest form a pool at the core of RM. Although the water-RM is consistent point of attention several other non-aqueous polar solvents have been studied extensively inside RM confinements. To the best of our knowledge the first report on non-aqueous reverse micelles was found with glycerol[64] and formamide[65] which are highly structured and able to donate and accept hydrogen bonds. The research on non aqueous polar-solvent loaded RM expanded day by day with several solvents like methanol,[14, 66-72] glycerol,[64, 73-77] ethylene glycol,[14, 75, 77-80] formamide,[14, 69, 81, 82] N-methylformamide,[83] dimethyl formamide (DMF),[14, 29, 75, 79] dimethylsulfoxide (DMSO),[84] acetonitrile (ACN),[14, 67-70] and many other solvents. The nanoscopic water pools inside RM have been used for a range of diverse applications like nanoparticle synthesis,[8, 85-89] controlling rate of chemical reactions,[90-92] detection of biomacromolecules,[93, 94] trapping of hydrogen bonded dry (without any intervening water molecules) urea,[18, 95] and a confined media for excited state proton transfer[96-100] reaction etc. Irrespective to the surfactant or the loaded solvents, RMs are the ever green working system for researcher for a prolonged duration of time. In my thesis AOT reverse micelle dispersed in n-heptane has been used for loading urea inside the core and to compare the dynamics with water (**Chapter 6**).

2.1b. Carbon Nanotube

The longstanding effort to achieve a purely two dimensional material was settled by the discovery of graphene in 2004. Eventually more than a decade before of graphene's birth, the carbon nanotube (CNT) was discovered by researchers. First time in 1991 Iijima observed the tubular carbon structure[101], where several graphitic layers were wrapped over one another. Notably it was the multi walled carbon nanotube (MWNT) (with adjacent shell separation of ~0.34 nm, diameters of ~1 nm and high Length by diameter ratio) but not the single walled carbon nanotube (SWNT) detected for the first time. After two years, Iijima and Ichihashi[102] and Bethune *et al.*[103] synthesized single-walled carbon nanotube (SWNT) by using of metal catalyst based arc-discharge method. When diverse terms like SWNT and MWNT appears together, here its pertinent to mention that depending over the number of graphene layers involved in rolling (**Scheme 2.2**), CNTs can be categorized in three types namely single walled (SWNT), double walled (DWNT) and multi walled carbon nanotube (MWNT) carbon nanotubes. For DWNT and MWNT the stability of the nanotube structure is governed by the π-π staking interaction between graphene layers wrapped over one another and this number of layers drastically modulates the properties of the nanotube.[101-103] After the first synthetic

track described, a number of other methods for CNT synthesis have been developed like laser-ablation[104], chemical vapor deposition (CVD)[105], sol-gel[106] method, gas phase metal catalysis[104] are few to name. Depending over the need of large scale synthesis and more precise modifications of CNT surface, the effort for new methods have been continued when Kirsten Edgar and John L. Spencer synthesized carbon nanotubes from an aerosol precursor[107] and Montoro *et al.* synthesized SWNT by arc water process[108]. In recent past few other methods like iron catalysis[109], fluidized-bed method[110], non-equilibrium plasma[111] and nebulizer-spray pyrolysis[112] became popular and till date are used extensively.

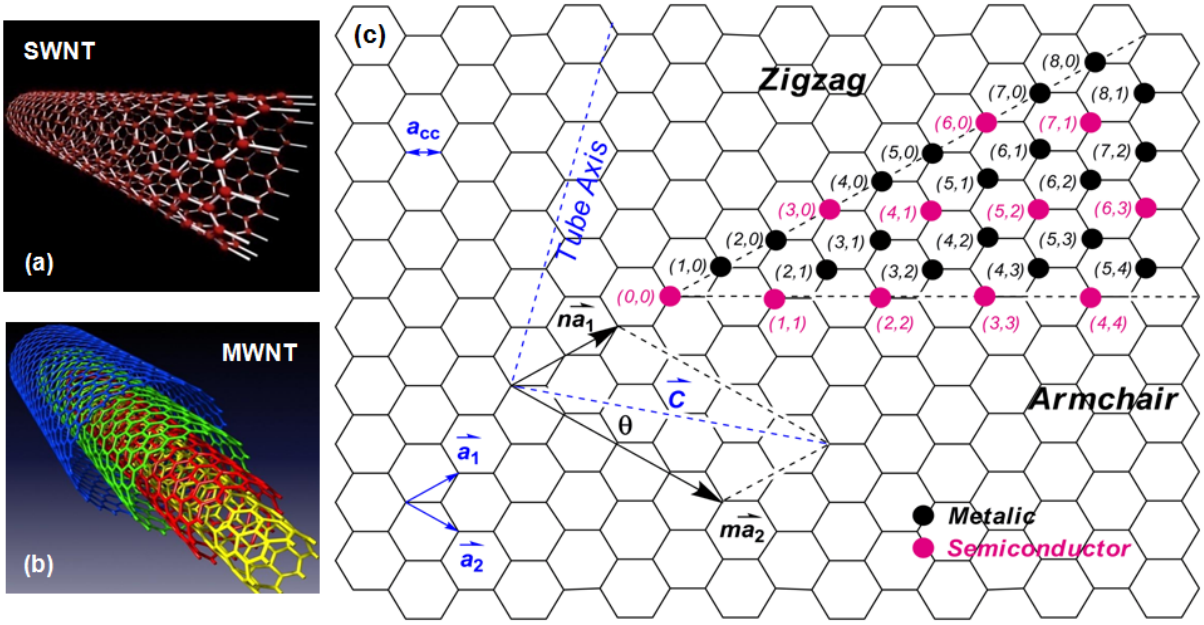

Scheme 2.2. *(a) Single (SWNT) and (b) multi (MWNT) walled carbon nanotube. (c) A two dimensional hexagonal graphene sheet with different chiral vectors and angles to define different kind of carbon nanotubes. Variable values of Chiral vector C (circumference of nanotube is given by the length of this chiral vector) and chiral angle θ (defined as the angle between chiral vector C and the zigzag axis) define a carbon nanotube. a_1 and a_2 are the unit cell vectors of the 2D sheet.*

Carbon nanotube (CNT) is defined as a seamlessly rolled-up graphene sheet in a tube form with a continuous unbroken hexagonal mesh and carbon molecules at the apexes of the hexagons. This carbon made tube-shaped materials (CNTs) usually offer a diameter (<1 nm to ~50 nm) in nanometer and the length (in μm) in thousand or million times higher than its diameter.[113] Some of the CNTs are also known to pursue a length-to-diameter ratio of up to 132,000,000:1.[114] Attention rises about this carbon based tubular materials due to its unusual

physical and electronic properties, which are valuable for nanotechnology, electronics, optics, materials, technology as well as for biological applications. Orbital hybridization theory describes the chemical bonding in nanotubes as an extended network of sp^2 carbons, similar to those of graphite or as a mixture of sp^2 and sp^3 (similar like alkanes and diamond) bonds at the point of surface modifications. Carbon nanotubes have many verities, differing in length, thickness, rolling angle of the graphene sheet, helicity and number of layers. Although nanotubes are formed from essentially the same graphite sheet, the physical characteristics differ depending on these variations. CNTs are majorly classified into two categories namely metallic (Met) and semiconducting (SC), depending over the sheet direction, along which graphite sheet is rolled to form nanotube cylinder.[113, 115] The direction in graphite sheet and nanotube diameter are denoted by structural indices (*n*, *m*) alternatively known as chiral vectors. Various combination of structural indices denote different nanotube types like armchair (*n*=*m*), zigzag (*n*=0 or *m*=0) and chiral (any other *n*, *m* combination) (**Scheme 2.2**). All armchair SWNTs are found to be metallic in nature. Those with *n*-*m*=3*k* (where *k* is a nonzero integer) condition are semiconducting with a tiny band gaps. For *n*-*m*=3*k*±1, semiconductor band gap is detected to be inversely proportional to the tube diameter.[113, 115] The most fascinating characteristics and similarities between graphene and CNT, are ultrahigh charge carrier mobility[116, 117], very high thermal conductivity[118, 119], extremely large surface area[120, 121], exceptional mechanical strength, and flexibility[122, 123], majorly arise from similar sp^2 hybrid network with extensively delocalized π-electrons[124-126]. These unique properties along with atomic dimensions are causing rapid advances of various relevant applications of CNT, extending from electronics[127-131], energy conversion/storage devices[132], catalysis[133-136] to nano-composites[136-139]. CNT based materials are also emerging as outstanding coating materials, such as MWNT-containing paints are anti-corrosive and can strongly repulse algae and barnacles from ship hull.[140] CNT based materials has been extended day by day where CNT thin-film transistors (TFTs)[141], organic light emitting diodes (OLEDs)[142], CNT based printing[130], radiofrequency identification tags[131] and nonvolatile memory based molecular dimension computation devices[143] are a few to talk about.

The burning problem of today's world is energy storage and environmental issues. From recent past carbon nanotube have started aiding relief for such issues. MWNTs are extensively used in lithium ion batteries of laptops, mobiles and pads.[144, 145] 1 wt % of CNT loading in $LiCoO_2$ cathodes and graphite anodes enhances the electrical connectivity and mechanical integrity.[151, 153] It further influences the rate of electrical production and cycle life

of the batteries, hence a huge commercialization of CNT doped batteries have been started.[144, 146] Application of CNT based water purification has become an upcoming domain of research. A cross-linked CNT sheet provides mechanically and electrochemically robust networks with controlled nano-porosity. These porous CNT structures are used to oxidize organic contaminants[147], bacteria, and viruses[148]. Researchers are trying to generate drinking water by separating salt even at sea water concentrations.[149] Eventually, SWNT can be used in future to resolve the drinking water problem on earth.

Although we have provided an extensive discussion about the major advances in CNT based technologies, it is necessary to mention the contribution of CNT towards the field of biology and medicine. Ongoing interest in the field of biotechnology is up-rising majorly due to two reasons: (i) the nano-dimension of CNT and (ii) compatibility with biomolecules like DNA and proteins. Moreover, CNT based fluorescent measurements[150], photo-acoustic imaging[151] and localized photo-excitation therapy using near-IR radiation[152] have raised as dominant medical technologies. CNT based biosensors offer large changes in electrical impedance[153] and optical properties,[154] which is typically controlled by adsorption of the target drug molecule on the CNT surface. Very recently scientists developed CNT strips for estrogen and progesterone hormones detection, microarrays of DNA and protein detection.[155] Moreover, CNT based NO_2 and cardiac troponin sensors have revolutionized carbon-biotechnology.[155] Detection of toxins and gases in food industry, military and industrial applications became possible by CNT based materials.[156, 157] The applications of CNT never restrict *in-vitro* but extended to intra cellular limits. CNTs are found penetrating the cell walls by binding their tips on the cell membrane receptors.[158] This mechanism facilitates the transfer of drug molecules to the target by either electrical impulses or by near-IR radiation.[159] Recently Liu *et al.* showed 60 weight percent loading on CNT of an anticancer drug doxorubicin compared to the negligible loading capability in liposome (10 wt %).[160] The possible quest of CNT cytotoxicity has been answered in terms of surface modifications. It has been observed that the geometry and surface modifications of CNT gives reasonable impact over its cytotoxicity.[161] In 2008 Poland *et al.* reported that injection of subsequent amount of MWNT in rat lungs causes asbestos like pathogenicity[162] whereas a recent report shows properly dispersed SWNTs offer insignificant impact over rat lungs.[163] As in therapeutic applications dispersion of SWNT is of primary importance, and hence, the behavior of CNTs in water is always a point of interest. In the thesis, I have used different kinds of SWNT to study the dynamic behavior of water molecule over the surface.

2.1c. Serum Albumin

The term albumin was originated from a German word '*albumane*' which evolved from the Latin word '*albus*' meaning white. Before 16th century Greek physician Hippocrates of Cos first noted a foamy part of urine containing albumin.[164] In 16th century Swiss physician Paracelsus precipitated this protein from urine using vinegar. Later Frederick Dekkers reported the serum albumin precipitation by heating.[164] In 1616 when Henry described the mechanism of blood circulation in mammals[164], researchers started gaining interest about serum albumin, which is continued till date. Serum albumin (SA) is the most abundant protein in blood matrix. Depending over the origin, albumins are named after the source name, like human serum albumin (HSA, produced from human blood plasma), bovine serum albumin (BSA, obtained from bovine serum) etc. In present thesis, we are majorly concerned about HSA and BSA, as these two are extensively used for experiments. Almost half (albumin concentration in serum is ~35 - 50 g/L)[164] of the total serum protein content in human blood plasma is albumin which is mainly produced from liver. Albumin is synthesized in the liver as proalbumin. Proalbumin contains an N-terminal peptide which is removed before nascent protein is released from the rough endoplasmic reticulum. Thereafter, the Proalbumin is slashed in the Golgi body to produce the secreted albumin in blood. This albumin lives approximately ~20 days within which newly generated albumin molecules replace the older.

The complete sequence of HSA was determined almost simultaneously by Brown and co-workers in Austin (in 1975) and Meloun *et al.* in Prague (in 1975).[164] Later Cater *et al.* reported the crystal structure of HSA.[165, 166] Human serum albumin (HSA) is a monomeric α-helical globular protein with 585 amino acids in its sequence with a molecular weight of 66.5 k.Da.[167, 168] HSA contains three homologous domains (I, II, III), each of which is constituted by two sub-domains A and B (**Scheme 2.3**).[167, 168] There are 17 disulfide linkages present (high cysteine content) in HSA which holds the domains together. As the domains II and III share a common motif, conformational change or effect of binding in one of the domain is complementary to another.[167, 168] The principal ligand (consider the term ligand valid for anything binds to the protein) binding sites are well explored from crystal structure analysis and named as Sudlow's site I (SS1) and Sudlow's site II (SS2). Warfarin like bulky heterocyclic anions are well known marker for SS1, located at subdomain IIA, whereas ibuprofen and other aromatic extended conformers of carboxylates are extensively used as SS2 at sub-domain of IIIA (**Scheme 2.3**) marker.[169-172] In comparison, BSA is also a *α*-

helical monomeric protein but contains 583 amino acids. Interestingly it is again the Brown and co-workers who first reported the complete sequence of BSA.[164] BSA is homologous to HSA only with a minute structural difference. The major portion of HSA fame as a model protein lies on the fact that HSA contents a single tryptophan residue at the position 214 (TRP-214). This single tryptophan moiety makes easier monitoring the native and also the

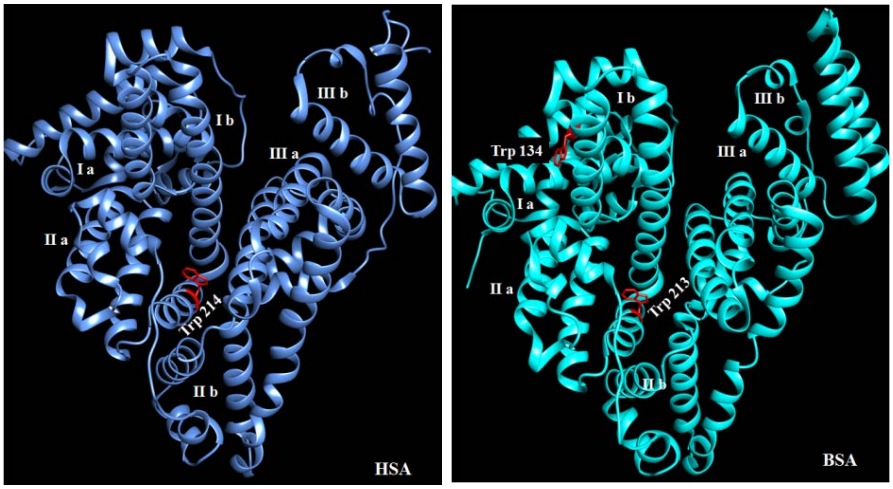

Scheme 2.3. *Crystal structure of HSA (PDB ID:2VUF) and BSA (PDB ID: 4F5S), where the idivisual domains are marked by white and the tryptophan residues are marked by red color.*

ligand bound structure of HSA through fluorescence measurement. On the other hand, two different tryptophan residues at 134 and 213 (TRP-134, TRP-213) position in BSA complicate the fluorescence analysis. Still from the day of crystal structure and sequence determination, serum albumins are the top listed choice for the researchers, as a model protein and a countless number of studies have been reported till date.

Basic structure, conformation, structural modifications and denaturation of SA were always a topic of interest for a prolonged duration.[173-179] Long back Eisenberg *et al.* have tried the pH induced structural deformation of HSA.[173] HSA denaturation have been reported by using heat in presence of perfluorooctans.[174] Recently, Amdadul *et al.* monitored the drying induced denaturation of BSA, and they concluded that though 10 wt percent of α- and β-lactoglobulin gets denatured using conditioned air (65° and 80°C, 2-3% RH, 0.5 m/s velocity for 600 s) but no significant effect has been observed for BSA.[180] Although well known but recently the effect of several unfolding dynamics of serum protein re-explored by temperature and guanidium hydrochloride using FCS.[181] Kooshk *et al.* observed the effects of

hypochlorite-mediated oxidation and its impact over BSA structural stability, surface hydrophobicity and they concluded an enhanced ability of ligand binding under oxidized condition.[182] Sekhar *et al.* have shown that a variable viscosity gradient can also act as the protein denaturant.[183] On the other hand Norberto *et al.* have used a combined effect of pressure and urea for denaturation of serum protein.[184] Very recently Ghosh *et al.* have shown denaturation of HSA by anionic surfactant using variation of fluorescence from the drug norharmane.[179] Effect of several toxic materials like cadmium (Cd)[185, 186], silica nanoparticles[187-189], naphthoquinone derivatives,[190] and bisphenols,[191] have resulted structural deformation of serum albumins in different extents. Serum proteins are also extensively used for synthesizing several bio and composite materials. MWNT-BSA based composite nano-material (CNM) has been reported for solid state film preparations.[192] Technique has been developed for preparation of a novel gold nano-particles trapped within a fiber of unfolded proteins which appears useful for conductive chip designing.[193] Cai *et al.* fabricated photonic crystal protein hydrogels by using pure BSA and HSA hydrogels and explored multiple high-affinity BSA and HSA binding sites for salicylates, ibuprofen and picosulfate.[194] Its becoming a trivial practice devising protein coated nanoparticles[195, 196], SA based logic gates[197], ultrathin hybrid film[198, 199] and serum based hydrogels[200] for diverse biophysical applications. Serum proteins are well known for their applications in biotechnological devices. Very recently Chunsheng *et al.* have used BSA for developing light-addressable DNA chips for label free DNA detection.[201] BSA has been used as scaffold for pt-nanoparticles,[202] and chiral conducting polyaniline nanospheres[203] synthesis. Martins *et al.* designed trans-dermal hyaluronic acid (HA) conjugated- BSA nano-dispersions for in vivo delivery of HA.[204] In last few years several other serum composites are developed among which Gd_2O_3 nanoperticle-SA conjugates for MRI applications[205, 206], protein-wafers for enzyme inhibition[207, 208], BSA-AU composite[209, 210], serum albumin-CNT composites[211] for modified electrical signal transition are a few to mention about.

When it relates to biological application the most common application for serum proteins are maintaining the osmotic pressure of blood and transport of thyroid hormones. Moreover, it is responsible for the transport of a diverse kind of hormones, fatty acids, small molecules and essential as well as trace metal ions to its destination in the body.[167, 168] Till date a colossal number of ligands or drugs[212-235], surfactants[236], polymers/dendrimers[237], synthetic molecules[238-243], nanoparticles[244, 245], quantum dots[246] have been investigated with serum proteins and the effort is being continued. The first application of serum protein as a

drug was started during world war-II, when SA had been used for treatment of shock on battlefield. HSA fraction V (fraction V is the commercial name of > 96% pure albumin used for medical purpose. In the 5th step of "Cohen method" of commercial fractionation >96% pure albumin is obtained, hence named as fraction V) was and still is an attractive option for Hypovolemia corrections for shock related trauma.[165] Very recently Kooshk *et al.* have shown native and modified BSA can be used as a cargo for several poorly water soluble non-steroidal anticancer drugs like Curcumin.[247] Bujacz *et al.* have reported naproxen bound BSA crystal structure.[248] Wang *et al.* has shown delocalized lipophilic cations (DLC), which are recently marked as anti-carcinogens can be delivered to the target by using serum proteins as the cargo.[249] Present thesis concern about the molecular interaction of flavins and ellipticine with serum protein described in respective chapters.

2.1d. Aptamer

The term "Aptamer" originated from the combination of a Latin word '*aptus'*, which means "fit", and Greek term '*meros'* meaning "part". Hence aptamers are the sequence of nucleotides or amino acids which can fit by part. In general, aptamer can be defined as small sequence of oligonucleic acid or peptide molecules that bind to a specific target molecule with a high selectivity. Depending over the monomeric building blocks of aptamer it can be classified as:

- DNA or RNA aptamers which consist of (usually short) oligonucleotide strands.
- Peptide aptamers, consist of a variable short length of peptide scaffolds.

Nucleic acid aptamers are the short sequences of nucleotides that can be engineered through repeated rounds of *in vitro selection* or SELEX[250] (systematic evolution of ligands by exponential enrichment) method and bind with various targets including small molecules, proteins, nucleic acids, and even cells, tissues and organisms. These are useful in biotechnology and therapeutic applications, as they offer high extent of molecular recognition properties. Aptamers are in advantageous position compared to antibodies, as these can be synthesized in a test tube, along with a desirable storage and offers almost negligible immunogenicity in therapeutic applications. In 1990, the Gold *et al.*[251] and Szostak group[252] almost simultaneously discovered the technique of in vitro selection for aptamer

detection from a pool of sequences. Gold group processed RNA aptamer against T4 DNA polymerase[251]; and the Szostak lab, utilized *in-vitro* selection of RNA ligands against various

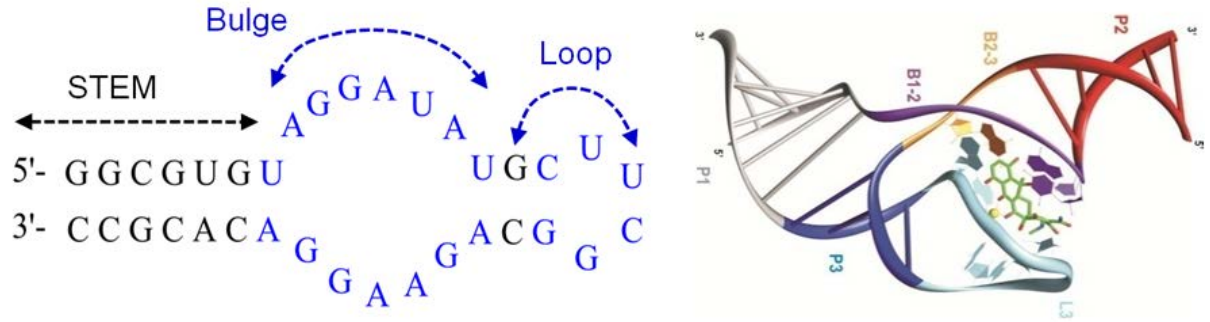

Scheme 2.4. *RNA aptamer showing the stem, bulge and loop region along with a ligand bound RNA aptamer[253] structure.*

organic dyes[252]. Szostak first coined the term aptamer for these nucleic acid-based systems. From recent past both of DNA and RNA aptamers are igniting upraising interest, as they pursue a number of advantages such as;

- Very high selectivity to its targets.
- Used for selective separation of a particular target ligand from a pool of molecules.
- Inherently low molecular weight for non-modified aptamers
- A short half-life of few minutes to hours.
- Well known to be cleared rapidly from the bloodstream, mainly due to nuclease degradation followed by clearance from by the kidneys.

Aptamers have enormous potential as therapeutics due to their ability to bind with proteins and specifically inhibit their functions with minimal or no harmful side-effects. Note that the concept of aptamer based sensing emerged in the 1980s from research on human immunodeficiency virus (HIV) and adenovirus. For the first time researchers noticed these viruses encode a small structured RNA that can bind to cellular proteins with high affinity and specificity.[254] A continuous attempts resulted various target selective aptamers including lysozyme[255], thrombin[256], human immunodeficiency virus trans-acting responsive element (HIV TAR)[257], hemin[258], interferon-γ[259], vascular endothelial growth factor (VEGF)[260], prostate specific antigen (PSA)[261], and dopamine[262]. Padlan *et al.* first

reported the crystal structure of lysozyme bound aptamer and have shown that bio-catalytic activity of lysozyme has been inhibited while it binds to aptamer.[263]

Among many others, fluorescence based aptamer are the simplest. An aptamer itself labeled with a fluorophore and/or a quencher acts as an on-off sensor. As for example cocaine-specific aptamer detects it target using a FRET interaction between fluorescein and DABCYL moieties.[264] Recently few other FRET pair based sensing[265, 266] are also reported. Aptamer beacons with a pairs of changing conformations such as hairpin shape or a hybridization form are also known to monitor the presence of the target in solutions through fluorescence. Additionally, many aptamer composite nano-materials, including nanoparticles[267, 268], quantum dots (QDs)[269, 270], AuNPs[271], CNTs[270, 272, 273], graphene oxide (GO)[274, 275], polymer nanobelts, and coordination polymers, have been investigated using their fluorescence-quenching/enhancement effect instead of using a more traditionally quencher. Pothoulakis *et al.* presented the Spinach RNA aptamer, a selective binder to green fluorescent protein (GFP) as a tool to characterize mRNA expression in Escherichia coli.[276] Later Han *et al.* reported illumination of the Spinach-DFHBI RNA Aptamer-fluorogen complex by photo-conversion and subsequent dissociation leads to fast fluorescence recovery as a tool for living cell RNA imaging.[277] The living cell imaging technique by aptamer sensing has been boosted by the fluorescent modified 99mTc-MAG3-Aptamer which acts as a marker for human tumor cells.[278] Costa *el al.* have shown adaptive sensing of several tri-phenyl dyes by malachite green (MG) aptamer.[279] Weakly fluorescent MG emits strongly while binds to its aptamer; which can be used as a detection device for the folded structure of MG sensing RNA aptamer. Recently Randall *et al.* have used fluoregenic MG binding aptamer nanoparticles to detect the *in-vivo* half-life of the aptamer, and they concluded it to be ~4.3 hrs.[280]

Not only fluorescence, but various other aptamers such as affinity sensors[281], biosensors[282] surface acoustic wave (SAW)[283], micro channel plates[284], QCM[285], and micro channel cantilever sensors[286] have been exploited. Recently Singh *et al.* has nicely modulated the high selectivity of RNA aptamer to exclude tautomeric forms of oxythiamin pyrophosphate (OxyTPP) and oxythiamin (OxyT) using 2D-IR and NMR spectroscopy.[287] A nanoaptasensor using a single wall nanotube (SWNTs) device was developed for detecting small molecules.[288] These methods generally do not require target labeling; they only observe the differential changes in optical properties and mass. Therefore, these methods are primarily appropriate for relatively large molecules but not for small molecules, including

organic molecules, toxins, and metabolites.[289, 290] Muslum *et al.* have reported neomycin-B detecting aptamer structure from NMR studies.[291] The ongoing fame of aptamer has also been extended in sensor[292-298]. The high affinity detection of botulinum neurotoxin within a detection period of 90 minute revolutionize the field of biosensing.[299]

In 2004 Food and Drug Administration (FDA) approved vascular endothelial growth factor (VEGF) specific aptamer for the treatment age-related disorders.[300] Since then, aptamer technology has been emerged as more effective and authoritative, and the number of studies is exponentially increasing. Macugen, a pegylated aptamer drug developed by Pfizer and Eyetech, is already commercially available. It's a single strand nucleic acid with specificity to VEGF165, plays a critical role in angiogenesis and permeability.[301] Recently Regado Bioscience developed REG1, a aptamer drug, for anticoagulation, which is in Phase II clinical trials.[302] In addition AS1411 (a nuclein-specific aptamer for acute myeloid leukemia), ARC1779 (a vonWillebrand factor-specific aptamer for carotid artery disease) and NU172 (a thrombin-specific aptamer for anticoagulation) are currently in a clinical trials.[303-308] Moreover, cell surface receptors binding aptamers have been exploited to deliver drugs and a variety of other cargo into cells. For example, PSMA (prostate-specific membrane antigen) is an important prostate cancer marker.[309, 310] Small interfering RNAs (siRNAs) are sharing spotlight recently as a new class of therapeutics. Levy and co-workers introduced an siRNA-aptamer conjugate via a modular streptavidin bridge using an anti-PSMA aptamer for prostate cancer cells (LNCaP).[311] When therapeutic world has burning problem with amyloid fibrils, aptamer aided relief for the same. Christian *et al.* reported fluorescently tagged anti-Aβ RNA aptamer which binds amyloid plaques in both ex and in vivo human Alzheimer's tissues and omits the complication of protein tagging.[312] Sulforhodamine-B and the SRB-2 aptamer are used to monitor transcriptions in live bacteria.[313] RNA based gene therapy is emerging technology for days. Whatley *et al.* screened 100 full length and >60 truncated aptamer sequences and detected RNA aptamers that bind the reverse transcriptase (RT) of human immunodeficiency virus (HIV).[314] Recently Salmonella Enteritidis detecting aptamer came into the picture, which inhibits the bacteria and its harmful effects.[315] Various other aptamers like, tetracycline binding aptamer[316], Streptavidin[317] binding aptamer, Guanosine triphosphate[318] binding aptamer, Vitamin B_{12} detecting nano-RNA aptamer wire[319] etc. are the major point of attention for researchers. In our study, we have used flavin binding RNA aptamer for selective detection of flavin and modulating the folding dynamics of FAD discussed in the respective chapter.

2.2. Materials

In the present section I have listed several fluorescent drugs, molecules as well as non-fluorescent solvents, salts used for different experiments mention in chapter 4 and onwards. To overcome the unnecessary lengthening of the thesis these are given in tabular form.

Table 2.2.1. *Different materials, its source and purity along with the chapter number it has been used is mentioned in the table.*

Name	Source	Grade (Purity)	Ch.
Flavin Adenine Dinucelotide (FAD)	Sigma Aldrich	HPLC (≥ 96%)	4
Flavin mononucleotide (FMN)	Fluka	HPLC (~ 90%)	4
Riboflavine (RF)	Sigma Aldrich	HPLC (≥ 96%)	4
Ellipticine	Sigma Aldrich	Purity ≥ 99%	5
Human serum albumin (HSA)	Sigma Aldrich	Molecular Biology (99%)	4,5
Bovine serum albumin (BSA)	Sigma Aldrich	Molecular Biology (99%)	5
Calf thymus DNA Na salt (1000 bp long)	Sigma Aldrich	Molecular Biology	5
Salmon sperm DNA (2000 bp long)	Sigma Aldrich	Molecular Biology	5
Urea	Sigma Aldrich	Molecular Biology	4
HEPES	Sigma Aldrich	BioUltra (≥ 95.5%)	4
Sodium phosphate dibasic (NaH_2PO_4)	SRL, India,	Purity 99.5%	4,5
Sodium phosphate dibasic (Na_2HPO_4)	SRL, India,	Purity 99.5%	4,5
Sodium chloride (NaCl)	Sigma Aldrich	BioXtra ≥ 99.5%	4,5
Potassium chloride (KCl)	Sigma Aldrich	BioXtra ≥ 99%	5
Ethylenediaminetetraacetic acid (EDTA)	Sigma Aldrich	BioUlra (≥99%)	4
Citric acid	Sigma Aldrich	purity ≥ 99.5%	4
Hydrochloric acid	Merck, India	Purity 90%	4
Sodium hydroxide (NaOH)	SRL, India	Purity 98%	4
1% (w/v) SDS dispersed SWNT	NanoIntegris	Purity ~98%	6
Sodium dodecyl sulfate (SDS)	SRL, India	Purity ~99%	6
Dioctyl sulfosuccinate sodium salt (AOT)	Sigma Aldrich	Purity ~98%	6
Coumarin 153 (C153)	Sigma Aldrich	Purity ~99%	6
Coumarin 343 (C343)	Sigma Aldrich	Purity ~99%	6
n-heptane	Sigma Aldrich	Spectroscopy	6
Magnesium chloride ($MgCl_2$)	Sigma Aldrich	Biograde (99%)	6

2.3. Methods (Experimental and Theoretical Method)

All the methods of sample preparations, experimental methods as well as theoretical methods of calculation are described in this section. The corresponding chapter at which the methodologies have been used are mentioned at the respective position.

2.3a. Buffer Preparation

All the experiments (expect solvation dynamics experiments) described in the thesis are carried out in buffer solutions. We have used mainly three different kinds of buffers; (i) citrate buffer and (ii) phosphate buffer which are mainly salt based buffer and (iii) HEPES, which is an organic buffer. A 10 mM citrate buffer was prepared by mixing of dibasic anhydrous sodium phosphate (Na_2HPO_4) and citric acid ($C_6H_8O_7$) solutions. Whereas, 10 mM Phosphate buffer was prepared by mixing sodium dihydrogen phosphate (NaH_2PO_4) and disodium hydrogen phosphate (Na_2HPO_4) of appropriate calculated weight mixed in water. On the other hand HEPES buffer is used for flavin-serum protein interaction. HEPES (*4-(2-hydroxyethyl)-1-piperazineethanesulfonic acid*) is a zwitterionic organic buffering agent. The pK_a for HEPES is 7.5 and well accepted buffer agent within pH = 6.8 to 8.2. A 10 mM HEPES solution was prepared by dissolving appropriate amount of solid HEPES in Millipore water. The fine adjustment of lower pH was done by drop wise addition of dilute phosphoric acid and for higher pH range 0.5 M sodium hydroxide solution was used. For RNA aptamer samples Phosphate buffer (Na_2HPO_4 + NaH_2PO_4, 10 mM) saline (PBS) of pH 7.2 (containing 137 mM NaCl, 3 mM KCl and 0.1 mM EDTA) was used for all respective experiments. The Mg^{+2}, Na^+ and K^+ ion concentrations were maintained by addition of concentrated stock of $MgCl_2$, NaCl and KCl respectively. The pH of the solutions was measured by using pH-1500 (Eutech Instruments) and it was further cross checked by silicon micro sensor pocket sized pH meter (ISFETCOM. Co. Ltd., Japan). All of the solutions were prepared in Millipore water showing resistance of 18.2 $\mu\Omega$ cm^{-1}. All the buffers were prepared and kept at the experimental temperature (25ºC).

2.3b. Sample Preparation

FAD, FMN and RF were brought from as mentioned earlier (**Table 2.2.1**) and were used without any further purification. For all the fluorescence studies, the concentrations of FAD,

FMN and RF were kept mostly at ~ 10^{-6} M to avoid the effect of molecular aggregation. Moreover to overcome the effect of hydrolysis of FAD instead all the experiments were performed in buffer at the very low and high pH, all the measurements were done within 15-20 minutes after addition of FAD in buffer and for every experiments freshly prepared samples were used instead using any stock solutions.

Ellipticine (**Table 2.2.1**) being sparingly soluble in water, we have used DMSO stock solution of ellipticine for all experiments. A 2 μL stock of ellipticine in DMSO was dissolved in 2.5 ml of PBS, and then the solution was strongly sonicated in a thermostat for ~1 hr (avoiding heating effect) to obtain a homogeneous ellipticine solution in water. This solution of ellipticine found to be stable enough for long duration even for few days, without any separation or precipitation of ellipticine from PBS. The working concentration of ellipticine was kept fixed at 10 μM for all the studies.

Coumarin 153 (C-153) was used without any further purification. C-153 is hydrophobic in nature; hence its solubility is very low in normal water. However, in presence of surfactant and nanotubes (C-153 is used for nanotube solvation project) its solubility is quite good. Even though, before taking measurements, all the solutions were filtered through Whatman 42 filter paper to eliminate any undissolved particle of C-153 from the solution. C-153 concentration was maintained at ~3 × 10^{-5} M. All of the solutions were prepared in Millipore water (18.2 μΩ cm^{-1}). Coumarin 343 (C-343) was used also without further purification (**Table 2.2.1**). Coumarin 343 (C-343) being hydrophilic in nature, solubilizes in urea loaded RM after mild sonication. Dye concentration was kept at 3 × 10^{-5} M for all the experiments of solvation dynamics of urea inside reverse micelle.

For urea induced unfolding of FAD, FAD concentration was kept fixed at 10 μM Urea concentration was varied form 0 M to 12 M respectively. All samples were prepared in Milipore water showing resistance of 18.2 μΩ cm^{-1}. Freshly prepared and properly equilibrated solutions were used for each set of data collection. Experimental temperature was kept at 298 K, unless otherwise specified.

Human and Bovine serum albumin (**Table 2.2.1)** were used as purchased. Serum proteins were quantified using its respective molar extinction coefficient at 280 nm, 43,824 $M^{-1}cm^{-1}$ for BSA and 36500 $M^{-1}cm^{-1}$ for HSA.[320] Freshly prepared and properly equilibrated solutions were used to collect the spectral data. Experimental temperature was kept at 298 K, unless otherwise specified.

Calf Thymus DNA Na Salt) and salmon sperm DNA (**Table 2.2.1)** were used as purchased. The concentration of DNA stock solution was determined by using molar extinction coefficient 6600 $M^{-1}.cm^{-1}$/base for DNA at 260 nm. From absorption ration value (<1.8) at 260 nm/280 nm we have confirmed that DNA samples are void of any protein contamination. The individual solutions with different concentration were prepared by adding respective amount from stock to a buffer of pH 7.2. The samples were annealed at 90ºC for 3 minutes and allowed to come back at room temperature normally to ensure the maximum extent for hybridization. After annelation the samples were kept at 4ºC overnight and used next day as required.

RNA aptamer (100 nano-moles synthesis scale, HPLC purified) brought from integrated DNA technology (IDT) as mentioned in the **Table 2.2.1**. The molar extinction coefficient 3,47,200 M^{-1} cm^{-1} (from IDT) at 260 nm was used for preparation of RNA solution. From absorption ration value (<1.8) at 260 nm/280 nm we have confirmed that RNA samples are void of any protein contamination. Before using RNA, it was annealed up to 90°C in phosphate buffer saline (PBS) with respective Mg^{+2} ion concentration and kept overnight at 4°C to have a stable tertiary structure of the RNA. All the spectroscopic and calorimetric data collections were done at 298 K, unless otherwise mentioned.

1% SDS (w/v) dispersed metallic and semiconducting single walled carbon nano-tubes were used as purchased (**Table 2.2.1**). The concentration of nanotubes in the solution was 0.01 mg/ml.

2.3c. Reverse Micelle Preparation

Dioctyl sulfosuccinate sodium salt (AOT) was dried under high vacuum for 24 hours to eliminate the adsorbed water before use. *n*-heptane was used as received. The AOT concentration was fixed at 0.38 M in all the RM. RMs having three different concentrations of urea (0.0458 M, 0.2128 M and 0.30 M) were prepared by adding precisely weighted solid urea to the AOT/*n*-heptane solution containing probe molecule (C-343). The urea solubilization in AOT/*n*-heptane solutions was expedited by the ultrasounds. Each solution was sonicated for 1 hour with an interval of 5 minutes and kept overnight at 25°C water bath. The maximum amount of urea that can be dissolved in these solutions (expressed as [urea]/[AOT] = 0.96 at 25°C) is equivalent to 0.3 M urea in AOT-RM.[18, 95] This amount was practically independent of the AOT concentration and nature of apolar solvents used.[18, 95] The w_0 value for water RM is defined by the molar ratio of water to surfactant, w_0 =

[water]/[AOT]. Water RM solutions of various w_0 were prepared by the addition of appropriate amount of water to the AOT/*n*-heptane system and each of the solution was equilibrated for several hours before use. Water RM having different urea concentrations were prepared by adding aqueous solution of different urea concentration at a fixed w_0 (w_0 = 10).

2.3d. Experimental Specifications

In case of absorption and steady state fluorescence measurements the concentration of fluorophores (flavins/coumarins/ellipticine) for all cases were kept fixed. The different analytes were added with increasing concentration either solid or from concentrated stock solution as required for a particular sample.

For CD macormolecular concentration (BSA/HSA (~10 μM) /RNA aptamer (~2 μM)) was kept fixed and titrated with increasing flavin concentrations (up to ~10 times of bio-macromolecular concentration). CD spectrum of an identical concentration of blank flavin (either for FAD, FMN or RF) were collected and subtracted from CD spectrum of flavin containing biomolecular spectra.

Energetics of the binding of flavins to BSA/HSA/RNA aptamer was estimated using isothermal titration calorimeter (Microcal, ITC 200, USA). A fixed concentration of BSA/HSA/RNA stock solution (20 μM) was kept in titration cell as a titer and was titrated by flavins (FAD and FMN individually) having a concentration of 120 μM. Each experiment consisted of 20 injections (each containing 2 μL titrant volume, except the first injection as its volume was 0.5 μL) with a successive time gap of 200 sec between two injections. For proper mixing the solutions, the stirring speed was maintained at 1000 rotations/minute (RPM). Cell temperature was kept fixed at 298 K and nearly 3 successive titrations were used to confirm the ITC curves and was fitted using 'single site binding' model. A blank titration of identical flavin concentration (~120 μM) with blank PBS (for BSA/HSA) containing respective Mg^{+2} ion (for RNA aptamer) concentration was subtracted from the sample data in order to correct the dilution enthalpy.

For time resolved lifetime traces and anisotropy measurements all the fluorophore (flavins/coumarins/ellipticine) concentrations were kept fixed and the analyte concentrations were changed maintaining identical concentrations as used in case of steady state experiments. Although the TCSPC results do not depend over the fluorophore concentration

but its customary to maintain identical concentrations like steady state experiments to avoid any kind of artifact.

Field emission scanning electron microscopy experiment was carried out toexplore the non specific protein-DNA interaction. This experiment was done in same Phosphate buffer (Na_2HPO_4 + NaH_2PO_4, 10 mM) saline (PBS) of pH 7.2 (containing 137 mM NaCl, 3 mM KCl and 0.1 mM EDTA) as used for fluorescence, CD and ITC. Respective concentration of protein and DNA had been maintained in PBS, drop-casted in a silicon wafer and dried in vacuum overnight. Then the drop-casted samples were kept in vacuum for 12 hours and afterward the SEM data were recorded.

2.3e. Simulation Method and Molecular Docking

We mainly used the theoretical calculations and molecular dynamics simulation for two chapters. This part being descriptive is separately described under the chapter title.

2.3e.1. Urea Induced Unfolding Dynamics of FAD (Chapter 4b)

FAD was optimized quantum mechanically using HF/6-31G* basis set in GAUSSIAN03 software.[321] Further, restricted electrostatic potential (resp) charges on the atoms of FAD were calculated using ANTECHAMBER module of AMBER11 software.[322, 323] The general amber force field (GAFF)[324] for flavin adenine dinucleotide (FAD) and urea were constructed using AmberTools software.[322] The topology and co-ordinates generated from AmberTools were converted into GROMACS format using a perl program amb2gmx.pl.[325] Following two systems were created for subsequent study: (i) FAD in water only and (ii) FAD in water-urea mixture. To create the FAD-water system, FAD was solvated with 2581 TIP3P water molecules[326] in a cubic box of dimension 42.8 Å. To create FAD-water-urea system, 372 urea molecules and 2581 TIP3P water molecules were added to FAD to make 8 M urea solution. Additionally, two sodium ions were added to neutralize the system.

Both the systems were taken through usual equilibration processes. All the simulations were performed using molecular dynamics software GROMACS.[327] each system was minimized using the steepest descent[328] method, followed by heating to 300 K in 100 ps by using Berendsen thermostat[329] with coupling constant of 0.2 ps. During the heating process, a harmonic restraint of 25 kcal/mol was applied to the heavy atoms of FAD. The harmonic restraint was gradually reduced to 0.25 kcal/mol in six steps. In each step, 100 ps

equilibration was carried out at constant temperature (300 K) and pressure (1 bar) using Berendsen thermostat and barostat[330] with coupling constants of 0.2 ps each. This was then followed by energy minimization using steepest descent method.[328] All bonds were constrained using LINCS algorithm.[327] Particle Mesh Ewald (PME) method[331] was used for the electrostatics with a 10 Å cut-off for the long range interaction. Cut-off for the van der Waals (vdW) interaction was kept at 10 Å. Simulations were performed by 1 fs time step. At the final equilibration step, we performed the 1 ns unrestrained equilibration by using the Berendsen thermostat and barostat[21] with coupling constant of 0.2 ps each.

After the equilibration steps, a final unrestrained simulation of 200 ns was performed at constant temperature 300 K and constant pressure 1 bar using the Nose-Hoover thermostat [332]and Parrinello-Rahman barostat[333], respectively, with 0.2 ps coupling constant for each. Results reported here were obtained from this final simulation.

2.3e.2. Comparative Study of Flavins Binding with HSA (Chapter 4c)

The computational study comprises molecular dynamics of the protein and the complex created by docking. The crystal structure of HSA (PDB ID 1AO6) was obtained from Protein Data Bank with a resolution of 2.5 Å.[334] Crystal structure of HSA contains A and B polypeptide chains. We selected chain A for the present study. While we used GROMACS[329] to perform the molecular dynamics simulation, we used modified AMBER99SB force-field[335] to generate the topology and parameter of HSA.

We have added the missing hydrogen atoms after removing B chain, and performed vacuum minimization of the protein with no constraints by using steepest descent method for 1000 steps[328] followed by conjugate gradient method[328] for 1000 steps. The optimized protein structure was then solvated with water in a cubic box using tip4pEW water model.[336] We have added 15 sodium ions to neutralize the system. After adding water and ions, the system was again energy minimized using conjugate gradient method and heated up to 300 K during 100 ps of simulation time using V-rescale[337] thermostat at constant pressure of 1 bar using Parrinello-Rahman[333] barostat. Temperature coupling constant was kept at 0.4 ps, while pressure coupling was kept at 0.6 ps. During the heating, heavy atoms of the protein were restrained by a harmonic force with a force constant 25 kcal/mol. After heating, equilibration was performed at constant temperature and pressure for 100 ps. Finally, molecular dynamic simulation was carried out for 10ns at constant temperature of 300 K using nose-hoover thermostat.[338] The ribbon diagram of optimized structure of HSA after 10 ns of simulation is

shown in **Scheme 2.3**, where six different sub domains are shown in different colours. **Scheme 2.3** also shows three binding sites: A is showing Sudlow's site-1 (SS1), B is showing the site close to LYS444 (SL) and C is showing Sudlow's site-2(SS2).

Following the usual method for creating the general amber force field (GAFF),[324] we have optimized the flavins using Hartree Fock theory with 6-31G* basis set using Gaussian03,[321] which is followed by calculation of Merz-Kollmann ESP charges.[339] Finally, restrained electrostatic potential (RESP) charges[323] for each atom were calculated using AMBER tools (Figure S8)[322]. The total charge of RF, FMN and FAD is 0, -1 and -2, respectively. Preliminary docking studies with predefined charges showed that FAD binds to HSA mainly in the 'unstack' or extended conformation. Hence, we have used an extended initial conformation of FAD for optimization and subsequent charge calculation using quantum chemistry calculation.

The final structure of HSA obtained at the end of 10 ns simulation was used as receptor and the three flavin molecules (RF, FMN and FAD) were docked into it using AutoDock[340] software. AMBER99SB charges of the protein and quantum chemically derived charges for the flavin were kept unchanged during docking. Initially, the whole protein was used to search for a binding site with a coarse grid spacing 0.16 Å. Genetic algorithm[341] was used as a search method. Out of the 10 different docked structures for each flavin, the best one in terms of binding free energy was selected for subsequent molecular dynamic simulation.

The best docked structures for each of the HSA-flavin complexes were subjected to similar initial preparation (vacuum minimization for 10000 steps, followed by solvation withtip4pEW water and neutralization by addition of Na^+ ion), energy minimization, and position restraint. Finally 4 ns simulation was performed at constant temperature 300 K and pressure 1 bar with integration time step 1 fs. Thermostat and barostat at each step were same as described above. During the simulation, FMN was unstable due to terminal phosphate group. Therefore, following the protocol of Case *et al.*,[342] we joined terminal hydrogen atom with the phosphate atom through a bond such that the terminal P-O-H is confined like rigid TIP3P water model.

2.3e.3. An Anticancer Drug to Probe Non-Specific Protein–DNA Interactions (Molecular Docking Study) (Chapter 5)

The crystal structure of protein was taken from RSCB protein Data Bank (PDB) having a PDB ID:3V03[343]. A dimeric BSA crystal structure was obtained with associated crystalline water molecules and calcium ions. One of the monomeric units of BSA, water molecules and calcium ions were removed from the crystal structure. The energy optimization of ellipticine conformers have been done using HF/6-31G level of Gaussian 09[321] and the resultant energy minimized geometry was saved in Autodock 4.2[340, 344] compatible format. We have used Lamarckian Generic Algorithm[340, 344] to find out the binding locations of ellipticine in BSA in Autodock 4.2 software. At the beginning of the study all water molecules was removed and Gasteiger charges were computed followed by addition of hydrogen as required by Lamarckian Generic Algorethm.[341, 344] At the initial stage as the approximate location of binding was not known, we fixed a 126 ×126 × 126 grid box dimensions along x, y, and z axes with grid spacing 0.56 Å to cover all the atoms of BSA, and a blind docking was performed to locate the possible position of the probe in BSA. Ellipticine was docked in BSA with 150 GA population size and 100 GA runs. The lowest possible energy structure has been searched out using rank by energy presentation. After respective three repetitions, the minimum energy structure was taken for further analysis. After selecting the possible locations of ellipticine, the size of grid box was decreased to 60 × 60 × 60 in respective directions with a grid spacing 0.375 Å to generate most stable docked form through finite docking studies. The respective structure has been used for visualization through python molecular viewer.[343, 347] The final structure for presentation has been generated using chimera.[345]

2.4. Reference

1. Levinger, N.E. & Swafford, L.A. Ultrafast dynamics in reverse micelles. *Annu. Rev. Phys. Chem.* **60**, 385-406 (2009).
2. Schulman, J.H., Stoeckenius, W. & Prince, L.M. Mechanism of formation and structure of micro emulsions by electron microscopy. *J. Phys. Chem.* **63**, 1677-1680 (1959).
3. Correa, N.M., Silber, J.J., Riter, R.E. & Levinger, N.E. Nonaqueous polar solvents in reverse micelle systems. *Chem. Rev.* **112**, 4569-4602 (2012).
4. Levinger, N.E. Water in confinement. *Science* **298**, 1722-1723 (2002).
5. Luisi, P.L., Giomini, M., Pileni, M.P. & Robinson, B.H. Reverse micelles as hosts for proteins and small molecules. *Biochim. Biophys. Acta, Rev. Biomembranes* **947**, 209-246 (1988).
6. Fayer, M.D. & Levinger, N.E. Analysis of water in confined geometries and at interfaces. *Annu. Rev. Anal. Chem.* **3**, 89-107 (2010).
7. De, T.K. & Maitra, A. Solution behaviour of aerosol OT in non-polar solvents. *Adv. Colloid Interface Sci.* **59**, 95-193 (1995).
8. Pileni, M.P. Reverse micelles as microreactors. *J. Phys. Chem.* **97**, 6961-6973 (1993).
9. Flynn, P.F., Simorellis, A.K. & Van Horn, W.D. in Annual Reports on NMR Spectroscopy (ed. Webb, G.A.) 179-219 (Academic Press, 2007).
10. Moulik, S.P. & Paul, B.K. Structure, dynamics and transport properties of microemulsions. *Adv. Colloid Interface Sci.* **78**, 99-195 (1998).
11. Zulauf, M. & Eicke, H.F. Inverted micelles and microemulsions in the ternary system water/aerosol-OT/isooctane as studied by photon correlation spectroscopy. *J. Phys. Chem.* **83**, 480-486 (1979).
12. Bohidar, H.B. & Behboudnia, M. Characterization of reverse micelles by dynamic light scattering. *Colloids Surf., A* **178**, 313-323 (2001).
13. Vasquez, V.R., Williams, B.C. & Graeve, O.A. Stability and comparative analysis of AOT/water/isooctane reverse micelle system using dynamic light scattering and molecular dynamics. *J. Phys. Chem. B* **115**, 2979-2987 (2011).
14. Riter, R.E., Kimmel, J.R., Undiks, E.P. & Levinger, N.E. Novel reverse micelles partitioning nonaqueous polar solvents in a hydrocarbon continuous phase. *J. Phys. Chem. B* **101**, 8292-8297 (1997).
15. Laia, C.A.T., López-Cornejo, P., Costa, S.M.B., d'Oliveira, J. & Martinho, J.M.G. Dynamic light scattering study of AOT microemulsions with nonaqueous polar additives in an oil continuous phase. *Langmuir* **14**, 3531-3537 (1998).
16. Chen, S.H. Small angle neutron scattering studies of the structure and interaction in micellar and microemulsion systems. *Annu. Rev. Phys. Chem.* **37**, 351-399 (1986).
17. Steytler, D.C., Jenta, T.R., Robinson, B.H., Eastoe, J. & Heenan, R.K. Structure of reversed micelles formed by metal salts of bis(ethylhexyl) phosphoric acid. *Langmuir* **12**, 1483-1489 (1996).

18. Caponetti, E., Chillura-Martino, D., Ferrante, F., Pedone, L., Ruggirello, A. & Turco Liveri, V. Structure of urea clusters confined in AOT reversed micelles. *Langmuir* **19**, 4913-4922 (2003).
19. Calandra, P., Giordano, C., Ruggirello, A. & Turco Liveri, V. Physicochemical investigation of acrylamide solubilization in sodium bis(2-ethylhexyl)sulfosuccinate and lecithin reversed micelles. *J. Colloid Interface Sci.* **277**, 206-214 (2004).
20. Shrestha, L.K., Shrestha, R.G. & Aramaki, K. Intrinsic parameters for the structure control of nonionic reverse micelles in styrene: SAXS and rheometry studies. *Langmuir* **27**, 5862-5873 (2011).
21. Simmons, B.A., Taylor, C.E., Landis, F.A., John, V.T., McPherson, G.L., Schwartz, D.K. & Moore, R. Microstructure determination of AOT + phenol organogels utilizing small-angle X-ray scattering and atomic force microscopy. *J. Am. Chem. Soc.* **123**, 2414-2421 (2001).
22. Kaler, E.W., Bennett, K.E., Davis, H.T. & Scriven, L.E. Toward understanding microemulsion microstructure: A small-angle x-ray scattering study. *J. Chem. Phys.* **79**, 5673-5684 (1983).
23. Elson, E.L. & Magde, D. Fluorescence correlation spectroscopy. I. Conceptual basis and theory. *Biopolymers* **13**, 1-27 (1974).
24. Magde, D., Elson, E.L. & Webb, W.W. Fluorescence correlation spectroscopy. II. An experimental realization. *Biopolymers* **13**, 29-61 (1974).
25. McPhee, J.T., Scott, E., Levinger, N.E. & Van Orden, A. Cy3 in AOT reverse micelles II. Probing intermicellar interactions using fluorescence correlation spectroscopy. *J. Phys. Chem. B* **115**, 9585-9592 (2011).
26. A. Hohner, J. Bayer & Rädler, J.O. Wormlike lipid/DNA micelles in a non-polar solvent. *Eur. Phys. J. E.* **21**, 41-48 (2006).
27. Kinugasa, T., Kondo, A., Nishimura, S., Miyauchi, Y., Nishii, Y., Watanabe, K. & Takeuchi, H. Estimation for size of reverse micelles formed by AOT and SDEHP based on viscosity measurement. *Colloids Surf., A* **204**, 193-199 (2002).
28. Mathew, C., Saidi, Z., Peyrelasse, J. & Boned, C. Viscosity, conductivity, and dielectric relaxation of waterless glycerol–sodium bis(2-ethylhexyl) sulfosuccinate–isooctane microemulsions: The percolation effect. *Phys. Rev. A* **43**, 873-882 (1991).
29. Ray, S. & Moulik, S.P. Dynamics and thermodynamics of aerosol OT-aided nonaqueous microemulsions. *Langmuir* **10**, 2511-2515 (1994).
30. Brown, D. & Clarke, J.H.R. Molecular dynamics simulation of a model reverse micelle. *J. Phys. Chem.* **92**, 2881-2888 (1988).
31. Linse, P. Molecular dynamics study of the aqueous core of a reversed ionic micelle. *J. Chem. Phys.* **90**, 4992-5004 (1989).
32. Salaniwal, S., Cui, S.T., Cummings, P.T. & Cochran, H.D. Self-assembly of reverse micelles in water/surfactant/carbon dioxide systems by molecular simulation. *Langmuir* **15**, 5188-5192 (1999).
33. Tobias, D.J. & Klein, M.L. Molecular dynamics simulations of a calcium carbonate/calcium sulfonate reverse micelle. *J. Phys. Chem.* **100**, 6637-6648 (1996).

34. Senapati, S. & Berkowitz, M.L. Water structure and dynamics in phosphate fluorosurfactant based reverse micelle: A computer simulation study. *J. Chem. Phys.* **118**, 1937-1944 (2003).
35. Senapati, S. & Berkowitz, M.L. Computer simulation studies of water states in perfluoro polyether reverse micelles: Effects of changing the counterion. *J. Phys. Chem. A* **108**, 9768-9776 (2004).
36. Allen, R., Bandyopadhyay, S. & Klein, M.L. C12E2 reverse micelle: A molecular dynamics study. *Langmuir* **16**, 10547-10552 (2000).
37. Abel, S., Waks, M., Marchi, M. & Urbach, W. Effect of surfactant conformation on the structures of small size nonionic reverse micelles: A molecular dynamics simulation study. *Langmuir* **22**, 9112-9120 (2006).
38. Rodriguez, J., Martí, J., Guàrdia, E. & Laria, D. Protons in non-ionic aqueous reverse micelles. *J. Phys. Chem. B* **111**, 4432-4439 (2007).
39. Rodriguez, J., Laria, D., Guardia, E. & Marti, J. Dynamics of water nanodroplets and aqueous protons in non-ionic reverse micelles. *Phys. Chem. Chem. Phys.* **11**, 1484-1490 (2009).
40. Chowdhary, J. & Ladanyi, B.M. Molecular dynamics simulation of aerosol-OT reverse micelles. *J. Phys. Chem. B* **113**, 15029-15039 (2009).
41. Abel, S., Sterpone, F., Bandyopadhyay, S. & Marchi, M. Molecular modeling and simulations of AOT−water reverse micelles in isooctane: structural and dynamic properties. *J. Phys. Chem. B* **108**, 19458-19466 (2004).
42. Dokter, A.M., Petersen, C., Woutersen, S. & Bakker, H.J. Vibrational dynamics of ice in reverse micelles. *J. Chem. Phys.* **128**, - (2008).
43. Jain, T.K., Varshney, M. & Maitra, A. Structural studies of Aerosol OT reverse micellar aggregates by FT-IR spectroscopy. *J. Phys. Chem.* **93**, 7409-7416 (1989).
44. Nandi, N., Bhattacharyya, K. & Bagchi, B. Dielectric relaxation and solvation dynamics of water in complex chemical and biological systems. *Chem. Rev.* **100**, 2013-2046 (2000).
45. Bhattacharyya, K. & Bagchi, B. Slow dynamics of constrained water in complex geometries. *J. Phys. Chem. A* **104**, 10603-10613 (2000).
46. Silber, J.J., Biasutti, A., Abuin, E. & Lissi, E. Interactions of small molecules with reverse micelles. *Adv. Colloid Interface Sci.* **82**, 189-252 (1999).
47. Setua, P., Ghatak, C., Rao, V.G., Das, S.K. & Sarkar, N. Dynamics of solvation and rotational relaxation of coumarin 480 in pure aqueous-AOT reverse micelle and reverse micelle containing different-sized silver nanoparticles inside its core: A comparative study. *J. Phys. Chem. B* **116**, 3704-3712 (2012).
48. Faeder, J. & Ladanyi, B.M. Solvation dynamics in reverse micelles: The role of headgroup−solute interactions. *J. Phys. Chem. B* **109**, 6732-6740 (2005).
49. Dutt, G.B. Does the onset of water droplet formation alter the microenvironment of the hydrophobic probes solubilized in nonionic reverse micelles? *J. Phys. Chem. B* **108**, 7944-7949 (2004).
50. Fenn, E.E., Wong, D.B., Giammanco, C.H. & Fayer, M.D. Dynamics of water at the interface in reverse micelles: Measurements of spectral diffusion with two-dimensional infrared vibrational echoes. *J. Phys. Chem. B* **115**, 11658-11670 (2011).

51. Moilanen, D.E., Fenn, E.E., Wong, D. & Fayer, M.D. Water dynamics at the interface in AOT reverse micelles. *J. Phys. Chem. B* **113**, 8560-8568 (2009).
52. Costard, R. & Elsaesser, T. Femtosecond OH bending dynamics of water nanopools confined in reverse micelles. *J. Phys. Chem. B* **117**, 15338-15345 (2013).
53. Fenn, E.E., Wong, D.B. & Fayer, M.D. Water dynamics in small reverse micelles in two solvents: Two-dimensional infrared vibrational echoes with two-dimensional background subtraction. *J. Chem. Phys.* **134**, - (2011).
54. Moilanen, D.E., Fenn, E.E., Wong, D. & Fayer, M.D. Water dynamics in large and small reverse micelles: From two ensembles to collective behavior. *J. Chem. Phys.* **131**, - (2009).
55. Moilanen, D.E., Fenn, E.E., Wong, D. & Fayer, M.D. Geometry and nanolength scales versus interface interactions: Water dynamics in AOT lamellar structures and reverse micelles. *J. Am. Chem. Soc.* **131**, 8318-8328 (2009).
56. Moilanen, D.E., Levinger, N.E., Spry, D.B. & Fayer, M.D. Confinement or the nature of the interface? Dynamics of nanoscopic water. *J. Am. Chem. Soc.* **129**, 14311-14318 (2007).
57. Park, S., Moilanen, D.E. & Fayer, M.D. Water dynamics the effects of ions and nanoconfinement. *J. Phys. Chem. B* **112**, 5279-5290 (2008).
58. Piletic, I.R., Moilanen, D.E., Levinger, N.E. & Fayer, M.D. What nonlinear−IR experiments can tell you about water that the IR spectrum cannot. *J. Am. Chem. Soc.* **128**, 10366-10367 (2006).
59. Piletic, I.R., Moilanen, D.E., Spry, D.B., Levinger, N.E. & Fayer, M.D. Testing the core/shell model of nanoconfined water in reverse micelles using linear and nonlinear IR spectroscopy. *J. Phys. Chem. A* **110**, 4985-4999 (2006).
60. Piletic, I.R., Tan, H.-S. & Fayer, M.D. Dynamics of nanoscopic water: Vibrational echo and infrared pump−probe studies of reverse micelles. *J. Phys. Chem. B* **109**, 21273-21284 (2005).
61. Spry, D.B., Goun, A., Glusac, K., Moilanen, D.E. & Fayer, M.D. Proton transport and the water environment in nafion fuel cell membranes and AOT reverse micelles. *J. Am. Chem. Soc.* **129**, 8122-8130 (2007).
62. Deàk, J.C., Pang, Y., Sechler, T.D., Wang, Z. & Dlott, D.D. Vibrational energy transfer across a reverse micelle surfactant layer. *Science* **306**, 473-476 (2004).
63. Dokter, A.M., Woutersen, S. & Bakker, H.J. Ultrafast dynamics of water in cationic micelles. *J. Chem. Phys.* **126**, - (2007).
64. Fletcher, P.D.I., Galal, M.F. & Robinson, B.H. Structural study of aerosol-OT-stabilised microemulsions of glycerol dispersed in n-heptane. *J. Chem. Soc. Faraday Trans. 1; Phys. Chem. Condensed Phases* **80**, 3307-3314 (1984).
65. Rico, I. & Lattes, A. Waterless microemulsions. 2. Use of formamide in place of water in the preparation of large monophasic areas of perfluorinated microemulsions. *J. Colloid Interface Sci.* **102**, 285-287 (1984).
66. Mehta, S.K., Kawaljit & Bala, K. Phase behavior, structural effects, and volumetric and transport properties in nonaqueous microemulsions. *Phys. Rev. E* **59**, 4317-4325 (1999).

67. Shirota, H. & Horie, K. Solvation dynamics in nonaqueous reverse micelles. *J. Phys. Chem. B* **103**, 1437-1443 (1999).
68. Hazra, P., Chakrabarty, D. & Sarkar, N. Solvation dynamics of Coumarin 152A in methanol and acetonitrile reverse micelles. *Chem. Phys. Lett.* **358**, 523-530 (2002).
69. Hazra, P., Chakrabarty, D. & Sarkar, N. Intramolecular charge transfer and solvation dynamics of coumarin 152 in aerosol-OT, water-solubilizing reverse micelles, and polar organic solvent solubilizing reverse micelles. *Langmuir* **18**, 7872-7879 (2002).
70. Hazra, P. & Sarkar, N. Solvation dynamics of Coumarin 490 in methanol and acetonitrile reverse micelles. *Phys. Chem. Chem. Phys.* **4**, 1040-1045 (2002).
71. Hazra, P., Chakrabarty, D. & Sarkar, N. Solvation dynamics of Coumarin 153 in aqueous and non-aqueous reverse micelles. *Chem. Phys. Lett.* **371**, 553-562 (2003).
72. Özçelik, S. & Zeynep Atay, N. Optical transition rates of a meso-substituted thiacarbocyanine in methanol-in-oil reverse micelles. *J. Lumin.* **113**, 1-8 (2005).
73. Fletcher, P.D.I., Galal, M.F. & Robinson, B.H. Structural study of microemulsions of glycerol stabilised by cetyltrimethylammonium bromide dispersed in heptane + chloroform mixtures. *J. Chem. Soc. Faraday Trans. 1; Phys. Chem. Condensed Phases* **81**, 2053-2065 (1985).
74. Falcone, R.D., Correa, N.M., Biasutti, M.A. & Silber, J.J. Properties of AOT aqueous and nonaqueous microemulsions sensed by optical molecular probes. *Langmuir* **16**, 3070-3076 (2000).
75. Silber, J.J., Falcone, R.D., Correa, N.M., Biasutti, M.A., Abuin, E., Lissi, E. & Campodonico, P. Exploratory Study of the Effect of Polar Solvents upon the Partitioning of Solutes in Nonaqueous Reverse Micellar Solutions. *Langmuir* **19**, 2067-2071 (2003).
76. Falcone, R.D., Correa, N.M., Biasutti, M.A. & Silber, J.J. The use of acridine orange base (AOB) as molecular probe to characterize nonaqueous AOT reverse micelles. *J. Colloid Interface Sci.* **296**, 356-364 (2006).
77. Durantini, A.M., Falcone, R.D., Silber, J.J. & Correa, N.M. Effect of the constrained environment on the interactions between the surfactant and different polar solvents encapsulated within AOT reverse micelles. *ChemPhysChem* **10**, 2034-2040 (2009).
78. Mehta, S.K. & Kawaljit. Phase diagram and physical properties of a waterless sodium bis(2-ethylhexylsulfosuccinate)- ethylbenzene-ethyleneglycol microemulsion: An insight into percolation. *Phys. Rev. E* **65**, 021502 (2002).
79. Novaira, M., Moyano, F., Biasutti, M.A., Silber, J.J. & Correa, N.M. An Example of How to Use AOT Reverse Micelle Interfaces to Control a Photoinduced Intramolecular Charge-Transfer Process. *Langmuir* **24**, 4637-4646 (2008).
80. Moore, S.A. & Palepu, R.M. Fluorometric investigations on the transition from reverse micelles to microemulsions in non-aqueous microemulsions. *J. Mol. Liq.* **135**, 123-127 (2007).
81. Pomata, M.H.H., Laria, D., Skaf, M.S. & Elola, M.D. Molecular dynamics simulations of AOT-water/formamide reverse micelles: Structural and dynamical properties. *J. Chem. Phys.* **129**, - (2008).

82. Correa, N.M., Pires, P.A.R., Silber, J.J. & El Seoud, O.A. Real structure of formamide entrapped by AOT nonaqueous reverse micelles: FT-IR and 1H NMR studies. *J. Phys. Chem. B* **109**, 21209-21219 (2005).
83. Arcoleo, V., Aliotta, F., Goffredi, M., La Manna, G. & Liveri, V.T. Study of AOT-stabilized microemulsions of formamide and n-methylformamide dispersed in n-heptane. *Mat. Sci. Eng. C* **5**, 47-53 (1997).
84. Elles, C.G. & Levinger, N.E. Reverse micelles solubilizing DMSO and DMSO/water mixtures. *Chem. Phys. Lett.* **317**, 624-630 (2000).
85. Pileni, M.P. Nanosized particles made in colloidal assemblies. *Langmuir* **13**, 3266-3276 (1997).
86. Xia, Y., Rogers, J.A., Paul, K.E. & Whitesides, G.M. Unconventional methods for fabricating and patterning nanostructures. *Chem. Rev.* **99**, 1823-1848 (1999).
87. Pileni, M.-P. The role of soft colloidal templates in controlling the size and shape of inorganic nanocrystal. *Nature Mat.* **2**, 145-150 (2003).
88. Singha, D., Barman, N. & Sahu, K. A facile synthesis of high optical quality silver nanoparticles by ascorbic acid reduction in reverse micelles at room temperature. *J. Colloid Interface Sci.* **413**, 37-42 (2014).
89. Setua, P., Chakraborty, A., Seth, D., Bhatta, M.U., Satyam, P.V. & Sarkar, N. Synthesis, optical properties, and surface enhanced Raman scattering of silver nanoparticles in nonaqueous methanol reverse micelles. *J. Phys. Chem. C* **111**, 3901-3907 (2007).
90. Carvalho, C.M.L. & Cabral, J.M.S. Reverse micelles as reaction media for lipases. *Biochimie* **82**, 1063-1085 (2000).
91. Holmberg, K. Organic reactions in microemulsions. *Curr. Opin. Colloid & Interface Sci.* **8**, 187-196 (2003).
92. Klyachko, N.L. & Levashov, A.V. Bioorganic synthesis in reverse micelles and related systems. *Curr. Opin. Colloid & Interface Sci.* **8**, 179-186 (2003).
93. Das, K., Maiti, S. & Das, P.K. Probing enzyme location in water-in-oil microemulsion using enzyme–carbon dot conjugates. *Langmuir* **30**, 2448-2459 (2014).
94. Valentine, K.G., Mathies, G., Bédard, S., Nucci, N.V., Dodevski, I., Stetz, M.A., Can, T.V., Griffin, R.G. & Wand, A.J. Reverse micelles as a platform for dynamic nuclear polarization in solution NMR of proteins. *J. Am. Chem. Soc.* **136**, 2800-2807 (2014).
95. Calvaruso, G., Minore, A. & Liveri, V.T. FT-IR investigation of the urea state in AOT reversed micelles. *J. Colloid Interface Sci.* **243**, 227-232 (2001).
96. Banerjee, C., Ghatak, C., Mandal, S., Ghosh, S., Kuchlyan, J. & Sarkar, N. Curcumin in reverse micelle: An example to control excited-state intramolecular proton transfer (ESIPT) in confined media. *J. Phys. Chem. B* **117**, 6906-6916 (2013).
97. Kuchlyan, J., Banik, D., Kundu, N., Ghosh, S., Banerjee, C. & Sarkar, N. Effect of confinement on excited-state proton transfer of firefly's chromophore d-luciferin in AOT reverse micelles. *J. Phys. Chem. B* **118**, 3401-3408 (2014).
98. Choudhury, S.D. & Pal, H. Modulation of excited-state proton-transfer reactions of 7-hydroxy-4-methylcoumarin in ionic and nonionic reverse micelles. *J. Phys. Chem. B* **113**, 6736-6744 (2009).

99. Cohen, B., Huppert, D., Solntsev, K.M., Tsfadia, Y., Nachliel, E. & Gutman, M. Excited state proton transfer in reverse micelles. *J. Am. Chem. Soc.* **124**, 7539-7547 (2002).
100. Mukherjee, T.K., Panda, D. & Datta, A. Excited-state proton transfer of 2-(2‘-Pyridyl)benzimidazole in microemulsions: Selective enhancement and slow dynamics in aerosol OT reverse micelles with an aqueous core. *J. Phys. Chem. B* **109**, 18895-18901 (2005).
101. Iijima, S. Helical microtubules of graphitic carbon. *Nature* **354**, 56-58 (1991).
102. Iijima, S. & Ichihashi, T. Single-shell carbon nanotubes of 1-nm diameter. *Nature* **363**, 603-605 (1993).
103. D. S. Bethune, C. H. Klang, M. S. de Vries, G. Gorman, R. Savoy, J. Vazquez & Beyers, R. Cobalt-catalysed growth of carbon nanotubes with single-atomic-layer wal. *Nature* **363**, 605-607 (1993).
104. Thess, A., Lee, R., Nikolaev, P., Dai, H., Petit, P., Robert, J., Xu, C., Lee, Y.H., Kim, S.G., Rinzler, A.G., Colbert, D.T., Scuseria, G.E., Tománek, D., Fischer, J.E. & Smalley, R.E. Crystalline ropes of metallic carbon nanotubes. *Science* **273**, 483-487 (1996).
105. Li, W.Z., Xie, S.S., Qian, L.X., Chang, B.H., Zou, B.S., Zhou, W.Y., Zhao, R.A. & Wang, G. Large-scale synthesis of aligned carbon nanotubes. *Science* **274**, 1701-1703 (1996).
106. Xie, S., Li, W., Pan, Z., Chang, B. & Sun, L. Carbon nanotube arrays. *Mat. Sci. Eng. A* **286**, 11-15 (2000).
107. Edgar, K. & Spencer, J.L. Aerosol-based synthesis of carbon nanotubes. *Curr. Appl Phys.* **4**, 121-124 (2004).
108. Qiu, J., Li, Y., Wang, Y. & Li, W. Production of carbon nanotubes from coal. *Fuel Process. Technol.* **85**, 1663-1670 (2004).
109. Shao, M., Wang, D., Yu, G., Hu, B., Yu, W. & Qian, Y. The synthesis of carbon nanotubes at low temperature via carbon suboxide disproportionation. *Carbon* **42**, 183-185 (2004).
110. Li, Y.-L., Kinloch, I.A., Shaffer, M.S.P., Geng, J., Johnson, B. & Windle, A.H. Synthesis of single-walled carbon nanotubes by a fluidized-bed method. *Chem. Phys. Lett.* **384**, 98-102 (2004).
111. Li, M.-w., Hu, Z., Wang, X.-z., Wu, Q., Chen, Y. & Tian, Y.-L. Low-temperature synthesis of carbon nanotubes using corona discharge plasma at atmospheric pressure. *Diamond Relat. Mater.* **13**, 111-115 (2004).
112. Rao, C.N.R., Govindaraj, A., Gundiah, G. & Vivekchand, S.R.C. Nanotubes and nanowires. *Chem. Eng. Sci.* **59**, 4665-4671 (2004).
113. Baughman, R.H., Zakhidov, A.A. & de Heer, W.A. Carbon nanotubes-the route toward applications. *Science* **297**, 787-792 (2002).
114. Wang, X., Li, Q., Xie, J., Jin, Z., Wang, J., Li, Y., Jiang, K. & Fan, S. Fabrication of ultralong and electrically uniform single-walled carbon nanotubes on clean substrates. *Nano Lett.* **9**, 3137-3141 (2009).
115. Belin, T. & Epron, F. Characterization methods of carbon nanotubes: a review. *Mat. Sci. Eng. B* **119**, 105-118 (2005).

116. Javey, A., Guo, J., Wang, Q., Lundstrom, M. & Dai, H. Ballistic carbon nanotube field-effect transistors. *Nature* **424**, 654-657 (2003).
117. A. K. Geim & Novoselov, K.S. The rise of graphene. *Nature Mat.* **6**, 183-191 (2007).
118. Berber, S., Kwon, Y.-K. & Tománek, D. Unusually high thermal conductivity of carbon nanotubes. *Phys. Rev. Lett.* **84**, 4613-4616 (2000).
119. Seol, J.H., Jo, I., Moore, A.L., Lindsay, L., Aitken, Z.H., Pettes, M.T., Li, X., Yao, Z., Huang, R., Broido, D., Mingo, N., Ruoff, R.S. & Shi, L. Two-dimensional phonon transport in supported graphene. *Science* **328**, 213-216 (2010).
120. Peigney, A., Laurent, C., Flahaut, E., Bacsa, R.R. & Rousset, A. Specific surface area of carbon nanotubes and bundles of carbon nanotubes. *Carbon* **39**, 507-514 (2001).
121. Rao, C.N.R., Sood, A.K., Subrahmanyam, K.S. & Govindaraj, A. Graphene: The new two-dimensional nanomaterial. *Angew. Chem. Int. Ed.* **48**, 7752-7777 (2009).
122. Yu, M.-F., Lourie, O., Dyer, M.J., Moloni, K., Kelly, T.F. & Ruoff, R.S. Strength and breaking mechanism of multiwalled carbon nanotubes under tensile load. *Science* **287**, 637-640 (2000).
123. Lee, C., Wei, X., Kysar, J.W. & Hone, J. Measurement of the elastic properties and intrinsic strength of monolayer graphene. *Science* **321**, 385-388 (2008).
124. Avouris, P. Graphene: electronic and photonic properties and devices. *Nano Lett.* **10**, 4285-4294 (2010).
125. Castro Neto, A.H., Guinea, F., Peres, N.M.R., Novoselov, K.S. & Geim, A.K. The electronic properties of graphene. *Rev. Modern Phys.* **81**, 109-162 (2009).
126. Gupta, S., Dharamvir, K. & Jindal, V.K. Elastic moduli of single-walled carbon nanotubes and their ropes. *Phys. Rev. B* **72**, 165428 (2005).
127. Qing Cao, Hoon-sik Kim, Ninad Pimparkar, Jaydeep P. Kulkarni, Congjun Wang, Moonsub Shim, Kaushik Roy, Muhammad A. Alam & Rogers, J.A. Medium-scale carbon nanotube thin-film integrated circuits on flexible plastic substrates. *Nature* **454**, 495-500 (2008).
128. Zhang, M., Fang, S., Zakhidov, A.A., Lee, S.B., Aliev, A.E., Williams, C.D., Atkinson, K.R. & Baughman, R.H. Strong, transparent, multifunctional, carbon nanotube sheets. *Science* **309**, 1215-1219 (2005).
129. Hwang, S.K., Lee, J.M., Kim, S., Park, J.S., Park, H.I., Ahn, C.W., Lee, K.J., Lee, T. & Kim, S.O. Flexible multilevel resistive memory with controlled charge trap B- and N-doped carbon nanotubes. *Nano Lett.* **12**, 2217-2221 (2012).
130. Chen, P., Fu, Y., Aminirad, R., Wang, C., Zhang, J., Wang, K., Galatsis, K. & Zhou, C. Fully printed separated carbon nanotube thin film transistor circuits and its application in organic light emitting diode control. *Nano Lett.* **11**, 5301-5308 (2011).
131. Minhun Jung, Jaeyoung Kim, Jinsoo Noh, Namsoo Lim, Chaemin Lim, Gwangyong Lee, Junseok Kim, Hwiwon Kang, Kyunghwan Jung, Leonard, A.D., our, J.M. & Cho, G. All-printed and roll-to-roll-printable 13.56-MHz-operated 1-bit RF tag on plastic foils. *IEEE Trans. Electron Devices* **57**, 571-580.
132. Seung Woo Lee, Naoaki Yabuuchi, Betar M. Gallant, Shuo Chen, Byeong-Su Kim, Paula T. Hammond & Shao-Horn, Y. High-power lithium batteries from functionalized carbon-nanotube electrodes. *Nat. Nanotechnol.* **5**, 531-537 (2010).

133. Lee, K.S., Lee, W.J., Park, N.-G., Kim, S.O. & Park, J.H. Transferred vertically aligned N-doped carbon nanotube arrays: use in dye-sensitized solar cells as counter electrodes. *Chem. Commun.* **47**, 4264-4266 (2011).
134. Lee, D.H., Lee, W.J., Lee, W.J., Kim, S.O. & Kim, Y.-H. Theory, synthesis, and oxygen reduction catalysis of Fe-porphyrin-like carbon nanotube. *Phys. Rev. Lett.* **106**, 175502 (2011).
135. Gong, K., Du, F., Xia, Z., Durstock, M. & Dai, L. Nitrogen-doped carbon nanotube arrays with high electrocatalytic activity for oxygen reduction. *Science* **323**, 760-764 (2009).
136. G.F. Zou, H.M. Luo, S. Baily, Y.Y. Zhang, N.F. Haberkorn, J. Xiong, E. Bauer, T.M. McCleskey, A.K. Burrell, L. Civale, Y.T. Zhu, J.L. MacManus-Driscoll & Jia, Q.X. Highly aligned carbon nanotube forests coated by superconducting NbC. *Nat. Commun.* **2** (2011).
137. Ajayan, P.M., Stephan, O., Colliex, C. & Trauth, D. Aligned carbon nanotube arrays formed by cutting a polymer resin-nanotube composite. *Science* **265**, 1212-1214 (1994).
138. Alan B. Dalton, Steve Collins, Edgar Muñoz, Joselito M. Razal, Von, H.E., John P. Ferraris, Jonathan N. Coleman, Bog G. Kim & Baughman, R.H. Super-tough carbon-nanotube fibres. *Nature* **423**, 703-703 (2003).
139. Lee, W.J., Lee, J.M., Kochuveedu, S.T., Han, T.H., Jeong, H.Y., Park, M., Yun, J.M., Kwon, J., No, K., Kim, D.H. & Kim, S.O. Biomineralized N-Doped CNT/TiO_2 Core/Shell Nanowires for Visible Light Photocatalysis. *ACS Nano* **6**, 935-943 (2011).
140. Beigbedera A., Degeea P., Sheelagh L. Conlanb, Robert J. Muttonb, Anthony S. Clareb, Michala E. Pettittc, Maureen E. Callowc, James A. Callowc & Duboisa, P. Preparation and characterisation of silicone-based coatings filled with carbon nanotubes and natural sepiolite and their application as marine fouling-release coatings. *Biofouling* **24**, 291-302 (2008).
141. Sun, D.-m., Timmermans, M.Y., Tian, Y., Nasibulin, A.G., Kauppinen, E.I., Kishimoto, S., Mizutani, T. & Ohno, Y. Flexible high-performance carbon nanotube integrated circuits. *Nat. Nano* **6**, 156-161 (2011).
142. McCarthy, M.A., Liu, B., Donoghue, E.P., Kravchenko, I., Kim, D.Y., So, F. & Rinzler, A.G. Low-voltage, low-power, organic light-emitting transistors for active matrix displays. *Science* **332**, 570-573 (2011).
143. Rueckes, T., Kim, K., Joselevich, E., Tseng, G.Y., Cheung, C.-L. & Lieber, C.M. Carbon nanotube-based nonvolatile random access memory for molecular computing. *Science* **289**, 94-97 (2000).
144. Dai, L., Chang, D.W., Baek, J.-B. & Lu, W. Carbon nanomaterials for advanced energy conversion and storage. *Small* **8**, 1130-1166 (2012).
145. Köhler, A.R., Som, C., Helland, A. & Gottschalk, F. Studying the potential release of carbon nanotubes throughout the application life cycle. *J. Cleaner Prod.* **16**, 927-937 (2008).
146. Evanoff, K., Khan, J., Balandin, A.A., Magasinski, A., Ready, W.J., Fuller, T.F. & Yushin, G. Towards ultrathick battery electrodes: Aligned carbon nanotube-enabled architecture. *Adv. Mater.* **24**, 533-537 (2012).

147. Gao, G. & Vecitis, C.D. Electrochemical carbon nnanotube filter oxidative performance as a function of surface chemistry. *Environ. Sci. Technol.* **45**, 9726-9734 (2011).
148. Rahaman, M.S., Vecitis, C.D. & Elimelech, M. Electrochemical carbon-nanotube filter performance toward virus removal and inactivation in the presence of natural organic matter. *Environ. Sci. Technol.* **46**, 1556-1564 (2011).
149. Corry, B. Designing carbon nanotube membranes for efficient water desalination. *J. Phys. Chem. B* **112**, 1427-1434 (2007).
150. Heller, D.A., Baik, S., Eurell, T.E. & Strano, M.S. Single-walled carbon nanotube spectroscopy in live cells: Towards long-term labels and optical sensors. *Adv. Mater.* **17**, 2793-2799 (2005).
151. De La Zerda, A., Zavaleta, C., Keren, S., Vaithilingam, S., Bodapati, S., Liu, Z., Levi, J., Smith, B.R., Ma, T.-J., Oralkan, O., Cheng, Z., Chen, X., Dai, H., Khuri-Yakub, B.T. & Gambhir, S.S. Carbon nanotubes as photoacoustic molecular imaging agents in living mice. *Nat. Nano* **3**, 557-562 (2008).
152. Kam, N.W.S., O'Connell, M., Wisdom, J.A. & Dai, H. Carbon nanotubes as multifunctional biological transporters and near-infrared agents for selective cancer cell destruction. *Proc. Natl. Acad. Sci. U.S.A.* **102**, 11600-11605 (2005).
153. Kurkina, T., Vlandas, A., Ahmad, A., Kern, K. & Balasubramanian, K. Label-free detection of few copies of DNA with carbon nanotube impedance biosensors. *Angew. Chem. Int. Ed.* **50**, 3710-3714 (2011).
154. Heller, D.A., Jin, H., Martinez, B.M., Patel, D., Miller, B.M., Yeung, T.-K., Jena, P.V., Hobartner, C., Ha, T., Silverman, S.K. & Strano, M.S. Multimodal optical sensing and analyte specificity using single-walled carbon nanotubes. *Nat. Nano* **4**, 114-120 (2009).
155. Star, A., Tu, E., Niemann, J., Gabriel, J.-C.P., Joiner, C.S. & Valcke, C. Label-free detection of DNA hybridization using carbon nanotube network field-effect transistors. *Proc. Natl. Acad. Sci. U.S.A.* **103**, 921-926 (2006).
156. Snow, E.S., Perkins, F.K., Houser, E.J., Badescu, S.C. & Reinecke, T.L. Chemical detection with a single-walled carbon nanotube capacitor. *Science* **307**, 1942-1945 (2005).
157. Esser, B., Schnorr, J.M. & Swager, T.M. Selective detection of ethylene gas using carbon nanotube-based devices: Utility in determination of fruit ripeness. *Angew. Chem. Int. Ed.* **51**, 5752-5756 (2012).
158. Shi, X., von dem Bussche, A., Hurt, R.H., Kane, A.B. & Gao, H. Cell entry of one-dimensional nanomaterials occurs by tip recognition and rotation. *Nat. Nano* **6**, 714-719 (2011).
159. Hong, S.Y., Tobias, G., Al-Jamal, K.T., Ballesteros, B., Ali-Boucetta, H., Lozano-Perez, S., Nellist, P.D., Sim, R.B., Finucane, C., Mather, S.J., Green, M.L.H., Kostarelos, K. & Davis, B.G. Filled and glycosylated carbon nanotubes for in vivo radioemitter localization and imaging. *Nat. Mater.* **9**, 485-490 (2010).
160. Liu, Z., Sun, X., Nakayama-Ratchford, N. & Dai, H. Supramolecular chemistry on water-soluble carbon nanotubes for drug loading and delivery. *ACS Nano* **1**, 50-56 (2007).

161. Bianco, A., Kostarelos, K. & Prato, M. Making carbon nanotubes biocompatible and biodegradable. *Chem. Commun.* **47**, 10182-10188 (2011).
162. Poland, C.A., Duffin, R., Kinloch, I., Maynard, A., Wallace, W.A.H., Seaton, A., Stone, V., Brown, S., MacNee, W. & Donaldson, K. Carbon nanotubes introduced into the abdominal cavity of mice show asbestos-like pathogenicity in a pilot study. *Nat. Nano* **3**, 423-428 (2008).
163. Mutlu, G.k.M., Budinger, G.R.S., Green, A.A., Urich, D., Soberanes, S., Chiarella, S.E., Alheid, G.F., McCrimmon, D.R., Szleifer, I. & Hersam, M.C. Biocompatible nanoscale dispersion of single-walled carbon nanotubes minimizes in vivo pulmonary toxicity. *Nano Lett.* **10**, 1664-1670 (2010).
164. Theodore Peters, J. All about albumin: Biochemistry, genetics, and medical applications (Academic Press: San Diego, CA, 1996).
165. Caironi, P., Tognoni, G., Masson, S., Fumagalli, R., Pesenti, A., Romero, M., Fanizza, C., Caspani, L., Faenza, S., Grasselli, G., Iapichino, G., Antonelli, M., Parrini, V., Fiore, G., Latini, R. & Gattinoni, L. Albumin replacement in patients with severe sepsis or septic shock. *N. Engl. J. Med.* **370**, 1412-1421 (2014).
166. Vinod P. Veedu, Anyuan Cao, Xuesong Li, Kougen Ma, Caterina Soldano, Swastik Kar, Pulickel M. Ajayan & Ghasemi-Nejhad, M.N. Multifunctional composites using reinforced laminae with carbon-nanotube forests. *Nature Mat.* **5**, 457-462 (2006).
167. Carter, D.C. & Ho, J.X. in Adv. Protein Chem. (eds. C.B. Anfinsen, J.T.E.F.M.R. & David, S.E.) 153-176, 176a, 176b, 176c, 176d, 176e, 176f, 176g, 176h, 176i, 176j, 176k, 176l, 177-203 (Academic Press, 1994).
168. He, X.M. & Carter, D.C. Atomic structure and chemistry of human serum albumin. *Nature* **358**, 209-215 (1992).
169. Wanwimolruk, S., Birkett, D.J. & Brooks, P.M. Structural requirements for drug binding to site II on human serum albumin. *Mol. Pharmacol.* **24**, 458-463 (1983).
170. Sudlow, G., Birkett, D.J. & N., W.D. The characterization of two specific drug binding sites on human serum albumin. *Mol. Pharmacol.* **11**, 824-832 (1975).
171. Sudlow, G., Birkett, D.J. & N., W.D. Further characterization of specific drug binding sites on human serum albumin *Mol. Pharmacol.* **12**, 1052-1061 (1976).
172. Wilding, G., Blumberg, E.S. & Vesell, E.S. Reduced warfarin binding of albumin variants. *Science* **195**, 991-994 (1977).
173. Eisenberg, D.S. & Edsall, J.T. Spectrophotometric titrations of human serum albumin and reduced carboxymethylated albumin. *Science* **142**, 50-51 (1963).
174. Ellenbogen, E. & Maurer, P.H. Heat denaturation of serum albumin in presence of perfluorooctanoic acid. *Science* **124**, 266-267 (1956).
175. Luck, J.M. Mandelate as a stabilizer of serum albumin. *J. Phys. Colloid Chem.* **51**, 229-239 (1947).
176. Jonas, A. & Weber, G. Partial modification of bovine serum albumin with dicarboxylic anhydrides. Physical properties of the modified species. *Biochemistry* **9**, 4729-4735 (1970).
177. Hunter, M.J. & McDuffie, F.C. Molecular weight studies on human serum albumin after reduction and alkylation of disulfide bonds. *J. Am. Chem. Soc.* **81**, 1400-1406 (1959).

178. Noort, D., Hulst, A.G., de Jong, L.P.A. & Benschop, H.P. Alkylation of human serum albumin by sulfur mustard in vitro and in vivo: Mass spectrometric analysis of a cysteine adduct as a sensitive biomarker of exposure. *Chem. Res. Toxicol.* **12**, 715-721 (1999).
179. Ghosh, S., Chakrabarty, S., Bhowmik, D., Kumar, G.S. & Chattopadhyay, N. Stepwise unfolding of bovine and human serum albumin by an anionic surfactant: An investigation using the proton transfer probe norharmane. *J. Phys. Chem. B*, Ahead of print (2014).
180. Haque, A., Aldred, P., Chen, J., Barrow, C.J. & Adhikari, B. Drying and denaturation characteristics of α-lactalbumin, β-lactoglobulin and bovine serum albumin in convective drying process. *J. Agric. Food Chem.*, Ahead of Print (2014).
181. Yadav, R., Sengupta, B. & Sen, P. Conformational fluctuation dynamics of domain I of human serum albumin in the course of chemically and thermally induced unfolding using fluorescence correlation spectroscopy. *J. Phys. Chem. B*, Ahead of Print (2014).
182. Ashrafi Kooshk, M.R., Khodarahmi, R., Karimi, S.A. & Nikbakht, M.R. Structural and functional impacts of albumin oxidation by hypochlorite: possible changes in drug binding characteristics upon myeloperoxidase-mediated oxidation in vivo. *J. Rep. Pharm. Sci.* **1**, 86-98 (2012).
183. Sekhar, A., Latham, M.P., Vallurupalli, P. & Kay, L.E. Viscosity-dependent kinetics of protein conformational exchange: microviscosity effects and the need for a small viscogen. *J. Phys. Chem. B* **118**, 4546-4551 (2014).
184. Norberto, D.R., Vieira, J.M., Rabelo de Souza, A., Bispo, J.A.C. & Bonafe, C.F.S. Pressure- and urea-induced denaturation of bovine serum albumin: considerations about protein heterogeneity. *Open J. Biophys.* **2**, 4-14 (2012).
185. Chen, M., Guo, H., Liu, Y. & Zhang, Q. Structural Changes of Human Serum Albumin Induced by Cadmium Acetate. *J. Biochem. Mol. Toxicol.*, Ahead of Print (2014).
186. Morris, T.T., Keir, J.L.A., Boshart, S.J., Lobanov, V.P., Ruhland, A.M.A., Bahl, N. & Gailer, J. Mobilization of Cd from human serum albumin by small molecular weight thiols. *J. Chromatogr. B: Anal. Technol. Biomed. Life Sci.* **958**, 16-21 (2014).
187. Yadav, I., Kumar, S., Aswal, V.K. & Kohlbrecher, J. Small-angle neutron scattering study of differences in phase behavior of silica nanoparticles in the presence of lysozyme and bovine serum albumin proteins. *Phys. Rev. E: Stat., Nonlinear, Soft Matter Phys.* **89**, 032304/1-032304/9 (2014).
188. Brown, D.M., Johnston, H., Gubbins, E. & Stone, V. Serum enhanced cytokine responses of macrophages to silica and iron oxide particles and nanomaterials: a comparison of serum to lung lining fluid and albumin dispersions. *J. Appl. Toxicol.*, Ahead of Print (2014).
189. Saha, S., Kamilya, T., Bhattacharya, R. & Bhunia, A.K. Unfolding of blood plasma albumin protein in interaction with CdS nanoparticles. *Sci. Adv. Mater.* **6**, 56-62 (2014).
190. Jali, B.R., Kuang, Y., Neamati, N. & Baruah, J.B. Selective binding of naphthoquinone derivatives to serum albumin proteins and their effects on cytotoxicity. *Chem.-Biol. Interact.* **214**, 10-17 (2014).

191. Mathew, M., Sreedhanya, S., Manoj, P., Aravindakumar, C.T. & Aravind, U.K. Exploring the interaction of bisphenol-S with serum albumins: A better or worse alternative for bisphenol A? *J. Phys. Chem. B* **118**, 3832-3843 (2014).
192. Ichkitidze, L., Podgaetsky, V., Prihodko, A., Selishchev, S., Blagov, E., Galperin, V., Shaman, Y. & Tabulina, L. Bulk composite nanomaterial with multiwall carbon nanotubes. *Mater. Sci. Appl.* **3**, 728-732 (2012).
193. Hartings, M.R., Benjamin, N., Briere, F., Briscione, M., Choudary, O., Fisher, T.L., Flynn, L., Ghias, E., Harper, M., Khamis, N., Koenigsknecht, C., Lazor, K., Moss, S., Robbins, E., Schultz, S., Yaman, S., Haverhals, L.M., Trulove, P.C., De Long, H.C., Miller, A.E. & Fox, D.M. Concurrent zero-dimensional and one-dimensional biomineralization of gold from a solution of Au^{3+} and bovine serum albumin. *Sci. Technol. Adv. Mater.* **14**, 065004/1-065004/8 (2013).
194. Cai, Z., Zhang, J.-T., Xue, F., Hong, Z., Punihaole, D. & Asher, S.A. 2D photonic crystal protein hydrogel coulometer for sensing serum albumin ligand binding. *Anal. Chem. (Washington, DC, U. S.)*, Ahead of Print (2014).
195. Wang, Y.-P., Li, X., Xue, J.-Y., Zhang, Y.-S. & Feng, X.-Z. Developmental and cartilaginous effects of protein-coated SiO_2 nanoparticle corona complexes on zebrafish larvae. *RSC Adv.* **4**, 18541-18548 (2014).
196. Mortimer, G.M., Butcher, N.J., Musumeci, A.W., Deng, Z.J., Martin, D.J. & Minchin, R.F. Cryptic epitopes of albumin determine mononuclear phagocyte system clearance of nanomaterials. *ACS Nano* **8**, 3357-3366 (2014).
197. Dong, Z., Le, X., Zhou, P., Dong, C. & Ma, J. Sequential recognition of zinc ion and hydrogen sulfide by a new quinoline derivative with logic gate behavior. *RSC Adv.* **4**, 18270-18277 (2014).
198. Yan, Y.-X., Yao, H.-B., Smart, S., Mao, L.-B., Hu, W., Yuan, S.-T., Du-Thumm, L., Masters, J.G., Yu, S.-H. & Pan, L. Ultrathin hybrid films of polyoxohydroxy clusters and proteins: Layer-by-layer assembly and their optical and mechanical properties. *Langmuir*, Ahead of Print (2014).
199. Beilis, E., Belgorodsky, B., Fadeev, L., Cohen, H. & Richter, S. Surface-induced conformational changes in doped bovine serum albumin self-assembled monolayers. *J. Am. Chem. Soc.* **136**, 6151-6154 (2014).
200. Manokruang, K., Lym, J.S. & Lee, D.S. Injectable hydrogels based on poly(amino urethane) conjugated bovine serum albumin. *Mater. Lett.* **124**, 105-109 (2014).
201. Wu, C., Bronder, T., Poghossian, A., Werner, C.F., Baecker, M. & Schoening, M.J. Label-free electrical detection of DNA with a multi-spot LAPS: First step towards light-addressable DNA chips. *Phys. Status Solidi A*, Ahead of Print (2014).
202. He, S.-B., Deng, H.-H., Liu, A.-L., Li, G.-W., Lin, X.-H., Chen, W. & Xia, X.-H. Synthesis and peroxidase-like activity of salt-resistant platinum nanoparticles by using bovine serum albumin as the scaffold. *ChemCatChem*, Ahead of Print (2014).
203. Guo, H., Chen, J. & Xu, Y. Protein-induced synthesis of chiral conducting polyaniline nanospheres. *ACS Macro Lett.* **3**, 295-297 (2014).
204. Martins, M., Azoia, N.G., Shimanovich, U., Matama, T., Gomes, A.C., Silva, C. & Cavaco-Paulo, A. Design of novel BSA/hyaluronic acid nanodispersions for transdermal pharma purposes. *Mol. Pharmaceutics* **11**, 1479-1488 (2014).

205. Ahmad, M.W., Kim, C.R., Baeck, J.S., Chang, Y., Kim, T.J., Bae, J.E., Chae, K.S. & Lee, G.H. Bovine serum albumin (BSA) and cleaved-BSA conjugated ultrasmall Gd2O3 nanoparticles: Synthesis, characterization, and application to MRI contrast agents. *Colloids Surf., A* **450**, 67-75 (2014).
206. Liu, Q., Zhu, H., Qin, J., Dong, H. & Du, J. Theranostic vesicles based on bovine serum albumin and poly(ethylene glycol)-block-poly(L-lactic-co-glycolic acid) for magnetic resonance imaging and anticancer drug delivery. *Biomacromolecules*, Ahead of Print (2014).
207. Boateng, J.S. & Ayensu, I. Preparation and characterization of laminated thiolated chitosan-based freeze-dried wafers for potential buccal delivery of macromolecules. *Drug Dev. Ind. Pharm.* **40**, 611-618 (2014).
208. Cobbina, E., Mehtab, S., Correia, I., Goncalves, G., Tomaz, I., Cavaco, I., Jakusch, T., Enyedi, E., Kiss, T. & Pessoa, J.C. Binding of oxovanadium(IV) complexes to blood serum albumins. *J. Mex. Chem. Soc.* **57**, 180-191 (2013).
209. Unnikrishnan, B., Wei, S.-C., Chiu, W.-J., Cang, J., Hsu, P.-H. & Huang, C.-C. Nitrite ion-induced fluorescence quenching of luminescent BSA-Au25 nanoclusters: mechanism and application. *Analyst (Cambridge, U. K.)* **139**, 2221-2228 (2014).
210. Soptei, B., Mihaly, J., Visy, J., Wacha, A. & Bota, A. Intercalation of bovine serum albumin coated gold clusters between phospholipid bilayers: Temperature-dependent behavior of lipid-AuQC-BSA assemblies with red emission and superlattice structure. *J. Phys. Chem. B* **118**, 3887-3892 (2014).
211. Guan, Y., Zhang, H. & Wang, Y. New insight into the binding interaction of hydroxylated carbon nanotubes with bovine serum albumin. *Spectrochim. Acta, Part A* **124**, 556-563 (2014).
212. Yue, Y., Liu, R., Liu, J., Dong, Q. & Fan, J. Experimental and theoretical investigation on the interaction between cyclovirobuxine D and human serum albumin. *Spectrochim. Acta, Part A* **128**, 552-558 (2014).
213. Han, M., Yu, X., Guo, Y., Wang, Y., Kuang, H. & Wang, X. Honokiol nanosuspensions: Preparation, increased oral bioavailability and dramatically enhanced biodistribution in the cardio-cerebro-vascular system. *Colloids Surf., B* **116**, 114-120 (2014).
214. Yang, H., Liu, Q., Zhao, L., Yuan, Y., Fan, D., Deng, J. & Zhang, R. Fluorescence spectroscopic studies on the interaction of oleanolic acid and its triterpenoid saponins derivatives with two serum albumins. *J. Solution Chem.* **43**, 774-786 (2014).
215. Orlov, S., Goncharova, I. & Urbanova, M. Circular dichroism study of the interaction between mutagens and bilirubin bound to different binding sites of serum albumins. *Spectrochim. Acta, Part A* **126**, 68-75 (2014).
216. Dong, S., Li, Z., Shi, L., Huang, G., Chen, S. & Huang, T. The interaction of plant-growth regulators with serum albumin: Molecular modeling and spectroscopic methods. *Food Chem. Toxicol.* **67**, 123-130 (2014).
217. Ji, Z., Liang, X., Sun, Y. & Fan, J. Study of interaction between sodium fluorescein and human serum albumin by multi-spectroscopic method. *Asian J. Chem.* **26**, 521-526 (2014).

218. Ganguly, A., Paul, B.K., Ghosh, S., Dalapati, S. & Guchhait, N. Interaction of a potential chloride channel blocker with a model transport protein: a spectroscopic and molecular docking investigation. *Phys. Chem. Chem. Phys.* **16**, 8465-8475 (2014).
219. Tang, L., Zhang, D., Xu, S., Zuo, H., Zuo, C. & Li, Y. Different spectroscopic and molecular modeling studies on the interaction between cyanidin-3-O-glucoside and bovine serum albumin. *Luminescence* **29**, 168-175 (2014).
220. Yue, Y., Liu, J., Liu, R., Dong, Q. & Fan, J. Binding of helicid to human serum albumin: A hybrid spectroscopic approach and conformational study. *Spectrochim. Acta, Part A* **124**, 46-51 (2014).
221. Pantusa, M., Bartucci, R. & Rizzuti, B. Stability of trans-resveratrol associated with transport proteins. *J. Agric. Food Chem.*, Ahead of Print (2014).
222. Rehman, M.T., Shamsi, H. & Khan, A.U. An insight into the binding mechanism of imipenem to human serum albumin by spectroscopic and computational approaches. *Mol. Pharmaceutics*, Ahead of Print (2014).
223. Galpothdeniya, W.I.S., Das, S., De Rooy, S.L., Regmi, B.P., Hamdan, S. & Warner, I.M. Fluorescein-based ionic liquid sensor for label-free detection of serum albumins. *RSC Adv.* **4**, 17533-17540 (2014).
224. Liu, X. & Li, H. Spectroscopic studies on the interaction of polydatin with bovine serum albumin. *Asian J. Chem.* **26**, 1052 (2014).
225. Zhang, G., Hu, Y. & Pan, J. Interaction between toddalolatone and human serum albumin. *J. Solution Chem.* **43**, 727-745 (2014).
226. Islam, M.M., Moyon, N.S., Gashnga, P.M. & Mitra, S. Interaction of sulfadiazine with model water soluble proteins: A combined fluorescence spectroscopic and molecular modeling approach. *J. Fluoresc.* **24**, 579-588 (2014).
227. Liu, Y., Chen, M., Wang, S., Lin, J., Cai, L. & Song, L. New insight into the stereoselective interactions of quinine and quinidine, with bovine serum albumin. *J. Mol. Recognit.* **27**, 239-249 (2014).
228. Zhang, W., Zhang, K., Zheng, J., Chen, H., Chen, W. & Jing, X. Interaction mechanism between bovine serum albumin and polyethylene glycol revealed with elastic light scattering spectroscopy. *Adv. Mater. Res. (Durnten-Zurich, Switz.)* **704**, 43-50 (2013).
229. Lou, H., Li, X., Guo, X., Yang, T. & Li, S. Investigation of the interaction of the synthesized chitosan-5-fluorouracil with bovine serum albumin using spectroscopy. *J. Chem. Pharm. Res.* **5**, 1496-1499 (2013).
230. Jiang, B., Hu, Y., Zhao, A., Luo, X., Pan, W. & Lin, C. Characterization of taurine and its derivative binding to HSA using calorimetry and docking. *J. Chem. Pharm. Res.* **5**, 1529-1536 (2013).
231. Li, M., McAuley, E., Zhang, Y., Kong, L.L., Yang, F., Zhou, Z.P., Wu, X.Y. & Liang, H. Comparison of binding characterization of two antiviral drugs to human serum albumin. *Chem. Biol. Drug Des.* **83**, 576-582 (2014).
232. Naso, L.G., Valcarcel, M., Roura-Ferrer, M., Kortazar, D., Salado, C., Lezama, L., Rojo, T., Gonzalez-Baro, A.C., Williams, P.A.M. & Ferrer, E.G. Promising antioxidant and anticancer (human breast cancer) oxidovanadium(IV) complex of chlorogenic acid. Synthesis, characterization and spectroscopic examination on the

transport mechanism with bovine serum albumin. *J. Inorg. Biochem.* **135**, 86-99 (2014).

233. Seedher, N. & Kanojia, M. Fluorescence spectroscopic study for competitive binding of antidiabetic drugs and endogenous substances on serum albumin. *Drug Metab. Drug Interact.* **28**, 107-114 (2013).
234. Rahnama, E., Mahmoodian-Moghaddam, M., Khorsand-Ahmadi, S., Saberi, M.R. & Chamani, J. Binding site identification of metformin to human serum albumin and glycated human serum albumin by spectroscopic and molecular modeling techniques: a comparison study. *J. Biomol. Struct. Dyn.*, Ahead of Print (2014).
235. Li, M. & Hagerman, A.E. Role of the Flavan-3-ol and Galloyl Moieties in the Interaction of (-)-Epigallocatechin Gallate with Serum Albumin. *J. Agric. Food Chem.* **62**, 3768-3775 (2014).
236. Delgado-Magnero, K.H., Valiente, P.A., Ruiz-Pena, M., Perez-Gramatges, A. & Pons, T. Unraveling the binding mechanism of polyoxyethylene sorbitan esters with bovine serum albumin: A novel theoretical model based on molecular dynamic simulations. *Colloids Surf., B* **116**, 720-726 (2014).
237. Sisavath, N., Le Saux, T., Leclercq, L. & Cottet, H. Effect of Dendrimer Generation on the Interactions between Human Serum Albumin and Dendrigraft Polylysines. *Langmuir* **30**, 4450-4457 (2014).
238. Garg, S. & Raghav, N. Synthesis of novel chalcones of Schiff's bases and to study their effect on bovine serum albumin. *Asian J. Pharm. Clin. Res.* **6**, 181-184 (2013).
239. Selvakumaran, N., Bhuvanesh, N.S.P., Endo, A. & Karvembu, R. Synthesis, structure, DNA and protein binding studies, and cytotoxic activity of nickel(II) complexes containing 3,3-dialkyl/aryl-1-(2,4-dichlorobenzoyl)thiourea ligands. *Polyhedron* **75**, 95-109 (2014).
240. Rathi, P.P., More, V.S., Deshmukh, V.K. & Chaudhari, S.R. Invitro anti-inflammatory activity of newly synthesized mannich base 2-[(1,3-benzothiazol-2-ylamino)methyl]-5-methyl-2,4-dihydro-3H-pyrazol-3-one and its derivatives. *Curr. Pharma Res.* **3**, 983-988 (2013).
241. Lokhande, R.P., Deshmukh, V.K. & Chaudhari, S.R. Synthesis and biological activities of 5-(1,3-benzthiazol-2-ylamino)-4-phenyl-2,4-dihydro-3h-1,2,4-triazole-3-thione and its derivatives. *Int. J. Pharm. Sci. Rev. Res.* **22**, 60-65 (2013).
242. Grewar, T. & Gericke, M. Technical note: synthesis and characterization of anisotropic gold nanoparticles. *Adv. Nanopart.* **1**, 15-20 (2012).
243. Alagesan, M., Bhuvanesh, N.S.P. & Dharmaraj, N. An investigation on new ruthenium(II) hydrazone complexes as anticancer agents and their interaction with biomolecules. *Dalton Trans.* **43**, 6087-6099 (2014).
244. Liang, S., Liu, Y., Xiang, J., Qin, M., Yu, H. & Yan, G. Fabrication of a new fluorescent polymeric nanoparticle containing naphthalimide and investigation on its interaction with bovine serum albumin. *Colloids Surf., B* **116**, 206-210 (2014).
245. Thioune, N., Lidgi-Guigui, N., Cottat, M., Gabudean, A.-M., Focsan, M., Benoist, H.-M., Astilean, S. & de la Chapelle, M.L. Study of gold nanorods-protein interaction by localized surface plasmon resonance spectroscopy. *Gold Bull. (Berlin, Ger.)* **46**, 275-281 (2013).

246. Chatterjee, S. & Mukherjee, T.K. Spectroscopic investigation of interaction between bovine serum albumin and amine-functionalized silicon quantum dots. *Phys. Chem. Chem. Phys.* **16**, 8400-8408 (2014).
247. Ashrafi Kooshk, M.R., Mansouri, K., MostafaNadi, M., Khodarahmi, S. & Khodarahmi, R. In vitro anti-cancer activity of native curcumin and "protein-curcumin" systems: a perspective on drug-delivery application. *J. Rep. Pharm. Sci.* **2**, 66-74 (2013).
248. Bujacz, A., Zielinski, K. & Sekula, B. Structural studies of bovine, equine, and leporine serum albumin complexes with naproxen. *Proteins: Struct., Funct., Bioinf.*, Ahead of Print (2014).
249. Wang, J., Xiang, C., Tian, F.-F., Xu, Z.-Q., Jiang, F.-L. & Liu, Y. Investigating the interactions of a novel anticancer delocalized lipophilic cation and its precursor compound with human serum albumin. *RSC Adv.* **4**, 18205-18216 (2014).
250. Szeto, K., Latulippe, D.R., Ozer, A., Pagano, J.M., White, B.S., Shalloway, D., Lis, J.T. & Craighead, H.G. RAPID-SELEX for RNA aptamers. *PLoS One* **8**, e82667/1-e82667/11 (2013).
251. Tuerk, C. & Gold, L. Systematic evolution of ligands by exponential enrichment: RNA ligands to bacteriophage T4 DNA polymerase. *Science* **249**, 505-510 (1990).
252. Andrew D. Ellington & Szostak, J.W. In vitro selection of RNA molecules that bind specific ligands. *Nature* **346**, 818-822 (1990).
253. Süß, B. RNA-ligand interaction. *http://www.bio.tu-darmstadt.de/ag/fachgebiete/synthetic_genetic_circuits/intro_suess.en.jsp*.
254. C.M. Dollins, S. Nair & B.A. Sullenger. Aptamers in immunotherapy. *Hum. Gene. Ther.* **19**, 443-450 (2008).
255. Potty, A.S.R., Kourentzi, K., Fang, H., Jackson, G.W., Zhang, X., Legge, G.B. & Willson, R.C. Biophysical characterization of DNA aptamer interactions with vascular endothelial growth factor. *Biopolymers* **91**, 145-156 (2009).
256. Long, S.B., Long, M.B., White, R.R. & Sullenger, B.A. Crystal structure of an RNA aptamer bound to thrombin. *RNA* **14**, 2504-2512 (2008).
257. Darfeuille, F., Reigadas, S., Hansen, J.B., Orum, H., Di Primo, C. & Toulmé, J.-J. Aptamers targeted to an RNA hairpin show improved specificity compared to that of complementary oligonucleotides. *Biochemistry* **45**, 12076-12082 (2006).
258. M. Liu, T. Kagahara, H. Abe & Ito, Y. Direct in vitro selection of hemin-binding DNA aptamer with peroxidase activity. *Bull. Chem. Soc. Jpn.* **82**, 99-104 (2009).
259. Min, K., Cho, M., Han, S.-Y., Shim, Y.-B., Ku, J. & Ban, C. A simple and direct electrochemical detection of interferon-γ using its RNA and DNA aptamers. *Biosens. Bioelectron.* **23**, 1819-1824 (2008).
260. Ng, E.W.M., Shima, D.T., Calias, P., Cunningham, E.T., Guyer, D.R. & Adamis, A.P. Pegaptanib, a targeted anti-VEGF aptamer for ocular vascular disease. *Nat. Rev. Drug Discov.* **5**, 123-132 (2006).
261. Jeong, S., S.R. Han, Y.J. Lee & Lee, S.W. Selection of RNA aptamers specific to active prostate-specific antigen. *Biotechnol. Lett* **32**, 379-385 (2010).
262. Walsh, R. & DeRosa, M.C. Retention of function in the DNA homolog of the RNA dopamine aptamer. *Biochem. Biophys. Res. Commun.* **388**, 732-735 (2009).

263. Padlan, C.S., Malashkevich, V.N., Almo, S.C., Levy, M., Brenowitz, M. & Girvin, M.E. An RNA aptamer possessing a novel monovalent cation-mediated fold inhibits lysozyme catalysis by inhibiting the binding of long natural substrates. *RNA* **20**, 447-461 (2014).
264. Stojanovic, M.N., de Prada, P. & Landry, D.W. Aptamer-based folding fluorescent sensor for cocaine. *J. Am. Chem. Soc.* **123**, 4928-4931 (2001).
265. Schifferer, M. & Griesbeck, O. A dynamic FRET reporter of gene expression improved by functional screening. *J. Am. Chem. Soc.* **134**, 15185-15188 (2012).
266. Wood, S., Ferre-D'Amare, A.R. & Rueda, D. Allosteric tertiary interactions preorganize the c-di-GMP riboswitch and accelerate ligand binding. *ACS Chem. Biol.* **7**, 920-927 (2012).
267. Shwetha, N., Selvakumar, L.S. & Thakur, M.S. Aptamer-nanoparticle-based chemiluminescence for p53 protein. *Anal. Biochem.* **441**, 73-79 (2013).
268. Wu, Z., Tang, L.-J., Zhang, X.-B., Jiang, J.-H. & Tan, W. Aptamer-modified nanodrug delivery systems. *ACS Nano* **5**, 7696-7699 (2011).
269. Nam, H.Y., Cho, Y.S., Jung, W., Kang, H.-J. & Hah, S.S. RNA aptamer-functionalized quantum dots for detection of his-tagged proteins in Escherichia coli. *Bull. Korean Chem. Soc.* **34**, 997-999 (2013).
270. Olek, M., Büsgen, T., Hilgendorff, M. & Giersig, M. Quantum dot modified multiwall carbon nanotubes. *J. Phys. Chem. B* **110**, 12901-12904 (2006).
271. Y. Huang, S. Zhao, H. Liang, Z.F. Chen & Y.M. Liu. Multiplex detection of endonucleases by using a multicolor gold nanobeacon. *Chemistry* **17**, 7313-7319 (2011).
272. Qureshi, A., Roci, I., Gurbuz, Y. & Niazi, J.H. An aptamer based competition assay for protein detection using CNT activated gold-interdigitated capacitor arrays. *Biosens. Bioelectron.* **34**, 165-170 (2012).
273. Habenicht, B.F. & Prezhdo, O.V. Nonradiative quenching of fluorescence in a semiconducting carbon nanotube: A time-domain ab initio study. *Phys. Rev. Lett.* **100**, 197402 (2008).
274. Liu, M., Zhao, H., Chen, S., Yu, H., Zhang, Y. & Quan, X. A “turn-on” fluorescent copper biosensor based on DNA cleavage-dependent graphene-quenched DNAzyme. *Biosens. Bioelectron.* **26**, 4111-4116 (2011).
275. Chang, H., Tang, L., Wang, Y., Jiang, J. & Li, J. Graphene fluorescence resonance energy transfer aptasensor for the thrombin detection. *Anal. Chem.* **82**, 2341-2346 (2010).
276. Pothoulakis, G., Ceroni, F., Reeve, B. & Ellis, T. The spinach RNA aptamer as a characterization tool for synthetic biology. *ACS Synth. Biol.* **3**, 182-187 (2014).
277. Han, K.Y., Leslie, B.J., Fei, J., Zhang, J. & Ha, T. Understanding the photophysics of the spinach-DFHBI RNA aptamer-fluorogen complex to improve live-cell RNA imaging. *J. Am. Chem. Soc.* **135**, 19033-19038 (2013).
278. Da Rocha Gomes, S., Miguel, J., Azema, L., Eimer, S., Ries, C., Dausse, E., Loiseau, H., Allard, M. & Toulme, J.-J. 99mTc-MAG3-aptamer for imaging human tumors associated with high level of matrix metalloprotease-9. *Bioconjugate Chem.* **23**, 2192-2200 (2012).

279. Da Costa, J.B., Andreiev, A.I. & Dieckmann, T. Thermodynamics and kinetics of adaptive binding in the malachite green RNA aptamer. *Biochemistry* **52**, 6575-6583 (2013).
280. Reif, R., Haque, F. & Guo, P. Fluorogenic RNA nanoparticles for monitoring RNA folding and degradation in real time in living cells. *Nucleic Acid Ther.* **22**, 428-437 (2012).
281. Luzi, E., Minunni, M., Tombelli, S. & Mascini, M. New trends in affinity sensing: aptamers for ligand binding. *TrAC, Trends Anal. Chem.* **22**, 810-818 (2003).
282. Tombelli, S., Minunni, M., Luzi, E. & Mascini, M. Aptamer-based biosensors for the detection of HIV-1 Tat protein. *Bioelectrochemistry* **67**, 135-141 (2005).
283. Bini, A., Minunni, M., Tombelli, S., Centi, S. & Mascini, M. Analytical performances of aptamer-based sensing for thrombin detection. *Anal. Chem.* **79**, 3016-3019 (2007).
284. Savran, C.A., Knudsen, S.M., Ellington, A.D. & Manalis, S.R. Micromechanical detection of proteins using aptamer-based receptor molecules. *Anal. Chem.* **76**, 3194-3198 (2004).
285. Hianik, T., Ostatná, V., Zajacová, Z., Stoikova, E. & Evtugyn, G. Detection of aptamer–protein interactions using QCM and electrochemical indicator methods. *Bioorg. Med. Chem. Lett.* **15**, 291-295 (2005).
286. Hwang, K.S., Lee, S.-M., Eom, K., Lee, J.H., Lee, Y.-S., Park, J.H., Yoon, D.S. & Kim, T.S. Nanomechanical microcantilever operated in vibration modes with use of RNA aptamer as receptor molecules for label-free detection of HCV helicase. *Biosens. Bioelectron.* **23**, 459-465 (2007).
287. Singh, V., Peng, C.S., Li, D., Mitra, K., Silvestre, K.J., Tokmakoff, A. & Essigmann, J.M. Direct observation of multiple tautomers of oxythiamine and their recognition by the thiamine pyrophosphate riboswitch. *ACS Chem. Biol.* **9**, 227-236 (2014).
288. Cella, L.N., Sanchez, P., Zhong, W., Myung, N.V., Chen, W. & Mulchandani, A. Nano aptasensor for protective antigen toxin of anthrax. *Anal. Chem.* **82**, 2042-2047 (2010).
289. Wang, L., Zhu, C., Han, L., Jin, L., Zhou, M. & Dong, S. Label-free, regenerative and sensitive surface plasmon resonance and electrochemical aptasensors based on graphene. *Chem. Commun.* **47**, 7794-7796 (2011).
290. Song, S., Wang, L., Li, J., Fan, C. & Zhao, J. Aptamer-based biosensors. *TrAC, Trends Anal. Chem.* **27**, 108-117 (2008).
291. Ilgu, M., Fulton, D.B., Yennamalli, R.M., Lamm, M.H., Sen, T.Z. & Nilsen-Hamilton, M. An adaptable pentaloop defines a robust neomycin-B RNA aptamer with conditional ligand-bound structures. *RNA* (2014).
292. Vorobjeva, M.A., Krasitskaya, V.V., Fokina, A.A., Timoshenko, V.V., Nevinsky, G.A., Venyaminova, A.G. & Frank, L.A. RNA aptamer against autoantibodies associated with multiple sclerosis and bioluminescent detection probe on its basis. *Anal. Chem. (Washington, DC, U. S.)* **86**, 2590-2594 (2014).
293. Schoukroun-Barnes, L.R., Wagan, S. & White, R.J. Correction to enhancing the analytical performance of electrochemical RNA aptamer-based sensors for sensitive detection of aminoglycoside antibiotics. *Anal. Chem.* (2014).

294. Schoukroun-Barnes, L.R., Wagan, S. & White, R.J. Enhancing the analytical performance of electrochemical RNA aptamer-based sensors for sensitive detection of aminoglycoside antibiotics. *Anal. Chem. (Washington, DC, U. S.)* **86**, 1131-1137 (2014).
295. Paniel, N., Baudart, J., Hayat, A. & Barthelmebs, L. Aptasensor and genosensor methods for detection of microbes in real world samples. *Methods (Amsterdam, Neth.)* **64**, 229-240 (2013).
296. Schoukroun-Barnes, L.R., Wagan, S., Liu, J., Leach, J.B. & White, R.J. Biocompatible hydrogel membranes for the protection of RNA aptamer-based electrochemical sensors. *Proc. SPIE* **8719**, 87190I/1-87190I/8 (2013).
297. Wang, Y., Li, Z., Weber, T.J., Hu, D., Lin, C.-T., Li, J. & Lin, Y. In situ live cell sensing of multiple nucleotides exploiting DNA/RNA aptamers and graphene oxide nanosheets. *Anal. Chem. (Washington, DC, U. S.)* **85**, 6775-6782 (2013).
298. Liang, M., Liu, R., Su, R., Qi, W., Wang, L. & He, Z. Aptamer-based sensing technology towards food safety analysis. *Huaxue Jinzhan* **24**, 1378-1387 (2012).
299. Janardhanan, P., Mello, C.M., Singh, B.R., Lou, J., Marks, J.D. & Cai, S. RNA aptasensor for rapid detection of natively folded type A botulinum neurotoxin. *Talanta* **117**, 273-80 (2013).
300. Bunka, D.H.J. & Stockley, P.G. Aptamers come of age-at last. *Nat. Rev. Micro.* **4**, 588-596 (2006).
301. Lee, J.-H., Jucker, F. & Pardi, A. Imino proton exchange rates imply an induced-fit binding mechanism for the VEGF165-targeting aptamer, Macugen. *FEBS Lett.* **582**, 1835-1839 (2008).
302. R.C. Becker & M.Y. Chan. REG-1, a regimen comprising RB-006, a Factor IXa antagonist, and its oligonucleotide active control agent RB-007 for the potential treatment of arterial thrombosis. *Curr. Opin. Mol. Ther.* **11**, 707-715 (2009).
303. Bates, P.J., Laber, D.A., Miller, D.M., Thomas, S.D. & Trent, J.O. Discovery and development of the G-rich oligonucleotide AS1411 as a novel treatment for cancer. *Exp. Mol. Pathol.* **86**, 151-164 (2009).
304. Bates, P.J., Kahlon, J.B., Thomas, S.D., Trent, J.O. & Miller, D.M. Antiproliferative activity of G-rich oligonucleotides correlates with protein binding. *J. Biol. Chem.* **274**, 26369-26377 (1999).
305. Teng, Y., Girvan, A.C., Casson, L.K., Pierce, W.M., Qian, M., Thomas, S.D. & Bates, P.J. AS1411 Alters the localization of a complex containing protein arginine methyltransferase 5 and nucleolin. *Cancer Res.* **67**, 10491-10500 (2007).
306. Krieg, A.M. Therapeutic potential of Toll-like receptor 9 activation. *Nat. Rev. Drug Discov.* **5**, 471-484 (2006).
307. Sheehan, J.P. & Lan, H.-C. Phosphorothioate oligonucleotides inhibit the intrinsic tenase complex. *Blood* **92**, 1617-1625 (1998).
308. Keefe, A.D., Pai, S. & Ellington, A. Aptamers as therapeutics. *Nat. Rev. Drug Discov.* **9**, 537-550 (2010).
309. Lupold, S.E., Hicke, B.J., Lin, Y. & Coffey, D.S. Identification and characterization of nuclease-stabilized RNA molecules that bind human prostate cancer cells via the prostate-specific membrane antigen. *Cancer Res.* **62**, 4029-4033 (2002).

310. Min, K., Jo, H., Song, K., Cho, M., Chun, Y.-S., Jon, S., Kim, W.J. & Ban, C. Dual-aptamer-based delivery vehicle of doxorubicin to both PSMA (+) and PSMA (−) prostate cancers. *Biomaterials* **32**, 2124-2132 (2011).
311. Chu, T.C., Twu, K.Y., Ellington, A.D. & Levy, M. Aptamer mediated siRNA delivery. *Nucleic Acids Res.* **34**, e73-e73 (2006).
312. Farrar, C.T., William, C.M., Hudry, E., Hashimoto, T. & Hyman, B.T. RNA aptamer probes as optical imaging agents for the detection of amyloid plaques. *PLoS One* **9**, e89901 (2014).
313. Sunbul, M. & Jaeschke, A. Contact-mediated quenching for RNA imaging in bacteria with a fluorophore-binding aptamer. *Angew. Chem., Int. Ed.* **52**, 13401-13404 (2013).
314. Whatley, A.S., Ditzler, M.A., Lange, M.J., Biondi, E., Sawyer, A.W., Chang, J.L., Franken, J.D. & Burke, D.H. Potent inhibition of HIV-1 reverse transcriptase and replication by nonpseudoknot, "UCAA-motif" RNA aptamers. *Mol. Ther. Nucleic Acids* **2**, e71, 11 pp. (2013).
315. Hyeon, J.-Y., Chon, J.-W., Choi, I.-S., Park, C., Kim, D.-E. & Seo, K.-H. Development of RNA aptamers for detection of Salmonella Enteritidis. *J. Microbiol. Methods* **89**, 79-82 (2012).
316. Foerster, U., Weigand, J.E., Trojanowski, P., Suess, B. & Wachtveitl, J. Conformational dynamics of the tetracycline-binding aptamer. *Nucleic Acids Res.* **40**, 1807-1817 (2012).
317. Le, T.T., Scott, S. & Cass, A.E.G. Streptavidin binding bifunctional aptamers and their interaction with low molecular weight ligands. *Anal. Chim. Acta* **761**, 143-148 (2013).
318. Singh, T.S., Rao, B.J. & Krishnamoorthy, G. GTP binding leads to narrowing of the conformer population while preserving the structure of the RNA aptamer: A site-specific time-resolved fluorescence dynamics study. *Biochemistry* **51**, 9260-9269 (2012).
319. Selvakumar, L.S. & Thakur, M.S. Nano RNA aptamer wire for analysis of vitamin B12. *Anal. Biochem.* **427**, 151-157 (2012).
320. Froehlich, E., Mandeville, J.S., Jennings, C.J., Sedaghat-Herati, R. & Tajmir-Riahi, H.A. Dendrimers bind human serum albumin. *J. Phys. Chem. B* **113**, 6986-6993 (2009).
321. Frisch, M.J., Trucks, G.W., Schlegel, H.B., Scuseria, G.E., Robb, M.A., Cheeseman, J.R., Montgomery, J.A.J., Vreven, T., Kudin, K.N., Burant, J.C., Millam, J.M., Iyengar, S.S., Tomasi, J., Barone, V., Mennucci, B., Cossi, M., Scalmani, G., Rega, N., Petersson,, G. A., N., H., Hada, M., Ehara, M., Toyota, K., Fukuda, R., Hasegawa, J., Ishida, M.,, Nakajima, T., Honda, Y., Kitao, O., Nakai, H., Klene, M., Li, X., Knox, J. E., Hratchian,, H. P., C., J. B., Bakken, V., Adamo, C., Jaramillo, J., Gomperts, R., Stratmann, R. E.,, Yazyev, O., Austin, A. J., Cammi, R., Pomelli, C., Ochterski, J.W., Ayala, P. Y.,Morokuma,, K., V., G. A., Salvador, P., Dannenberg, J. J., Zakrzewski, V. G., Dapprich, S., Daniels,, A. D., S., M. C., Farkas, O., Malick, D. K., Rabuck, A. D., Raghavachari, K., Foresman,, J. B., O., J. V., Cui, Q., Baboul, A. G., Clifford, S., Cioslowski, J., Stefanov, B. B., Liu,, G., L., A., Piskorz, P., Komaromi, I., Martin, R. L., Fox, D. J., Keith, T., Al-Laham,, M. A., P., C. Y.,

Nanayakkara, A., Challacombe, M., Gill, P. M. W., Johnson, B., Chen, & W., W., M. W., Gonzalez, C., Pople, J. A. Gaussian 03. *Gaussian Inc.* **Revision C.02.** (2004).

322. Case, D.A., Cheatham, T.E., Darden, T., Gohlke, H., Luo, R., Merz, K.M., Onufriev, A., Simmerling, C., Wang, B. & Woods, R.J. The Amber biomolecular simulation programs. *J. Comput. Chem.* **26**, 1668-1688 (2005).
323. Cornell, W.D., Cieplak, P., Bayly, C.I. & Kollmann, P.A. Application of RESP charges to calculate conformational energies, hydrogen bond energies, and free energies of solvation. *J. Am. Chem. Soc.* **115**, 9620-9631 (1993).
324. Wang, J., Wolf, R.M., Caldwell, J.W., Kollman, P.A. & Case, D.A. Development and testing of a general amber force field. *J. Comput. Chem.* **25**, 1157-1174 (2004).
325. Sorin, E.J. & Pande, V.S. Exploring the helix-Coil transition via all-atom equilibrium ensemble simulations. *Biophys. J.* **88**, 2472-2493 (2005).
326. Jorgensen, W.L., Chandrasekhar, J., Madura, J.D., Impey, R.W. & Klein, M.L. Comparison of simple potential functions for simulating liquid water. *J. Chem. Phys.* **79**, 926-935 (1983).
327. Hess, B., Kutzner, C., van der Spoel, D. & Lindahl, E. GROMACS 4: Algorithms for highly efficient, load-balanced, and scalable molecular simulation. *J. Chem. Theo. Comput.* **4**, 435-447 (2008).
328. Press, W.H., Teukolsky, S.A., Vetterling, W.T. & Flannery, B.P. Numerical recipes: The art of scientific computing (Cambridge University Press: U.K.,, 2007).
329. Van Der Spoel, D., Lindahl, E., Hess, B., Groenhof, G., Mark, A.E. & Berendsen, H.J.C. GROMACS: Fast, flexible, and free. *J. Comput. Chem.* **26**, 1701-1718 (2005).
330. Berendsen, H.J.C., Postma, J.P.M., van Gunsteren, W.F., DiNola, A. & Haak, J.R. Molecular dynamics with coupling to an external bath. *J. Chem. Phys.* **81**, 3684-3690 (1984).
331. Darden, T., York, D. & Pedersen, L. Particle mesh Ewald: An N·log(N) method for Ewald sums in large systems. *J. Chem. Phys.* **98**, 10089-10092 (1993).
332. Nosé, S. A molecular dynamics method for simulations in the canonical ensemble. *Mol. Phys.* **52**, 255-268 (1984).
333. Parrinello, M. & Rahman, A. Polymorphic transitions in single crystals: A new molecular dynamics method. *J. Appl. Phys.* **52**, 7182-7190 (1981).
334. Sugio, S., Kashima, A., Mochizuki, S., Noda, M. & Kobayashi, K. Crystal structure of human serum albumin at 2.5 A resolution. *Protein Eng.* **12**, 439-446 (1999).
335. Hornak, V., Abel, R., Okur, A., Strockbine, B., Roitberg, A. & Simmerling, C. Comparison of multiple Amber force fields and development of improved protein backbone parameters. *Proteins Struct. Funct. Bioinf.* **65**, 712-725 (2006).
336. Horn, H.W., Swope, W.C., Pitera, J.W., Madura, J.D., Dick, T.J., Hura, G.L. & Head-Gordon, T. Development of an improved four-site water model for biomolecular simulations: TIP4P-Ew. *J. Chem. Phys.* **120**, 9665-9678 (2004).
337. Bussi, G., Zykova-Timan, T. & Parrinello, M. Isothermal-isobaric molecular dynamics using stochastic velocity rescaling. *Acc. Chem. Res.* **130**, 074101-9 (2009).
338. Nosé, S. Dynamical behavior of a thermostated isotropic harmonic oscillator. *Phys. Rev. E* **47**, 164 (1993).
339. Besler, B.H., Merz, K.M. & Kollman, P.A. Atomic charges derived from semiempirical methods. *J. Comput. Chem.* **11**, 431-439 (1990).

340. Morris, G.M., Huey, R., Lindstrom, W., Sanner, M.F., Belew, R.K., Goodsell, D.S. & Olson, A.J. AutoDock4 and AutoDockTools4: Automated docking with selective receptor flexibility. *J. Comput. Chem.* **30**, 2785-2791 (2009).
341. Morris, G.M., Goodsell, D.S., Halliday, R.S., Huey, R., Hart, W.E., Belew, R.K. & Olson, A.J. Automated docking using a Lamarckian genetic algorithm and an empirical binding free energy function. *J. Comput. Chem.* **19**, 1639-1662 (1998).
342. Case, D.A. terminal phosphate group in RNA. *http://ambermd.org/Questions/mail/251.html* (2003).
343. ID:3V03, P. http://www.rcsb.org/pdb/explore/explore.do?structureId=3V03.
344. Hetényi, C. & van der Spoel, D. Blind docking of drug-sized compounds to proteins with up to a thousand residues. *FEBS Lett.* **580**, 1447-1450 (2006).
345. Pettersen, E.F., Goddard, T.D., Huang, C.C., Couch, G.S., Greenblatt, D.M., Meng, E.C. & Ferrin, T.E. UCSF Chimera-A visualization system for exploratory research and analysis. *J. Comput. Chem.* **25**, 1605-1612 (2004).

End of Chapter 2

Chapter 3

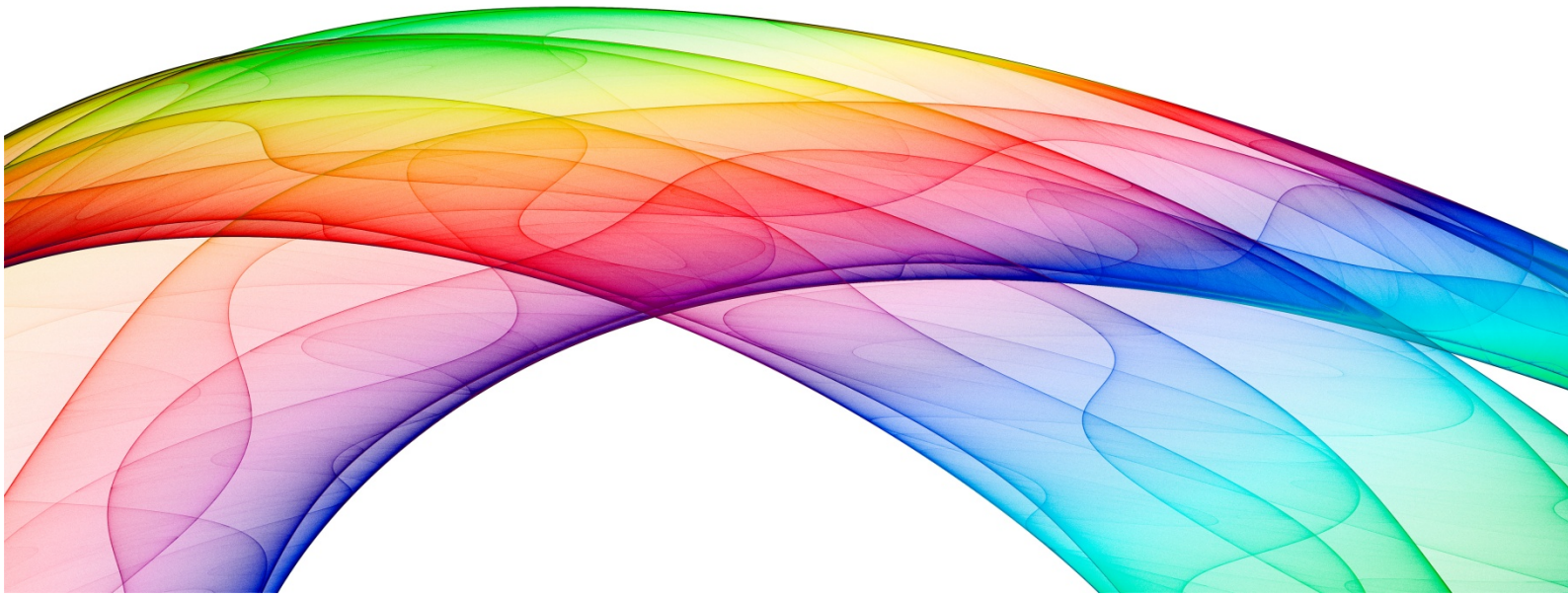

Instrumentation, Technique and Analysis

Present chapter contains a brief description of several instrumentations including absorption spectrophotometer, steady state fluorescence spectrophotometer, time correlated single photon counting (TCSPC), femtosecond fluorescence up-conversion, circular dichroism (CD) and isothermal titration calorimetry (ITC), which have been extensively used for completing the projects described in this thesis. The working principles, specification of the instrumentation as well as the data analysis processes are also included in this chapter.

3.1. Absorption

Absorption spectroscopy refers to the technique, which measures the absorption of radiation as a function of frequency (cm^{-1}) or wavelength (nm), resulted from the interaction between incident light with the sample.[1, 2] When a sample is subjected to light irradiation of appropriate energy, it causes the rotational and vibrational transition followed by electronic transition in the molecule. During these processes a fraction of the light intensity gets absorbed and remaining passes through the sample. A detector placed at the opposite side of excitation source detects the change in intensity compared to a blank. The resultant difference of intensity is said to be absorbed by the sample and plotted against wavelength known as absorption spectrum.[1, 2]

All the absorption measurements are carried out in a double beam, ultraviolet-visible (UV-Vis) spectrophotometer (Shimadzu UV2600). **Figure 3.1** shows the simplified schematic diagram of a commercially available double beam absorption UV-Vis spectrometer. A lamp covering the range of near ultra-violet to near-infrared (IR) (~200 nm to ~900 nm) light is required as an excitation source. As a single lamp emission cannot cover the whole range with equal efficiency, hence combination of two lamps; a deuterium lamp for the absorption event in the UV region and a tungsten/halogen lamp (50 W Halogen Lamp for

Shimadzu UV 2600) for the change in the absorption phenomenon in the visible to near-IR is used. The combined output of these two sources is focused on a rotating diffraction grating. A rotating diffraction grating allows particular wavelength of the light of whole spectrum through the slit towards the optics inside the instrument. After entering through the slit, the light faces rotating disk, a clever device which acts as the control unit of double beam instrumentation. The rotating disk consists of three segments, a transparent section (devised for complete passage of light), a reflecting section (acting like a mirror) and an absorbing section (acts as a light sink). When the incident light falls over the disk three things may happen. (a) Light faces the transparent section of RD1, (**Figure 3.1**) follows the red colored path through sample cell. After sample cell it bounces by the mirror and falls on RD2.

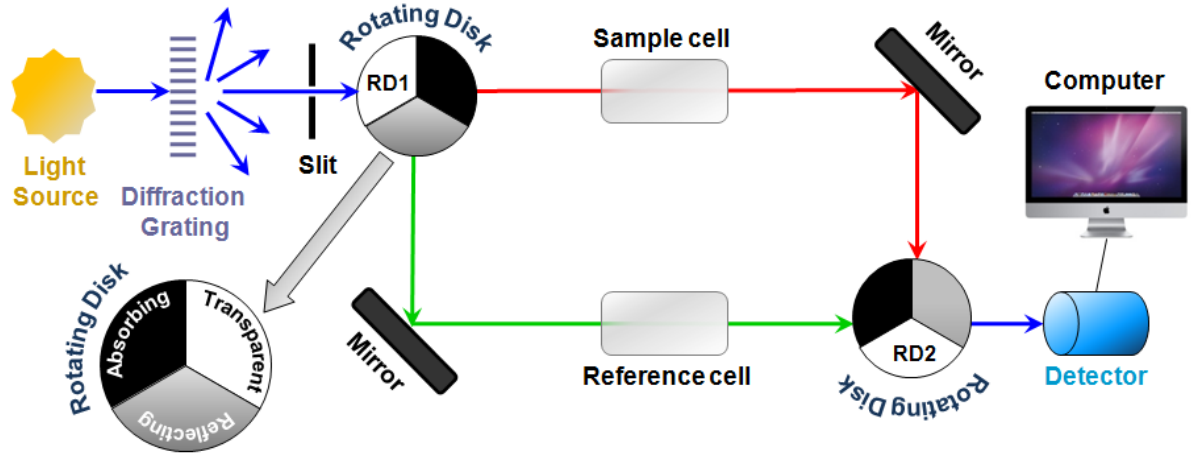

Figure 3.1. *Schematic representation of absorption spectrometer. The color codes of light (blue, green and red) do not mean any wavelength of light but represents different paths of light.*

Rotation of RD1 and RD2 is programmed in such a way that if light falls in RD1 (transparent section) then it faces the reflecting section in RD2. Hence, light is reflected towards detector (a photodiode). (b) If light encounters the reflecting section in RD1, then it follows the green path and falls on RD2. After that light passes through the transparent section of RD2 and reaches the detector. (c) If light falls over the absorbing section, all the light gets absorbed. It allows the computer within a small while to verify whether any current (dark counts) is detected by the instrument in absence of photons. Samples in absorption spectrometer are filled in cell which is a rectangular quartz container (usually 1 cm path length). A reference

cell is an identical quartz cell filled with blank solvent. A reference cell is used to correct the blank absorption of cell and solvent if any.

The detector in spectrometer is the photon counting device. The photons detected by the detector are converted into current where intensity of absorbance is directly proportional to the measured current. An intensity of absorbance *vs.* wavelength (nm) plot is called an absorbance curve. Each absorption band is known to offer idea about the energy of a typical electronic transition in a molecule. The absorbance (*A*) of an absorber (at a particular concentration *C*) having a molar extinction coefficient $\mathcal{E}_\lambda$ at a particular wavelength (λ) is governed by Lambet-Beers law;[1, 2]

$$A = \log\frac{I_0}{I} = \varepsilon_\lambda C l \qquad \ldots 3.1$$

where, I_0 and I are the intensities of the incident and transmitted light respectively and l is the path length of the light beam passing through the sample in the cuvette (quartz). In all experimental conditions the ligand or small molecular (molecule subjected to absorption and fluorescence studies) concentrations were kept very low (5 µM - 10 µM) to avoid molecular aggregations and other artifacts. Path length of the cuvette was kept fixed at 1cm for all the measurements. Moreover, all the absorption measurements were carried out at room temperature (25ºC) until otherwise specified.

3.2. Steady State Emission

Steady state emission spectrophotometer is an instrument which can measure both excitation and emission spectra. Emission spectrum is the "wavelength distribution of an emission measured at a single excitation wavelength"[3, 4]. On the other hand an "excitation spectrum is the dependence of emission intensity, measured at a single emission wavelength, upon scanning the excitation wavelength"[3, 4]. Emission or excitation spectra can be represented either in wavelength (nm unit) scale or a wave number (cm^{-1}) scale. **Figure 3.2** represents a block diagram of a commercially available conventional spectrofluoremeter. The light source is generally a high-pressure xenon arc lamp (power 150 Watt), which results a continuous emission from ~250 nm to the infrared ~800 nm.[3, 4] Using a monochromator, one can easily select a particular excitation wavelength. Fluorescence is collected at right angle with respect to the incident beam in order to avoid stray light coming from the light source and detected

through a monochromator by a photomultiplier tube (PMT).[3, 4] photomultiplier tube or PMT is the detection device which works based on photoelectric current generation phenomenon. When a photon emitted from sample strikes over metal array kept in vacuum and high voltage (950 V), it generates electrons. The flow of electron along the voltage bias results the signal. In advanced instrumentation, the photon counting module of detection is used preliminary with photomultiplier tubes, where discrete current pulses from the tube are integrated and net photons counted up. This method minimizes the inherent noise (dark count ~1000 counts/sec) in detector (compared to traditional voltage detection module) and results much sensitive detection. Monochromators controlling the excitation and emission wavelengths are automated and computer controlled. Scanning information along with the intensity at each wavelengths are stored in computer and analyzed to extract information like peak intensity, area under the curve, quantum yield (described in **Chapter 1**) etc.

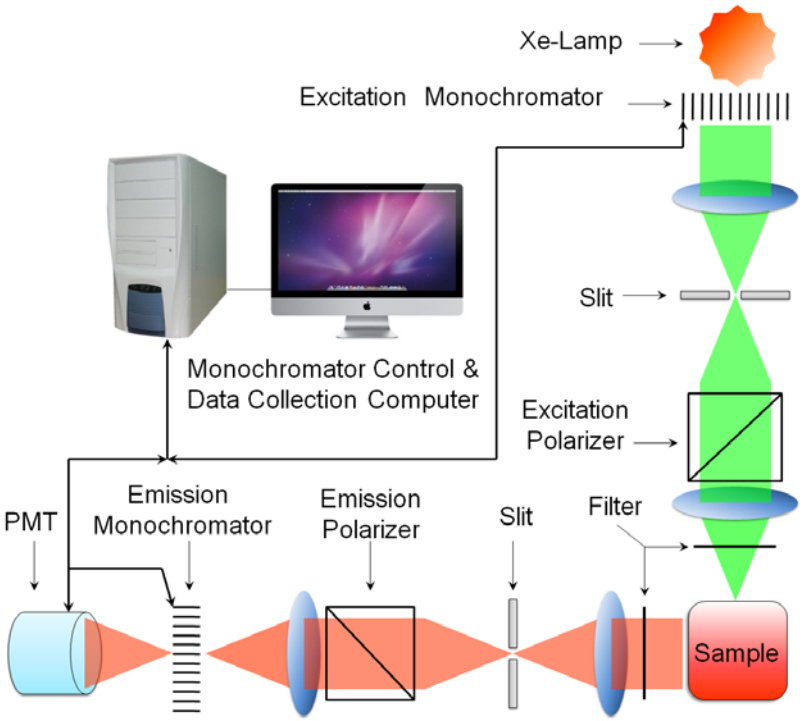

Figure 3.2. *Schematic representation of steady state fluorescence spectrophotometer.*

All the steady state fluorescence measurements were carried out on Fluoromax-4 and Fluorolog-3 (Horiba Jobin Yvon, U.S.A.) spectrofluoremeters. Although the basic working principle for both of the models are same but it differs in terms of monochomator. Fluorolog-3 contains double monochomator at both of excitation and emission side whereas Fluoromax-

4 has the single monochomator. A high pressure 450 Watt Xe lamp is used as excitation source for Fluorolog-3, whereas 150 Watt Xe lamp is used for Fluoromax-4. For all solution state measurements the right angle (RA) geometry (**Figure 3.2** shows a typical right angle oriented fluoremeter) were chosen. Emission intensity data has been extensively used to calculate the association/binding constants using two different methods namely (i) modified Scatchard method[5, 6] and (ii) Benesi-Hildebrand method[7, 8] described in detail hereunder.

3.2a. Modified Scatchard Method for Binding Constant Determination

For fluorophore-macromolecular titration, a successive change (either increase or decrease) of fluorescence can be utilized to calculate the binding constant using Scatchard plot. We have used the Scatchard method to calculate the binding constant for ellipticine-DNA, ellipticine-serum albumin (SA) and flavin-RNA aptamer interactions. The general Scatchard plot (for saturation emission intensity) is the ratio of (bound/free) *vs*. bound ligand. For a simple reaction like; $M + L \rightarrow ML$ the association/binding constant (K_a) can be represented by the following equation;

$$K_a = \frac{[ML]}{[M] \times [L]} \quad \ldots 3.2$$

where, [*ML*] and [*M*] are the number of occupied and unoccupied macromolecular sites/unit volume respectively. [*L*] is the concentration of the ligand. If n_{occ} is considered as the average number of sites/macromolecule (*M*) occupied by the ligand and *n* represents the total number of binding sites available/macromolecule, then, K_a can be represented in other way as;

$$\frac{N_{occ}}{N} = \frac{[ML]}{[M] + [L]} \quad \ldots 3.3$$

Substituting the value of K_a in equation 3.3 it gives;

$$N_{occ} = N \frac{K_a[L]}{K_a[L] + 1} \quad \ldots 3.4$$

The N_{occ} vs. $[L]$ (from equation 3.4) generates a hyperbolic curve which is difficult to analyze and hence needs simplification which can be done using modified Scatchard plot.[5, 6] For linearization, a factor '*f*' has been introduced which represents the fraction of ligand bound during macromolecular-ligand titration and *f* is represented as;

$$f = \frac{F_{obs} - F_L}{F_{max} - F_L} \quad \ldots 3.5$$

where, F_{obs} is the observed fluorescence intensity at each titration point, F_L is fluorescence from the free ligand and F_{max} is the intensity when all possible ligand are bound to the possible macromolecular sites. Spectroscopic determination of *f* allows the experimental determination of N_{occ} by realizing that under pre-saturation concentrations of ligand and macromolecule;

$$N_{occ} = \frac{f[L]_{total}}{[M]_{total}} = N\frac{K_a[L]}{K_a[L] + 1} \quad \ldots 3.6$$

Taking the reciprocal of each side in equation 3.6 and multiplying through by $[L]_{total}$ gives;

$$\frac{[M]_{total}}{f} = \frac{[L]_{total}}{NK_a[L]} + \frac{[L]_{total}}{N} \quad \ldots 3.7$$

It is quite obvious that fraction of free ligand can be measured experimentally [which corresponds to (1- *f*)], using the following relation;

$$(1 - f) = \frac{[L]}{[L]_{total}} \quad \ldots 3.8$$

Finally, substituting equation 3.8 into equation 3.7 gives the final form of modified Scatchard equation appears as;

$$\frac{[M]_{total}}{f} = \frac{1}{NK_a(1 - f)} + \frac{[L]_{total}}{N} \quad \ldots 3.9$$

where, $[M]_{total}$ is the total macromolecular concentration, *N* stands for the number of possible binding sites and $[L]_{total}$ represents total concentration of ligand. A plot of ($[M]_{total}/f$) vs [1/(1-*f*)] offers a straight line and from its slope of the association constant (K_a) can be determined. The free energy of binding can be determined from the following equation;

$$\Delta G^0 = -2.303\, RT \log K_a \qquad \ldots 3.10$$

The value of Gibbs free energy gives insight about the feasibility of the association between fluorophore and macromolecule/host.

3.2b. Benesi-Hildebrand Method for Binding Constant Determination

A quantitative estimation of the fluorophore-macromolecular/host binding interaction can also be obtained with the help of binding constant, elucidated from Benesi-Hildebrand (B-H) plot.[7, 8] We have used B-H plot for binding constant determination in case of flavin-serum protein interaction. For a binding interaction between macromolecule (M) and ligand (L) like $M + L \rightarrow ML$ the association constant K_a can be described by the equation 3.2. This can be rearranged in terms of saturation binding interaction as;

$$K_a = \frac{[ML]}{[L_0 - ML][M_0 - ML]} \qquad \ldots 3.11$$

where *ML* is the saturation concentration of macromolecular-ligand interaction, L_0 and M_0 are the initial concentrations of ligand and macromolecules, respectively. Cases when the unbound macromolecular concentration is higher than *ML* i.e $M_0 >> ML$, equation 3.11 modifies as;

$$K_a = \frac{[ML]}{[L_0 - ML][M_0]} \qquad \ldots 3.12$$

The process of complexation can be expressed in terms of fluorescence intensity when free and bound ligand offers different emission intensities;

$$\frac{[ML]}{[L]} = \frac{I_0 - I_\infty}{I_0 - I_x} \quad \ldots 3.13$$

where, I_0, I_x and I_∞ are the fluorescence intensities of the free ligand, ligand bound to macromolecule after each addition and intensity of the saturated ligand-macromolecular complex. Combining equation 3.12 and 3.13 along with little rearrangements one can get the double reciprocal Benesi-Hildebrand (BH) equation in following form;

$$\frac{1}{\Delta I} = \frac{1}{\Delta I_{max}} + \left(\frac{1}{K_a[L]} \times \frac{1}{\Delta I_{max}}\right) \quad \ldots 3.14$$

Here, $\Delta I = (I_x - I_0)$ and $\Delta I_{max} = (I_\infty - I_0)$ where I_0, I_x and I_∞ carries similar meaning mentioned earlier. The plots of $(1/\Delta I)$ against $[L]^{-1}$ provides the quantitative estimation of association constant. Notably, Benesi-Hildebrand equation in above mentioned form is applicable only for 1:1 complexation process. If a complexation occurs with two distinct steps, such as, $M + L \rightarrow ML; ML + M \rightarrow LM_2$; the Benesi-Hildebrand equation appears as follows;

$$\frac{1}{\Delta I} = \frac{1}{\Delta I_{max}} + \left(\frac{1}{K_{a1}K_{a2}[L]^2} \times \frac{1}{\Delta I_{max}}\right) \quad \ldots 3.15$$

where, K_{a1} and K_{a2} are the equilibrium constants for the two different steps, respectively, and all other terms carry the similar meaning as mentioned earlier.

3.3. Time Resolved Fluorescence Measurements

3.3a. Time Correlated Single Photon Counting Technique (TCSPC); Fluorescence Lifetime Measurements

Pulsed excitation is the most popular technique for the determination of fluorescence lifetime (or decay parameters). Most instruments operation by pulsed excitations are based on the time-correlated single photon counting (TCSPC)[3, 4, 9, 10]method, also called as single-photon timing (SPT). The basic principle of TCSPC depends over the fact that the probability of detecting a single photon at time *t* after an exciting pulse is proportional directly to the

fluorescence intensity at that time.[3, 4] **Figure 3.3** shows the outline of a conventional fluorescence single-photon counting instrument. The excitation source can be a flash lamp, nano-LED or a mode-locked laser. An electrical pulse associated with optical pulse is generated which excites the sample as well as sends a signal to constant fraction discriminator (CFD) through synchronizer (SYNC) (it synchronizes the optical and electrical

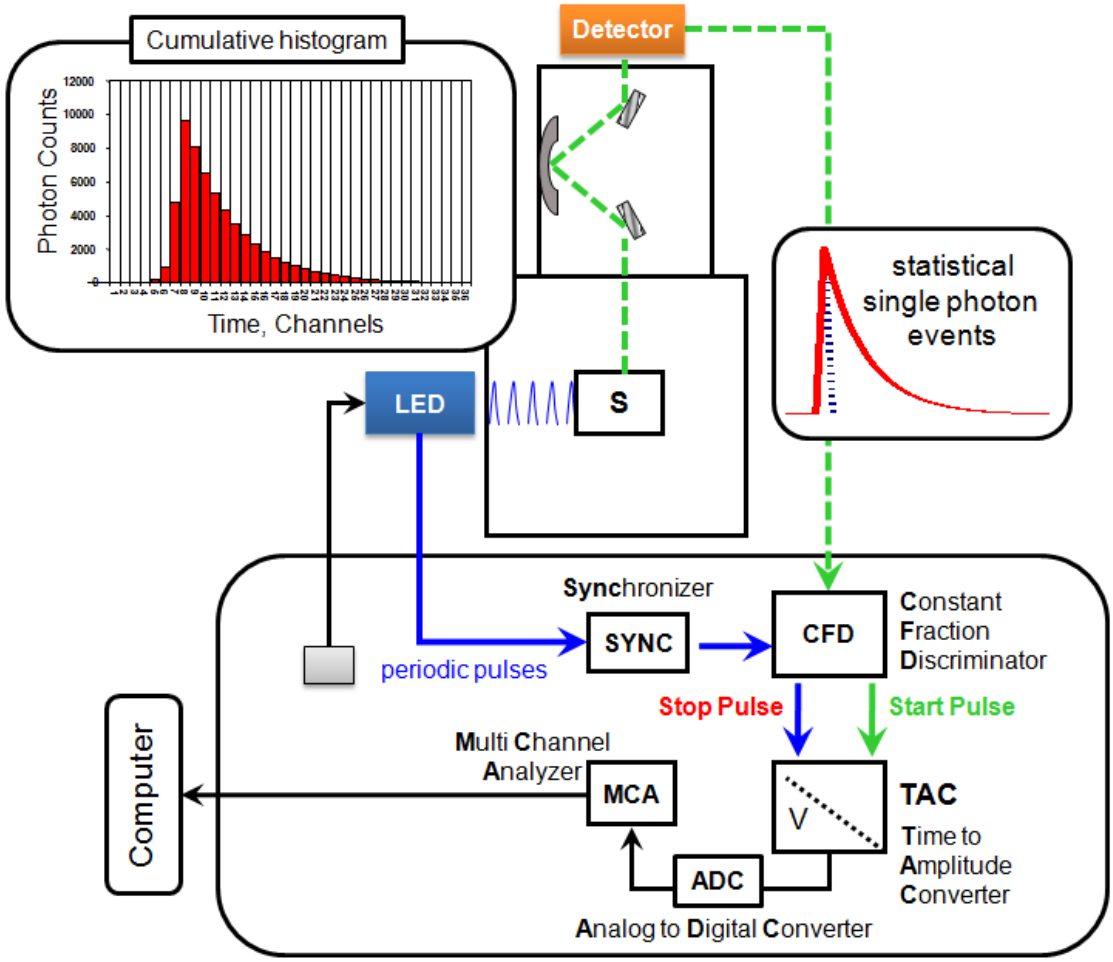

Figure 3.3. *Schematic representation of TCSPC[11] instrument.*

pulses). CFD accurately records the arrival time of the photons. After passing through CFD, the excitation pulse reaches to TAC (time to amplitude converter) and immediately starts charging the capacitor inside TAC. Charging of the TAC capacitor starts a voltage ramp. TCSPC instruments are set in such a way that after the excitation only one stop photon from the sample is detected for every 100-200 excitations. An emission photon resulting from the sample excitation meanwhile reaches to TAC and stops the charging of TAC capacitor. TAC

is the heart of the TCSPC system. It acts as a stopwatch and measures the time gap between the start (LED photon) and stop (sample photon) pulses. The amplitude of this pulse is proportional to the charge in the capacitor, and hence to the time difference between the start and stop pulses. The TAC output pulse is given a numerical value within the analog-to-digital converter (ADC) and a count is stored in the data storage corresponding to that number. This process is repeated several times to generate a histogram corresponding to the lifetime decay of the sample. The so called decay result from TCSPC instrument can be either deconvoluted considering the effect of the pulse or can be analyzed by graph plotting software by neglecting the effect of the excitation pulse.

Its pertinent to mention that the TCSPC instrument, we use runs in reverse mode i.e. emission photon resulting from the sample excitation acts as starts pulse for the TAC and an excitation pulse resulting from the laser/LED acts as stop pulse. The reason for such reverse orientation is a high repetition rate of excitation LEDs. When TCSPC operates in forward mode due to a high repetition rate of the excitation lasers and LEDs, start pulse reaches prior to reset time of the electronics. To overcome such problem from the electronic response time, modern days TCSPC set up operate in reverse mode. We have used majorly three LEDs for sample excitation, namely, 375 nm (FWHM < 100ps), 402 nm (FWHM < 100 ps) and 444 nm (FWHM < 120 ps). Instrument response of our TCSPC set-up using the above mentioned diode lasers was ~100 ps, and with the help of deconvolution method (discussed next section) we could able to detect lifetime of ~40 ps. The detector used in this TCSPC set-up is a MCP-PMT. Instead of PMT, TCSPC used micro-channel plate PMT (MCP-PMT). In comparison to simple dynode chains in PMT, MCP-PMT consists of numerous small holes. The holes in these plates are micro-channels, and the generated photoelectrons are proximity focused into the MCP. As here electrons travel short distances, this type of PMT shows fastest time response compare to conventional PMT, and is used in most of the time-resolved measurements.

3.3a.1. Deonvolution Method and Analysis of Fluorescence Lifetime Decays

When a sample is excited with δ-pulse (having infinite intensity at a particular time and zero intensity at rest of the times) and respective decay time is shorter than the FWHM (Full Width Half Maximum) of the excitation pulse, distortion of the experimental data occurs due to 3 factors which are (1) a finite decay time of the laser pulse, (2) response time of the photomultiplier and (3) response lag from the associated electronics.[3, 9, 10] Since the measured

decay function is now a convolution of the measured instrumental prompt response *P*(t) and the theoretical fluorescence response function *F*(t), the net result (*R*(t)) obtained for δ function excitation will be;

$$R(t) = \int_0^t P(t') \times F(t - t') dt' \quad \ldots 3.16$$

Where, *t*′ defines the variable time delays (in practice, channel numbers) of the infinitesimally small widths dt′ (i.e, channel widths) of which *P*(t′) is composed. By measuring *P*(t) experimentally over '*i*' channels of data, the convoluted form of *R*(t) can be obtained from equation 3.16. Here one has to assume a functional form of *F*(t), for example one, two or three exponentials. By iterating the values of the decay components until good agreement is obtained, the best fit values are determined.

$$F(t) = \sum_i a_i e^{-t/\tau_i} \quad \ldots 3.17$$

The standard statistical procedure to confirm goodness of fit is the χ^2 test. The χ^2 is given by;

$$\chi^2 = \sum_{i=1}^{n} \omega_i [R(t) - R_c(t)]^2 \quad \ldots 3.18$$

where, R_c(t) is calculated values by assuming functional form of *F*(t) (equation 3.17) and ω_i =1/*R*(t). The χ^2 value ~1 indicates good fit, where a small deviation from 1 sometime is considered to be acceptable for complicated heterogeneous systems.

The analysis of fluorescence decays were performed using the commercially available global lifetime analysis software of IBH (UK).

3.3b. Fluorescence Anisotropy Measurement and Analysis

3.3b.1. Steady state Anisotropy

Fluorescence anisotropy is a powerful tool to probe the association between a drug/ligand to bio-macromolecule or encapsulation of molecule in a restricted environment. [3, 12, 13] Upon excitation with polarized light, the emission from the samples is expected to have same

polarization as that of excitation light. However, due to random orientation of the molecules and rotational diffusion of the molecule, the polarization of resulted emission is not same as that of excitation light. Therefore, anisotropy measures the extent of depolarization of emission, when the molecules are selectively excited by a polarized light, and it is defined by;

$$r = \frac{I_{\parallel} - I_{\perp}}{I_{\parallel} + 2I_{\perp}} \qquad \ldots 3.19$$

where $I_{\parallel}$ and $I_{\perp}$ are the intensities (**Figure 3.4**) of the emitting light for parallel and perpendicular polarizations (*w.r.t.* polarization of the exciting light). The measurement of fluorescence anisotropy is illustrated in Figure 3.4. When the emission polarizer is oriented parallel (||) to the direction of the polarized excitation, the observed intensity is called $I_{\parallel}$. When the polarizer is perpendicular (⊥) to the excitation, the intensity is called $I_{\perp}$. These intensity values are used to calculate the anisotropy. The anisotropy is a dimensionless quantity and it is independent of the total intensity of the sample. This is because the difference ($I_{\parallel} - I_{\perp}$) is normalized by the total intensity, which is $I_T = I_{\parallel} + 2I_{\perp}$. Therefore, the anisotropy is an intensity ratio metric measurement. Since the monochromator has different transition efficiency for vertically and horizontally polarized light, rotation of emission polarizer changes the effective sensitivity of the emission channel. Moreover, the sensitivity

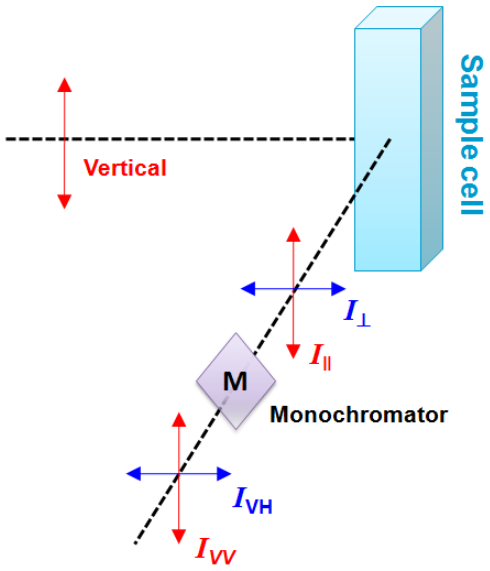

Figure 3.4. *Schematic diagram of measurements of fluorescence anisotropy.*

of the detection system depends on the polarization of the emission light, and hence, must be corrected by applying a correction factor known as the G factor. G factor was measured using horizontally polarization excitation light and measuring the horizontal (I_{HH}) and vertical (I_{HV}) polarization component of the emitted light.[12] The G factor is defined as the ration of perpendicular and parallel intensities (I_{HV}/I_{HH}) and the corrected anisotropy is given by,

$$r = \frac{I_{\parallel} - GI_{\perp}}{I_{\parallel} + 2GI_{\perp}} \qquad \ldots 3.20$$

Notably the steady state fluorescence anisotropy, r is related to fluorescence lifetime (τ) and rotational correlation time (τ_r) by the Perrin's equation;[3, 4]

$$\frac{r_0}{r} = 1 + \frac{\tau}{\tau_r} \qquad \ldots 3.21$$

Immediately after photo-excitation when the fluorophore has yet to reorient, the observed anisotropy (r) should be equal to r_0 (the fundamental anisotropy). As time passes, the molecules re-orient and the anisotropy decays toward zero. The r_0 value depends on the relative angular orientation between the absorption and emission transition moments. Equation 3.21 indicates that when $\tau_r >> \tau$, the observed anisotropy (r) equals to r_0 which is given by the following equation;

$$r_0 = \frac{2}{5}\left(\frac{3cos^2\alpha - 1}{2}\right) \qquad \ldots 3.22$$

where, α is the angle between absorption and emission transition dipoles. Since, the orientation of the absorption dipole differs for each absorption band; the angle α varies with excitation wavelength. However, α does not depend on the excitation wavelength as emission always occurs from lowest singlet state. r_0 has a maximum value 0.4 (α=0º) and minimum value of –0.2 (α=90º). The dependence of the anisotropies upon the rotational diffusion has resulted in numerous applications in various fields of research. In this thesis, the anisotropy value of the fluorophore is applied to determine the folding-unfolding dynamics of FAD as well as for location determination of the probe inside the reverse micelle, and in protein, DNA, RNA systems.

3.3b.2. Time Dependent Anisotropy

Time dependent anisotropy decays offer excellent information about the diffusive motion of the fluorophore, which can reveal whether a fluorophore rotates freely or the surrounding environment of the fluorophore restricts its rotational motion.[3, 4, 9] Therefore, the time-resolved fluorescence anisotropy measurement has been extensively utilized to study the rotational dynamics of fluorophore in micelles, reverse micelles, and inside the protein nano-cavity, DNA/RNA and in protein-DNA complex. During anisotropy measurement, the sample is excited with a polarized light pulses and the time dependent parallel [$I_{\parallel}$(t)] and perpendicular [$I_{\perp}$(t)] components of the fluorescence are used to form the time-resolved fluorescence anisotropy, r(t), which is governed by the following equation;

$$r(t) = \frac{I_{\parallel}(t) - I_{\perp}(t)}{I_{\parallel}(t) + 2I_{\perp}(t)} \quad \ldots 3.23$$

To compensate the polarization biased of the detection system and monochromator efficiency, the above equation is modified to;

$$r(t) = \frac{I_{\parallel}(t) - GI_{\perp}(t)}{I_{\parallel}(t) + 2GI_{\perp}(t)} \quad \ldots 3.24$$

where, G is the instrumental correction factor introduced for the polarization sensitivity of the detection system and monochromator.

The time-resolved anisotropy measurements were done by automated toggling method using time-correlated single photon counting set-up and exciting the sample by different diode lasers (375 nm (IBH, UK, Nano LED, FWHM ~100 ps) and 444 nm (IBH, UK, Nano LED, FWHM ~120 ps) in order to excite FAD, FMN and RF containing samples, and 405 nm (IBH, UK, FWHM ~100 ps) was used for excitation of C153 and C343 containing samples) for different systems. In toggling method, a motorized polarizer was used in the emission side, whereas the excitation polarizer was kept fixed at vertical position. This polarizer toggles between parallel and perpendicular orientations and the emission intensities at parallel [$I_{\parallel}$(t)] and perpendicular [$I_{\perp}$(t)] polarization were collected alternatively for 30 seconds until a certain peak difference between parallel [$I_{\parallel}$(t)] and perpendicular [$I_{\perp}$(t)] decay is reached. For typical anisotropy decay the difference between the peak counts at

parallel and perpendicular polarization were kept at 5000. The G factor was measured by taking two additional decay measurements [I_{HV}(t) and I_{HH}(t)] of the same sample with the excitation polarizer toggling between perpendicular or horizontal positions. Value of G factor is given by, G = I_{HV}(t)/I_{HH}(t), where I_{HV}(t) and I_{HH}(t) denotes the fluorescence decay kinetics of the sample measured using horizontally or perpendicularly (H) polarized exciting light and detecting the emission components polarized vertically (V) and horizontally (H), respectively. For a simple isotropic rotor, r(t) decays with a single rotational correlation time[3, 4, 9] (τ_r) represented by the following equation;

$$r(t) = r_0 exp^{-(\frac{t}{\tau_r})} \quad \ldots 3.25$$

For more complicated systems, r(t) takes the form of a sum of exponentials;

$$r(t) = r_0 \sum \beta_i \, exp^{-(\frac{t}{\tau_{ri}})} \quad \ldots 3.26$$

where, β and τ_{ri} are the fractional contribution of total depolarization and rotational correlation times of the i[th] component, respectively. r_0 represents fundamental anisotropy discussed in the previous section. In terms of Stokes-Einstein theory, τ_r is related to the medium viscosity by;

$$\tau_r = \frac{\eta V}{kT} = \frac{1}{6D} \quad \ldots 3.27$$

where, η is the viscosity coefficient of the medium, V is the molecular volume, k is the Boltzmann's constant, T is the absolute temperature, and D is the rotational diffusion coefficient. If the rotational motions are hindered or otherwise restricted, one would see that the anisotropy does not decay to zero at longer time. In this case, limiting anisotropy (r_∞) is observed at times which are long compared to fluorescence lifetime, and the decay can be represented as;

$$r(t) = (r_0 - r_\infty) \, exp^{-\left(\frac{t}{\tau_r}\right)} + r_\infty \quad \ldots 3.28$$

This behavior is encountered in two important areas, namely, for a fluorophore non-covalently bound to a macromolecule (e.g. probe-protein and probe-DNA systems) and for a fluorophore rotating inside restricted environments, like reverse micelle, inside the binding pocket of protein etc.

3.3c. Solvation Time Measurement

According to the previous discussions (**Chapter 1**) about solvation dynamics, solvent reorientation around a photo-excited fluorophore always leads to dynamic Stokes' shift. When one observe dynamic Stokes' shift in the emission spectra, the time-resolved emission spectra (TRES) have been constructed from a set of decays at 15-20 nm intervals following the procedure given by Fleming and Maroncelli.[14] The TRES at a given time *t*, $I(\lambda,t)$, is obtained by the fitting the decays $S(t,\lambda)$, by relative normalization to the steady-state spectrum $I_0(\lambda)$, as follows;

$$I(\lambda,t) = S(\lambda,t)\frac{I_0(\lambda)}{\int_0^\infty S(\lambda,t)dt} \quad \ldots 3.29$$

Each time-resolved emission spectrum is usually fitted by the "log-normal line shape function"[14] which is defined as follows;

$$g(\nu) = g_0 \exp(-ln\,(2) \times [\frac{ln\,(1+\alpha)}{b}]^2) \quad \ldots 3.30$$

where, $\alpha = \frac{2b(\nu-\nu_p)}{\Delta}$ and g_0, b, ν_p, and Δ are the peak height, asymmetric parameter, peak frequency, and width parameter, respectively. The peak frequency (ν_p) obtained from this log-normal fitting of TRES are then used to construct the decay of solvent correlation function [$C(t)$], which is defined as;

$$C(t) = \frac{\nu(t) - \nu(\infty)}{\nu(0) - \nu(\infty)} \quad \ldots 3.31$$

where, $\nu(0)$ is the peak frequency at time $t = 0$ when electronic excitation occurs, and $\nu(0)$ is calculated by the extrapolation of the $\nu(t)$ data to $t \rightarrow 0$. $\nu(t)$ is the peak frequency at time = *t*.

$\nu(\infty)$ is the peak frequency at infinite time when solvent molecules are in equilibrium position around the photo-excited solute molecule. The choice of $\nu(\infty)$ is critical and we have chosen $\nu(\infty)$ at longer time scale, when the changes of $\nu(t)$ as small as 10-20 cm^{-1}. As decay kinetics are inherently exponential in nature, hence decay of $C(t)$ with time can be fitted by using a single or multi exponential fit function which appears as follows;

$$C(t) = \sum \alpha_i exp^{-t/\tau_i} \quad \ldots 3.32$$

where, τ_i is the solvation time of i-th component with amplitudes of α_i. The average solvation time is calculated as $<\tau_{av}> = \sum_{i=1}^{n} a_i \tau_i$. When the system is heterogeneous and complex in nature, one can also try to fit $C(t)$ by stretch exponential function, which is;

$$C(t) = Aexp^{-(t/\tau_s)^{\beta_s}} + Bexp^{-(t/\tau_l)^{\beta_l}} \quad \ldots 3.33$$

where τ_s and τ_l are short and long time constant, respectively. β_s and β_l are the two exponents in long and short time-scales, respectively. However, if fitting offers the values of β_l and β_s close to 1, it indicates that stretch exponential fitting is not at all necessary for the system.

3.3d. Femtosecond Time Resolved Fluorescence Upconversion

For certain fluorophores, lifetime component appears within tens of pico-second, which appears impossible to be resolved by TCSPC set-up. In such cases, we have used the femtosecond fluorescence up-conversion set-up to detect the fast dynamics taking place within ~ 10 pico-seconds or lesser time-scale. In femtosecond up-conversion a tunable Mai Tai HP (Spectra Physics, USA) is used as excitation source. Mai-Tai is one box Ti:Sapphire oscillator, which provides <100 fs pulse width, and therefore, helps to resolve lifetime components of picoseconds to sub picoseconds time-scale. The high tuneability (690-1040 nm) of Mai-Tai oscillator is also appropriate to excite different kinds of samples. Furthermore, high quality, stable, horizontally polarized (>500:1 horizontal), Gaussian pulses (TEM_{00}, M^2<1.1) with stable average power (>2.5 W) and very high peak power (>300 kW) offers minimum fluctuation of the laser pulse. The greatest advantage of Mai-Tai is that it provides excellent beam pointing stability, minimal average power fluctuations, as well as it eliminates wavelength drift. Mai Tai uses the output from the high power fiber coupled diode

laser module(s) to end-pump Nd^{+3} ion doped Yttrium Vanadate crystalline matrix ($Nd:YVO_4$). The triply ionized neodymium act as an active medium for this four-level solid state pump laser, which has principle absorption bands in the red and near infra-red region. While excited with a diode laser, the strongest lasing form $Nd:YVO_4$ occurs at a wavelength ~1064 nm. The resulting 1064 nm emission is converted to a visible wavelength (532 nm)

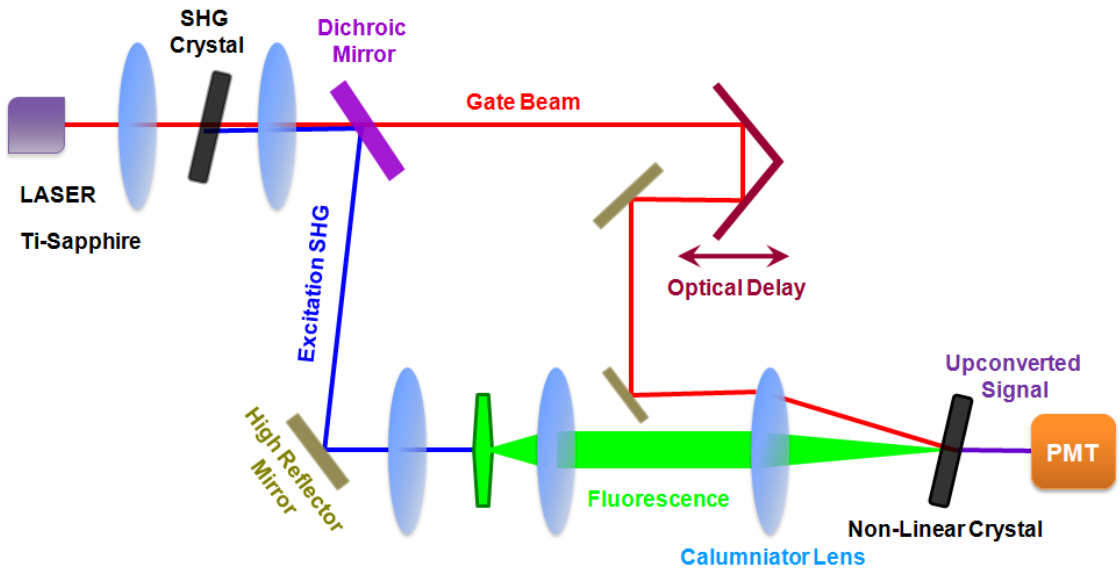

Figure 3.5. *Schematic representation of upconversion set up.*

through frequency doubling (also known as second harmonic generation or SHG) in a nonlinear crystal. A 90º, non-critically phase-matched, temperature tuned, lithium triborate (LBO) nonlinear crystal is used as a frequency doubling (or SHG) medium inside Mai-Tai one box oscillator. A dichroic output coupler allows the 532 nm light to exit from the pump cavity, but reflects the 1064 nm light back to the cavity. This 532 nm continues wave (CW) from a frequency doubled output of the $Nd:YVO_4$ pump laser is used to pump Ti-Sapphire laser, which in turn produces the Mai Tai output. Ti-Sapphire is a crystalline material produced by introducing Ti_2O_3 into a melt of Sapphire (Al_2O_3). The Ti^{+3} ion is responsible for the lasing action of Ti-Sapphire. Although the fluorescence band of Ti^{+3} extends from wavelengths as short as 600 nm to wavelength greater than 1000 nm, the lasing action is possible at greater than 670 nm (most strong emission band ~795 nm). Mai Tai uses an acousto-optic modulator (AOM) (constitutes a high quality optical material like quartz) to ensure the mode locked output from Ti-Sapphire. The Mai Tai reliability is maintained using

the ultra-stable regenerative modelocking technique proven with the Spectra-Physics Tsunami® oscillator.

Figure 3.5 represents schematic diagram of a femtosecond up-conversion system. The sample (flavin) was excited at 420 nm using the second harmonic of a mode-locked Ti-sapphire laser (Mai-Tai, Spectra Physics). The emitted fluorescence from sample was up-converted in another nonlinear crystal using the gated pulse of the fundamental beam (**Figure 3.6**). The sum frequency of fluorescence and the gate pulse was detected as a function of the time delay between excitation and gate pulses. The angle between the polarization of the pump and gate pulses was kept at magic angle (54.7^{o}) to eliminate effects from rotational diffusion. The up-converted signal is dispersed in a monochromator and detected using

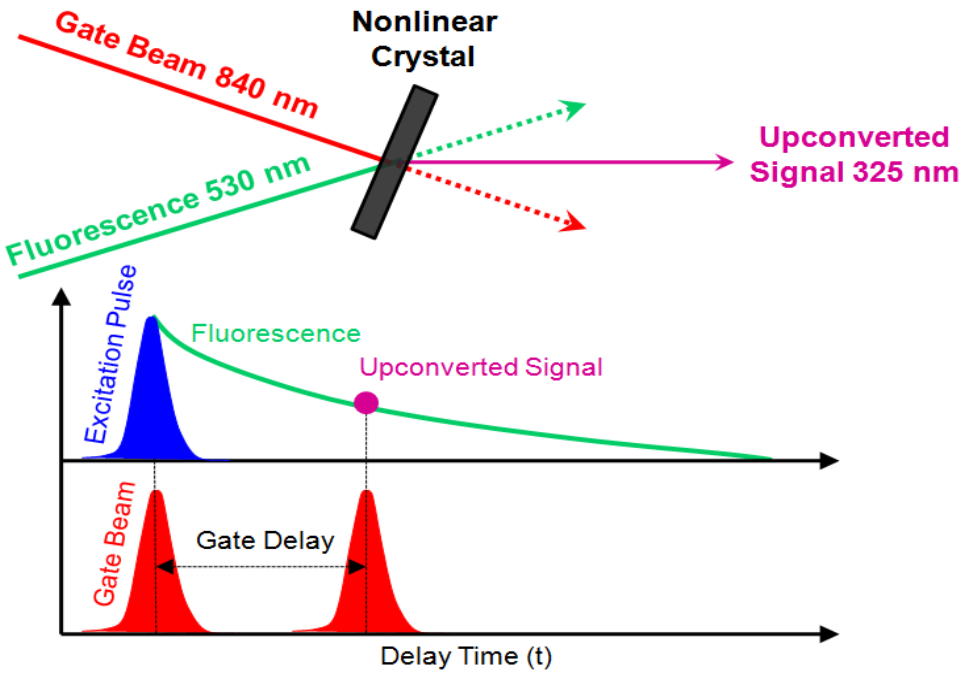

Figure 3.6. *Schematic representation of upconversion phenomenon.*

photon counting electronics. A cross-correlation function obtained using the Raman scattering from ethanol displayed a full-width at half-maximum (FWHM) of ~350 fs. Error in up-conversion measurements obtained from our results is ~10%. The data was analyzed using Igor software using cross correlation function obtained from Raman scattering. During data fitting, the long component appeared decay profile is usually guessed from the average lifetime value resulted from the TCSPC setup.

3.4. Circular Dichroism (CD)

Asymmetric chromophores or symmetric chromophores in asymmetric environments interact differently with right- and left-circularly polarized light resulting in two related phenomena.[15-17] Circularly-polarized light rays travel through an optically active medium with different velocities due to the different refraction indices for right- and left-circularly polarized light called optical rotation or circular birefringence. The variation of optical rotation as a function of wavelength (in nm unit) is called optical rotary dispersion (ORD). Right- and left-circularly polarized light is absorbed to different extents at some wavelengths due to differences in extinction coefficients for the two polarized rays called circular dichroism (CD).[15-17] Optical rotary dispersion enables a chiral molecule to rotate the plane of polarized light. ORD spectra are dispersive (called a Cotton effect[15-17] for a single band) whereas circular dichroism spectra are absorptive. The two phenomena are related by the so-called Kramers–Kronig transformation.[15-17] **Figure 3.7** shows the schematic representation of a commercially available CD instrument.

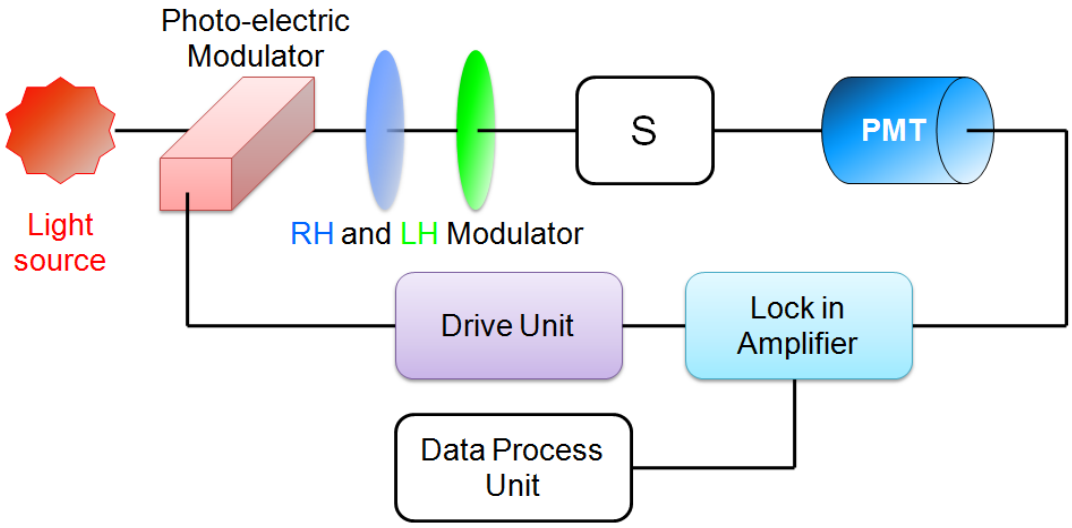

Figure 3.7. *Block diagram of circular dichroism (CD) spectrophotometer.*

CD spectra were recorded on a JASCO-800 automatic recording circular dichroism spectrophotometer. Quartz cuvette with 1.0 cm path length was used for measurements. CD spectra were accumulated at 25ºC at a scan rate of 100 nm/min, between 200-400 nm. A fixed concentration of macromolecules (≤10 μM of DNA/protein/RNA) was titrated with

increasing concentration of ligand (up to 10 times of the macromolecular concentration). Sometimes the chiral ligand produces a self CD signal, which was corrected by taking the blank of the individual ligand concentrations.

3.5. Isothermal Titration Calorimetry (ITC)

ITC is used to measure Bio-macromolecule-ligand interactions in solution phase without the need of any immobilization or modification.[18] The number of binding sites, the association constant (K_a), and the thermodynamic parameters including changes in enthalpy (ΔH), entropy (ΔS) and Gibbs free energy (ΔG) can be determined directly via the measurement of reaction heat. The greatest advantage in the ITC measurement is all the measurements are direct, excluding any indirect calculative measurements like Scatchard or Benesi-Hildebrand plot generation from fluorescence data. Another advantage of the technique is its cheap maintenance cost and the evaluation of the data is simple and computer-controlled. Disadvantage of ITC is that its need of a higher amount of material. Moreover, if either of the samples is not soluble then solvent-dispersed samples create problem for titration due to the

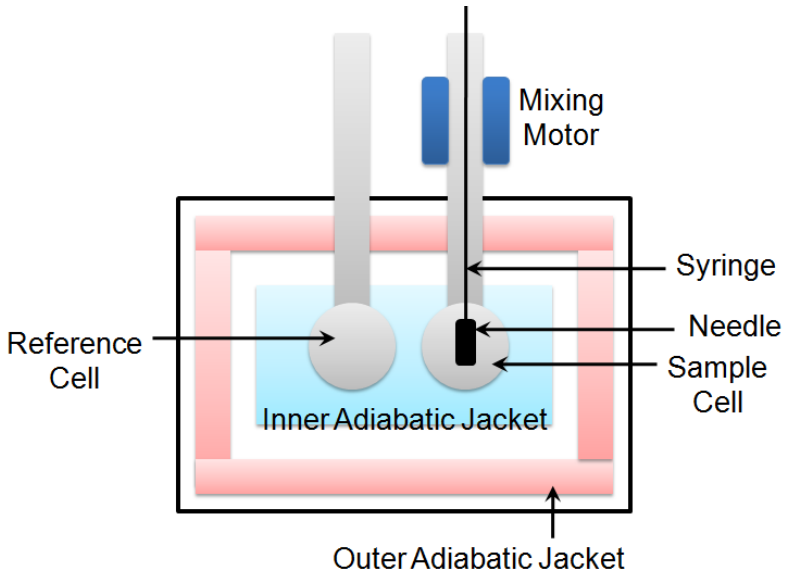

Figure 3.8. *A schematic representation of isothermal titration calorimeter (ITC).*

precipitation in cell and over syringe surface. For certain binding interaction, where the association constant is just equal or below the order of ~10^3, it falls beyond the detection

limit of the instrument. Sometime heterogeneous solvent medium in cell and syringe generates high dilution enthalpy, which interfere with the binding enthalpy of association process. Hence, similar solvent in cell and syringe is preferred in case of ITC.

Figure 3.8 shows a schematic diagram of a commercially available ITC instrument. The calorimeter has two cells; a reference and a sample cell. The reference cell is filled with water (or base solvent). The sample cell contains the macromolecule/host (protein/DNA/RNA) solution, which is titrated stepwise with its binding partner through a computer-controlled injector or syringe. The syringe contains concentrated solution (usually 10 times or higher in concentration than cell solution) small molecule. During the experiment, the reference cell is heated with a small power, which does not increase the temperature of the cell significantly during the measurement. The essence of the measurement is that the temperature of the sample cell is kept the same as that of the reference cell with high accuracy. For this purpose, a variable heating power should be introduced on the sample cell, driven by feedback depending on the studied reaction. In the absence of reaction, the sample cell needs to be heated with a power similar to that of the reference cell. In the case of an endothermic reaction that consumes heat, the sample cell needs to be heated with higher power than the reference. When the reaction is exothermic, less heating power is needed to keep the temperature constant.

During experiment small aliquots of the titrant are injected into the cell at defined time intervals, and the reaction heat is measured. The reaction heat is proportional to the bound fraction of the injected molecules. At the beginning, a larger fraction of ligand is bound, whereas no binding occurs upon injection when the binding sites have become saturated at the end of the titration. During such titration in ITC instrument the liberated heat is measured by the following equation;

$$Q = V_0 \Delta H_b [M]_t K_a [L]/(1 + K_a [L]) \quad \ldots 3.34$$

where, V_0 is the cell volume, ΔH_b is the enthalpy change corresponding to the binding of one mole of ligand, $[M]_t$ is the total macromolecule concentration in the cell, K_a is the association constant, and [L] is the free ligand concentration. In the case of multiple binding sites, the equation is summed up for all binding sites.

The accurate determination of concentration is highly important in ITC. After subtracting the baseline (solvent to solvent dilution enthalpy), the areas under the observed

peaks give the enthalpy changes that belong to the reactions occurring upon injection steps. It is very important that the macromolecule/host and the ligand should have in the same buffer solution at identical pH to avoid a large dilution and ionization enthalpy. To account for such effects, control measurements should be carried out by injecting buffer to buffer, titrant to buffer, and buffer to the protein solution.

3.6. Field Emission Scanning Electron Microscopy (FE-SEM)

In modern era scanning electron microscopy (SEM) is the most powerful tool which offers a direct visual of sample topology and morphology. SEM uses an electron beam focused into a small probe and is scanned across the surface of a specimen. As the excitation electrons penetrate the surface, interactions between the electron and sample result emission of electrons or photons collected by a detector. The most immediate observation in the scanning electron microscope is that it displays the topology of the sample. The resolution limit (arises majorly due to the light diffraction limits) of optical microscope was the basic trigger for electron microscope development. Optical resolution is estimated by $\lambda/2NA$ (where NA is the numerical aperture of lens, usually ~1.0) and mostly depends over the excitation light wavelength. Thus for visible light wave of ~500 nm, the highest achievable resolution is few micrometers (μm). Hence by decreasing the light wavelength the resolution of microscope can be improved, however, very low wavelength (which can give maximum resolution) like UV light is not recommended for biological samples. In contrary SEM uniquely uses the electron wave in imaging. By accelerating the electrons into high energy beam (via high voltage), a far shorter wavelength than visible light can be generated. For example, for an electron beam produced from a 20 kV gun, the wavelength is ~0.6 Å (1240.7/20,000 (eV) = 0.06 nm = 0.6 Å) corresponding to a resolution limit of $\lambda/2$ = 0.3 Å, which can be theoretically used to image a species even small as 0.3 Å, where most atoms are in size of 2-3 Å, and here comes the uniqueness of the electron microscopy technique. The development of SEM instrument of modern age is aided by several longstanding inventions and modifications. The first electromagnetic lens was developed in 1926 by Hans Busch. In 1931 German physicist Ernst Ruska and the electrical engineer Max Knoll constructed the prototype electron microscope, which experimentally demonstrated the principle of electron microscopy for the first time. In 1933, Ernst Ruska built an electron microscope that exceeded the resolution limit attainable with an optical (light) microscope. In 1965 the first commercial scanning electron microscope appeared in market by Cambridge Scientific

Instruments. In 1986 Ernst Ruska received Nobel Prize in Physics for his fundamental work in electron optics, and for the design of the first electron microscope.

Figure 3.9 shows the schematic diagram of a field emission scanning electron microscopy (FE-SEM). The term "field emission" is actually associated with the electron source in the instrument. In a standard electron microscope a tungsten filament is used to generate electron beam by heating up to 2800°C using current source. Instead of heating, in

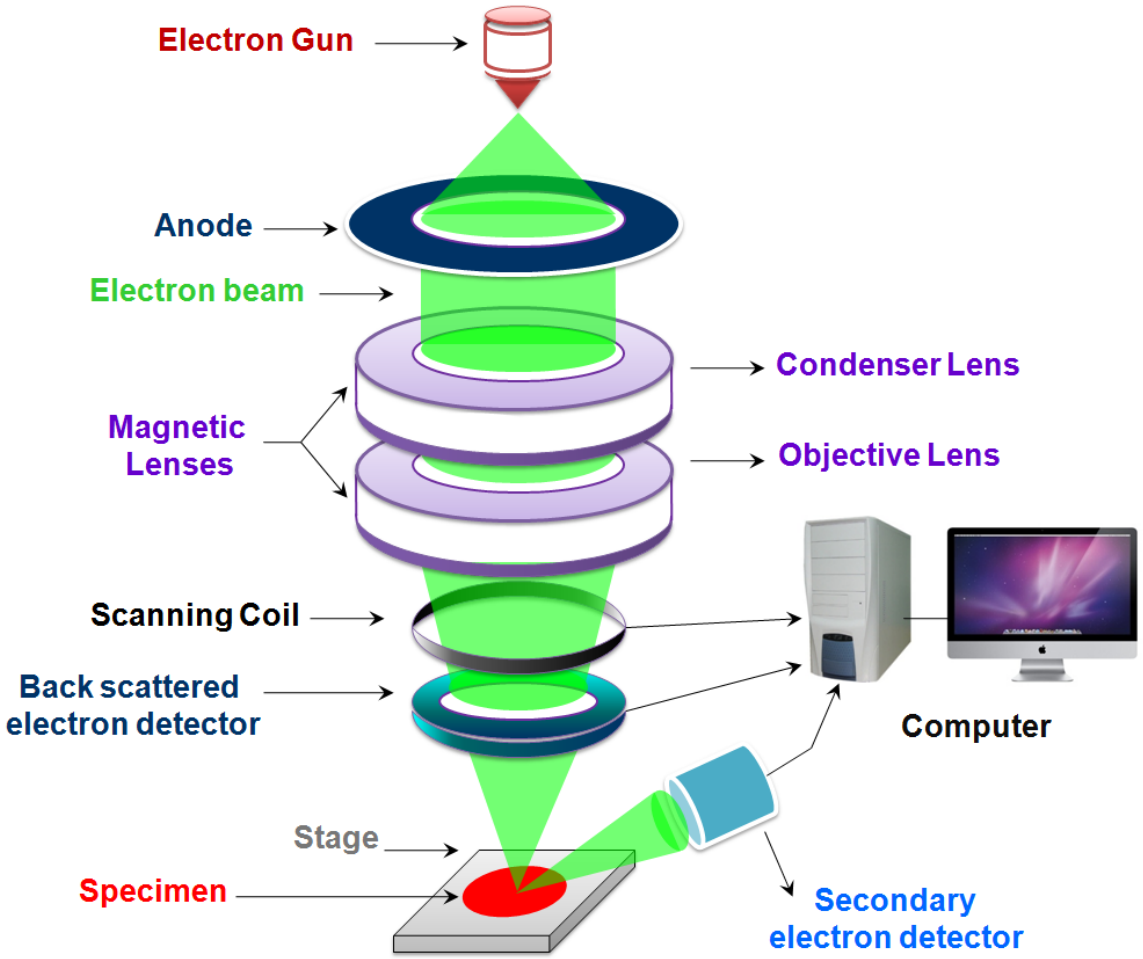

Figure 3.8. *A schematic representation of trivial field emission scanning electron microscope (FE-SEM), where individual parts of the instrument is labeled.*

case of field emission (FE), scanning electron microscope (SEM) a "cold" source is employed in an extreme vacuum (10^{-8} Torr). Here, extremely thin and sharp tungsten needle (tip diameter 10^{-7} to10^{-8} m) functions as a cathode in front of a primary and secondary anode. The potential difference between cathode and anode varies in order of 0.5 to 30 KV. In contrast to

a conventional tungsten filament, theoretically a FE tip can last for lifetime provided the system vacuum is maintained stable so that the tip does not come in contact of air. Sometimes lanthanum hexaboride (LaB_6) crystal is mounted on a tungsten filament, to result a higher electron density in the beam and a better resolution than with the conventional device. The electron beam produced by the FE source is about 1000 times smaller in diameter than in a standard microscope and produces an image markedly better in resolution than normal electron microscope. After the anode a condenser lens is used to focus the electron beam to objective lens (the condenser lens and the objective lens are collectively known as magnetic lenses). The objective lens controls the size of electron beam impinging on sample surface. An electromagnetic coil or scanning coil controls the raster scanning (scanning in rectangular shape) by deflecting the electron beam. A sample stage is used to mount the samples. The specimen mounted on a stage can freely move at all three dimensions, to achieve the maximum possible resolution. When the probe electron beam interacts with the atoms at or close to sample surface, produces signals that contain information about the sample's surface topography and composition. Basically two different kinds of signals are produced by SEM, which are secondary electrons and back-scattered electrons (BSE). Secondary electrons are generated as ionization products and called 'secondary' because they are obtained by other radiation (the primary/probe electron beam). Secondary electrons can be in form of ions, electrons, or photons with sufficiently high energy. The secondary electron detectors are common in all SEMs. A SEM with secondary electron imaging or SEI can produce very high-resolution images of a sample surface, revealing details less than 1 nm in size. Back-scattered electrons (BSE) are the reflected beam of electrons, which are reflected from the sample by elastic scattering. BSE are often used in analytical SEM and this process of analysis is known as energy dispersive spectroscopy or in short EDS. As the intensity of the BSE signal is strongly related to the atomic number (Z) of the specimen, it provides information about the distribution of different elements in the sample.

We have collected the SEM images for serum protein (BSA and HSA), DNA (CT-DNA and SS-DNA) and protein-DNA complex using ZEISS Ultra plus FE-SEM (U.S.A.) instrument, where a ultra high stable beam current up to 100 nA and sub-nm resolution produced by a 15 kV electron gun shots has been used to collect the data.

3.7. Reference

1. Bauman, R.P. Absorption spectroscopy (Wiley, 1962).
2. Sathyanarayana, D.N. Electronic absorption spectroscopy and related techniques (Universities Press, 2001).
3. Lakowicz, J.R. Principles of fluorescence spectroscopy (Springer Verlay, 2007).
4. Valeur, B. Molecular fluorescence: principles and applications (Wiley-VCH, 2002).
5. Healy, E.F. Quantitative determination of DNA–ligand binding using fluorescence spectroscopy. *J. Chem. Educ.* **84**, 1304 (2007).
6. Silverstein, T.P. Quantitative determination of DNA–ligand binding: Improved data analysis. *J. Chem. Educ.* **85**, 1192 (2008).
7. Benesi, H.A. & Hildebrand, J.H. A spectrophotometric investigation of the interaction of iodine with aromatic hydrocarbons. *J. Am. Chem. Soc.* **71**, 2703-2707 (1949).
8. Nigam, S. & Durocher, G. Spectral and photophysical studies of inclusion complexes of some neutral 3H-indoles and their cations and anions with β-cyclodextrin. *J. Phys. Chem.* **100**, 7135-7142 (1996).
9. D. V. O'Conor & Philips, D. Time correlated single photon counting (Academic Press, New York, 1984).
10. Fleming, G.R. Chemical applications of ultrafast spectroscopy (Oxford University Press, New York, 1986).
11. (*http://www.horiba.com/scientific/products/fluorescence-spectroscopy/application-notes/quantum-yields/*, 2014).
12. Eisenthal, K.B. Liquid interfaces. *Acc. Chem. Res.* **26**, 636-643 (1993).
13. Thomas, J.K. Physical aspects of photochemistry and radiation chemistry of molecules adsorbed on silica, .gamma.-alumina, zeolites, and clays. *Chem. Rev.* **93**, 301-320 (1993).
14. Maroncelli, M. & Fleming, G.R. Picosecond solvation dynamics of coumarin 153: The importance of molecular aspects of solvation. *J. Chem. Phys.* **86**, 6221-6239 (1987).
15. Nina Berova, Koji Nakanishi & Woody, R. Circular dichroism: Principles and applications (John Wiley & Sons, 2000).
16. Rodgers, D.S. Circular dichroism: Theory and spectroscopy (Nova Science Publishers, 2012).
17. Bengt Nordén, Alison Rodger & Dafforn, T. Linear dichroism and circular dichroism: A textbook on polarized-light spectroscopy (Royal Society of Chemistry, 2010).
18. Frederic P. Miller, Agnes F. Vandome & Joh, M. Isothermal titration calorimetry (VDM Publishing, 2010).

End of Chapter 3

Chapter 4

Modulation of Flavin Adenine Dinucleotide (FAD) Dynamics and Selective Detection of Flavins

4

4.1. Introduction

Since earth being blessed with sunlight, living organisms are utilizing light energy through various oxidation-reduction reactions, ubiquitously controlled by flavoproteins. Flavins (riboflavin [RF] or vitamine B_2, flavin mononucleotide [FMN], flavin adenine dinucleotide [FAD]) are the cofactors in flavoproteins, and act as a versatile electron shuffling agents for a wide variety of nature mediated redox reactions.[1-4] A huge assortment of FAD and FMN containing photoreceptors like *DNA-photolyase* [1, 4, 5], *BLUF* protein [4, 6, 7], *Phototropin* [1, 4, 8], and *Cryptocrome* [4, 5, 9, 10] are well known due to their photo-induced electron and proton (in *BLUF protein*) shuffling activities. Close structural inspection of flavins indicates that an isoalloxazine ring (flavin) (**Scheme 4.1**) is common for all these flavocofactors and responsible for fluorescence from flavins and its derivatives. Moreover, the flavin moiety

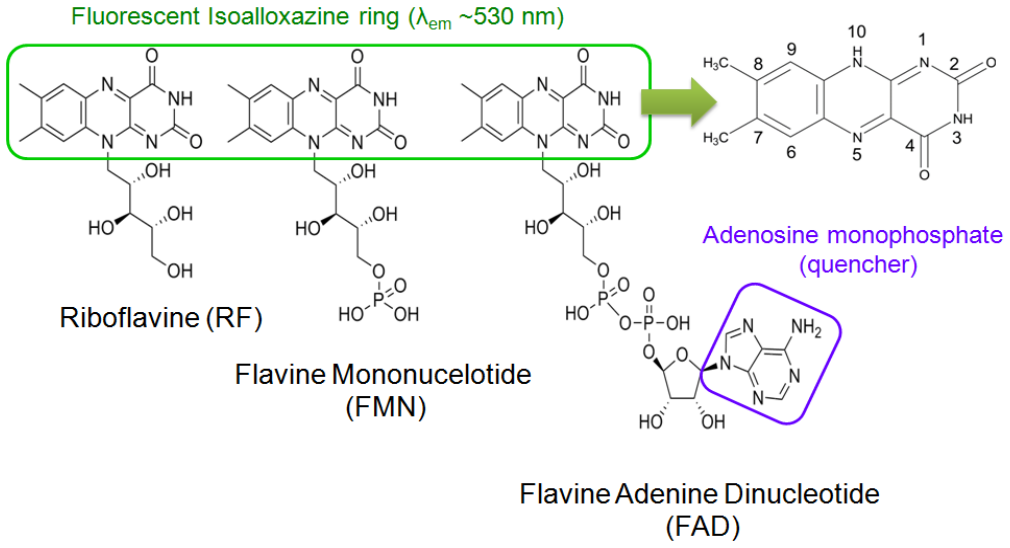

Scheme 4.1. *Molecular structure of riboflavin (RF), flavin mononucleotide (FMN) and flavin adenine dinucleotide (FAD).*

controls electron and photon transfer activities in these flavoproteins. Among flavins, only FAD has conformational flexibility due to the existence of a quencher moiety (adenine) along with the fluorescent isoalloxazine (or flavin) ring. Depending over the proximity of the two moieties FAD exists in different forms like 'stack' (close) and 'unstack' (open or extended) along with few other intermediate conformers, known as 'partially stack'. The 'stack' conformer is believed to be stabilized through the π-π interaction between the flavin and adenine ring.[10, 11] Due to photo-induced intra-molecular electron transfer from flavin to adenine ring, the stack conformer is almost non-fluorescent and exhibits a short lifetime of ~10 ps.[11-13] On the other hand unstack conformer is fluorescent showing reasonably long lifetime of ~4 ns.[14, 15] In pH 7, FAD mainly exists in stack conformer, and exhibits a very low

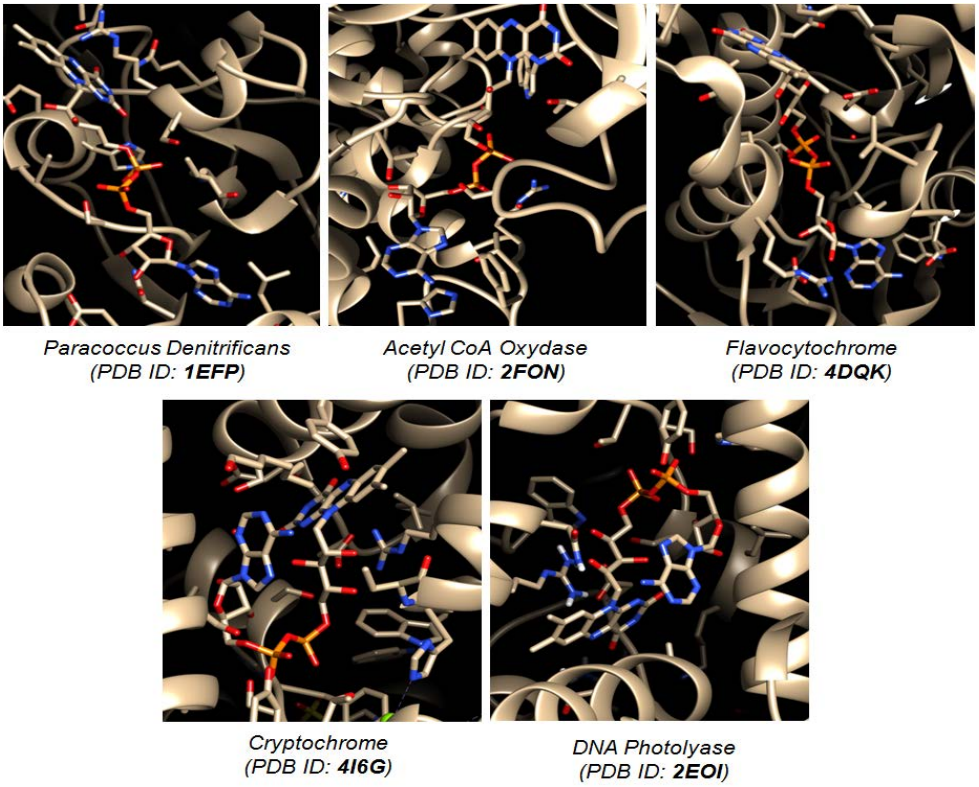

Scheme 4.2. *FAD in unstack and stack form inside different flavoprotein.*

fluorescence quantum yield (~0.03).[14, 15] Interestingly, the conformational flexibility of FAD not only restricted in solution, but also exists inside the several flavoproteins. A number of flavoproteins (**Scheme 4.2**) are known, where FAD exists in unstack or open form (e.g. *Paracoccus Denitrificans*[16], *Acetyl CoA Oxidase*[17], *Flavocytochrome*[18]), whereas in many others (e.g. *Cryptochrome*[19], *DNA Photolyase*[20]) FAD resides in folded or U form. Depending

over the orientation and the several flavoproteins behave drastically different from each other. Hence, the folding unfolding dynamics of FAD is the incessant point of interest. Present chapter describes the impact of several external stimuli (like pH, denaturant, nano-confinement of protein binding pocket and binding interaction with RNA aptamer) over the folding-unfolding dynamics of FAD.

4a. pH Dependent Dynamics of Flavin Mononucleotide (FMN) and Flavin Adenine Dinucleotide (FAD): a Femtosecond to Nanosecond Study

4a.1. Motivation

Till date several spectroscopic techniques have been applied to explore the 'stack-unstack' behavior of FAD[11-15, 21-26] and its observed that pH dependent fluorescence behaviors of flavins are very interesting.[15, 23] It was detected that fluorescence mainly appears from the neutral form, whereas cationic form is practically non-fluorescent and the anionic form is weakly fluorescent.[15, 23] Drössler and Islam and *et al.* investigated pH dependence behavior of riboflavin, FMN and FAD in detail.[15, 23] They observed the quantum yield of FAD is maximum around pH = 2.5 and then it decreases sharply until pH = 5[15]. Quantum yield almost remains same from pH = 5 to pH = 9. Afterward it starts decreasing and reaches almost zero at pH ~13[15]. However, the quantum yield of riboflavin and FMN is maximum around pH = 4 and remains almost constant from pH = 4 to pH = 8[23]. The results were explained in terms of two different conformations of FAD. In the pH range pH ~ 3.5 to pH ~ 11, stack (closed) conformer of FAD dominates over unstack (open) conformer, whereas at higher and lower pH unstack conformer dominates over stack conformer[15]. Although, they measured lifetime of FAD in all pH ranges with a time resolution of ~400 ps, but they were unable to monitor stack conformer due to short lifetime of stack conformer. Until now, large numbers of spectroscopic techniques have been used to explore the excited state photochemistry of FAD, but there are few studies in very fast time scale (femtosecond to picosecond time resolution).[11, 13, 24, 27] First time, van den Berg *et al.* have monitored the dynamics of FAD with the help of TCSPC technique with an instrument response of 40 ps.[24] They observed that in neutral pH (pH = 7.5) fluorescence intensity decay of FAD mainly contributed by two components: a dominant 7 ps component contribution that is characteristic of ultrafast fluorescence quenching due to electron transfer from adenine moiety to flavin and a 2.7 ns contribution resulting from moderate quenching[24]. Their molecular dynamics study also concludes the same lifetime with an affirmation about the co-planner stacking between adenine moiety and flavin.[24] As the lifetime of 7 ps is close to the detection limit, the fluorescence upconversion technique has been used to examine the picosecond decay kinetics of FAD.[12, 13] It has been observed that stack conformer has a quenched lifetime of around 5-9

ps and this can be attributed to a very efficient quenching route via electron transfer from adenine to light excited flavin.[13, 27] Transient absorption studies also provide conclusive evidence that the excited state quenching observed in FAD occurs in less than 5 ps time scale.[11] Fluorescence decay dynamics of FAD in a mixture of alcohol and water has been studied in the femtosecond to nanosecond time range and it has been observed that population of open conformation increases with the decrease in dielectric constant of the medium.[25]

Albeit most of the studies have been focused on the dynamic behavior of FAD,[11, 12, 24, 25] a very few studies have been devoted to pH dependence dynamic behavior of FAD in femtosecond to nanosecond time scale. Previously Li *et al.* from their transient absorption study inferred that at low and high pH, FAD adopts an unstack conformation and behaves same as that of FMN.[26] They also suggested conformational changes of FAD at pH ~3 (because of adenine protonation) and pH ~ 10 (because of flavin deprotonation) from their transient absorption results.[26] Moreover, they observed a dynamics of ~20 ps in neutral pH range, responsible for the stacking interaction between flavin (or isoalloxazine ring) and adenine moiety of FAD.[26] In this work, we intend to explore the dynamics of stacking interaction of FAD with the help of state-of-arts fluorescence spectroscopic techniques, e.g. fluorescence up-conversion and time correlated single photon counting (TCSPC), in five decades of time span from ~300 fs to ~10 ns throughout the pH range of pH = 0.5 to pH = 13.0. To the best of my knowledge, this work is the first fluorescence up-conversion and ultra-fast anisotropy study on the pH dependence dynamic behaviors of FAD and FMN.

4a.2. Results and Discussions

4a.2a. Absorption and Fluorescence Characteristics of FMN and FAD

Absorption spectral features of FMN and FAD at different pH are same as reported by others.[15, 26] Characteristic absorption spectra for both FMN and FAD are similar and consist of two peaks, one peak is at ~375 nm, and another is at ~ 448 nm. The peak at ~375 nm corresponds to $S_0 \rightarrow S_2$ transition, whereas the later peak corresponds to $S_0 \rightarrow S_1$ transition.

The emission spectral features of both FMN and FAD are same as reported in literature.[15, 26] Their fluorescence quantum yield behaviors at various pH are shown in **Figure4a** and reflects almost similar trend as published in literature.[15] The quantum yield of both FMN and FAD is almost zero at very low pH (pH = 0.5). After that it increases with the increase in pH and FAD exhibits maximum quantum yield ($\Phi_{FAD} \approx 0.13$) at pH = 3. Then,

fluorescence quantum yield of FAD drops down sharply. At biological pH, the quantum yield of FAD is ~0.035. For FMN, the quantum yield increases with the increase in pH until pH = 4, remains almost constant from pH = 4 to pH = 10 and then sharply decreases above pH = 10. In this context, it should be mentioned that flavin in oxidized redox state is non-fluorescent in the cationic form (FLH^+), weakly fluorescent in anionic form (FL^-) and is fluorescent in neutral form.[23] In the lower pH range (pH = 0.5 to pH = 1), there is a reasonable amount of FLH^+ as pK_a of N1 protonation of flavin (**Scheme 4.1**) is 0.5[23], and this explains the observed low fluorescence quantum yield in this pH range. The calculations of ground and excited state π electron densities suggest that protonation site of flavin ring in the ground state is at N1 position, whereas in the excited state it is at N5 position[28] (**Scheme 4.1**). Moreover, it was previously observed that acidity constant of the flavin derivatives in the excited state is ~ 2.5.[23] This suggests that excited state protonation at N5 position of neutral flavin ring is the likely reason for relatively low fluorescence quantum yield of FMN and FAD in the range of pH = 1 to pH ≤ 2.5. The difference in fluorescence quantum yield between FMN and FAD in the pH range of 3 to 10 arises due to the existence of adenine

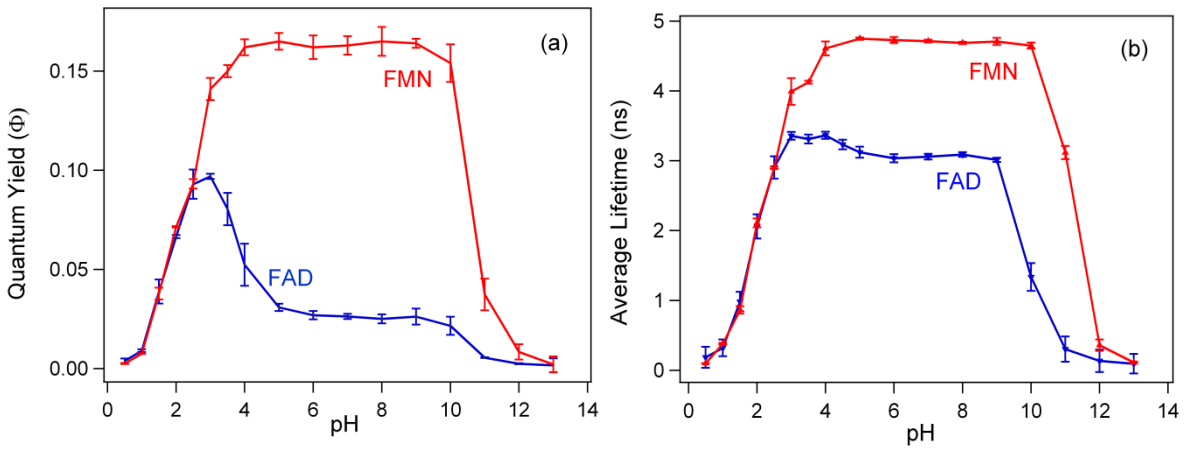

Figure 4a.1. *(a) Relative quantum yield of FAD and FMN at various pH. (b) Average lifetime of FAD and FMN at various pH. Error bars are indicated.*

moiety in FAD, which is absent in case of FMN. Adenine moiety favors the formation of stack conformer of FAD in which flavin moiety forms intramolecular complex with adenine moiety and this intramolecular complex is almost non-fluorescent due to excited state electron transfer between adenine and flavin moiety of FAD.[11-13, 24-26] Presence of this stack conformer reduces the quantum yield of FAD compared to FMN in the above mentioned pH

range. Above pH = 10, deprotonation of N3 nitrogen (**Scheme 4.1**) in flavin ring (the reported pK_a of this process is 9.75[26]) lowers the quantum yield of both FMN and FAD. Although the fluorescence quantum yield behavior predicts the existence of stack conformer in FAD, it can't give detail understandings of the stack and unstack behavior unless we monitor the dynamics of these conformers. To get insight about the dynamics, we have carried out fluorescence lifetime measurements in whole pH range of pH = 0.5 to pH = 13.

4a.2b. Time Resolved Fluorescence of FMN and FAD Measured by TCSPC Set-up

The excited state fluorescence lifetime of FAD and FMN are measured in the whole pH range with the help of TCSPC set-up with a time resolution of ~40 ps. Lifetime data is analyzed by deconvolution method using minimum number of exponentials. The characteristics of fluorescence lifetime of FAD and FMN are tabulated in **Table 4a.1** and **Table 4a.2,**

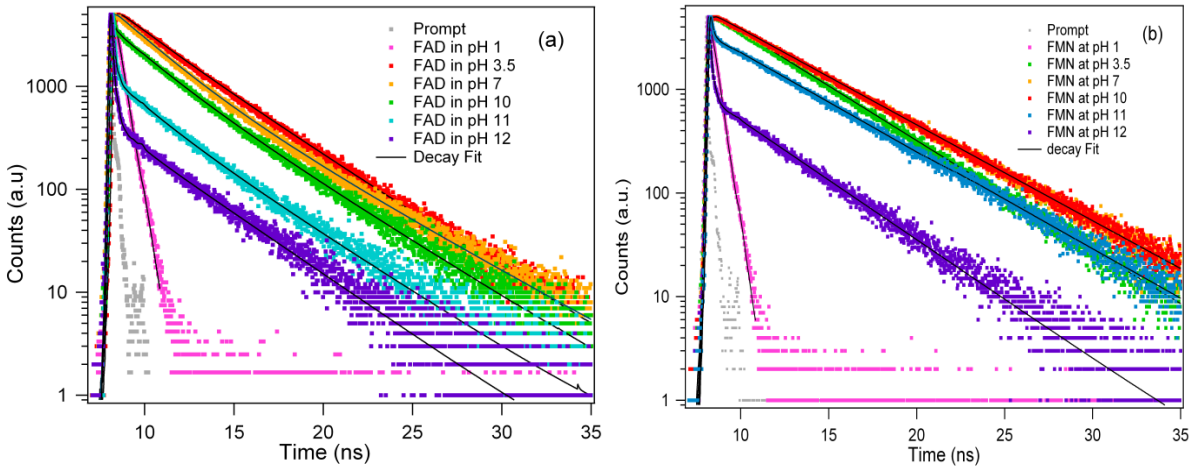

Figure 4a.2. *TCSPC fluorescence decays of FAD and FMN at different pH monitored at 535 nm. (a) and (b) represent FAD and FMN, respectively. The solid gray lines denote the line of best fit.*

respectively. The representative decay profiles of FAD and FMN at different pH are shown in **Figure.4a.2**. Inspection of the results indicate that FAD decay exhibits single exponential feature from pH = 0.5 to pH = 2.5 with the increase in lifetime from 0.18 ns to 2.76 ns. The lower value of lifetime in this pH range may be due to excited state protonation of flavin moiety of FAD or due to dynamic quenching of flavin by adenine moiety. To confirm that we have also measured lifetime of FMN in the above mentioned pH range. However, we found that the equal extent of quenching in FMN lifetime, which is void of adenine moiety.

Therefore, we can rule out the possibility of dynamic quenching for the quenched lifetime of FAD in this pH range. Moreover, acidity constant of flavin in the excited state is pK_a^* ~ 2.5.[23] Thus, the excited state protonation of flavin ring as the prime reason for the quenched lifetime of FMN and FAD in this pH range.

FAD decays exhibit bi-exponential feature from pH = 3 to pH = 9. One component has a lifetime of ~2.2 ns and another component has a lifetime between ~3.5 ns to ~4.0 ns (**Table 4a.1**). The slow component may represent the lifetime of unstack conformer of FAD, as it is reported that free flavin has a lifetime of 4.7 ns.[23] For affirmation, we have also collected the lifetime of FMN in the same pH range and we have observed that all these decays consist of single component having lifetime between 4.1 ns to 4.7 ns (**Table 4a.2**).

Table 4a.1. *Fluorescence Lifetime Parameters of FAD at different pH measured at 535 nm in TCSPC set-up.*

Sample Name	τ_1 (ns)	τ_2 (ns)	τ_3 (ns)	a_1	a_2	a_3	τ_{av} (ns)	χ^2
FAD at pH 0.5	0.18	-	-	1	-	-	0.18	1.17
FAD at pH 1.0	0.38	-	-	1	-	-	0.38	1.15
FAD at pH 1.5	0.77	-	-	1	-	-	0.77	0.82
FAD at pH 2.0	1.85	-	-	1	-	-	1.85	0.98
FAD at pH 2.5	2.76	-	-	1	-	-	2.76	1.06
FAD at pH 3.0	3.52	2.11	-	0.89	0.11	-	3.32	1.07
FAD at pH 3.5	3.74	2.16	-	0.78	0.22	-	3.39	1.05
FAD at pH 4.0	3.92	2.25	-	0.67	0.33	-	3.36	0.92
FAD at pH 4.5	4.08	2.22	-	0.54	0.46	-	3.22	0.96
FAD at pH 5.0	4.31	2.24	-	0.43	0.57	-	3.12	1.08
FAD at pH 6.0	4.42	2.27	-	0.37	0.63	-	3.06	1.07
FAD at pH 7.0	4.44	2.27	-	0.36	0.64	-	3.06	0.96
FAD at pH 8.0	4.46	2.27	-	0.36	0.64	-	3.06	1.01
FAD at pH 9.0	4.39	2.28	-	0.37	0.63	-	3.06	1.08
FAD at pH 10.0	4.44	2.28	0.10	0.19	0.28	0.54	1.50	0.97
FAD at pH 11.0	3.60	-	0.08	0.06	-	0.94	0.30	0.99
FAD at pH 12.0	3.52	-	0.08	0.02	-	0.98	0.15	1.07
FAD at pH 13.0	-	-	0.08	-	-	1.00	0.08	1.08

This confirms that slow component is responsible for the lifetime of unstack conformer of FAD. The slight difference in lifetime between the FMN and unstack conformer of FAD might arise due to presence of extra phosphate group and adenine moiety in FAD, which slightly modifies the excited state character of FAD. The observed ~2.2 ns component might

reflect the presence of stack conformer of FAD, as FMN is devoid of ~2.2 ns component. However, stack conformer has a quenched lifetime of 5-9 ps due to the excited state

Table 4a.2. *Fluorescence Lifetime Parameters of FMN at different pH measured at 535 nm in TCSPC set-up.*

Sample Name	τ_1 (ns)	τ_2 (ns)	a_1	a_2	τ_{av} (ns)	χ^2
FMN at pH 0.50	0.10	-	1	-	0.10	1.10
FMN at pH 1.0	0.34	-	1	-	0.34	0.85
FMN at pH 1.5	0.88	-	1	-	0.88	0.89
FMN at pH 2.0	2.00	-	1	-	2.00	1.10
FMN at pH 2.5	2.93	-	1	-	2.93	0.99
FMN at pH 3.0	4.14	-	1	-	4.14	0.98
FMN at pH 3.5	4.14	-	1	-	4.14	1.03
FMN at pH 4.0	4.68	-	1	-	4.68	0.97
FMN at pH 5.0	4.76	-	1	-	4.76	0.99
FMN at pH 6.0	4.70	-	1	-	4.70	0.97
FMN at pH 7.0	4.70	-	1	-	4.70	0.99
FMN at pH 8.0	4.68	-	1	-	4.68	1.05
FMN at pH 9.0	4.71	-	1	-	4.71	1.03
FMN at pH 10.0	4.62	-	1	-	4.62	1.07
FMN at pH 11.0	4.51	0.107	0.32	0.68	1.51	0.96
FMN at pH 12.0	3.77	0.093	0.06	0.94	0.31	1.04
FMN at pH 13.0	1.70	0.093	0.02	0.98	0.13	0.96

intramolecular electron transfer from adenine to flavin moiety.[11-13, 24-26] Thus, the ~2.2 ns component is not responsible for the stack conformer of FAD, instead, it represents lifetime of a new conformer of FAD in which flavin does not stack but interacts with the other parts of the molecule, resulting in less efficient quenching (hereafter we will call this conformer as 'partially stack' conformer of FAD).

FAD decay exhibits tri-exponential feature at pH = 10 (**Table 4a.1**). Here, in addition to the above mentioned components, a third component with a lifetime of ~90 ps arises. As the pK_a value for the deprotonation of N3 nitrogen (**Scheme 4.1**) of the flavin ring is ~9.75[26], we believe that this ~90 ps component is the lifetime of deprotonated FAD. Islam *et al*. also pointed out that presence of ~100 ps component from the simulation of their observed data.[15] The percentage of this ~90 ps component increases with the increase in pH, and at pH = 12 the contribution of this component reaches 100% (**Table 4a.1**). For FMN (**Table 4a.2**), this ~90 ps component starts appearing from slightly higher pH (pH > 10) compared to FAD. This

suggests that pK_a value for the deprotonation of N3 nitrogen of the flavin ring of FMN is slightly higher compared to FAD. This is reasonable as the electron density of flavin in FAD is less compared to FMN, because of the presence of one more phosphate group in FAD, which draws more electron cloud from the flavin moiety. Around pH ≥ 11, almost all the FAD molecules are deprotonated (**Table 4a.1**). Hence, there is less possibility of existence of stack conformer due to electrostatic repulsion between the negatively charged flavin ring and phosphate groups of FAD. Moreover, deprotonated flavin can be solvated better than the neutral flavin ring and the solvents around the flavin ring may prevent stacking interaction between flavin ring and adenine moiety. We have also plotted average lifetime of FMN and FAD against pH as some of the decays are non-exponential in nature (**Figure 4a.1**). Interestingly, average lifetime plot of FAD deviates significantly from fluorescence quantum yield plot (**Figure 4a.1**), particularly from pH = 3 to pH = 10. In contrast, features of the quantum yield and average lifetime plots of FMN almost remain same (**Figure 4a.1**). This is because quantum yield (or fluorescence intensity) reflects average fluorescence property of all types of conformers of FAD (stack, unstack, partially stack conformers) present in the solution, whereas lifetime data measured by TCSPC are not able to detect stack conformer due to short lifetime (~9 ps) of stack conformer of FAD. Thus, the mismatch of the features between average lifetime and quantum yield plots of FAD give an indirect hint for the existence of stack conformer of FAD, which could not be detected by our TCSPC set-up.

4a.2c. Time Resolved Fluorescence Features of FMN and FAD Measured by Femtosecond Up-conversion Set-up

In order to probe the dynamics of stack conformer, we have measured the lifetime of FAD using femtosecond fluorescence up-conversion set-up with a time resolution of ~300 fs. The representative femtosecond fluorescence transients are shown in **Figure 4a.3** and the results are tabulated in **Table 4a.3**. Unless noted otherwise, during the analysis of decay profiles the long component (detected by TCSPC set-up) is kept fixed. It was noticed that at pH = 2, the decay profile of FAD consist of ~1 ps component with a relative contribution of 14% and the remaining decay is contributed by a long component (~2 ns), which is measured by TCSPC set-up. The ~1 ps dynamics reflects the relaxation of flavin moiety of FAD, where solvation dynamics is not yet completed. This ~1 ps dynamics is also reported by other groups and they also have concluded that it is connected to water relaxation around flavin.[12,]

[25] The decay profile of FAD at pH = 2 lacks of ~10 ps component, which is lifetime of stack conformer of FAD.[11, 12, 25] This suggests that the stack conformer doesn't exist at pH = 2. ~10 ps component starts appearing around pH = 3.0 with a relative contribution of 12%, along with the ~1 ps component (with a relative contribution of 26%) and a long component of ~3.0 ns (with a relative contribution of 62%). At pH = 3.0, the relative contribution of long component (contributed by unstack or partially stack conformer of FAD) is more compared

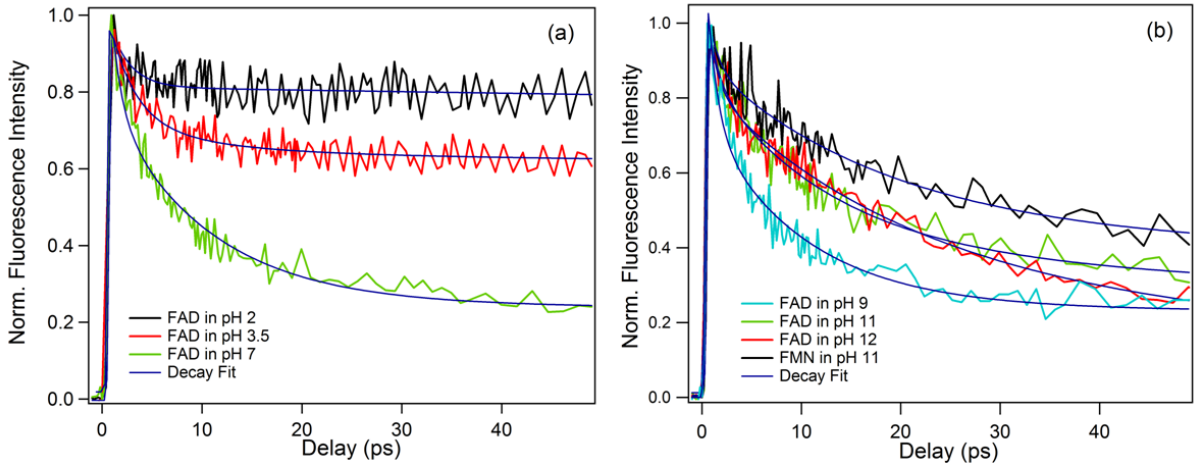

Figure 4a.3. *Femtosecond fluorescence decays of FAD and FMN at different pH monitored at 535 nm. (a) Represents decay profiles of FAD at pH = 2, pH = 3.5 and pH = 7.0, respectively. (b) Represents decay profiles of FAD at pH = 9.0, pH = 11.0 and pH = 12.0, respectively. Grey color line in (b) represents decay profile of FMN at pH = 11.0. The solid blue lines denote the line of best fit.*

to stack component. Hence, FAD exhibits higher quantum yield at pH = 3.0. At pH = 5, the relative contribution of this ~10 ps component is 44%; at biological pH = 7, the same has a contribution of 45%; at pH = 9, it has a contribution of almost 48% of the total decay. This indicates that the relative contribution of the stack conformer remains almost constant in the pH range from pH = 5 to pH = 9. This is consistent with the quantum yield results, where we also found that quantum yield remains unaltered in the pH range of pH = 5 to pH = 9 (**Figure 4a.1**). Moreover, in the pH range pH > 3 to pH = 9, the relative contribution of long component is less compared to stack component. Therefore, FAD exhibits lower quantum yield in this pH range (see **Figure.4a.1**). After pH ≥ 11, the flavin ring of FAD contains negative charge as the pK_a value for the deprotonation of N3 nitrogen of the flavin ring is 9.75[26]. So, one could expect that decay profile of FAD should be devoid of ~10 ps component, due to electrostatic repulsion between negatively charged flavin and phosphate

group. Although, we have noticed that ~10 ps dynamics is absent in the decay profile of FAD at pH = 11, but a new dynamics of ~20 ps appears with a relative contribution of 47%. To understand this dynamics, we have also collected the decay profile of FMN at same pH (**Figure.4a.3**) and we have observed that the decay profile of FMN also consists of ~26 ps component with a relative contribution of 52%. Moreover, this newly observed dynamics exists in the decay profiles of FMN and FAD at pH = 12 along with the other component(s). The origin of this dynamics is not fully understood. However, it was reported that fluorescence behavior of anionic flavin at high pH is determined by the intramolecular

Table 4a.3. *Fitting parameters of femtosecond fluorescence decays of FAD and FMN at different pH monitored at 535 nm.*

Name of the sample	τ_1 (ps)	a_1 (%)	τ_2 (ps)	a_2 (%)	τ_3[a] (ps)	a_3 (%)
FAD at pH = 2.0	1(±0.2)	14(±2)	-	-	1850	86(±4)
FAD at pH = 3.0	1(±0.2)	26(±2)	10(±1)	12(±2)	3320	62(±4)
FAD at pH = 5.0	1(±0.2)	35(±2)	10(±1)	44(±3)	3120	21(±2)
FAD at pH = 7.0	1(±0.2)	31(±2)	10(±1)	45(±2)	3000	24(±2)
FAD at pH = 9.0	1(±0.2)	27(±2)	10(±1)	48(±3)	3000	25(±2)
FAD at pH = 11.0	1.2(±0.2)	25(±2)	20(±2)	47(±3)	300	28(±2)
FAD at pH = 12.0	1.2(±0.2)	24(±2)	22(±2)	55(±3)	150	21(±2)
FMN at pH = 11.0	1.2(±0.2)	28(±2)	26(±2)	52(±3)	1510	20(±2)
FMN at pH = 12.0	1.2(±0.2)	24(±2)	29(±2)	52(±2)	310	22(±2)

[a] *Long lifetimes were taken from TCSPC measurement and it was fixed during analysis.*

electron transfer (negative charge movement either from N3 to O2 or from N3 to O4) from locally excited (LE) to charge transfer state (CT)[29]. The very less fluorescence quantum yield and moderate fluorescence lifetime (~90 ps) supports this hypothesis. Hence, we anticipate the observed ~20 ps dynamics might reflect the lifetime of CT state of anionic flavin moiety of FMN/FAD, whereas ~90 ps component indicates the lifetime of LE state of anionic flavin moiety of FMN and FAD.

4a.2d. Time-Resolved Fluorescence Anisotropy Features of FMN and FAD Measured by TCSPC Set-up

A very detail description of time resolved anisotropy is given in the experimental section and the results are shown in **Figure 4a.4**. From the anisotropy decay profiles, we have determined rotational relaxation time (τ_r) of FAD throughout the pH range pH = 1 to pH = 12 and the plot of rotational relaxation time (τ_r) against pH is shown in **Figure.4a.4** The plot indicates that there is a sudden jump of rotational correlation time of FAD around pH = 3 and just after pH = 10. All the solutions are homogeneous in nature and lack of any rigid environment. Therefore, observed changes in the rotational correlation time of FAD is most likely due to the conformational changes of FAD around above mentioned pH.

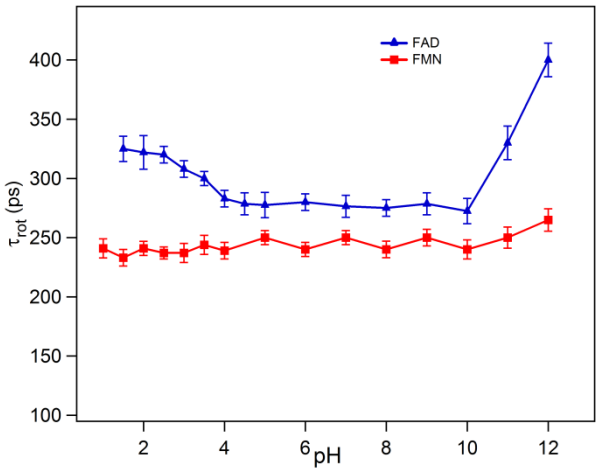

Figure 4a.4. *Rotational correlation time (measured in TCSPC set-up) of FAD and FMN at various pH monitored at 535 nm. Error bars are indicated.*

One obvious question may arise that the change of viscosity of the medium may also responsible for the observed change in anisotropy. To verify that we have also collected anisotropy decays of FMN in the whole pH range (**Figure.4a.4**). However, we have noticed that rotational correlation time of FMN is almost unchanged throughout the pH range from pH = 1 to pH = 10, but spanned in different time region. After pH = 10, there is slight increase in rotational correlation time of FMN up to pH = 12. This slight increase in the rotational correlation time of FMN after pH > 10 might arise due to the fact that in this pH range we have used dilute NaOH solution, which slightly increases the viscosity of the medium. However, in case of FAD, there is steady and sharp increase in the rotational

correlation time after pH = 10. Therefore, we believe that the change of rotational dynamics of FAD after pH = 10 is due to conformational change of FAD rather than viscosity change of the medium. Our anisotropy results nicely reconcile the earlier transient absorption results, which nicely explained the conformation change of FAD at pH ~ 3 and pH ~ 10.[26] Another important feature observed from our anisotropy study is that in both acidic and basic pH regions rotational relaxation time of FAD increases, which is attributable to unstack conformer of FAD that rotates at slower rate than the stack conformer. This is because unstack conformer occupies larger van der Waals volume compared to stack conformer.

4a.2e. Conformational Dynamics of FAD

FAD has pH dependent conformational flexibility. At lower pH range (pH < 3), excited state protonation of N5 nitrogen of flavin ring prevents intramolecular π complex formation between flavin and adenine moiety. Moreover, deprotonation pK_a adenine moiety is ~3.5[30] and the protonated adenine cannot participate in π complex formation with flavin moiety.

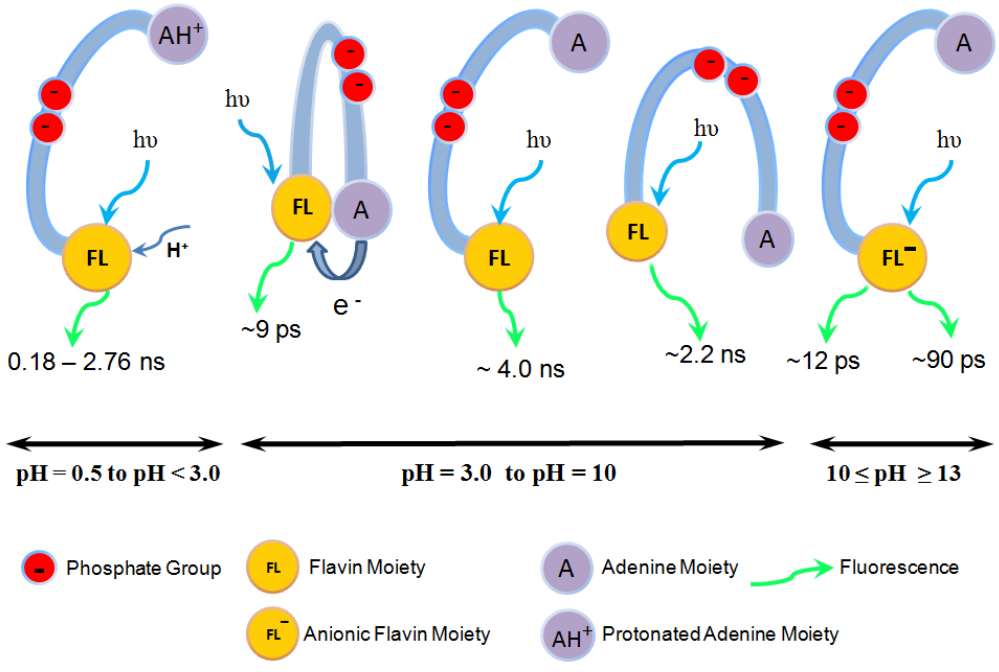

Scheme 4a.2. *Schematic representation for various structures and dynamics of FAD at different pH.*

This is supported by our femtosecond results, which indicate that stack conformer of FAD starts appearing around pH ~ 3. Moreover, there is a change of rotational dynamics of FAD

around this pH. Therefore, we conclude that a deprotonation of adenine moiety induces conformational change of FAD around this pH. From pH = 3 onwards, we have observed that FAD exist in three distinct conformations: one is stack conformer, another is unstack conformer, third one is the partially stack conformer, in which flavin ring does not stack but interacts with the other parts of the molecule. After pH = 10, introduction of negative charge in flavin induces the conformational change from stack to unstack as phosphate group and negatively charged flavin moiety repels each other. As a result, stack to unstack transition takes place just after pH = 10. All the structure and dynamics related to conformational flexibility of FAD is shown in **Scheme 4a.2**. Molecular dynamics simulation studies have been used to study the conformational dynamics of FAD.[24] The simulation studies confirmed the transition from unstack to stack conformer in which flavin and adenine ring stack coplanarly.[24] Simulations also characterized many intermediates in going from unstack to stack conformer and some of the conformations are long lived.[24] We believe that partially stack conformer of FAD is one of the long lived intermediate during transition from unstack to stack conformer.

The relative contribution of stack conformer of FAD dominates over other two conformers of FAD in a wide range of pH (from pH = 5 to pH ~ 10). This means that stack conformer gains extra stability compared to unstack conformer and this stabilization energy comes from the π-π interaction between flavin and adenine moiety of FAD. That's why FAD adopts stack conformer in many flavoproteins.[31, 32] However, FAD also pursue unstack conformer in many flavoproteins in spite of the stability of stack conformer compared to unstack conformer.[16, 33-35] This is probably due to the fact that if they would have been exist in stack conformation, then surrounding amino acid would have not been able to take part in electron transfer reaction (as adenine and flavin moiety already involved in electron transfer reaction in stack conformation), which is the key step for functioning of flavoproteins. This indicates that function of FAD in flavoproteins depends on its structure. But little insight has been given on the structure function relationship of FAD. We hope that the observed distinct dynamics controlled by the flavin ring flexibility as well as oxidation state of flavin, will help to elucidate the structure function relationship of FAD in various biological systems.

4a.3. Conclusion

pH dependent conformational dynamics of FAD is extensively monitored with the help of time resolved fluorescence techniques from femtosecond to nanosecond time scale. We have

observed that in low pH range (pH < 3), only unstack conformer of FAD is favored as either adenine or flavin moiety gets protonated in this pH range and the excited state protonation of flavin moiety results low fluorescence quantum yield and short lifetime of both FMN and FAD in this pH range. Stack conformer of FAD starts appearing from pH = 3 and relative population of stack conformer is significantly smaller than the unstack conformer at this pH. Therefore, FAD exhibits relatively higher quantum yield at pH = 3. The relative population of stack conformer increases with the increase in pH, and in between pH = 5 to pH < 10, relative contribution of stack conformer dominates over unstack conformer. Hence, FAD exhibits less fluorescence quantum yield between pH = 5 to pH = 10. Interestingly, in the pH range of pH = 3 to pH < 10, we have observed three distinct dynamics of FAD; one is ~10 ps dynamics (responsible for stack conformer), another is ~3.5 to ~4.5 ns dynamics (responsible for unstack conformer) and third one is ~2.2 ns component (responsible for the partial quenching of flavin by adenine moiety of FAD in the excited state lifetime of FAD). Around pH ≥ 10 the population of unstack conformer dominates over stack conformer as the deprotonated flavin ring and phosphate group repels each other. Moreover, at pH = 11, we have detected a new dynamics (~22 ps for FAD and ~26 ps for FMN) and this might reflect the lifetime of charge transfer (CT) state of photoexcited $FL^{\cdot-}$. Nonetheless, we also found change of rotational motion of FAD around pH ~3 and pH ~10 corresponding to conformational changes of FAD at these two pHs. Moreover, our time-resolved fluorescence anisotropy study indicates that the rotational motion of unstack conformer is slower than the stack conformer of FAD, which can be ascribed to the larger van der Waals volume of unstack conformer than that of stack conformer.

4b. Urea Induced Unfolding Dynamics of Flavin Adenine Dinucleotide (FAD): Spectroscopic and Molecular Dynamics Simulation Studies from Femto-Second to Nano-Second Regime

4b.1. Motivation

FAD being one of the most important cofactors for electron transportation and photoreceptors in living systems,[1-10] the photophysical properties of FAD have been extensively studied till date.[11, 24, 26, 36-39] A ~4 ps decaying component attributed to stack conformation was reported from the transient absorption and upconversion studies.[11, 12] Moreover, time resolved mid-IR transient absorption study shows a radical recombination dynamics of ~1.1 ps along with a stack dynamics of ~9 ps of FAD at higher concentrations in D_2O.[36] Ernsting and coworkers presented a detailed vibrational analysis based on hybrid density functional theory for riboflavin in the first excited state (S_1) and FAD in the ground state (S_0) using normal-mode analysis and resonance Raman.[37] Recently, it has been observed that the stacking dynamics of FAD in solution is largely affected by surrounding environment. In ethanol-water mixture, lowering of dielectric constant increases the contribution of unstack conformation of FAD. Moreover, fluorescence lifetime of the stacked conformation also increases with decreasing dielectric constant, suggesting an increasing intramolecular distance between the two aromatic rings in less dielectric media.[25] Furthermore, the study on glycerol-water mixture suggests that viscosity affects the lifetime of only 'open' confirmation of FAD.[25] A more detailed insight about the stacking dynamics of FAD in methanol-water mixture is offered by Gutman *et al.* through molecular dynamics simulation along with experiments for the same system. Interestingly, the results claim that the effect of methanol on the equilibrium is to destabilize the folded state of FAD, enhancing the contribution of the 'open' conformations.[38, 39] Overall, it concludes the solvent-dependent folding observed for FAD appears due to solvent-solute interactions.[38, 39] Very recently, we noticed dependence of FAD dynamics over the solvent polarity and viscosity inside the reverse micelles.[40] Now, based on such a diverse collection of literatures, it appears difficult to pin-point the factor(s) that is (are) responsible for folding dynamics of FAD. Stacking interaction between adenine and flavin might contribute significantly towards the stabilization of stack form of FAD. Recent

simulation studies predicted the hydrogen bonds between phosphodiester and ribityl chain as a possible reason for dominating percentage of stack conformation in water.[24, 38, 39] These ongoing quests about FAD folding dynamics fascinated us to pursue a thorough investigation to find out the role of stacking and/or hydrogen bond interactions in the FAD dynamics in urea, as it is widely accepted as chaotrope for creating chaos in hydrogen networked systems[41-44] and it is also well known for unfolding protein structures.[45-47] To do so, we have employed picoseconds time resolved (TCSPC), femtosecond fluorescence up-conversion techniques along with long (200 ns) the molecular dynamics simulations to study FAD in urea water mixture and compared that with the dynamics of FAD in pure water. Our study captures both the dynamics and structural aspects of FAD in presence of urea and provides the molecular origin of unfolding.

4b.2. Experimental Results and Discussions

4b.2a. Steady State Results

Flavin absorption in water is characterized by two intense π-π* transition bands originated from isoalloxazine chromophore corresponding to $S_0 \rightarrow S_1$ transition (λ_{abs}~450 nm) and $S_0 \rightarrow S_2$ transition (λ_{abs}~375 nm).[15, 23, 25, 26] When excited at either of absorption band, both FMN and FAD in water exhibit an unstructured emission at ~535 nm[15, 23, 25, 26] (**Figure 4b.1**). With the incremental addition of urea to the solution containing FMN (devoid of adenine moiety), emission exhibits almost negligible effect (**Figure 4b.1**). Interestingly, on gradual addition of urea to the solution containing FAD, the fluorescence intensity is enhanced more than double of its initial value (**Figure 4b.1**) at maximum urea concentration (12 M). It is reported that increasing urea concentration in water enhances the dielectric of the medium,[48] which is expected to stabilize the stack conformation of FAD[25, 38, 39]. We observed, however, a completely opposite trend for FAD intensity in presence of urea. Hence, the modulation of photophysics observed either for FAD in presence of urea is surely not an outcome of dielectric variation of the medium. The difference in fluorescence property between FMN and FAD in presence of urea thus arises due to the existence of adenine moiety in FAD, which is absent in case of FMN. Notably, adenine participates in the formation of weakly fluorescent stack conformation with flavin ring through photo-induced intramolecular electron transfer process.[11-13, 24-26] Here it is relevant to mention that the fluorescence property of the unstack conformation is believed to be similar to that of FMN, as the latter appears

solely from the isoalloxazine ring. Hence, we believe that the unstack conformation of FAD would also experience similar quenching as that of FMN even though we have observed continuous increment in emission intensity in presence of urea. Above observations suggests that there are two opposing factors that affect FAD fluorescence in presence of urea;

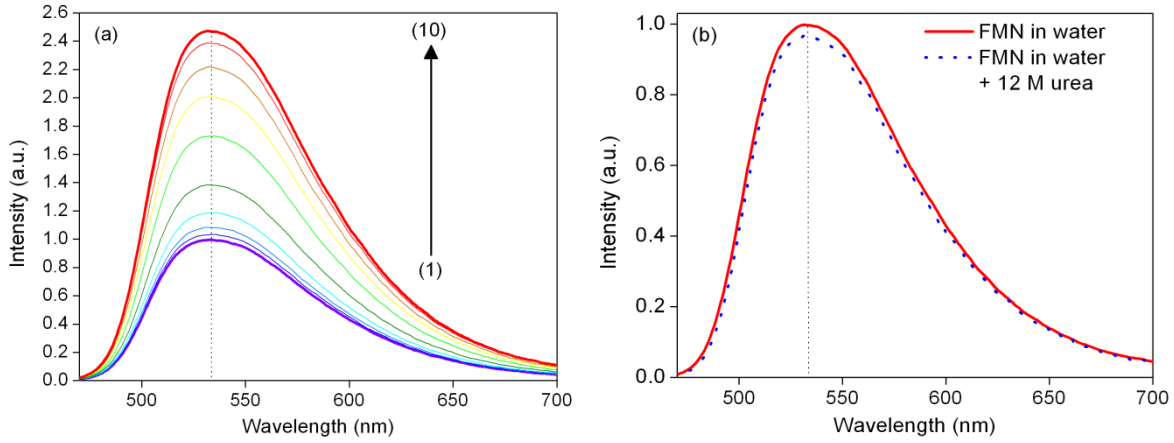

Figure 4b.1. *Emission profiles of (a) FAD with increasing concentration of urea where, (1) → (10) represents concentrations of urea 0, 0.25, 0.5, 1, 2, 4, 6, 8, 10 and 12 M, respectively, and (b) FMN in water and in presence of urea.*

however, the effect of enhancement dominates over the effect of quenching. The observed enhancement in fluorescence intensity is certainly due to the increased population of unstack conformation of FAD, as stack conformation is almost non-fluorescent in nature. This is corroborated by the molecular picture obtained from all-atom simulation as mentioned later. Therefore, we believe that urea affects the stacking interaction between adenine and isoalloxazine ring, and shifts the equilibrium towards the unstack conformation. A more detailed insight of interaction between flavin and urea can be obtained from the time-resolved as well as the molecular dynamics simulation studies discussed afterward.

4b.2b. Pico-second to Nano-Second Time-Resolved Decay Features of FAD with Increasing Urea Concentration

Figure 4b.2 depicts fluorescence decays of FMN and FAD collected using TCSPC technique and the results are tabulated in **Table 4b.1**. It is evident from the decay profiles that FMN exhibits single exponential decay in absence and presence of urea, as it does not have any

conformational flexibility. Lifetime of FMN is almost unchanged in the presence of urea. This indicates that the dynamics of FMN is almost unaffected by the presence of urea, which is corroborative with the steady state results. The decay characteristics of FAD in absence and presence of urea is bi-exponential in nature. The longest decaying lifetime component

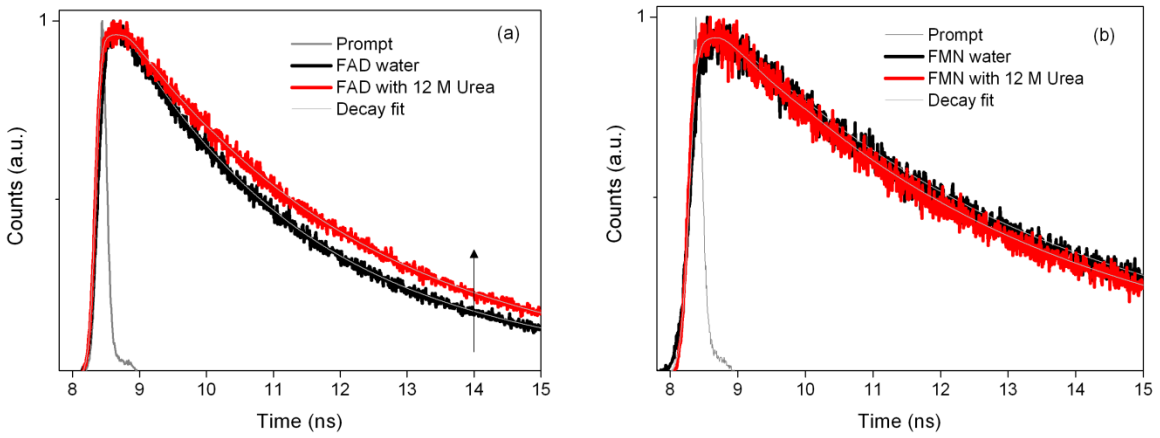

Figure 4b.2. *Time resolved decay profiles (measured in TCSPC set-up, λ_{ex}=440 nm and λ_{em}= 535 nm) of (a) FAD and (b) FMN water and in presence of urea. The legends carry the respective meanings.*

(4.6 ns) of FAD is already known to appear from unstack conformation of FAD, and is in good correlation with the single decaying component of FMN (**Figure 4b.2, Table 4b.1**). The short nano-second component (~2.5 ns) is assigned to be the lifetime of partially stack

Table 4b.1. *Fluorescence lifetime decay parameters (collected at 535 nm in TCSPC set-up) of FAD and FMN in water and presence of urea.*

	FAD						FMN		
Sample	τ_1 (ns)	a_1 (%)	τ_2 (ns)	a_2 (%)	χ^2	τ_{av} (ns)	τ_1 (ns)	a	χ^2
Urea 0M	2.32	47	4.62	53	0.95	3.54	4.98	100	1.15
Urea 0.5 M	2.37	46	4.62	54	0.95	3.58	4.82	100	1.10
Urea 1 M	2.46	56	4.62	44	0.99	3.41	4.76	100	1.18
Urea 2 M	2.60	59	4.65	41	1.10	3.44	4.74	100	0.95
Urea 4 M	2.85	64	4.60	36	1.10	3.48	4.72	100	1.00
Urea 6 M	3.06	70	4.60	30	0.95	3.78	4.65	100	1.13
Urea 8 M	3.32	67	4.60	33	0.85	3.74	4.63	100	1.00
Urea 10 M	3.42	72	4.62	28	1.00	3.75	4.62	100	1.13
Urea 12 M	3.52	73	4.62	27	0.99	3.82	4.62	100	1.10

conformation of FAD. It is noticeable that lifetime of unstack conformation is almost unchanged from bulk water to 10 M urea (**Table 4b.1**). This clearly implies that like FMN the unstack conformation of FAD is not getting affected by the urea. From the TCSPC results, we also infer that the population of unstack conformation increases, whereas the percentage contribution of partially stack conformation decreases (**Table 4b.1**), resulting in a marginal increase in the average lifetime. Note that TCSPC study cannot probe the dynamics of stack conformation of FAD due to the limited time resolution of the set-up. To probe the stacking dynamics of FAD in presence of urea, we employed femtosecond fluorescence up-conversion technique, discussed in the forthcoming section.

4b.2c. Femtosecond Time-Resolved Decay Features of FAD with Increasing Urea Concentration

The femtosecond decay profiles are depicted in **Figure 4b.3**. The results are summarized in **Table 4b.2**. All the femtosecond decay profiles are non-exponential in nature. We have used a tetra exponential fit function in order to fit the decay profiles in case of FAD as follows;

$$I(t) = a_1 \exp\left(-\frac{t}{\tau_1}\right) + a_2 \exp\left(-\frac{t}{\tau_2}\right) + a_3 \exp\left(-\frac{t}{\tau_3}\right) + a_4 \exp\left(-\frac{t}{\tau_4}\right) \quad \ldots 4b.1$$

where, a_i and τ_i represent the pre-exponential factor (reflecting the contribution of i^{th} species in the decay profile) and lifetime of the i^{th} species, respectively. From the fitting of the decay profile of FAD in water alone, we have obtained 1.5 ps, ~10 ps, and 200 ps lifetime components, which we have assigned as τ_1, τ_2 and τ_3, respectively. These lifetime components are in agreement with previous reports.[24, 25] The 1.5 ps component is ascribed to solvent relaxation around FAD, which is yet to be completed.[25] The major point of attention is the appearance of two the lifetime components, ~10 ps and ~200 ps. The ~10 ps component is attributed to the stack conformation, where the isoalloxazine and the adenine moieties residing within stacking distance (distance between center of mass of the two rings <5.5 Å[38, 39]) participate in an effective electron transfer process, which results in minimal fluorescence lifetime among all the conformations. Another picosecond decaying component (~200 ps) is in good agreement with ~220 picosecond component reported previously by van den Berg *et al.*[24] and Nakabayashi *et al.*[25]. This component was attributed to another type of stack conformation, where the intramolecular electron transfer (IET) is relatively less

effective due to slightly higher distance between flavin and adenine rings. Here it is pertinent to mention that the oxidation potential of adenine (E_{ox}=1.5 eV)[49] allows the electron transfer form adenine to photoexcited flavin ring (ground state reduction potential E_{red}=-0.24 eV),[50] resulting in a reduced fluorescence lifetime of the flavin ring. This intra-molecular electron

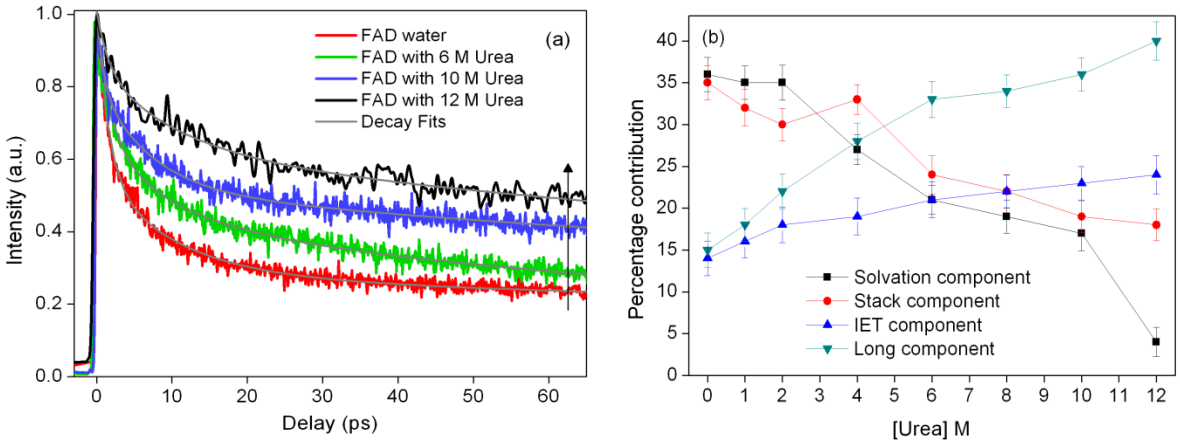

Figure 4b.3. *Femtosecond time resolved decay profiles of FAD and FMN (λ_{ex}=420 nm and λ_{em}= 535 nm) in water and with increasing concentrations of urea up to 12M. (b) Changes in percentage contribution in femtosecond decay components with variable urea concentrations. In all cases the legends carry respective meanings.*

transfer (IET) process is largely dependent over the distances between two rings. The existence of stack conformation is strongly supported by the FMN decay profile, which is devoid of any such picosecond components, as it lacks the adenine moiety (**Figure 4b.3, Table 4b.2**). The long component lifetime (τ_4, detected in TCSPC) is assigned to the average lifetime of 'open' and partially stack conformations of FAD and kept fixed during analysis. The analysis of all the decay profiles in presence of urea are fitted with the assumption that the same fast-decaying components having lifetime of 1.5 ps (τ_1) and ~10 ps (τ_2) exist in presence of urea with variable contribution and the long component lifetime (τ_4) obtained from TCSPC is also kept fixed during analysis.

It is noticeable from **Figure 4b.3** that the residual background having a long decay time increases with the increase in urea concentration. This indicates that the dynamics slows down in presence of urea. The fitting results clearly suggest that the population of solvation component (a_1) gradually decreases as the urea content of the solution increases. Decrease in the contribution of solvation component suggests a limited access of water around the flavin

ring with increasing urea concentration. Urea can disrupt the hydrogen bonding interaction; therefore, it is possible that solute-solvent interaction is affected by the presence of urea, which results in the small magnitude of a_1 in presence of urea. Plots of a_2 and a_3 against urea concentration are shown in **Figure 4b.3b**. Both a_2 and a_3 represent the value corresponding to the population of stack conformations in solution with different intramolecular distance between adenine and isoalloxazine (flavin) ring. As shown in **Table 4b.2**, the population of

Table 4b.2. *Fitting parameters of femtosecond time-resolved fluorescence decays of FAD in water and with increasing concentrations of urea.*

Sample	τ_1 (ps)	a_1 (%)	τ_2 (ps)	a_2 (%)	τ_3 (ps)	a_3 (%)	τ_4 (ps)	a_4 (%)
FAD water	1	36	12	35	212	14	3500	15
FAD + Urea 1 M	1	35	12	32	180	16	3500	18
FAD + Urea 2 M	1	35	12	30	162	18	3500	22
FAD + Urea 4 M	1	27	12	33	97	19	3500	28
FAD + Urea 6 M	1	21	12	24	104	21	3500	33
FAD + Urea 8 M	1	19	12	22	95	22	3500	34
FAD + Urea 10 M	1	17	10	19	84	23	3500	36
FAD + Urea 12 M	1	4	12	18	130	24	3500	40

a_2 decreases with increasing urea concentration, indicating a decrease in the population of stack conformation of FAD. Interestingly, the population of stack conformation having lifetime of ~200 ps in water increases with rise in urea concentration in solution, although its lifetime is getting faster in presence of urea. This indicates that IET rate also gets affected by the presence of urea. The population of long nano-second component (a_4) also increases significantly with the increase in urea concentration. These results clearly suggest that urea shifts the equilibrium from the stack towards unstack conformation. Recently, it has been shown by simulation as well as experiments in methanol-water binary mixture that with the decrease in the dielectric constant, the population of stack conformation decreases. It was argued that methanol affects the dynamics of the FAD by enhancing the frequency of unfolding events without affecting the lifetime of the open conformation.[38, 39] Literature reports that dielectric constant of the medium increases with increasing concentration of urea.[48, 51] Although an enhanced dielectric constant is well known to stabilize stack conformation of FAD,[25, 38, 39] we observe here that the population of stack conformation

significantly reduces in presence of urea. Therefore, it is reasonable to conclude that urea itself hampers the stacking interaction between adenine and isoalloxazine ring.

There are two plausible mechanisms by which the stacking interaction in FAD can be hindered. (a) A direct urea induced disruption of intramolecular hydrogen bonding network, which destabilizes stack conformation of FAD, and/or (b) solvation of aromatic moieties (adenine and/or isoalloxazine ring) by urea, which destabilizes the π-π stacking interaction within FAD. Recently, a few reports showed that urea can severely hinder π-π stacking interaction by solvating hydrophobic aromatic moieties, like adenine, thymine and uracil.[45, 52] Notably, FAD contains adenine in its structure, which can be easily solvated by urea, thereby, creates hindrance for intramolecular stacking. At the same time, it is well established that urea can interfere solute-solvent, solvent-solvent as well as intramolecular hydrogen bonding interaction in a molecule.[41-44] Recent simulation studies on FAD revealed that interplay of hydrogen bond formation between the ribityl chain and the phosphodiester bond might resulted in the formation of stack, unstack conformations of FAD.[24, 38, 39] Simulation study also found that there is a possibility of H-bond formation between hydroxyl group attached to C3/C4 of the ribityl chain and N1 of the flavin in stack conformation.[24] In order to probe the involvement of urea in folding-unfolding dynamics of FAD in molecular detail, we have carried out molecular dynamics simulation study (discussed next section). This provides the molecular picture of the interaction in terms of H-bonding and stacking between different parts of FAD and also between FAD and urea, corroborating the observations noted above.

4b.3. Molecular dynamics simulation

4b.3a. Structure and Dynamics of FAD

Simulation trajectories of 200 ns for each system were used to analyze the conformational sampling of FAD in pure water and water-urea mixture. The following three parameters were used to understand the conformational variations of FAD: (i) distance, *d*, between the center of masses (COMs) of the adenine (Ade) and isoalloxazine (Iso) rings (magnitude of the vector $\vec{e}$, **Figure 4b.4**), (ii) angle, θ, between the plane of the Ade and Iso rings (angle between the vectors $\hat{g}$ and $\hat{f}$ in **Figure 4b.4**), and (iii) angle, φ between the vector normal to the Iso ring and the vector from the COM of Iso to the COM of Ade (angle between two vectors $\hat{f}$ and $\hat{e}$ **Figure 4b.4**). Stack configuration is defined when d ≤ 6.0 Å[38],

and both angles (θ and φ) are either less than 40º or greater than 140º, i.e., 40 º ≥ (θ, φ) or (θ, φ) ≥ 140º, as shown schematically in **Figure 4b.4a**.

We also define the two different types of unstack conformations: (i) complete unstack conformation (U4) where d>10 Å and (ii) partially unstack where d<10 Å. Based on our observation of the geometry of FAD, we further divide the partially unstack into three categories: (i) U1, when d< 6.0 Å and 40° ≤ (θ, φ) or (θ, φ) ≤ 140° (ii) U2, when 6 Å ≤ d 10 Å and 40° ≥ (θ, φ) or (θ, φ) ≥ 140° (iii) U3, 6 Å ≤ d 10 Å and 40° ≤ (θ, φ) or (θ, φ) ≤ 140°.

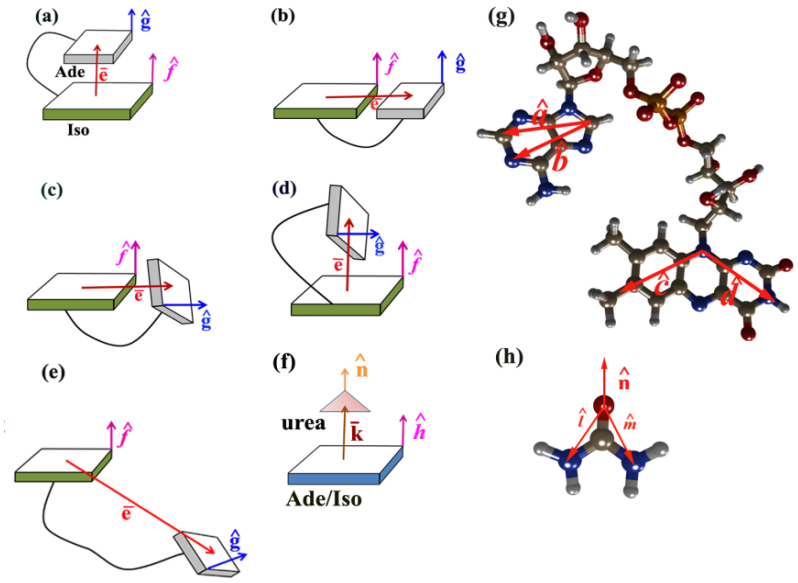

Figure 4b.4. *Schematic representation of the stack and unstack conformation; (a) represents the stack conformation, for which d ≤ 6.0 Å, and θ, φ = 0º. (b) Represents the unstack conformation, where d ≤ 6.0 Å, θ = 0º, φ = 90º. (c) Represents the unstack conformation, where d ≤ 6.0 Å, θ = 90º, φ = 90º. (d) Represents the unstack conformation, where d ≤ 6.0 Å, θ = 90º, φ = 0º. (e) Represents the unstack conformation, where d ≥10 Å. (f) represents the stack conformation of Ade/Iso with urea when k ≤ 5.2 Å, 40 ° ≤ (α, β) ≤ 140 °. $\vec{e}$ represents the vector from COM of Iso ring to Ade ring. $\hat{g}$ represents the vector normal to the plane of Ade ring, which is a cross product of two vectors, â and $\hat{b}$ (**Figure 4b.4g**). $\hat{f}$ represents the vector normal to the plane of Iso ring, which is a cross product of two vectors, ĉ and $\hat{d}$ (**Figure 4b.4g**). $\hat{n}$ represents the vector normal to the urea molecule, which is a cross product of two vectors, $\hat{l}$ and $\hat{m}$ (**Figure 4b.4h**).*

Therefore, U1 denotes the partial unstack configuration where Ade and Iso rings are close to each other, but not in the preferably stacked configuration. U2 and U3 denote intermediate distance separation. In U2, the angle between the planes conforms to stacked geometry; however, the rings are far away (>6 Å) to have perfect stacking interaction. Variations of these parameters for FAD in water are shown in **Figure 4b.5**. The time variation of the

distance between Iso and Ade rings in water is shown in **Figure 4b.5a,** while their distribution is shown in **Figure 4b.5d**. Distribution is peaked at 4.2 Å (with 0.6 Å standard deviation). This indicates that most of the time the two rings of FAD are in close proximity. Time variation of the two angles (θ,φ) are shown in **Figure 4b.5b** and **4b.5c,** while their corresponding distributions are shown in **Figure 4b.5e** and **4b.5f**, respectively. It is clear from the distribution that θ is peaked at 172.1º, while φ is peaked at 143.5º. Therefore, according to the stacking criteria (as mentioned above), FAD remains in the stacked conformation most of the time in water. Unstack conformation appears for short while for

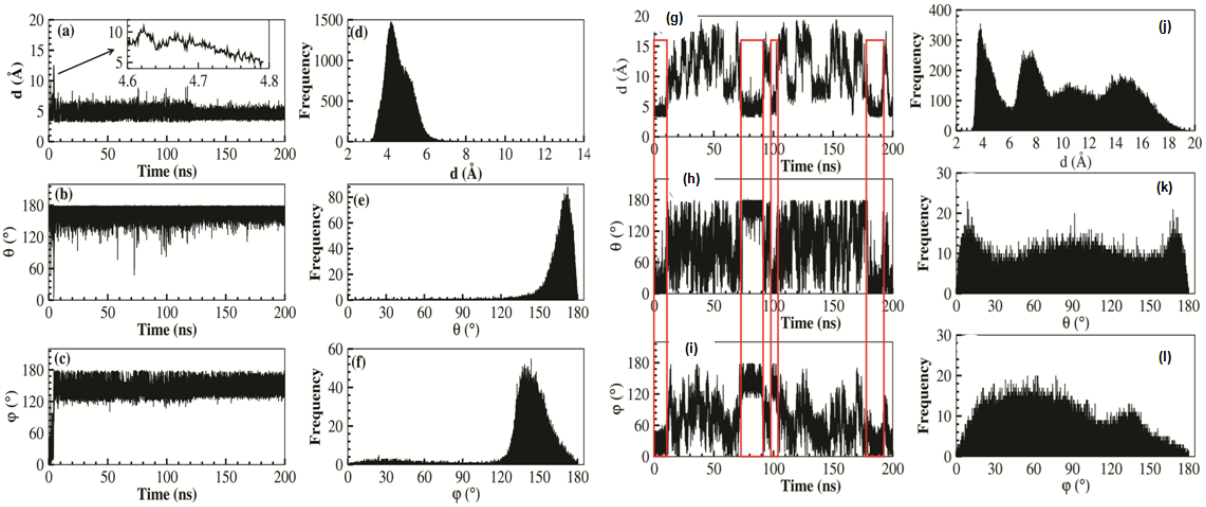

Figure 4b.5. *(a), (b) and (c) show the variation of d, θ, φ, respectively with time for FAD in water. (d), (e) and (f) are the distribution of the three parameters (d, θ and φ) in water solvent. (g), (h) and (i) represent variation of the three parameters (d, θ and φ) over trajectory for FAD in water urea mixture. (j), (k) and (l) are the distribution of the above mentioned three parameters for FAD in water-urea mixture.*

around 200 ps (inset of **Figure 4b.5a**). Orientation of water molecules in different possible conformations of FAD in water at different time trajectory is shown in **Appendix 4b.1.** It shows that a dominant number of stack conformations exist at almost all time frames, in perfect agreement with the experimental results[14, 24, 53].

Similar analysis of FAD is carried out for FAD in water-urea mixture (8M). Results are shown in **Figure 4b.5**. A dramatic fluctuation in FAD conformation is observed here. It is clear from the time-variation of the distance and angles that FAD prefers to exist in unstack conformation most of the time in the mixture. However, FAD does not remain always in the unstack conformation and stack-unstack equilibrium continues. Red boxes (**Figure 4b.5g,h,i)**

indicate the time zones where stack conformation appeared during the simulation. Distribution of the distance (*d*) between the two rings exhibits (**Figure 4b.5j**) distinct peaks at 4 Å, 8 Å, 11 Å and 15 Å. Interestingly, distribution of two angles θ and φ are almost uniform (**Figure 4b.5k,l**) which indicates that the preference for the stack conformation present in pure water is affected by urea.

Table 4b.3. *Percentage of stack and unstack conformation of FAD in water and water-urea mixture calculated over the whole trajectory.*

Solvent	Stack conformation	Unstack conformation			
		U1	U2	U3	U4
Water	64%	0.1%	0.2%	35.6%	0.07%
Water-urea mixture (8M)	14.4%	18.4%	5.4%	14.5%	47.3%

The stack-unstack equilibrium is analyzed to find the probability of each conformation in both water and water-urea mixture. **Table 4b.3** shows that 64% of FAD conformation is in stack conformation in water and the rest 36% is in unstack conformation, in close agreement with the experimental observation obtained here (**Table 4b.2**). Amongst the unstack conformation in water, a significant portion (35.6%) comes from partial unstack conformation U3, where the distance between two rings lies between 6 Å and 10 Å and the angles θ and φ are between 40º and 140º. This indicates that in water, FAD never actually goes to the fully unstack configuration, rather the rings adopt different orientations to get out from stacking interaction, which is evident from the different time snaps of water molecules around FAD (**Appendix 4b.1**). However, we have found that almost 25% molecules (excluding solvation component) exist in unstack conformation from fluorescence lifetime results (**Table 4b.2**). The slight discrepancy may arise by the precise definition of unstack conformations in our computational approach; whereas the populations of unstack conformations obtained in experiment was from unquenched lifetime only. Also note that, the molecular dynamics simulation provides the interaction amongst different species in their ground electronic state only, whereas the experiment gathers this information through the excited state only. However, it is not expected that the dynamical structures of isoalloxazine

in the ground and excited electronic state will show significant differences, as is evident from the reasonable agreement between experiment and theory obtained here.

Amazingly, in the water-urea mixture, only 14.4% FAD molecules exist in the stack conformation and the remaining 85% FAD molecules attains the unstack conformation

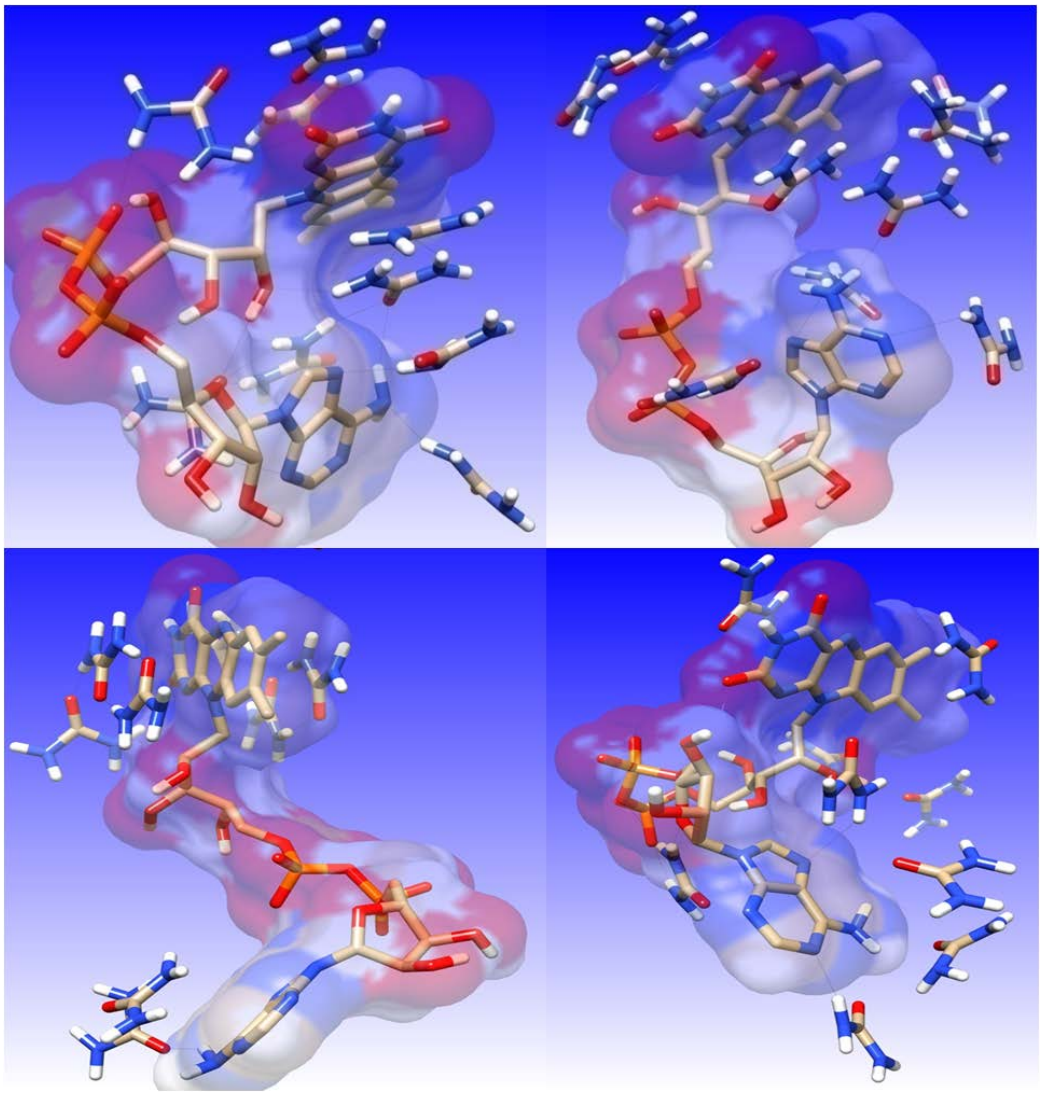

Figure 4b.6. *Orientations of urea molecules around isoalloxazine and adenine rings of FAD at different time points in the trajectory.*

(**Table 4b.3**). Some representative configuration of urea molecules around FAD in stack and unstack conformations obtained at different time frames are shown in **Figure 4b.6**. Among the total population of unstack conformation, majority of the structure exists in the completely unstack conformation U4 (47.3%), where distance between the two rings are

more than 10 Å. The partially unstack conformation contains all the three possibilities (U1, U2 and U3) discussed previously. 18.4% structures contain two rings close to each other with unfavorable stacking orientation (U1), while 5.4% structures are of U2 type, where angles are of stacking type, but the distance between the rings does not allow stacking interaction. Rest 14.5% structures exist in U3 conformation, where both the distance and the angles do not allow stacking to occur. Although the above results support our claim that the contribution of unstack conformations increases in presence of urea, we cannot correlate the exact population of stack and unstack conformations obtained from simulation with experiments. This is because, in experiment, a significant portion of the decay profile contains solvation component, which cannot be detected in simulation as it is done in the ground state. Secondly, in experiment we have identified the stack conformations through the quenched lifetime of FAD, and here the total population of stack conformations of FAD is a combination of A_2 and A_3. In simulation, on the other hand, we have defined stack conformation, which fulfill the angle and distance criteria (discussed previously); all other conformations were considered as unstack conformations.

4b.3b. Hydrogen-Bond Analysis

To understand the effect of water and urea on FAD conformation, we analyzed hydrogen bonds (HBs) between different parts of the FAD (Ade, Ribose (Rib), Iso rings and Phosphate

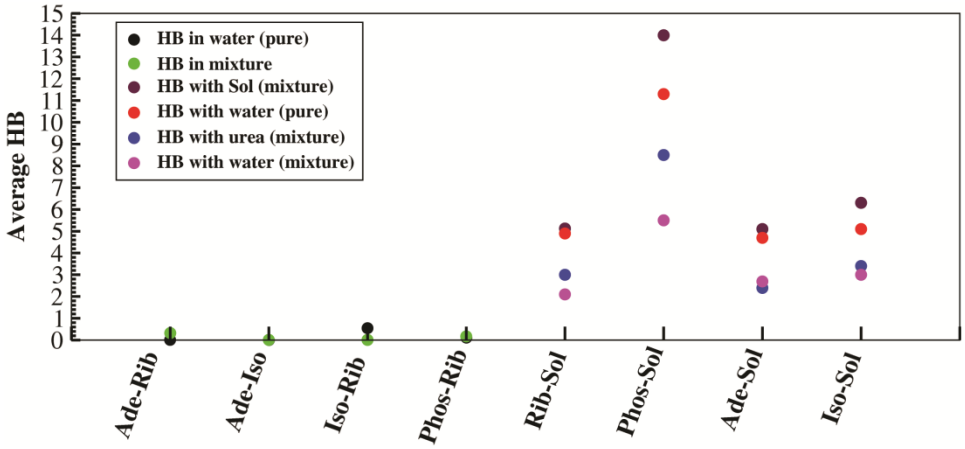

Figure 4b.7. *Average Hydrogen bonding (HB) of the different part of FAD and with the solvent (water and water-urea mixture). The black point is the average HB in the water solvent. The green point is the average HB in the water-urea mixture (8M).*

groups (Phos)), and with the solvent molecules (water and urea). HB was determined by defining a distance and an angle cut-off. Distance cut-off between the donor and acceptor was taken as 3.5 Å, while the cut-off for the angle formed by the donor, hydrogen, and acceptor was taken to be 30°.[54-56] Average HBs between different parts of FAD and with solvents are shown in **Figure 4b.7**. HBs between different parts of FAD (Ade, Iso, Rib and Phos) (intramolecular HBs) is almost non-existent in water, which is consistent with the simulation results reported by Radoszkowicz *et al.*[38] In urea-water mixture, number of HBs between different parts of FAD is also negligibly small. The number of HBs between different parts of FAD and the solvent molecules in general is similar in case of pure water and the mixture (**Figure 4b.7**). Interestingly, in the mixture, some of the water molecules get replaced by urea for making HBs with different parts of FAD as shown in **Figure 4b.7**. Phosphate (Phos) makes maximum HBs with water in pure solvent (11.3). However, in the urea-water mixture, on an average 5.5 water molecule and 8.5 urea molecules make HBs with the phosphate group. Similarly, average number of HBs of Ade and Iso with water in pure water is 4.7 and 5.1, respectively. This changes to 2.7 and 2.9 in the mixture, whereas average HBs of Ade and Iso with urea in the mixture is 2.4 and 3.4, respectively. Therefore, the simulation results suggest that hydrogen bond is not the major driving factor towards the stack to unstack dominance in presence of urea.

4b.3c. Structural Arrangement of Urea Around FAD

To see the effect of urea on the FAD conformation, we have monitored the stack-unstack behavior of urea with Ade and Iso ring by using three parameters: (i) distance k, between the COM of Ade/Iso to the urea molecule (magnitude of vector $\vec{k}$ in **Figure 4b.4f**), (ii) angle α, between the vector normal to the Ade or Iso ring and the vector normal to the urea molecule (angle between the unit vector $\hat{n}$ and $\hat{h}$ in **Figure 4b.4f**) (iii) angle β, between the vector normal to the Ade or Iso ring and the vector from the COM of Ade or Iso to the urea molecule (angle between the vector $\vec{k}$ and $\hat{h}$ in **Figure 4b.4**). To define the normal vector of the urea, we took the cross product of the two vectors $\hat{l}$ and $\hat{m}$ as shown in **Figure 4b.4h** **Figure 4b.8** shows the distribution of the above distance and angles of urea with the Ade/Iso rings in the urea-water mixture. Distribution of urea molecules around the rings exhibits two peaks. We defined the stack conformation, when $k \leq 5.2$ Å and $40° \leq (\alpha, \beta)$ or $(\alpha, \beta) \leq 140°$. Rest of the structural arrangements between the urea and Ade/Iso are defined as unstack

conformation. We classified the unstack conformation into two types: (i) Un1 for 40° ≤ α or α ≤140° and 40° ≥ β or β ≥ 140°. (iii) Un2 for 40° ≥ α or α ≥ 140° and any β value. From the above definition, we can see that Un1 denotes urea configuration where the plane of the urea molecule is perpendicular to the ring plane. Un2 denotes the configuration, where urea

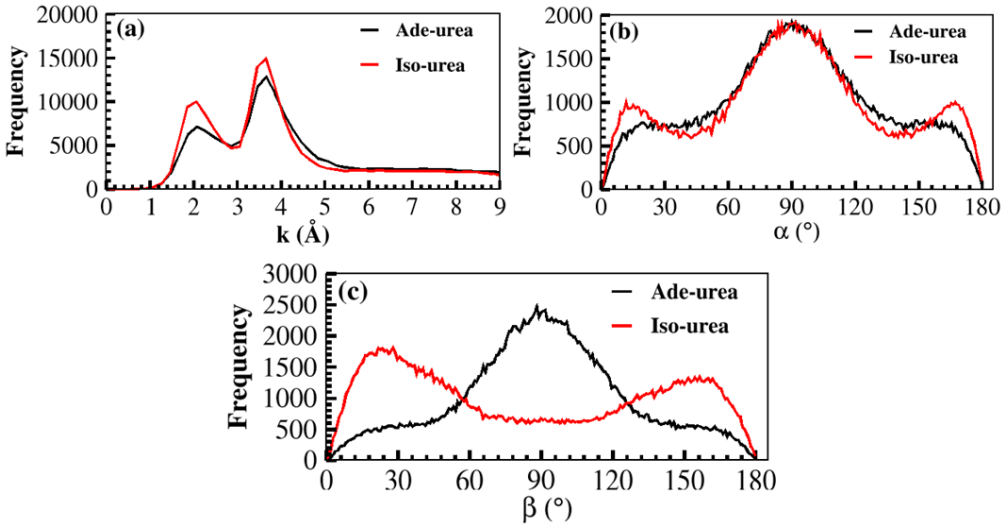

Figure 4b.8. *Distribution of k, α and β for Ade/Iso with urea. (a) distribution of distance (k) between the COMs of Ade and urea, Iso and urea. (b) Distribution of angle (α) between the Ade and urea, Iso and urea. (c) Distribution of angle (β) between Ade and urea, Iso and urea.*

molecules surround the ring in the periphery. From the distribution of the distance of urea from both the above rings, we assign the cut-off distance at 5.2 Å for direct interaction of urea with the rings. Subsequently, we have analyzed the conformation of the urea in proximity of the rings from the above-mentioned criteria. **Table 4b.4** shows the number of urea molecules around the Ade and Iso in both stacked and unstack conformation. We have

Table 4b.4. *Percentage of stack and unstack conformation of urea with both ring Ade and Iso.*

	Cut-off Distance (Å)	Number of urea molecule	% Stack	% Unstack	
				Un1	Un2
Ade	5.2	2.6	28.4%	15.0%	56.4%
Iso	5.2	3.0	39.0%	11.7%	48.5%

found that on an average, 2.6 urea molecules are within 5.2 Å distance from the Ade ring and 3 urea molecules are within 5.2 Å distance from the Iso ring. Orientation of the urea molecules around the Ade and Iso rings is different as mentioned in **Table 4b.4**. 39% of the urea molecules around the Iso ring form stack conformation, whereas 28.4% urea molecules stack around Ade. In unstack conformation, majority of the conformation exists in Un2 conformation for both the rings, and these urea molecules participate in hydrogen bond interactions with rings.

From the analysis of the structural arrangement or urea around FAD, we have observed that in the mixture, urea replaces water to interact with different parts of the ring. Although the overall number of hydrogen bonds between FAD and the solvent does not change from the pure water to the mixture, urea replaces some of the water molecules from both the rings to participate in stacking and hydrogen bonding interaction with Ade and Iso ring. Moreover, participation of urea around Ade and Iso is more when FAD is in unstack conformation. Number of urea around Ade and Iso is 2.0 in stack conformation; while this participation comes partially (~30-40%) from the stacking interaction of urea with Ade/Iso rings. This decreases the probability of FAD to be in the stack conformation in presence of urea, thereby shifting the equilibrium towards more unstack conformations.

4b.4. Conclusion

Present work focuses on the urea induced unfolding of FAD through steady state, femto to nanosecond time-resolved fluorescence spectroscopy, and molecular dynamics simulation studies. It is evident from steady state emission profiles that the intensity of FAD rises up with increasing urea concentration. A comparative study with FMN exhibits small decrement in intensity. As stack conformation is almost non-fluorescent in nature, above observation suggests that the population of unstack conformation increases in presence of urea. The fluorescence decay profiles collected in both TCSPC and up-conversion techniques slow down in presence of urea, indicating a significant change in the stack-unstack dynamics of FAD in presence of urea. Moreover, it is observed that unstack conformation population increases from 15% in pure water to 40% in 12 M urea. Results obtained from molecular dynamics simulation support this observation very well. It shows that although the total number of hydrogen bonds remains same in the water and urea-water mixture, urea replaces many of the water molecules around adenine and isoalloxazine rings of FAD. Moreover, MD simulation studies reveal that a major fraction of urea molecules (~30% to 40%) form

stacking interaction with both of the adenine and isoalloxazine rings. As a result, intramolecular stacking interaction between isoalloxazine and adenine ring is disrupted, and

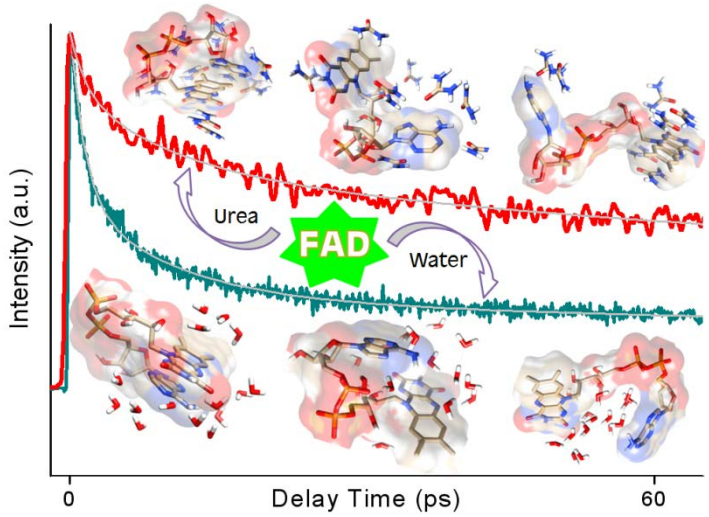

Scheme 4b.1. *Schematic representation of urea induced unfolding dynamics of FAD.*

thereby, the contribution of unstack conformation of FAD increases with increasing urea concentration in the medium (**Scheme 4b.1**).

4c. Comparative Study of Flavins Binding with Human Serum Albumin: A Fluorometric, Thermodynamic and Molecular Dynamics Approach

4c.1. Motivation

Protein-ligand binding offers a viable tool to elucidate structural information of the protein and their functional role in binding various ligands.[57-64] A transport protein, human serum albumin (HSA), has been used repeatedly for such investigations for its high capability to bind wide variety of endogenous and exogenous ligands of diverse chemical nature (fatty acids, amino acids, metals like Cu and Zn, drugs etc.).[65-70] HSA is a monomeric protein (**Scheme 2.3, Chapter 2**) containing three homologous domains (I, II, III), each of which is constituted by two sub-domains A and B.[67, 71] As the domains II and III share a common motif, conformational change or effect of binding in one of the domain is complementary to another.[67, 71] The principal ligand binding sites are now well explored from crystal structure analysis and named as Sudlow's site I (SS1) and Sudlow's site II (SS2). Warfarin like bulky heterocyclic anions prefer to bind in SS1, located at subdomain IIA, whereas ibuprofen and other aromatic extended conformers of carboxylates prefer SS2 at sub-domain of IIIA **(Scheme 2.3, Chapter 2)**.[68-70]

Riboflavin (RF, also known as vitamin B_2), Flavin mononucleotide (FMN), and Flavin adenine dinucleotide (FAD) are the common members of flavin family recognized for various biological activities. RF participates in iron metabolism and prevents light induced oxidative damage of lens proteins.[72] Some evidences also claim that riboflavin has been investigated as a treatment for recurrent migraine headaches.[73] FAD and FMN are present in various photoreceptors such as DNA-photolyase, photototropin and BLUF proteins etc.[1, 4-7] As we have already mentioned in the previous section (**Chapter 4a**) that among these flavins, only FAD has conformational flexibility in terms of 'stack' (closed) and 'unstack' (open or extended) structures both in solution and in flavoproteins,[15, 16, 26, 31-34, 53] however preference of either of the conformer in different proteins and the dynamic behavior is not well understood To understand the dynamic behavior of FAD inside the flavoproteins an extensive study is required using a model protein like HSA, which is widely used for protein-drug interaction studies.[65, 66, 68-70] Moreover, considering the importance of RF as a coenzyme to various important enzymatic transformations, it is surprising that present knowledge related

to its uptake, transport and incorporation into protein is scarcely available. Previously, a very few studies have been focused on understanding of binding interaction of RF with serum albumins, and in these reports intrinsic fluorescence property of tryptophan was utilized to understand the binding interaction of RF with serum albumin.[74-76] Moreover, the previously reported binding studies related to RF were solely focused on binding constant determination, without detail information about the thermodynamic parameters such as free energy, enthalpy and entropy which provide valuable information about the driving force of the binding process.

Here, we have used flavins as an extrinsic fluorescence marker, (mainly FAD, FMN and RF) to see the effect of binding in emission and lifetime decay profiles of extrinsic fluorophores using steady state and time-resolved fluorescence spectroscopy. We have measured thermodynamic parameters from fluorescence and isothermal calorimetric (ITC) studies to get knowledge about the nature as well as driving force of binding. We have also used docking followed by molecular dynamics method to understand the molecular picture of binding, which corroborate with the experimental results. The present study shows that flavins can be used as external fluorescence marker and provides new insights towards the understanding of interactions between flavins and surrounding amino acids in the binding pocket of flavoproteins.

4c.2. Results and Discussion

4c.2a. Steady State Results of Flavins

Absorption spectra of FAD, FMN and RF at pH 7 exhibits two prominent peaks (**Appendix 4c.1**) due to the main chromophoric unit isoalloxazine, one at ~ 375 nm, corresponding to $S_0 \rightarrow S_2$ transition, whereas the other at ~448 nm, characteristic of $S_0 \rightarrow S_1$ transition, in corroboration with previous studies[15, 26]. With the addition of HSA to the solution containing flavins, the absorbance at 375 nm increases with the simultaneous increase in the absorbance in the UV region (**Appendix 4c.1**). This might be the first indication towards the interaction between flavins and HSA. The room temperature emission spectra of FAD, FMN and RF in pH 7 buffer solution show a single unstructured band with a peak maximum around 535 nm **(Figure 4c.1**). With the addition of HSA, FAD exhibits ~7 nm and FMN exhibits ~5 nm blue shift at high protein concentration (0.3 mM) from its earliest position (**Figure 4c.1**), implying the strong interaction with protein. RF, however, does not show any blue shift. The

fluorescence intensity pattern, on the other hand, shows a decrease of ~67% in case of FAD, 88% in case of FMN and 17% in case of RF at 0.3 mM HSA concentration. This quenching

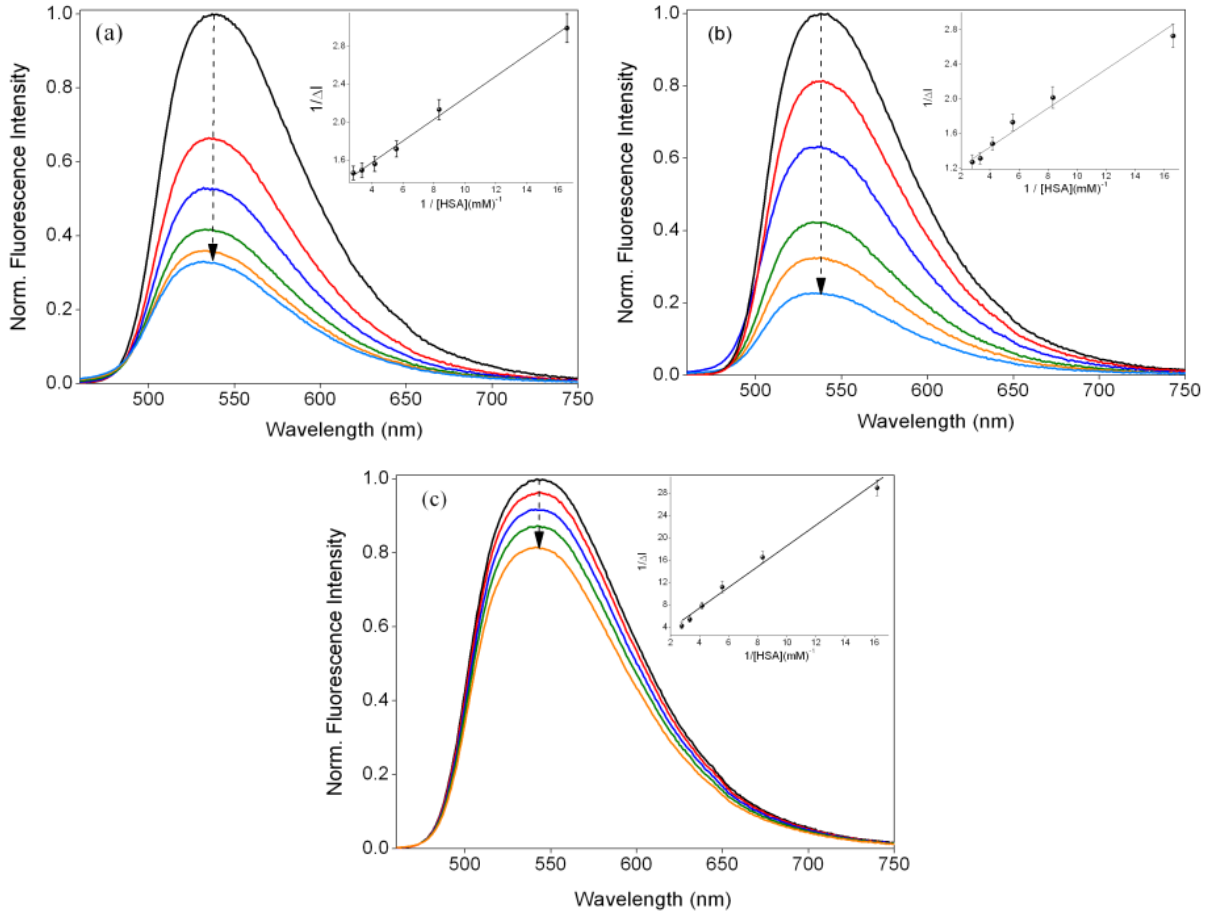

Figure 4c.1. *Emission spectral features of (a) FAD, (b) FMN and (c) RF with the various concentrations of HSA. Arrows indicate the trend from lowest (0 mM) to highest HSA concentration (0.3 mM). The Benesi-Hildebrand plots are shown as inset of each figure.*

can be attributed to the tryptophan residue present at primary sequence position 214 (TRP214) at the SS1. Note that, HSA also contains phenylalanine and tyrosine residues that share almost similar fluorescence property like tryptophan. However, separate experiments involving flavins and the above mentioned amino acid residues in solution show that tyrosine and phenylalanine do not have any significant quenching effect on flavins, but tryptophan exhibits severe quenching effect (**Appendix 4c.2**).

The blue shift in emission spectra along with fluorescence quenching gives an indication that FMN and FAD may bind to HSA in the SS1 binding pocket where tryptophan resides, considering the fact that SS1 is the usual binding pocket of many drugs.[77-79] The

conformational flexibility ('stack' and 'unstack') of FAD may be responsible for its lower extent of quenching by protein compared to FMN because in the 'stack' conformation, flavin ring is already involved in intramolecular quenching with adenine moiety. Insignificant quenching of RF alludes to its less binding affinity in SS1 pocket. The quenching results shown by flavins indicate that electrostatic interaction between flavins and protein may play a major role in binding process. FAD and FMN, containing negatively charged phosphate group(s) in structure, like to bind to SS1 which is surrounded by several positively charged amino acid residues (ARG252, ARG222, LYS199, HIS242, ARG218, LYS199)[80]. RF devoid of any negative charge is unable to have a strong electrostatic interaction. However, monitoring intrinsic fluorescence properties of TRP214 of HSA, it has been suggested that primary binding site for RF is close to TRP214.[74] Therefore, more studies like fluorescence lifetime, time-resolved anisotropy, molecular docking studies and molecular dynamics simulation are required to unambiguously conclude the binding position of RF to HSA.

After the structural aspects, we now focus on the probable mechanism of quenching. Usually, there are two possible quenching pathways: either resonance energy transfer or electron transfer from tryptophan to flavins. The possibility of energy transfer can be easily ruled out since there is no overlap between emission spectra of flavins (donor) with the absorption spectrum of tryptophan (acceptor). Therefore, most feasible reason for the quenching of flavins by HSA is the electron transfer between tryptophan and flavins. The redox potential of flavins and tryptophan also supports that electron transfer from tryptophan to flavin is the main quenching mechanism for flavin fluorescence inside the protein nano-cavity.[81, 82] It has been also shown that the electron transfer from tryptophan to flavins after photo-excitation is the primary step for the photocycle of flavins containing photoreceptor proteins.[83, 84] Although steady state studies cannot give the explicit picture of the interaction between flavins and HSA, it provides an indication that FAD and FMN bind to SS1 pocket containing tryptophan residue, whereas a small fraction of RF binds to the SS1 and larger fraction either binds to the surface of HSA or remains unbound.

The double reciprocal Benesi-Hildebrand[85] (**Chapter 3**) plots of $(1/\Delta I)$ against $[L]^{-1}$ produce a straight line for all flavins indicating 1:1 complex formation between flavins and HSA (insets in **Figure 4c.1**). The binding constant (K), which designates the strength of binding, is determined from the intercept to slope ratio of Benesi-Hildebrand plot, and the calculated values appears to be $2.4\times10^{4}M^{-1}$, $1.00\times10^{4}\ M^{-1}$ and $8.0\times10^{2}\ M^{-1}$ for FMN, FAD and RF, respectively. The standard free energy change (ΔG^{0}) of the flavins binding to HSA is

calculated from the standard thermodynamic relation ($\Delta G^0 = -RTlnK$). Using the values of K, the standard free energy change for this process of complexation is determined to be -6.0 kcal.mol^{-1}, -5.8 kcal.mol^{-1} and -3.9 kcal.mol^{-1} for FMN, FAD, and RF, respectively, at ambient temperature (298 K). From free energy change for this complex formation process, it is evident that RF does not form strong complex with HSA as that of FMN and FAD. This substantiates with the larger extents of fluorescence quenching of FMN and FAD compared to RF as mentioned before. The lowest binding free energy along with the negligible quenching of RF points toward the fact that only a small fraction of RF binds to SS1 site, and larger fraction of RF may bind to the surface of the protein or it remains unbound.

4c.2b. Excited State Lifetime Measurements

Fluorescence lifetime measurement is an excellent technique to explore the excited state environment around the fluorophore and is highly sensitive to the excited-state interaction between the probe and protein. Thus, lifetime measurements data can contribute significantly in realizing the interaction process between flavins and HSA. In buffer, at pH 7, FAD

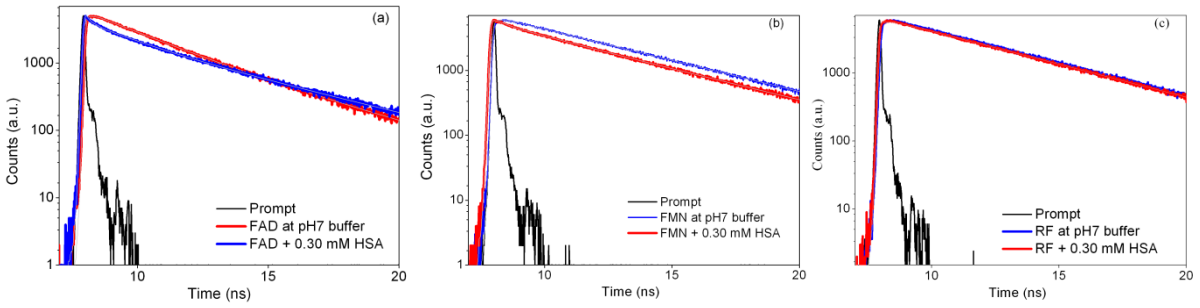

Figure 4c.2. *Lifetime decay profiles of (a) FAD, (b) FMN and (c) RF in pH 7 buffer and 0.3 mM of HSA media.*

exhibits a bi-exponential decay with two lifetimes of ~4.3 and ~2.3 ns having relative contribution of 33% and 67% (**Table 4c.1**, **Figure 4c.2**). The ~4.3 ns component represents the 'unstack' conformer, whereas the ~2.3 ns component represents 'partially stack' conformer of FAD in which the isoalloxazine moiety does not stack but interacts with the other parts of the molecule, resulting in a less efficient quenching. It is pertinent to mention that a reasonable percentage of 'stack' conformer also exists at this experimental condition; however, we could not able to monitor the dynamics of 'stack' conformer due to its quenched

lifetime of ~10 ps,[53] which is beyond of our instrument time-response (~40 ps). With the gradual increase of HSA concentration, the lifetime of the two conformers remains the same, but the contribution for the short component sharply falls down. Moreover, after a certain protein concentration a new component with a reduced lifetime of around 150-200 ps appears. This reduced lifetime is an outcome of the quenching effect of FAD by TRP214 in

Table 4c.1. *Fluorescence lifetime parameters of FAD, FMN and RF with different concentrations of HSA measured in TCSPC setup.*

Sample	a_1	τ_1 (ns)	a_2	τ_2 (ns)	a_3	τ_3 (ns)	$\langle\tau\rangle^{\#}$ (ns)	χ^2
FAD in pH 7	0.67	2.29	0.33	4.29	-	-	2.95	1.00
HSA 0.06 mM	0.56	2.04	0.44	4.31	-	-	3.04	1.00
HSA 0.18 mM	0.30	2.14	0.35	4.61	0.35	0.17	2.32	1.03
HSA 0.30 mM	0.23	2.00	0.29	4.80	0.48	0.16	1.93	1.08
FMN in pH 7	1.0	4.52	-	-	-	-	4.52	1.08
HSA 0.06 mM	1.0	4.44	-	-	-	-	4.44	1.11
HSA 0.18 mM	0.76	4.61	0.12	2.56	0.12	0.13	3.86	0.94
HSA 0.30 mM	0.62	4.71	0.15	2.52	0.23	0.34	3.38	0.99
RF in pH7	1.0	4.51	-	-	-	-	4.51	1.09
HSA 0.06 mM	1.0	4.50	-	-	-	-	4.50	1.03
HSA 0.18 mM	1.0	4.51	-	-	-	-	4.51	1.07
H SA 0.30 mM	1.0	4.48	-	-	-	-	4.48	1.08

$^{\#}\langle\tau\rangle = a_1\tau_1 + a_2\tau_2 + a_3\tau_3$

SS1 binding pocket of HSA. With the increase in protein concentration, the relative contribution of this new component enhances with subsequent decrease in contribution of the other two components. FMN in general exhibits a single exponential decay at pH 7 (**Table 4c.1**, **Figure 4c.2**). But after a certain concentration of protein (> 0.06 mM) a new short-lived component of ~650 ps appears and this component further quenches down as the HSA concentration increases. The reduced lifetime is originated due to quenching of FMN by TRP214 in SS1 binding pocket. The lifetime results of FMN and FAD support well our steady state results. FMN, FAD inside several flavoproteins also exhibits similar characteristics. The fluorescence decay profiles of FAD in the binding pockets of medium-chain acyl Co-A dehydrogenase (MCAD) and glucose oxidase (GOD) are extremely fast

compared to that of FAD in solution, which is attributed to the ultrafast electron transfer from surrounding TRP moiety to FAD.[27] FMN inside the binding pocket of flavodoxin also displays fast fluorescence decay due to the rapid electron transfer from the surrounding amino acid residue to the excited FMN.[86] Unlike FMN and FAD, RF does not show any quenching effect on lifetime with variable protein concentrations (**Table 4c.1**, **Figure 4c.2**); although in steady state spectra RF exhibits ~17% quenching (**Figure 4c.1**). Therefore, the decrease of emission intensity of RF in presence of HSA may be ascribed to static quenching. According to the earlier reports, the primary binding site of RF is close to TRP214.[74] Earlier reports as well as all the present evidences suggest that small fraction of RF molecules form dark complexes with TRP214 at SS1. The strong stacking interaction between neutral RF and tryptophan may be involved in electron transfer, which could result in the formation of dark complex. Mataga *et al.* also reported similar non-fluorescent riboflavin binding protein (RBF) in which the isoalloxazine ring of RF is stacked between tryptophan and tyrosine.[27] Computational studies (discussed later) show that RF is closer to TRP214 than both FMN and FAD. Detail insight about the molecular picture of complex formation will be discussed in the docking and molecular dynamics simulation section.

4c.2c. Time Resolved Anisotropy Measurements

When the probe binds to protein binding pocket, the rotational motion of the probe is expected to be restricted, which is reflected in the soaring rotational relaxation time of the probe. Time-resolved anisotropy results are presented in **Table 4c.2** and shown in

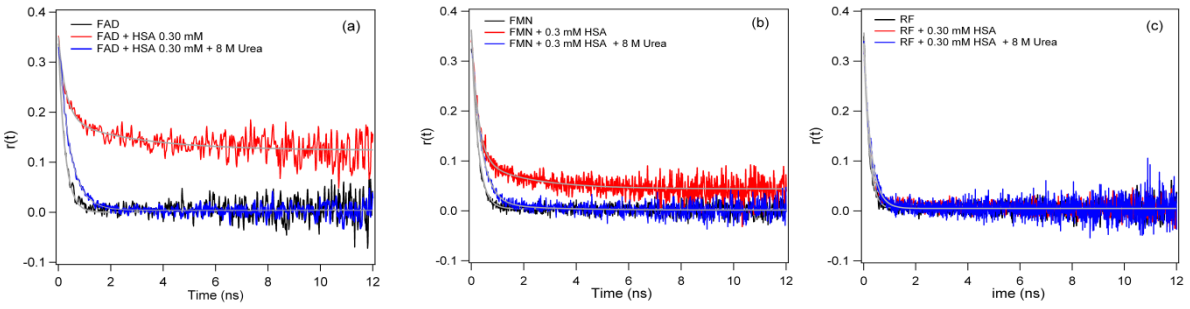

Figure 4c.3. *Anisotropy decay profiles of (a) FAD, (b) FMN and (c) RF in pH 7 buffer with 0.3 mM of HSA and 8 M urea containing 0.3 mM HSA*

Figure 4c.3. In the absence of HSA, single exponential anisotropy decay is observed with rotational correlation time ~250 ps and ~270 ps corresponding to FMN and FAD, respectively. This indicates that the probe molecules experience a homogeneous environment in normal buffer medium. In presence of HSA, the anisotropy decay is expected to be non-exponential because of distinctly different rotational relaxation times of the free and protein-bound molecules. This is indeed the case for FMN and FAD (**Figure 4c.3**). A nanosecond component along with the above mentioned 250-270 ps component appears in the anisotropy decay profiles of FMN and FAD (**Table 4c.2**). The fast anisotropy component represents the rotational time of unbound FMN and FAD, whereas the long component represents the rotational motion of protein-bound FMN and FAD. Another important feature observed in anisotropy study is that the anisotropy decay profile of FAD in presence of HSA is slower than that of FMN under the same condition, possibly due to stronger electrostatic interaction having two negatively charged phosphate groups compared to FMN, which consists of only

Table 4c.2. *Anisotropy decay characteristics of FAD, FMN & RF with different concentrations of HSA in native and denatured state measured in TCSPC setup.*

Sample	r_0	a_{1r}	τ_{1r} (ns)	a_{2r}	τ_{2r} (ns)	$\langle\tau_r\rangle$ (ns)
FAD in pH7	0.37	0.34	0.272	-	-	0.272
FAD + 0.06 mM HSA	0.38	0.36	0.299	-	-	0.299
FAD + 0.30 mM HSA	0.39	0.19	0.298	0.072	2.27	0.827
0.30 mM HSA + U 8 M	0.35	0.35	0.474	-	-	0.474
FMN in pH7	0.36	0.36	0.254	-	-	0.254
FMN + 0.06 mM HSA	0.35	0.35	0.261	-	-	0.261
FMN + 0.30 mM HSA	0.35	0.30	0.255	0.050	2.47	0.676
0.30 mM HSA + U 8 M	0.36	0.36	0.433	-	-	0.433
RF in pH7	0.36	0.36	0.200	-	-	0.200
RF + 0.06 mM HSA	0.33	0.33	0.230	-	-	0.210
RF + 0.30 mM HSA	0.35	0.35	0.240	-	-	0.233
0.30 mM HSA + U 8 M	0.34	0.34	0.284	-	-	0.284

one phosphate group. Therefore, rotational motion of FAD inside the SS1 binding pocket is more restricted than that of FMN. RF exhibits single exponential anisotropy with a rotational correlation time of ~200 ps in buffer solution of pH 7. Unlike FMN and FAD, the anisotropy

decay features of RF in presence of HSA are almost unchanged (**Figure 4c.3**). This suggests that RF does not sense any change of microenvironment even in the presence of HSA. However, it has already been established from the steady state fluorescence and lifetime results that RF inside the SS1 forms a dark complex with TRP214 and this dark complex cannot contribute to the anisotropy decay as it is almost non-fluorescent in nature. Therefore, we anticipate that the observed anisotropy decay profile for RF in presence of HSA is an outcome of unbound and (or) surface bound (binding to SL site) RF molecules.

If flavins (FMN, FAD) bind to HSA in its nano-cavity, unfolding of protein will lead to dissociation. Therefore, we studied the effect of protein denaturation on the rotational motion of flavins. Urea induced protein unfolding is a well-examined system,[47, 87-90] and this process for HSA takes place at a single two state transition with an intermediate at 4-6 M urea concentration.[91, 92] In the present work, a fixed concentration of HSA was titrated by raising concentration of urea and the fluorescence intensity change of tryptophan was plotted with variable urea concentrations. Sigmoidal feature of the curve clearly indicates that complete denaturation of HSA takes place at ~8 M urea, in agreement with a previous study.[77] On gradual addition of urea to the 0.3 mM HSA containing flavin solution, the anisotropy decay profiles become faster. At 8 M urea, the decay profiles have very close resemblance to that of flavin solutions at pH 7 buffer (**Figure 4c.3**). However, the anisotropy decay profiles of flavins do not coalesce to that of flavins at pH 7 buffer solution, as the viscosity of the medium is quite higher than that of pH 7 buffer medium due to the addition of 0.3 mM HSA as well as 8 M urea to flavins containing pH 7 buffer solution (**Figure 4c.3**). The above observation clearly implies that flavins were bound to the SS1 of HSA in its native state, and after denaturation all the flavin molecules come out from the binding pocket to the bulk medium. This gives the close resemblance of anisotropy decay profiles of flavins in the denatured state to that of flavins at pH 7 buffer.

4c.2d. Structural Information of Protein Using Circular Dichroism

Circular dichroism (CD) spectroscopy is vastly exploited to monitor structure, conformation and stability of proteins under both bound and unbound conditions with various drugs and ligands.[93-96] CD can provide a notion about the fraction of residue of the protein involved in the formation of α-helix, β-sheets or random coils. From CD spectra one can also have a good measure of the percentage variation of structural contents. To ascertain the possibility of structural change of HSA during the interaction with flavins, we employed far UV circular

dichroism studies within a range of 200 nm to 250 nm. In absence of any of the flavins, CD spectra show two minima at 208 nm and 222 nm, which is a clear signature of high content of α-helix structure in the protein under study (**Figure 4c.4**). These peaks are in good agreement with previous reports, which articulate that HSA contains around ~65% of α-helix in its native structure.[95, 97, 98] In the presence of flavins, the CD spectra are exactly superimposed with that of HSA alone (**Figure 4c.4**). This observation leads us to conclude that the binding

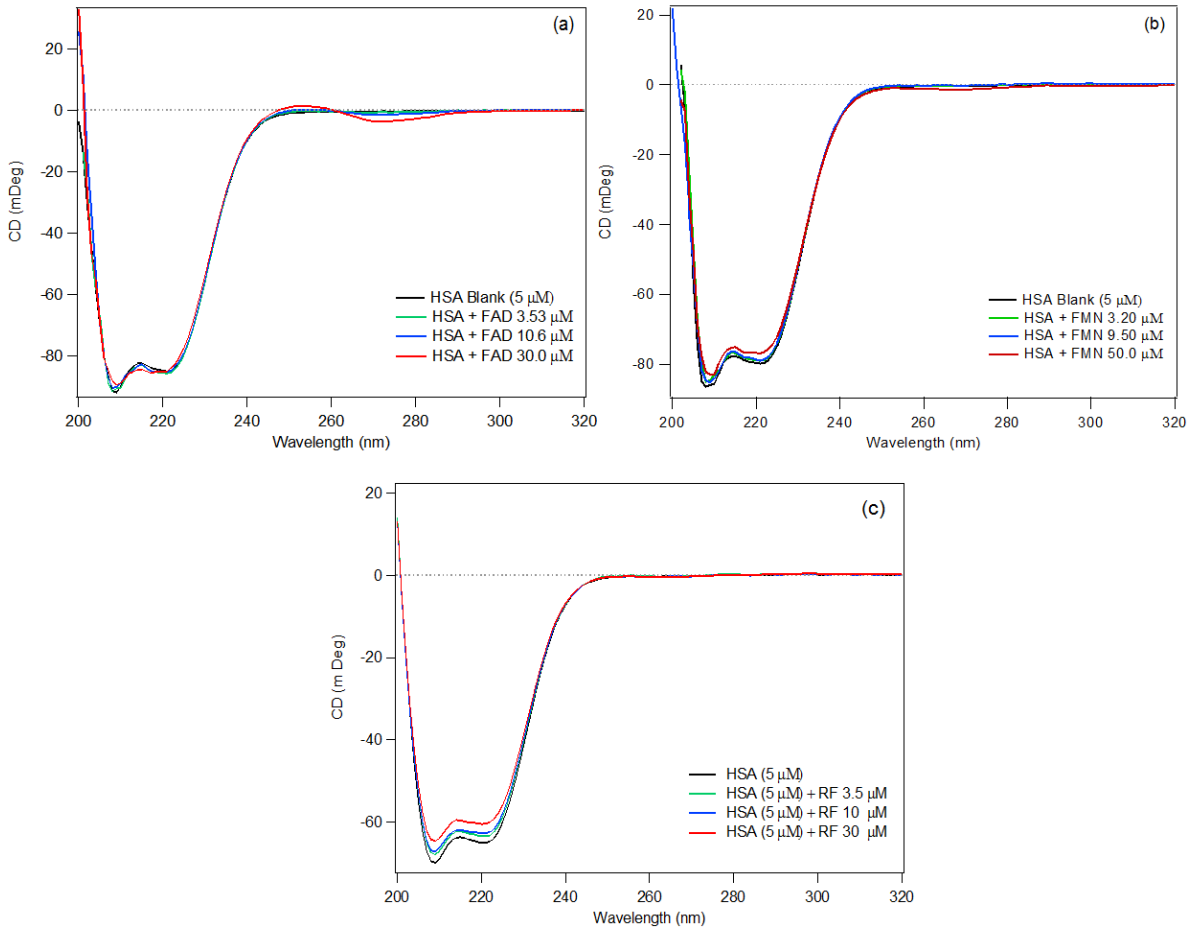

Figure 4c.4. *CD spectra of HSA with variable concentration of (a) FAD, (b) FMN and (c) RF.*

of flavins to HSA does not change the secondary structural pattern of the protein itself. RMSD values obtained from simulation studies (discussed later) also support the conclusion drawn from CD studies. We cannot exclude the possibility of tertiary structural change of protein upon binding with flavins. However, we cannot monitor the tertiary structural change of protein upon binding with the flavins as later exhibits strong CD signal in this region.

4c.2e. Thermodynamic Parameters from ITC

Isothermal titration calorimetric profiles for flavins with HSA are shown in **Figure 4c.5** and the results have been provided in **Table 4c.3**. Each peak of the binding isotherm in upper panel represents each of the flavin injections. The amount of heat liberated by successive addition of flavin is plotted against the molar ratio of flavin to HSA at lower panel. A standard nonlinear least-square regression binding model for one site binding is employed to fit the data. The best fit is shown in lower panel. From the fitting of binding curves, the binding stoichiometry of 0.54 and 0.65 are observed for FAD and FMN, respectively. The binding stoichiometry suggests that each flavin molecule binds to two different protein molecules at a time, or it might be portrayed that each flavin binds to a dimeric protein molecule. However, steady state results confirm 1:1 binding between HSA and flavin. If one flavin molecule simultaneously binds to two HSA, then it would be reflected in the Benesei-Hildebrand plot. Therefore, we infer that flavin may bind to one binding pocket of dimeric

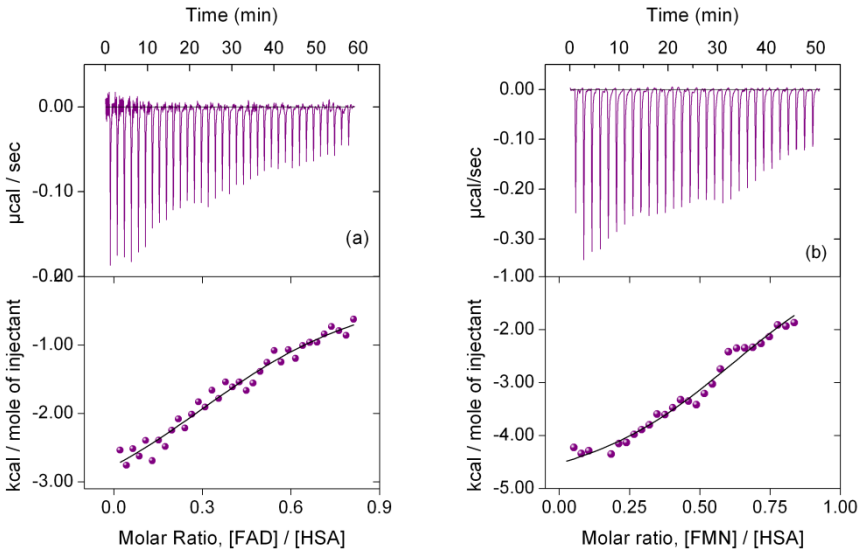

Figure 4c.5. *Isothermal calorimetric titration profiles of HSA by (a) FAD and (b) FMN at 298 K*

protein. In this context it is pertinent to mention that the titration method in ITC and fluorescence are quite different. In fluorescence, a flavin containing solution is titrated by HSA, whereas in ITC a protein solution is titrated by concentrated solution of flavin. Probably, the concentration of HSA taken for ITC study has propensity to form dimer. When same experiment was repeated with a lower concentration of HSA, maintaining the protein to

probe ratio same as 1:5, we did not get any binding enthalpy from that study. Therefore, we anticipate that the affinity of binding is not appropriate at lower concentration of HSA. **Table 4c.3** shows that the binding of both FAD and FMN shows negative heat of deflection, indicating an exothermic nature of binding. The favorable enthalpy change primarily reflects the strength of the interactions of the ligand (FMN/FAD) with the HSA (e.g. van der Waals, hydrogen bonds, etc.) is relatively higher than those existing with the solvent. However, entropy change during binding process is positive for both of FMN and FAD, and it can be inferred that these interactions are also entropy driven along with enthalpy. Here, it should be mentioned that ITC measures total entropy and it includes entropy change of the protein, water and ligand for binding. CD and simulation studies confirm that binding of flavins to HSA does not change the secondary structure of protein itself. Therefore, in

Table 4c.3. *Binding parameters of FAD and FMN with HSA obtained from ITC experiment.*

Sample	N	K (M^{-1})	ΔH^0 (cal/mol)	ΔS^0 (cal/mol/deg)	ΔG^0 (kcal/mol)
FAD in HSA	0.54	(3.28±0.18) x 10^3	-3715 ±250	8.21	-6.78
FMN in HSA	0.65	(5.54±0.35) x 10^4	-5168 ±375	4.38	-6.47

absence of conformational changes of protein, the positive entropy may originate from the increased solvent entropy due to burial of FMN/FAD inside protein binding pocket and release of water upon binding. The binding constants as well as free energy of association have a good agreement with the results evaluated form steady state fluorescence data. Moreover, the value of enthalpy and entropy change suggests that there are almost no structural changes when flavins bind with HSA.[99] Our CD results also support this conjecture. The higher binding constant as well as negative free energy change of FMN compared to FAD might be attributed to the smaller size of FMN compared to FAD. FMN probably fits better than FAD within the binding pocket in SS1 due to its smaller size. We are unable to get any result about the interaction of RF with HSA by ITC study under the same experimental condition. However, as discussed before, fluorescence studies suggest that only a fraction of RF molecules form dark complex with TRP214 at the SS1 site, which may not be strong enough to be detected by the ITC instrument.

4c.2f. Docking and Molecular Dynamics Simulation

Docking and molecular dynamics simulations are essential tools to understand the molecular interaction and dynamics of two bound species. To verify the experimental observations of FMN and FAD binding to SS1 and only a fraction of RF binding to the same SS1 pocket of HSA, we have employed docking studies of flavins with HSA followed by molecular dynamics (MD) simulation study, detailed outcome of which is presented here. We have first performed 10 ns simulation of the protein alone in water to observe its stability.

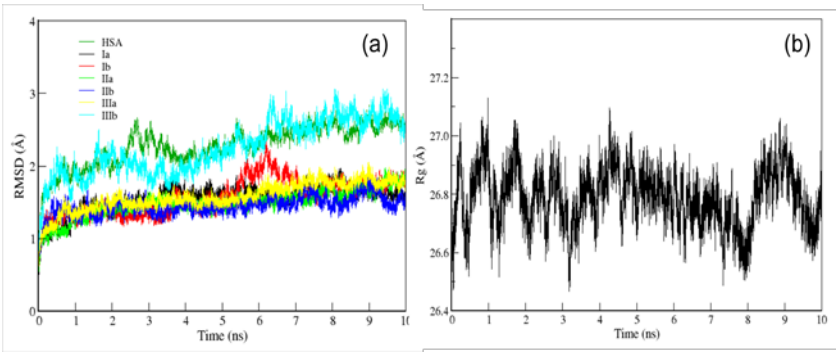

Figure 4c.6. *(a) Time evolution of the RMSD for the whole protein (HSA) and its different domains from the crystal structure, (b) time evolution of the radius of gyration (Rg).*

The root mean square deviation (RMSD) of the full protein and its different domains are shown in **Figure 4c.6a**, which suggests that the protein is well equilibrated as the RMSD value fluctuates around 2.5 Å for the last 4 ns. Radius of gyration (R_g), which is a measure of the size of the protein, is shown in **Figure 4c.6b**. The radius of gyration of HSA also fluctuates around 26.7 Å which is comparable to that of experimental value of 27.4±0.350 Å.[100] Note that neither the RMSD, nor the R_g shows large deviation from the crystal structure as opposed to Sudhamalla *et al.*[101] and in agreement with Deeb *et al.*[102]

To obtain preliminary information about the binding site, first we have searched the whole protein using genetic algorithm in docking software AutoDock.[103] This preliminary docking showed that RF binds to three different binding sites, SS1, SL, and SS2 (**Scheme 2.3, Chapter 2, Section 2.1c**), while FAD and FMN show binding affinity only to SS1 site that accommodates the amino acid tryptophan (TRP214, see **Scheme 2.3, Chapter 2, Section 2.1c**). To obtain best docked structures for all the flavins, we performed docking of each flavin to their preferred binding sites using more refined grid. **Table 4c.4** summarizes the

binding energy and other parameters of all the docking studies. To obtain more accurate and flexible bound complex, we performed molecular dynamic simulations of HSA-flavin systems for 4 ns starting with best docked structure of each flavin molecule onto previously 10 ns equilibrated protein.

RF shows affinity towards three different sites of the HSA, out of which two are comparable as shown in **Figure 4c.7** (**Figure 4c.7, 4c.8, 4c.9** and **Appendix 4c.3** are made using UCSF Chimera[104]). The binding energies of RF to the three sites are comparable (**Table 4c.4**). **Figure 4c.7a** shows RF bound to the SS1 pocket involving stacking interaction with TRP214. The hydroxyl groups of ribityl side chain of RF forms intermolecular hydrogen bonding with GLY196, LYS199, GLU153 and the carbonyl group of isoalloxazine ring involves in hydrogen bonding interaction with ARG218. The stability is also contributed by the electrostatic interaction between the side chain and basic amino acid residues present in

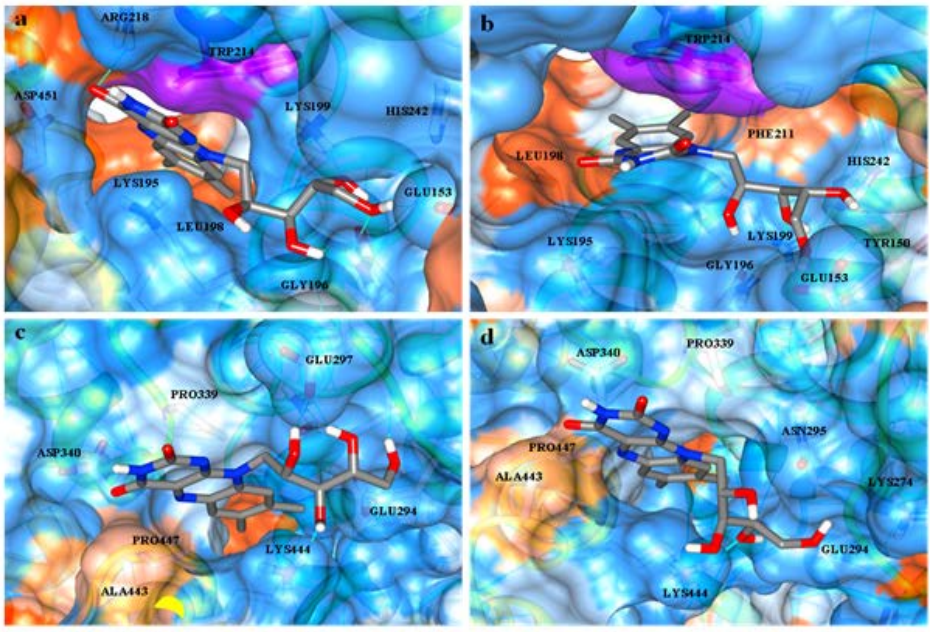

Figure 4c.7. *(a) RF bound to SS1 after docking (b) RF bound to SS1 after 4 ns simulation. (c) RF bound to SL after docking (d) RF bound to SL after 4 ns simulation. RF is given element-based colour. The amino acids are coloured according to hydrophobicity except TRP214 which coloured purple.*

the hydrophilic side of the binding pocket. The centre of mass distance between flavin and tryptophan rings is 5.41 Å. **Figure 4c.7b** shows the same structure obtained at the end of 4 ns molecular Therefore, this structure indicates better stacking interaction of RF with TRP214 compared to the docked complex. **Figure 4c.7c** shows the binding of RF to the surface of

HSA close to LYS444 at the SL site. This binding site is contributed by sub-domains IIIa, IIa and IIb. The isoalloxazine ring is flanked by PRO339 and PRO447. Ribityl side chain forms hydrogen bonding with GLU297, GLU294 and LYS444. **Figure 4c.7d** shows the same interaction obtained after 4 ns simulation, and it indicates that the surface binding pocket (SL site) of RF (close to LYS444) has also undergone conformational change 5.41 Å.

Table 4c.4. *Different interaction energies between flavin derivatives and the protein in the best docked structure obtained from AutoDock. Binding site for each is also mentioned.*

Flavin	Binding sites	Binding energy (kcal/mol)	vdw-hb-desolvation energy (kcal/mol)	Electrostatic interaction energy (kcal/mol)	Tortional energy (kcal/mol)
RF	SS1	-3.19	-4.32	-1.56	2.68
RF	SL	-2.32	-3.30	-1.70	2.68
RF	SS2	-0.86	-2.09	-1.45	2.68
FMN	SS1	-1.82	-3.30	-2.10	3.28
FAD	SS1	2.74	-0.72	-2.21	5.67

The third binding site of RF is the SS2 (**Appendix 4c.3**). Here, the methyl side chain of isoalloxazine ring forms hydrophobic interaction with LEU407 and ribityl side chain forms hydrogen bonding with ARG410 and LYS414. Binding of RF to SS1 can lead to strong

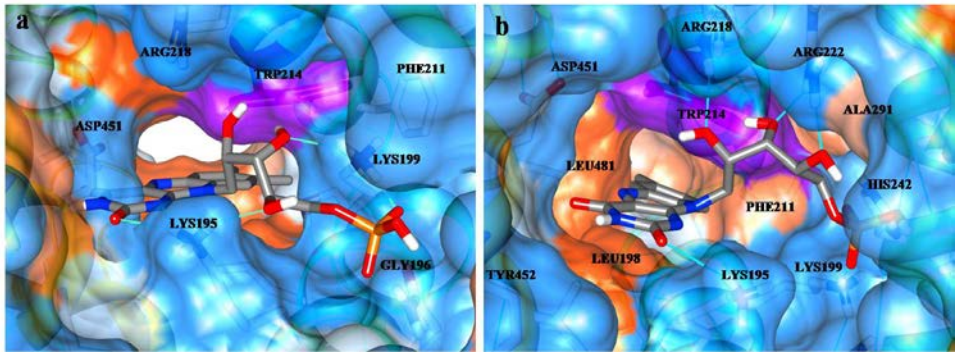

Figure 4c.8. *(a) FMN bound to SS1 after docking (b) FMN bound to SS1 after 4 ns simulation. Other details are same as that of* ***Figure 4c.7****.*

stacking interaction between tryptophan (TRP214) and isoalloxazine ring of RF, and this strong stacking interaction results in the formation of almost dark complex between two, as

they may be involved in intermolecular electron transfer process. However, binding to the other two sites will not affect the fluorescence of the RF (since these sites are away from TRP214). Steady state fluorescence experiment confirms ~20% reduction in fluorescence of RF on mixing with HSA. Therefore, presence of three comparable binding sites of RF results in binding a fraction of RF molecules to SS1 site, which leads to only a moderate quenching in the fluorescence.

Figure 4c.8a shows the binding of FMN to SS1 binding pocket of HSA only. Here, the negatively charged FMN molecule is more towards the hydrophilic region of the binding pocket and makes the interactions with surrounding positively charged amino residues such as ARG218 and LYS199. Like RF, FMN forms stacking interaction with TRP214 which is responsible for the drastic decrease in fluorescence intensity. The methyl groups of isoalloxazine ring face towards hydrophobic part of the SS1.Moreover, the isoalloxazine ring forms hydrogen bonding with ASP451 and LYS195, whereas ribityl side chain involves hydrogen bonding interaction with LYS195. The stability is also increased by electrostatic interaction between terminal phosphate group of FMN and surrounding two positively charged amino acid residues (LYS199 and GLY196). Consequently, the electrostatic interaction energy of FMN is more negative than RF (**Table 4c.4**). **Figure 4c.8b** shows the same structure after 4 ns of molecular dynamics simulation. In the case of FMN, SS1 has undergone more conformational change in order to involve in increased stacking interaction with TRP214. This also increases the electrostatic interactions between the basic amino acid residues and negatively charged side chain of FMN as shown in **Figure 4c.8b**.

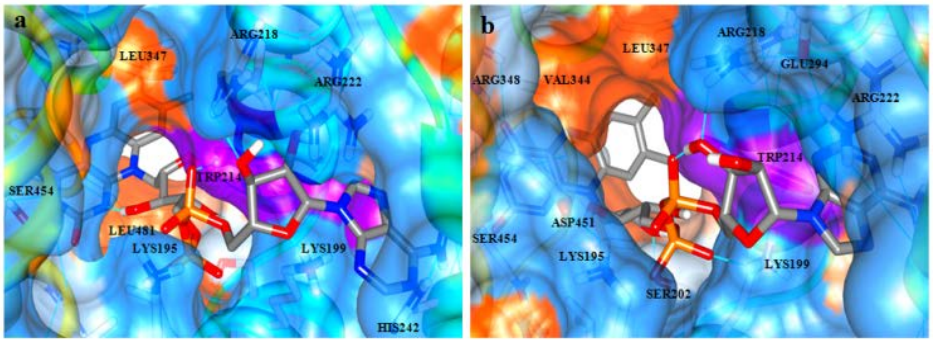

Figure 4c.9. *(a) FAD bound to SS1 after docking (b) FAD bound to SS1 after 4 ns simulation. Other details are same as that of* ***Figure 4c.7****.*

Figure 4c.9a displays the binding of FAD to SS1 site of HSA. FAD binds to this

binding pocket only in the 'unstack' conformation. Here, the isoalloxazine ring points more towards hydrophobic portion, whereas methyl groups face towards LEU347. The ribityl side chain directs towards the hydrophilic region of the binding pocket. The carbonyl groups of the ring make hydrogen bonding with SER454. Moreover, the stability is increased by hydrogen bonding between ribityl side chain and ARG218, ARG222, LYS195 and LYS199. The adenine ring of FAD is stabilized by interaction with HIS242. Furthermore, the stability is gained by the electrostatic interactions between two negatively charged phosphate groups and positively charged surrounding amino acid resides. However, total binding energy obtained for FAD from AutoDock is positive. The reason for the positive binding energy lies in the unusually high torsion energy of (5.7 kcal/mol) of the drug (**Table 4c.4**). It should be mentioned here that docking energy is only empirical in nature. Moreover, due to absence of dynamics, flexible optimization is also not possible. Therefore, molecular dynamics simulation was adopted to achieve proper bound complex and average energy. **Figure 4c.9b** shows the FAD bound to SS1 after 4 ns simulation. Here, conformational change has taken place to form hydrophobic interactions with VAL344 and LEU347. Here, adenine ring of FAD is shifted more towards TRP214. It is clear from **Figure 4c.9b** that isoalloxazine ring is on one side of tryptophan residue and adenine ring on the other side of tryptophan. Here the ring is close to TRP214 but the distance and orientation of the isoalloxazine ring is not suitable for stacking interactions like RF and FMN. However, the closeness of the flavin ring towards the tryptophan residue may be responsible for fluorescent quenching of FAD, albeit, lesser than FMN. Although RF has better stacking interaction than FMN and FAD, it has other competitive binding sites where quenching is not possible. Hence, overall RF exhibits trifling quenching than that of FMN and FAD.

Table 4c.5. *Short range Coulombic and Lennard-Jones potentials between HSA and different flavins.*

Systems	Coul-SR (kcal/mol)	LJ-SR (kcal/mol)
HSA-RF (SS1)	-37.46 ± 0.105	-31.930 ± 0.050
HSA-RF (SL)	-14.41 ± 0.048	-21.764 ± 2.318
HSA-FMN	- 51.77 ± 0.118	-36.921 ± 0.027
HSA-FAD	-77.61 ± 0.085	-77.995 ± 0.045

Table 4c.5 shows the average non-bonding interaction energy (electrostatic interaction and van der Waals interaction) between HSA and flavins obtained from molecular dynamics simulations. It shows that RF binds to SS1 pocket stronger than SL in terms of both

the van der Waals and electrostatic interaction. Both FMN and FAD show more electrostatic interaction energy compared to RF because of the presence of negatively charged terminal phosphate groups in the formers. In case of FMN, electrostatic interaction predominates over van der Waals interaction. Among FMN and FAD, later shows stronger electrostatic interaction with the basic amino acids present in the SS1 because of the presence of two phosphate groups in FAD. For binding of FAD in SS1 site, both electrostatic and van der Waals interactions contribute similarly.

It should be noted that the binding energy obtained from docking and molecular dynamics simulation are different due to the different force-field used in both cases. Docking uses empirical energy function based on specific atom types and fixed interaction energy. Molecular dynamics, on the other hand, uses quantum chemically derived all atom force-field and uses distance dependent energy functions. Therefore, the energy values obtained from two above methods are not comparable. However, they can be used to understand the qualitative aspect of the interaction between the protein and the ligands (flavins). Moreover, in molecular dynamics simulation, we provided only the average potential energy, not the free energy as the later would require much more extensive set of simulations and may be beyond the scope and the goal of the present article.

Average RMSD and radius of gyration of HSA in different systems are shown in **Table 4c.6**. (**Appendix 4c.4** and **Appendix 4c.5**). After 2.5 ns simulation RMSD fluctuation is around 2 Å in all the systems indicating the stability of systems and shows the reliability of the docking. The average RMSD for the whole protein in simulation of HSA alone is 2.09 Å as shown in Table 4c.6. RMSD's for protein-flavin complexes are also within permissible range of molecular dynamics simulation. The conformational fluctuation of each of the amino acids in the binding site (SS1) is analysed using root mean square fluctuation (RMSF) values.

Table 4c.6. *RMSD and Radius of Gyration values for HSA chain in different HSA-flavin systems*

Systems	RMSD (Å)	Radius of Gyration (Å)
HSA	2.09 ± 0.087	26.89 ± 0.095
HSA-RF (SS1)	2.52 ± 0.169	27.19 ± 0.097
HSA-RF (SL)	2.60 ± 0.119	27.10 ± 0.101
HSA-FMN	2.63 ± 0.120	27.13 ± 0.096
HSA-FAD	2.32 ± 0.128	27.26 ± 0.114

Appendix 4c.6A, **Appendix 4c.6B** and **Appendix 4c.6C** depict the RMSF of HSA complexed with RF, FMN and FAD, respectively compared to that of the un-complexed HSA.

4c.3. Conclusion

Three different flavins (RF, FMN and FAD) interact with HSA in different extents, and the binding interactions between flavins and HSA have been monitored with the help of steady state and time-resolved fluorescence spectroscopy, isothermal titration calorimetry, circular dichroism studies. Flavins have been reported for the first time as an extrinsic fluorescence marker for a model transport protein HSA. Steady state and time-resolved fluorescence studies confirm that major fraction of FMN and FAD molecules bind to the SS1 binding

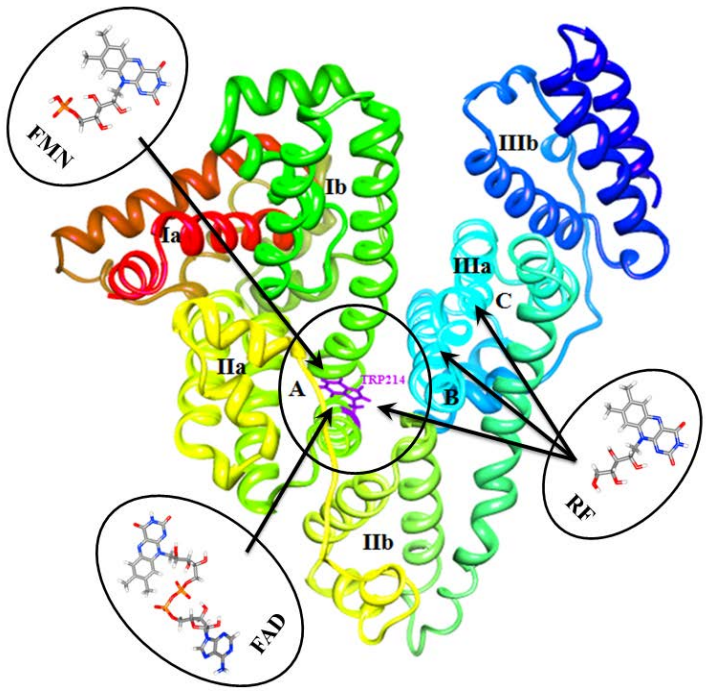

Scheme 4c.1. *Schematic representation of Flavin (FAD, FMN and RF) binding locations in HSA.*

pocket of HSA (**Scheme 4c.1**). For RF, a small fraction binds strongly with TRP214 in the SS1 binding pocket of HSA and forms a dark complex with TRP214 (**Scheme 4c.1**). The remaining fraction of RF molecules either reposes on protein surface or remains unbound. The thermodynamic parameters like free energy, enthalpy and entropy change of the binding interactions between flavins and HSA are determined with the help of ITC study. Finally, the

molecular picture of binding interaction between flavins and HSA are well explored by docking as well as molecular dynamics studies. This study might furnish a new perception towards the understanding of interactions between flavins and surrounding amino acids in the binding pocket of flavoproteins (**Scheme 4c.1**).

4d. Role of Mg^{+2} Ions over Flavin Recognition by RNA Aptamer: Spectroscopic and Thermodynamic Glimpse

4d.1. Motivation

Aptamers are small sequence of nucleotides engineered through repeated rounds of *in vitro* systematic evolution of ligands by exponential enrichment (SELEX) and can sense specific molecular targets with high selectivity.[105-108] RNA aptamers are characterized by unpaired or mismatched bases, which folds RNA into distinct secondary and tertiary structures containing loops and bulges suitable for selective interactions with small molecules, proteins, nucleic acids, cells, tissues and organisms.[109-115] Although the importance of RNA aptamer as small molecular target has been portrayed by a number of studies[116], a little has been focused on electron shuffling cofactor binding aptamers. The ubiquitous existence of flavins in nature[1-10, 16, 31-35] and its involvement in various biological activities like, efficiency to catalyze single and/or double electron transfer reactions, controlling circadian rhythm in higher organisms, directing the light induced tropism in plants etc. [1-10, 16, 31-35] have spurred enthusiasm about flavin binding RNA aptamers. Burgstaller *et al.* first isolated aptamer sequences, which are able to recognize flavin co-factors.[117, 118] NMR results conclude isoalloxazine ring of flavin mononucleotide (FMN) intercalates between G-G mismatch and G-U-A base triple, which results the selective affinity for flavins.[119] Moreover, this recognition specificity is associated with hydrogen bonding of the uracil like edge of isoalloxazine to Hoogsteen edge of adenine at the interaction site. This structural stabilization has been employed to the design allosteric ribozyme whose self-cleavage and self-ligation reactions are enhanced nearby 300-fold in

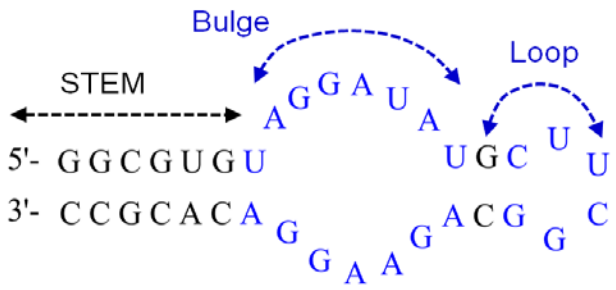

Scheme 4d.1. 35-mer self loop forming flavin binding RNA aptamer

presence of FMN because of structural stabilization upon binding with cofactors.[120, 121] Later Lauhon *et al.* isolated riboflavin and nicotinamide redox cofactors detecting RNA aptamer, for which riboflavin recognition leads to two-tiered G-quartet structural reformation.[122] Although selective to redox co-factors, aptamers never found to differentiate binding between oxidized and reduced form of 5-deazariboflavin derivative, which is a structural analog of riboflavin.[122] SELEX method has been used to identify RNA aptamers that recognizes flavin adenine dinucelotide (FAD) but unable to distinguish FAD from $FADH_2$.[123] Anderson *et al.* detected 14-mer RNA aptamer selective to flavins (riboflavin, FMN and FAD) through experimental and computational methodologies and showed better interaction with FMN compared to others.[124] The electron density on the phosphate group is speculated to partially delocalize on the flavin ring, which strengthen hydrogen bonding and π-stacking interactions between isoalloxazine and nucleobases.[124] Notably, literatures lack any detailing about higher selectivity towards FMN as well as structural information about FAD-aptamer complexation. The major complexity of FAD compared to FMN is the existence of FAD in variable conformations (namely, 'stack', 'partially stack' and 'unstack') in water, as it contains adenine and isoalloxazine moieties in its structure.[11-15, 23-26] Therefore, it seems interesting to find out particularly which conformer of FAD is appropriate for the interaction with aptamer. Since the dinucleotide cofactors seem to have special evolutionary importance, it is worth having a better insight about their interactions with RNA aptamer (**Scheme 4d.1**). Therefore, we intend to explore this understanding with the help of biophysical techniques, e.g., steady state, time-resolved fluorescence, circular dichorism (CD) and isothermal titration calorimetry (ITC). Although it's well established that thermodynamic parameters, like, enthalpy and entropy changes are the governing factors for small molecule detection, previous reports paid least attention to the thermodynamics insight of flavin recognition by RNA aptamer. Hence, a detailed investigation about thermodynamics of flavin-aptamer interaction is necessary in order to provide insight into the selectivity and feasibility of flavin sensing.

It is well known that few mono and bivalent metal ions at high concentrations stabilize RNA tertiary structures, though the exact mechanism is still under mist. Researchers found K^+ and Mg^{+2} offers most effective stability to RNA structures. Draper and co workers establishes that a folded RNA structure interacts in a better way to Mg^{+2} ions, as its phosphate charges are accumulated to a smaller volume, which results a strong electrostatic interaction with the metal ion.[125, 126] Moreover, a water solvated bivalent Mg^{+2} state is

speculated to interact through co-ordination and hydrogen bonding interactions, resulting a better stability of RNA.[127] A recent report by Fiore *et al.* shows the overall interaction between RNA and Mg^{+2} is exothermic and entropically costly.[128] In this work we intend to explore the effect of Mg^{+2} ion concentration over flavin detection by RNA aptamer.

In a nutshell, the present work is executed with three distinct targets, which are (a) exploring the binding interactions flavins (specially FAD and FMN, as they have vast structural diversity) by RNA aptamer and uncovering how the conformational flexibility of FAD affects the recognition, (b) a detailed thermodynamic insight of flavin recognition by RNA aptamer from steady state fluorescence and isothermal titration calorimetry studies, (c) the effect of Mg^{+2} ion concentrations over flavin recognition. These biophysical insights of flavin-aptamer interaction may improve the basic understanding of small molecule recognition by RNA aptamer.

4d.2. Results and Discussions

4d.2a. Steady State Absorption and Emission Results

FAD absorption in water and in presence of RNA aptamer containing 10 mM Mg^{+2} ion concentration is shown in **Figure 4d.1a** and the absorption spectra at lower Mg^{+2} ion

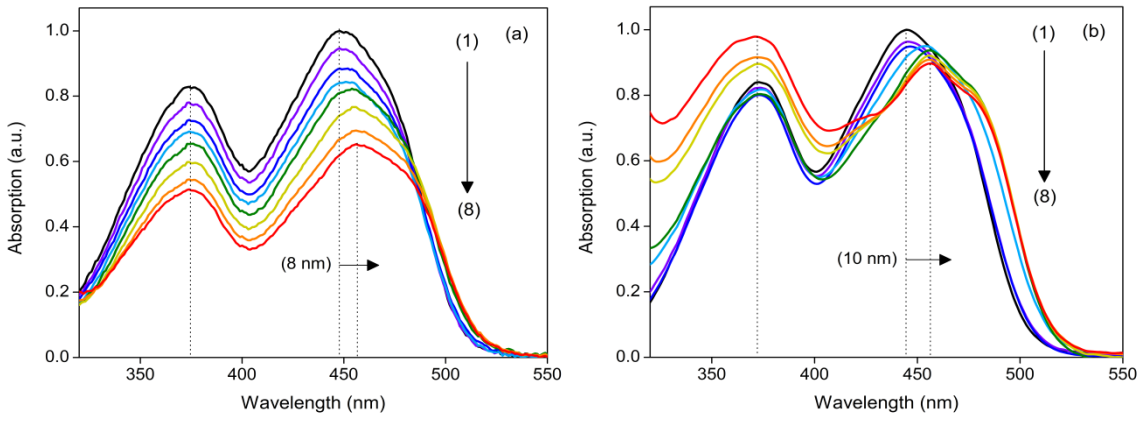

Figure 4d.1. *Absorption spectra of (a) FAD and (b) FMN in presence of 10 mM Mg^{+2} ion concentration with increasing RNA aptamer concentrations, where 1→ 8 represents concentration of RNA 0, 1, 3, 5, 10, 20, 30 and 50 μM, respectively.*

concentrations (2 mM and 4 mM) are provided in supporting information (**Appendix 4d.1**). Flavin absorption in water is characterized by two intense π-π* transition bands originated

from isoalloxazine chromophore corresponding to $S_0 \rightarrow S_1$ (λ_{abs}~450 nm) and $S_0 \rightarrow S_2$ (λ_{abs}~375 nm) transitions (**Figure 4d.1**).[15, 23, 25, 26] With increasing concentration of RNA aptamer, decreasing absorption at both of ~375 nm and ~450 nm bands of FAD is observed, which becomes more prominent with increasing Mg^{+2} ion concentrations. Moreover, a detectable red shift is found especially for $S_0 \rightarrow S_1$ band at higher RNA concentrations, which does not vary with Mg^{+2} ion concentration. FMN, a structural analog of FAD, exhibits comparable decrease in absorbance with increasing RNA concentration (**Figure 4d.1b**). A prominent red shift is also detected for FMN along with a peeping hump at ~480 nm, which might be

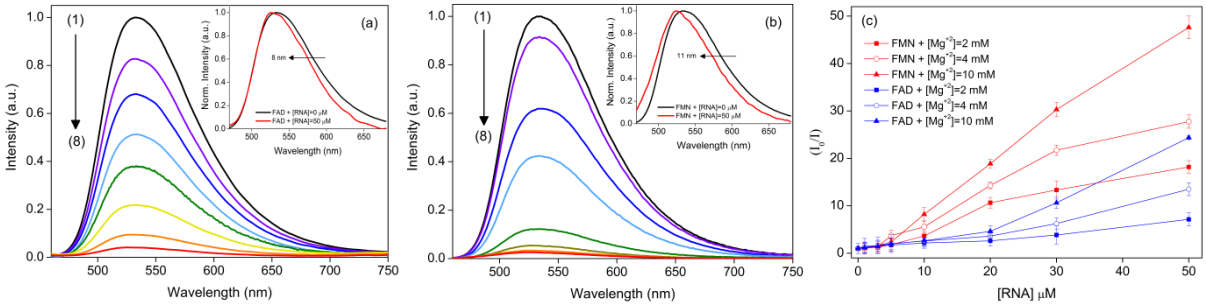

Figure 4d.2. *Emission profiles (λ_{ex} = 444 nm) of (a) FAD and (b) FMN in presence of 10 mM Mg^{+2} ion concentration, with increasing RNA aptamer concentrations, where 1→8 represents RNA concentration 0, 1, 3, 5, 10, 20, 30 and 50 μM, respectively. (c) Stern-Volmer plot of FAD and FMN in presence of different Mg^{+2} ion concentrations, where the legends carry respective meaning. Note that the line joining the point does not represent the actual fitting.*

originated due to lower energy transition of RNA-bound isoalloxazine chromophore. The red shift in absorption spectra for both FMN and FAD may be attributed to the H-bonding interaction between flavins and aptamer.[129] The decreasing absorption along with a red shift with increasing RNA aptamer and Mg^{+2} ion concentration is indicative towards interaction between FMN/FAD and RNA aptamer.

Flavins (FAD/FMN) exhibit an unstructured emission at ~530 nm in buffer (PBS, pH 7.2), which originates from isoalloxazine ring.[15, 23-26] To explore the effect of flavin fluorescence upon binding to aptamer, a fixed concentration of FAD/FMN in buffer containing 10 mM Mg^{+2} is titrated by rising concentration of RNA aptamer (**Figure 4d.2**). The emission spectra at lower Mg^{+2} concentrations are shown in supporting information (**Appendix 4d.2**). The emission intensity of both FMN and FAD decreases sharply with increasing RNA concentration. The extent of quenching for FMN is higher than FAD at any Mg^{+2} concentrations and is clearly visible from Stern-Volmer plots shown in **Figure 4d.2c.**

Moreover, FMN offers a more prominent hypsochromic shift in emission spectra compared to FAD (**Figure 4d.2,** insets). The blue shift along with strong quenching infers effective binding interactions between flavins and RNA aptamer. The extent of quenching as well as emission shift differs between FAD and FMN, and is attributed to different extent of affinity and selectivity of the aptamer towards flavins. A relatively lower extent of quenching for FAD can be attributed to its conformational flexibility ('stack' and 'unstack'). The 'stack' conformers of FAD (in which flavin ring is already involved in intramolecular quenching with adenine moiety) being almost non-fluorescent in nature, cannot participate in the interaction with RNA aptamer, and hence a lesser extent of quenching is observed for FAD. The binding interaction between FAD/FMN and aptamer is further confirmed from the changes observed in steady state anisotropy (**Figure 4d.3a**), as it provides insight about an association process. The increase in steady state anisotropy infers that the flavins experience rigid environment due to association with RNA aptamer.

Next, we focus on probable mechanism(s) of quenching, and two possibilities exist, either resonance energy transfer or electron transfer between RNA nucleobases and flavins. Since there is no overlap between the emission spectra of flavins (donor) and the absorption spectrum of any of the nucleobases (acceptor) the possibility of energy transfer can easily be ruled out. Therefore, plausible reason for quenching is the electron transfer between nucleobases and isoalloxazine ring where nucleobases (e.g. adenine E_{ox}=1.5 eV[130]/ adenosine E_{ox}=1.46 eV [130, 131], uracil (E_{ox} = 0.88 eV [132]), cytidine (E_{ox} = 1.6eV [130, 131]), and guanosine (E_{ox} = 1.29 eV[130, 131])) act as potential electron donor to photoexcited flavin ring (ground state reduction potential E_{red} =-0.24 eV[50]), and results a heavily quenched fluorescence of the flavin. Next obvious question is probable binding location of flavins in RNA aptamer. One possibility is flavin intercalates between the base pairs of complementary strand (**Scheme 4d.1**). To verify this possibility, we have checked the interaction scenario of flavin with 18-mer inter complimentary RNA ($(AU)_{18}$), and we found both FMN and FAD do not show any alteration in emission intensity by increasing $(AU)_{18}$ concentration (**Appendix 4d.3a**). Hence, we can rule out the intercalation mode of binding to RNA aptamer. The other possibility is flavin binds to the mismatch sequences of RNA aptamer (**Scheme 4d.1**), as it is well known that several ligands and small molecules bind to the bulge and loop segments of RNA.[109-115] Notably, NMR followed by MD simulation showed isoalloxazine ring of FMN involves in stacking interaction with the flanking G-G pair and G10.U12.A25 triple in bulge segment of the RNA aptamer.[119] In summary, steady state results provide strong evidence that ultrafast

electron transfer from nucleobases (mismatch bases like G9.G27, G10-U12-A25 triple and A13-G24 in the bulge segment of RNA aptamer) to flavin ring is accountable for the observed quenching effect of both FMN and FAD fluorescence in presence of RNA aptamer.

A very indulging care has been taken to the fluorescence study with variable concentrations of Mg^{+2} ion concentrations, as it's known that tertiary structure of RNA depends on Mg^{+2} ion concentration.[125, 126] We found with increasing Mg^{+2} ion concentration (from 2 mM to 10 mM), the relative quenching for both of FAD and FMN enhances significantly as shown in **Figure 4d.2c**. Moreover, the quenching is higher for FMN compared to FAD (**Figure 4d.2c**). To verify that FAD dynamics is not getting affected by Mg^{+2} ion, we titrated a fixed concentration of FAD with increasing Mg^{+2} under identical experimental condition, and interestingly we have found no variation in intensity or emission

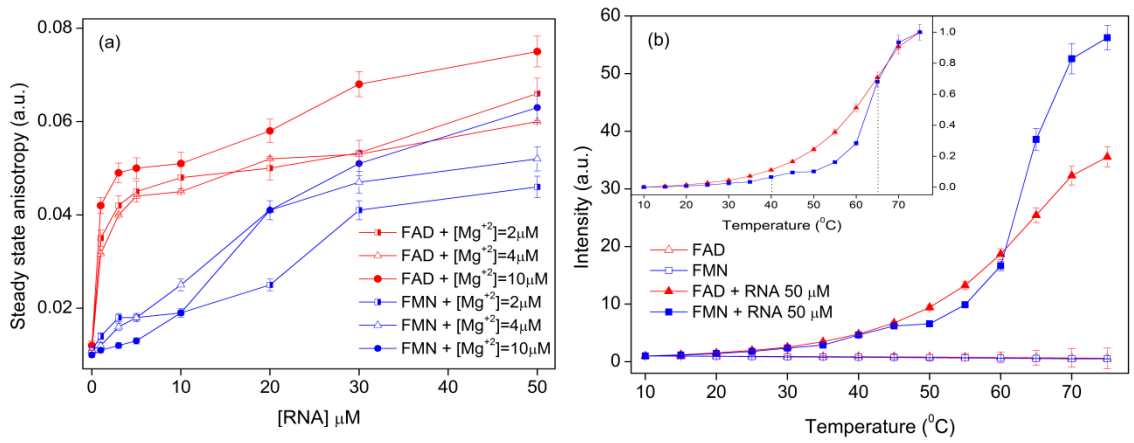

Figure 4d.3: *(a) Steady state anisotropy of FAD and FMN (λ_{ex} = 444 nm and collected at 535 nm) with increasing concentration of RNA aptamer recorded at variable Mg^{+2} concentrations. (b) Temperature dependent denaturation of RNA monitored by retrieval of flavin fluorescence. All the legends carry respective meaning.*

position (**Appendix 4d.3b**). Hence, variable effect in emission intensity at higher Mg^{+2} ion concentrations appears due to structural stabilization of flavin bound RNA aptamer by the Mg^{+2} ions. It is well established that Mg^{+2} ion stabilizes the tertiary structure of RNA by electrostatic screening of surface phosphates either by direct ion-dipole interaction or by hydrated ion and charge interaction.[125] The lesser extent of quenching in case of FAD at the same experimental condition indicates the aptamer has lesser binding affinity for FAD compared to FMN, as FAD has additional conformational flexibility.

To confirm the binding interaction of flavins with RNA aptamer and to check the reversibility of the binding process, temperature induced fluorescence measurement is

performed (**Figure 4d.3b**). We have noticed the emission intensity of flavins reverts back to its original intensity with increasing temperature. With increasing temperature, RNA aptamer structure collapses releases the aptamer-bound flavins into buffer. As free flavin in water is characterized by higher fluorescence quantum yield, hence, it can be concluded from this temperature induced denaturation of RNA aptamer that flavins are subjected to stacking interactions with the nucleobases in the bulge segment of the aptamer.

4d.2b. Association Behavior of Flavins-Aptamer Interaction

A quantitative estimation of binding affinity between flavins and aptamer can be obtained from Scatchard plot[133] (**Appendix 4d.4**). A systematic Mg^{+2} ion dependent study shows a monumental impact over binding constant of flavins with RNA aptamer. FAD at 2 mM Mg^{+2} concentration offers a binding constant 1.40×10^4 M^{-1}, which enhances ~100 fold at maximum Mg^{+2} ion concentration (10 mM) (**Table 4d.1**). A more intriguing results is observed for FMN, which shows a 10 fold higher association constant compared to FAD at 2 mM Mg^{+2} concentration and rises up to 2.0×10^7 M^{-1} at 10 mM Mg^{+2} ion concentration. The high binding affinity of FMN/FAD in presence of higher Mg^{+2} ion is attributed to the formation of a more stable tertiary structure of RNA aptamer in presence of high Mg^{+2} ion concentration. Moreover, Mg^{+2} ion favors the interactions between nucelobase and isoalloxazine by screening the negative charge of backbone phosphates. These results closely resemble to the binding constant determined from fluorescence assay performed by Anderson *et al.* and it was shown FMN exhibits three times higher binding affinity than that of FAD,[124] although the reason of lower binding affinity has not been addressed. In this work, we have addressed this issue and we have already mentioned that conformational flexibility of FAD may be intriguing factor for the lesser binding affinity as well as selectivity towards the RNA aptamer. Binding constants along with the free energy changes (**Table 4d.1**) infer that the detection of flavin by the aptamer is highly energy favored and Mg^{+2} ion dependent process, and we intend to depict a more detailed thermodynamic insight from ITC, described in latter part of these manuscript.

4d.2c. Impact over RNA Structure; CD and Thermal Melting Study

CD signal is sensitive to minute structural changes in bio-molecules like polynucleotides (DNA/RNA) or proteins during interaction with ions, ligands or other macromolecules.[93, 96]

Hence, the impact over aptamer structure due to Mg^{+2} ion as well as flavins binding is elucidated from circular dichroism studies (**Figure 4d.4a**). RNA aptamer alone in PBS exhibits two dips (at ~210 nm and ~235 nm) along with a peak at ~265 nm. A reasonable number of previous reports already characterized this features as a signature of A-form of RNA, where the base pairs are tilted relative to helix axis.[134-138] Note that most of the RNA structures found in nature are abundant in A from containing bulges and/or loops, which are able to selectively trap small molecules and ligands.[134-138] The CD spectra of aptamer shows dependence on Mg^{+2} ion concentration (as the peak at 265 nm is increased by ~20%, while moving from 2 mM to 10 mM of Mg^{+2} ion concentration), which infers that aptamer structure is gaining more stability at higher Mg^{+2} ion concentration. Here it is relevant to mention that Jack *et al.* also observed almost similar change in CD spectra of an antiterminator model RNA, when the Mg^{+2} ion concentration increases from 0 to 15 mM, and they attributed

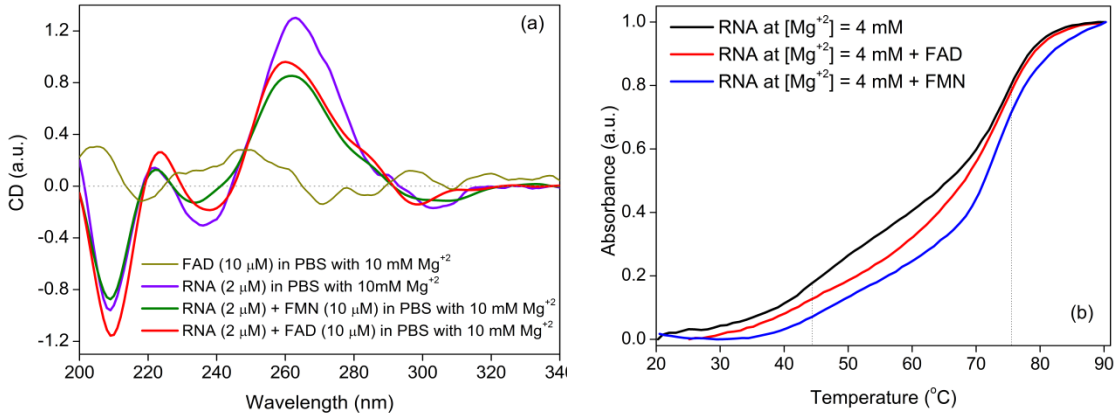

Figure 4d.4: *(a) CD Spectra of RNA aptamer with increasing concentrations of Mg^{+2} ion along with FAD and FMN. (b) Thermal melting data for RNA aptamer collected at 260 nm with FAD and FMN in presence of 4 mM Mg^{+2} ion. All the legends carry respective meaning.*

this small change due to increased base stacking interaction in presence of higher Mg^{+2} ion concentration.[138] In presence of flavin (either FAD or FMN) a detectable decrease in CD signal is noticed at ~265 nm (**Figure 4d.4a**). Moreover, a clear blue shift at ~265 nm peak is observed in CD spectra due to FAD and FMN binding. The decreasing CD signal along with blue shift infers about the interaction of FAD/FMN with RNA aptamer. The similar changes for FMN and FAD in CD spectra confirm that isoalloxazine ring is responsible for RNA interaction. Douthart *et al.* previously monitored intercalation of ethidium bromide in ds-RNA through CD spectroscopy, and a visible increase at ~ 265 nm CD signal was concluded

as an outcome of intercalation to RNA.[134] Therefore, the descending CD signal at ~265 nm for FAD and FMN infers about structural or conformational alteration of RNA aptamer upon binding to the bulge region of the aptamer.

The structural stability of aptamer during flavin binding is also verified through thermal melting study. The aptamer without flavins consist two distinct sigmoidal regions showing melting at 42°C and 72°C (**Figure 4d.4b)**. The lower melting temperature (42°C) may appear due to the opening of small stem-loop structure (from U14 to A23, **Scheme 4d.1**), whereas higher temperature (72°C) may be attributed to the global melting of the RNA structure. The global melting temperature matches well with the value checked from IDT under identical salt concentrations. In presence of FAD and FMN, the melting temperature of small stem-loop structure is found to be varied from 42°C for RNA alone to 46°C for FAD-bound RNA and 47°C for FMN bound RNA at 10 mM Mg^{+2} concentration. Interestingly, no such prominent change is observed for global melting temperature by interaction with either of the flavins. This observation might indicate that flavin binding stabilizes the stem-loop region of aptamer but does not perturb global melting of aptamer and also confirms that the isoalloxazine ring does not intercalate to the complimentary strands of aptamer, as intercalation between base pairs is known to alter global melting temperature to higher extent.

4d.2d. Isothermal Titration Calorimetry (ITC): A Thermodynamic Glimpse

In case of biomolecule-ligand interaction thermodynamic parameters play crucial role, as they provide detailed information about binding interaction, structural reformation or feasibility of the ligand-macromolecular association.[139-144] Therefore, we have used ITC study to get insight into the thermodynamic parameters during flavins-RNA interactions. ITC profiles of flavins-aptamer interaction are shown in **Figure 4d.5** and the results are depicted in **Table 4d.1**. Each enthalpy burst in upper panel represents individual RNA injections, and the amount of heat liberated by the successive additions is plotted against the molar ratio of flavin to aptamer in the lower panel. A standard nonlinear least-square regression binding model (single site) is employed to fit the results. Binding stoichiometries at low Mg^{+2} ion concentration are determined to be 0.80 and 0.78 for FAD and FMN, respectively. At higher Mg^{+2} ion concentrations (10 mM) the '*n*' (the molar ratio of ligand to macromolecule) values appear to be 0.7 and 0.67 for FAD and FMN, respectively and it suggests that each flavin molecule binds to single site of RNA aptamer, which is in agreement with our steady state and NMR[119] results, predicting 1:1 interaction between flavin and aptamer. The association

constant obtained for FMN (8.60×10^6 M^{-1}) is almost four times higher in magnitude compared to FAD (1.30×10^6 M^{-1}) in presence of RNA (at 10 mM of Mg^{+2} concentration), which corroborates well with steady state emission results under similar experimental

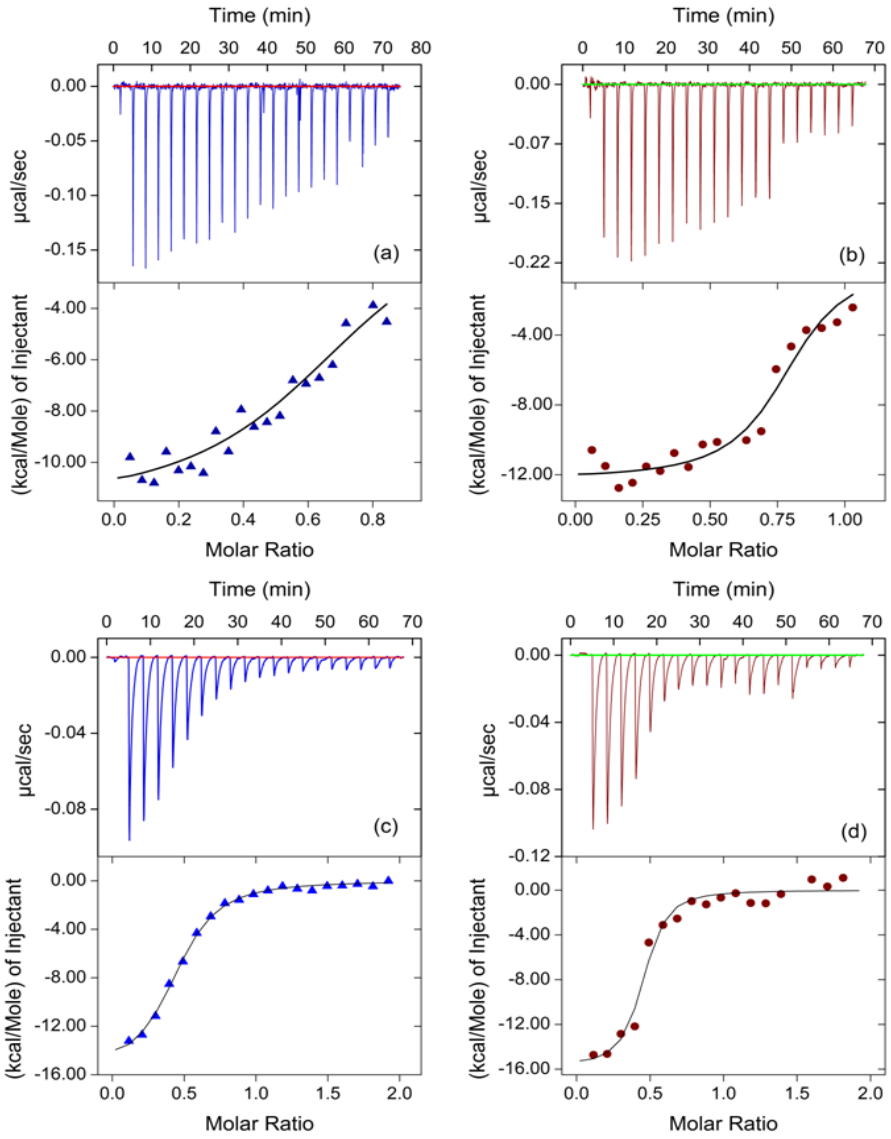

Figure 4d.5. *Isothermal Titration Calorimetry profiles of (a) FAD (in 4 mM Mg^{+2}) and (b) FMN (in 4 mM Mg^{+2}) with increasing concentration of RNA aptamer, whereas (c) and (d) represents ITC of FAD and FMN with RNA aptamer in presence of 10 mM Mg^{+2} ion concentration, respectively. The upper panels in all cases represent change in enthalpy at each injection, whereas the lower panels show the overall variation in enthalpy for the process.*

condition. The difference of association constant between FAD and FMN may appear due toconformational flexibility of FAD, which is not present in case of FMN. **Table 4d.1** offers a high negative heat of deflection for flavins binding to RNA aptamer, which indicates an

exothermic nature of binding. We have already anticipated from steady state emission, CD and melting studies that isoalloxazine ring of FMN/FAD interacts with mismatch nucleobases in the bulge segment of the aptamer. Therefore, we believe the high negative enthalpy values obtained from ITC studies are outcome of the above mentioned interactions, and it suggests

Table 4d.1. *Binding constant and detailed thermodynamic parameters of FAD and FMN binding interaction with RNA aptamer determined form steady state measurements and ITC.*

		$[Mg^{+2}]$=2mM	$[Mg^{+2}]$=4mM	$[Mg^{+2}]$=10mM
FAD				
From Fluorescence	K	1.40×10^{4} M^{-1}	1.20×10^{5} M^{-1}	5.52×10^{6} M^{-1}
	ΔG^0	-5.63 kcal/mol	-6.90 kcal/mol	-9.20 kcal/mol
From ITC	K		$(6.9 \pm 0.35) \times 10^{5}$ M^{-1}	$(1.30 \pm 0.15) \times 10^{6}$ M^{-1}
	ΔH		$-(1.17 \pm 0.09) \times 10^{4}$ cal/mol	$-(1.57 \pm 0.04) \times 10^{4}$ cal/mol
	ΔS		-12.3 cal/mol/deg	-24.6 cal/mol/deg
	ΔG^0		-8.03 kcal/mol	-8.50 kcal/mol
FMN				
From Fluorescence	K	6.50×10^{5} M^{-1}	1.07×10^{6} M^{-1}	2.0×10^{7} M^{-1}
	ΔG^0	-7.90 kcal/mol	-8.20 kcal/mol	-9.90 kcal/mol
From ITC	K		$(3.30 \pm 1.40) \times 10^{6}$ M^{-1}	$(8.60 \pm 2.23) \times 10^{6}$ M^{-1}
	ΔH		$-(1.22 \pm 0.05) \times 10^{4}$ cal/mol	$-(1.60 \pm 0.11) \times 10^{4}$ cal/mol
	ΔS		-11.1 cal/mol/deg	-22.5 cal/mol/deg
	ΔG^0		-9.00 kcal/mol	-9.30 kcal/mol

the bulge is sufficiently flexible and permits an optimal interaction with flavin. Interestingly, the change in entropy during flavins binding to aptamer is found to be negative for all cases, irrespective to Mg^{+2} ion concentration. A negative change in entropy can be attributed to the favorable electrostatic interactions between ligands and RNA.[143, 145] Note that the resultant entropy change appeared during flavins-aptamer binding is the combined effect of drug entropy change, RNA entropy change as well as entropy change of water during binding process.[146] It is obvious that drug entropy will decrease while binds to aptamer, and the flexibility of RNA decreases during drug or protein interacts[147]. On the other hand, water entropy generally increases when a drug binds to DNA/RNA.[146] Therefore, we feel that the negative entropy which appears in our study is due to the cancellation of positive entropy of water by the negative entropy change of RNA as well as falvins. Moreover, few previous

studies report about a large negative TΔS value, which is likely to reflect the ligand assisted refolding of RNA aptamer[148]. The standard free energy changes calculated from enthalpy as well as entropy contributions are well corroborative with steady state fluorescence measurements at 298 K. Finally, the negative values of standard free energy changes conclude that the binding of flavins to aptamer is highly spontaneous in nature.

4d.2e. Time Resolved Measurements

Time resolved fluorescence measurement is highly sensitive to the excited-state interaction between the probe and RNA, and hence is a unique technique to depict the environment around the fluorophore in excited state. Thus, fluorescence lifetime measurements are performed to understand the interaction scenario between flavins and RNA aptamer. FMN exhibits single exponential decay at pH 7 having a lifetime ~4.3 ns (**Figure 4d.6**). In presence

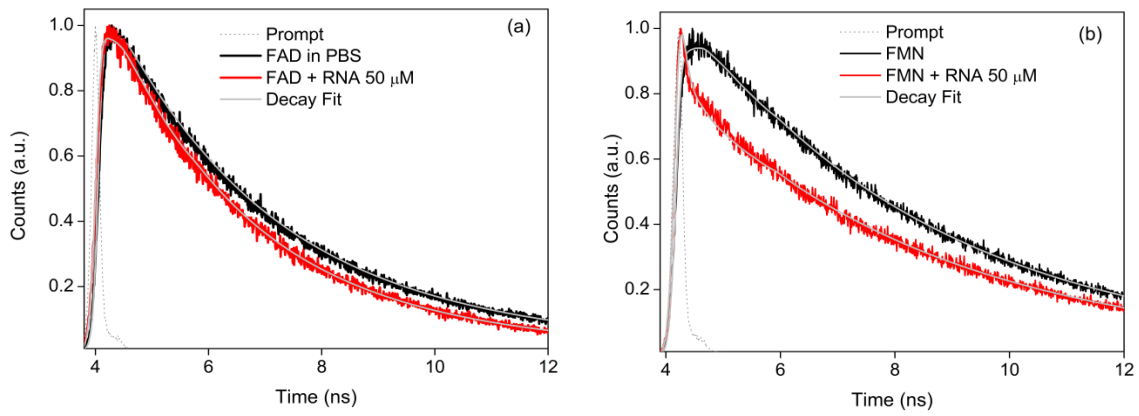

Figure 4d.6. *The decay profiles of (a) FAD and (b) FMN collected at 535 nm in absence and presence of RNA aptamer at 10 mM Mg^{+2} ion concentration (λ_{ex} = 444 nm).*

of RNA, a new short-lived component of ~200 ps appears for FMN, and overall average lifetime reduced in presence of RNA aptamer **(Figure 4d.6)**. Unlike FMN, FAD exhibits three distinct lifetime components at pH 7, a ~10 ps component (appears from stack conformer of FAD), ~2.2 ns (arises 'partially stack' conformer) and ~4 ns lifetime (appears from open conformer of FAD).[12, 24, 53] Note that due to limited time response of TCSPC (~40 ps) instrument, we are not able to detect the lifetime of 'stack' conformer. Hence, we detect a bi-exponential decay for FAD with two distinct lifetimes of ~4.3 and ~2.3 ns having relative contributions of 55% and 45%, respectively **(Figure 4d.6, Appendix 4d.t1)**. The ~4.3 ns

component represents the 'unstack' conformer, whereas the ~2.3 ns component corresponds to 'partially stack' conformer of FAD in which the isoalloxazine moiety does not stack but interacts with the other parts of the molecule.[25] With the gradual increase in RNA concentration, the lifetime of the two conformers remains same but offers a decreasing contribution of the long component. A new component with a reduced lifetime of around ~200 ps appears in presence of RNA. The reduced lifetime appeared in the decay profiles of both FMN and FAD (**Figure 4d.6, Appendix 4d.t1**) is an outcome of the quenching effect of isoalloxazine fluorescence by the nucleobases in the bulge segment of aptamer. In a nutshell, the lifetime results are in accordance with out steady state fluorescence results, where we have detected >90% quenching for flavin at higher concentration of RNA aptamer.

4d.3. Conclusion

Present work describes the detailed biophysical aspects of flavin (mainly FAD and FMN) recognition by RNA aptamer. Steady state fluorescence, time-resolved fluorescence, circular dichroism (CD) and thermal melting studies depict fluorescence quenching of flavin due to stacking interactions with mismatch bases like G9.G27, G10-U12-A25 triple and A13-G24

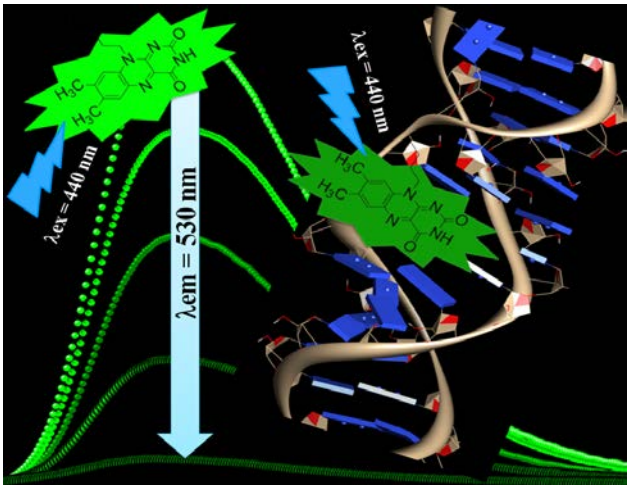

Scheme 4d.1. *Schematic representation of FAD-RNA aptamer interaction.*

and causes structural reformation, majorly in the small stem-loop segment of the aptamer (**Scheme 4d.1**). Isothermal titration calorimetry (ITC) study shows that flavin detection is highly enthalpy driven process. The negative changes in standard Gibb's free energy

conclude about the feasibility of interaction. We also observed that FMN shows a higher affinity to aptamer compared to FAD, and it is attributed to conformational flexibility of FAD, which does not exist in case of FMN. As 'stack' conformer of FAD remains silent during binding process due to the intramolecular stacking between isoalloxazine ring and adenine moiety, a reasonable population of FAD conformers cannot participate to further external stacking interaction with nucleobases of aptamer. Moreover, we have noticed that the feasibility of the recognition process is highly Mg^{+2} ion concentration dependent and it is attributed to the better stability of aptamer structure in presence of higher Mg^{+2} ion.

4.2. Reference

1. Begley, T.P. Photoenzymes: A novel class of biological catalysts. *Acc. Chem. Res.* **27**, 394-401 (1994).
2. Müller, F. in Radicals in biochemistry: The flavin redox-system and its biological function 71-107 (Springer Berlin Heidelberg, 1983).
3. Müller, F. Chemistry and biochemistry of flavoenzymes (CRCPress, Boca Raton,FL, FL, 1991).
4. van der Horst, M.A. & Hellingwerf, K.J. Photoreceptor proteins, "star actors of modern times": A review of the functional dynamics in the structure of representative members of Six different photoreceptor families. *Acc. Chem. Res.* **37**, 13-20 (2003).
5. Sancar, A. Structure and function of DNA photolyase and cryptochrome blue-light photoreceptors. *Chem. Rev.* **103**, 2203-2238 (2003).
6. Iseki, M., Matsunaga, S., Murakami, A., Ohno, K., Shiga, K., Yoshida, K., Sugai, M., Takahashi, T., Hori, T. & Watanabe, M. A blue-light-activated adenylyl cyclase mediates photoavoidance in Euglena gracilis. *Nature* **415**, 1047-1051 (2002).
7. Masuda, S. & Bauer, C.E. AppA is a blue light photoreceptor that antirepresses photosynthesis gene expression in rhodobacter sphaeroides. *Cell* **110**, 613-623 (2002).
8. Salomon, M., Christie, J.M., Knieb, E., Lempert, U. & Briggs, W.R. Photochemical and mutational analysis of the FMN-binding domains of the plant blue light receptor, phototropin. *Biochemistry* **39**, 9401-9410 (2000).
9. Langenbacher, T., Immeln, D., Dick, B. & Kottke, T. Microsecond light-induced proton transfer to flavin in the blue light sensor plant cryptochrome. *J. Am. Chem. Soc.* **131**, 14274-14280 (2009).
10. Huang, Y., Baxter, R., Smith, B.S., Partch, C.L., Colbert, C.L. & Deisenhofer, J. Crystal structure of cryptochrome 3 from Arabidopsis thaliana and its implications for photolyase activity. *Proc. Natl. Acad. Sci. U.S.A* **103**, 17701-17706 (2006).
11. Stanley, R.J. & MacFarlane. Ultrafast excited state dynamics of oxidized flavins: Direct observations of quenching by purines. *J. Phys. Chem. A* **104**, 6899-6906 (2000).
12. Chosrowjan, H., Taniguchi, S., Mataga, N., Tanaka, F. & Visser, A.J.W.G. The stacked flavin adenine dinucleotide conformation in water is fluorescent on picosecond timescale. *Chem. Phys. Lett.* **378**, 354-358 (2003).
13. Kao, Y.-T., Saxena, C., He, T.-F., Guo, L., Wang, L., Sancar, A. & Zhong, D. Ultrafast dynamics of flavins in five redox states. *J. Am. Chem. Soc.* **130**, 13132-13139 (2008).
14. Weber, G. Fluorescence of riboflavin and flavin-adenine dinucleotide. *Biochem. J.* **47**, 114–121. (1950).
15. Islam, S.D.M., Susdorf, T., Penzkofer, A. & Hegemann, P. Fluorescence quenching of flavin adenine dinucleotide in aqueous solution by pH dependent isomerisation and photo-induced electron transfer. *Chem. Phys.* **295**, 137-149 (2003).

16. Roberts, D.L., Salazar, D., Fulmer, J.P., Frerman, F.E. & Kim, J.-J.P. Crystal structure of paracoccus denitrificans electron transfer flavoprotein: Structural and electrostatic analysis of a conserved flavin binding domain. *Biochemistry* **38**, 1977-1989 (1999).
17. Powers, R.A., Rife, C.L., Schilmiller, A.L., Howe, G.A. & Garavito, R.M. Structure determination and analysis of acyl-CoA oxidase (ACX1) from tomato. *Acta Crystallogr., Sect. D* **62**, 683-686 (2006).
18. Joyce, M.G., Ekanem, I.S., Roitel, O., Dunford, A.J., Neeli, R., Girvan, H.M., Baker, G.J., Curtis, R.A., Munro, A.W. & Leys, D. The crystal structure of the FAD/NADPH-binding domain of flavocytochrome P450 BM3. *FEBS J.* **279**, 1694-1706 (2012).
19. Xing, W., Busino, L., Hinds, T.R., Marionni, S.T., Saifee, N.H., Bush, M.F., Pagano, M. & Zheng, N. SCFFBXL3 ubiquitin ligase targets cryptochromes at their cofactor pocket. *Nature* **496**, 64-68 (2013).
20. Fujihashi, M., Numoto, N., Kobayashi, Y., Mizushima, A., Tsujimura, M., Nakamura, A., Kawarabayasi, Y. & Miki, K. Crystal structure of archaeal photolyase from sulfolobus tokodaii with two FAD molecules: Implication of a novel light-harvesting cofactor. *J. Mol. Biol.* **365**, 903-910 (2007).
21. Raszka, M. & Kaplan, N.O. Intramolecular hydrogen bonding in flavin adenine dinucleotide. *Proc. Natl. Acad. Sci. U.S.A* **71**, 4546-4550 (1974).
22. Grininger, M., Seiler, F., Zeth, K. & Oesterhelt, D. Dodecin sequesters FAD in closed conformation from the aqueous solution. *J. Mol. Biol.* **364**, 561-566 (2006).
23. Drössler, P., Holzer, W., Penzkofer, A. & Hegemann, P. pH dependence of the absorption and emission behaviour of riboflavin in aqueous solution. *Chem. Phys.* **282**, 429-439 (2002).
24. van den Berg, P.A.W., Feenstra, K.A., Mark, A.E., Berendsen, H.J.C. & Visser, A.J.W.G. Dynamic conformations of flavin adenine dinucleotide: Simulated molecular dynamics of the flavin cofactor related to the time-resolved fluorescence characteristics. *J. Phys. Chem. B* **106**, 8858-8869 (2002).
25. Nakabayashi, T., Islam, M.S. & Ohta, N. Fluorescence decay dynamics of flavin adenine dinucleotide in a mixture of alcohol and water in the femtosecond and nanosecond time range. *J. Phys. Chem. B* **114**, 15254-15260 (2010).
26. Li, G. & Glusac, K.D. Light-triggered proton and electron transfer in flavin cofactors. *J. Phys. Chem. A* **112**, 4573-4583 (2008).
27. Mataga, N., Chosrowjan, H., Shibata, Y., Tanaka, F., Nishina, Y. & Shiga, K. Dynamics and mechanisms of ultrafast fluorescence quenching reactions of flavin chromophores in protein nanospace. *J. Phys. Chem. B* **104**, 10667-10677 (2000).
28. Song, P.-S. On the basicity of the excited state of flavins. *Photochem. Photobiol.* **7**, 311-313 (1968).
29. Tyagi, A. & Penzkofer, A. pH dependence of the absorption and emission behaviour of lumiflavin in aqueous solution. *J. Photochem. Photobiol., A* **215**, 108-117 (2010).
30. Saenger, W. Principles of nucelic acid structure (Springer New York, 1998).
31. Brazard, J., Usman, A., Lacombat, F., Ley, C., Martin, M.M., Plaza, P., Mony, L., Heijde, M., Zabulon, G. & Bowler, C. Spectro-temporal characterization of the

photoactivation mechanism of two new oxidized cryptochrome/photolyase photoreceptors. *J. Am. Chem. Soc.* **132**, 4935-4945 (2010).

32. Pokorny, R., Klar, T., Hennecke, U., Carell, T., Batschauer, A. & Essen, L.-O. Recognition and repair of UV lesions in loop structures of duplex DNA by DASH-type cryptochrome. *Proc. Natl. Acad. Sci. U.S.A.* **105**, 21023-21027 (2008).
33. Mattevi, A., Vanoni, M.A., Todone, F., Rizzi, M., Teplyakov, A., Coda, A., Bolognesi, M. & Curti, B. Crystal structure of D-amino acid oxidase: A case of active site mirror-image convergent evolution with flavocytochrome b2. *Proc. Natl. Acad. Sci. U.S.A.* **93**, 7496-7501 (1996).
34. Kim, J.J., Wang, M. & Paschke, R. Crystal structures of medium-chain acyl-CoA dehydrogenase from pig liver mitochondria with and without substrate. *Proc. Natl. Acad. Sci. U.S.A* **90**, 7523-7527 (1993).
35. Grinstead, J.S., Hsu, S.-T.D., Laan, W., Bonvin, A.M.J.J., Hellingwerf, K.J., Boelens, R. & Kaptein, R. The solution structure of the AppA BLUF domain: Insight into the mechanism of light-induced signaling. *ChemBioChem* **7**, 187-193 (2006).
36. Li, G. & Glusac, K.D. The role of adenine in fast excited-state deactivation of FAD: A femtosecond mid-IR transient absorption study. *J. Phys. Chem. B* **113**, 9059-9061 (2009).
37. Weigel, A., Dobryakov, A., Klaumünzer, B., Sajadi, M., Saalfrank, P. & Ernsting, N.P. Femtosecond stimulated Raman spectroscopy of flavin after optical excitation. *J. Phys. Chem. B* **115**, 3656-3680 (2011).
38. Radoszkowicz, L., Huppert, D., Nachliel, E. & Gutman, M. Sampling the conformation space of FAD in water-methanol mixtures through molecular dynamics and fluorescence measurements. *J. Phys. Chem. A* **114**, 1017-1022 (2009).
39. Radoszkowicz, L., Presiado, I., Erez, Y., Nachliel, E., Huppert, D. & Gutman, M. Time-resolved emission of flavin adenine dinucleotide in water and water-methanol mixtures. *Phys. Chem. Chem. Phys.* **13**, 12058-12066 (2011).
40. Sengupta, A., Gavvala, K., Koninti, R.K., Chaudhuri, H. & Hazra, P. Folding dynamics of flavin adenine dinucleotide (FAD) inside non-aqueous and aqueous reverse micelles. *Chem. Phys. Lett.* **584**, 67-73 (2013).
41. Hoccart, X. & Turrell, G. Raman spectroscopic investigation of the dynamics of urea-water complexes. *J. Chem. Phys.* **99**, 8498-8503 (1993).
42. Finer, E.G., Franks, F. & Tait, M.J. Nuclear magnetic resonance studies of aqueous urea solutions. *J. Am. Chem. Soc.* **94**, 4424-4429 (1972).
43. Hammes, G.G. & Schimmel, P.R. An investigation of water-urea and water-urea-polyethylene glycol interactions. *J. Am. Chem. Soc.* **89**, 442-446 (1967).
44. Funkner, S., Havenith, M. & Schwaab, G. Urea, a structure breaker? Answers from THz absorption spectroscopy. *J. Phys. Chem. B* **116**, 13374-13380 (2012).
45. Guinn, E.J., Pegram, L.M., Capp, M.W., Pollock, M.N. & Record, M.T. Quantifying why urea is a protein denaturant, whereas glycine betaine is a protein stabilizer. *Proc. Natl. Acad. Sci. U.S.A.* **108**, 16932-16937 (2011).
46. Kauzmann, W. & Simpson, R.B. The kinetics of protein denaturation. III. The optical rotations of serum albumin, β-lactoglobulin and pepsin in urea solutions. *J. Am. Chem. Soc.* **75**, 5154-5157 (1953).

47. Canchi, D.R., Paschek, D. & García, A.E. Equilibrium study of protein denaturation by urea. *J. Am. Chem. Soc.* **132**, 2338-2344 (2010).
48. Wyman, J. Dielectric constants: Ethanol-diethyl ether and urea-water solutions between 0 and 50°. *J. Am. Chem. Soc.* **55**, 4116-4121 (1933).
49. Seidel, C.A.M., Schulz, A. & Sauer, M.H.M. Nucleobase-specific quenching of fluorescent dyes. 1. Nucleobase one-electron redox potentials and their correlation with static and dynamic quenching efficiencies. *J. Phys. Chem.* **100**, 5541-5553 (1996).
50. Draper, R.D. & Ingraham, L.L. A potentiometric study of the flavin semiquinone equilibrium. *Arch. Biochem. Biophys.* **125**, 802-808 (1968).
51. Hayashi, Y., Katsumoto, Y., Omori, S., Kishii, N. & Yasuda, A. Liquid structure of the urea-water system studied by dielectric spectroscopy. *J. Phys. Chem. B* **111**, 1076-1080 (2007).
52. Guinn, E.J., Schwinefus, J.J., Cha, H.K., McDevitt, J.L., Merker, W.E., Ritzer, R., Muth, G.W., Engelsgjerd, S.W., Mangold, K.E., Thompson, P.J., Kerins, M.J. & Record, M.T. Quantifying functional group interactions that determine urea effects on nucleic acid helix formation. *J. Am. Chem. Soc.* **135**, 5828-5838 (2013).
53. Sengupta, A., Khade, R.V. & Hazra, P. pH dependent dynamic behavior of flavin mononucleotide (FMN) and flavin adenine dinucleotide (FAD) in femtosecond to nanosecond time scale. *J. Photochem. Photobiol., A* **221**, 105-112 (2011).
54. Alenka Luzar & Chandler, D. Hydrogen-bond kinetics in liquid water. *Nature* **379**, 55-57 (1996).
55. van der Spoel, D., van Maaren, P.J., Larsson, P. & Tîmneanu, N. Thermodynamics of hydrogen bonding in hydrophilic and hydrophobic media. *J. Phys. Chem. B* **110**, 4393-4398 (2006).
56. Luzar, A. Resolving the hydrogen bond dynamics conundrum. *J. Chem. Phys.* **113**, 10663-10675 (2000).
57. Boehr, D.D. & Wright, P.E. How do proteins interact? *Science* **320**, 1429-1430 (2008).
58. Ong, S.-E., Schenone, M., Margolin, A.A., Li, X., Do, K., Doud, M.K., Mani, D.R., Kuai, L., Wang, X., Wood, J.L., Tolliday, N.J., Koehler, A.N., Marcaurelle, L.A., Golub, T.R., Gould, R.J., Schreiber, S.L. & Carr, S.A. Identifying the proteins to which small-molecule probes and drugs bind in cells. *Proc. Natl. Acad. Sci. U.S.A.* **106**, 4617-4622 (2009).
59. Zhong, D., Douhal, A. & Zewail, A.H. Femtosecond studies of protein–ligand hydrophobic binding and dynamics: Human serum albumin. *Proc. Natl. Acad. Sci. U.S.A* **97**, 14056-14061 (2000).
60. Machida, S., Kato, N., Harada, K. & Ohkanda, J. Bivalent inhibitors for disrupting protein surface-substrate interactions and for dual inhibition of protein prenyltransferases. *J. Am. Chem. Soc.* **133**, 958-963 (2010).
61. Shan, Y., Kim, E.T., Eastwood, M.P., Dror, R.O., Seeliger, M.A. & Shaw, D.E. How does a drug molecule find its target binding site? *J. Am. Chem. Soc.* **133**, 9181-9183 (2011).

62. Edink, E., Rucktooa, P., Retra, K., Akdemir, A., Nahar, T., Zuiderveld, O., van Elk, R., Janssen, E., van Nierop, P., van Muijlwijk-Koezen, J., Smit, A.B., Sixma, T.K., Leurs, R. & de Esch, I.J.P. Fragment growing induces conformational changes in acetylcholine-binding protein: A structural and thermodynamic analysis. *J. Am. Chem. Soc.* **133**, 5363-5371 (2011).
63. Baldridge, A., Feng, S., Chang, Y.-T. & Tolbert, L.M. Recapture of GFP chromophore fluorescence in a protein host. *ACS Combinatorial Science* **13**, 214-217 (2011).
64. Peters Jr, T. in Adv. Protein Chem. (eds. C.B. Anfinsen, J.T.E. & Frederic, M.R.) 161-245 (Academic Press, 1985).
65. Nicoletti, F.P., Howes, B.D., Fittipaldi, M., Fanali, G., Fasano, M., Ascenzi, P. & Smulevich, G. Ibuprofen induces an allosteric conformational transition in the heme complex of human serum albumin with significant effects on heme ligation. *J. Am. Chem. Soc.* **130**, 11677-11688 (2008).
66. Olson, R.E. & Christ, D.D. Chapter 33: Plasma protein binding of drugs. *Annu. Rep. Med. Chem.* **31**, 327-336 (1996).
67. Carter, D.C. & Ho, J.X. in Adv. Protein Chem. (eds. C.B. Anfinsen, J.T.E.F.M.R. & David, S.E.) 153-176, 176a, 176b, 176c, 176d, 176e, 176f, 176g, 176h, 176i, 176j, 176k, 176l, 177-203 (Academic Press, 1994).
68. Wanwimolruk, S., Birkett, D.J. & Brooks, P.M. Structural requirements for drug binding to site II on human serum albumin. *Mol. Pharmacol.* **24**, 458-463 (1983).
69. Sudlow, G., Birkett, D.J. & N., W.D. The characterization of two specific drug binding sites on human serum albumin. *Mol. Pharmacol.* **11**, 824-832 (1975).
70. Sudlow, G., Birkett, D.J. & N., W.D. Further characterization of specific drug binding sites on human serum albumin *Mol. Pharmacol.* **12**, 1052-1061 (1976).
71. He, X.M. & Carter, D.C. Atomic structure and chemistry of human serum albumin. *Nature* **358**, 209-215 (1992).
72. Mares-Perlman, J.A., Brady, W.E., Klein, B.E., Klein, R., Haus, G.J., Palta, M., Ritter, L.L. & Shoff, S.M. Diet and nuclear lens opacities. *Am. J. Epidemol.* **141**, 322-34 (1995).
73. Schoenen, J., Jacquy, J. & Lenaerts, M. Effectiveness of high-dose riboflavin in migraine prophylaxis. A randomized controlled trial. *Neurology* **50**, 466-70 (1998).
74. Zhao, H., Ge, M., Zhang, Z., Wang, W. & Wu, G. Spectroscopic studies on the interaction between riboflavin and albumins. *Spectrochim. Acta, Part A* **65**, 811-817 (2006).
75. Wang, F., Huang, W. & Dai, Z. Spectroscopic investigation of the interaction between riboflavin and bovine serum albumin. *J. Mol. Struct.* **875**, 509-514 (2008).
76. Kamat, B.P., Seetharamappa, J. & Melwanki, M.B. Spectroscopic studies on the interaction of riboflavin with bovine serum albumin. *Ind. J. Biochem. Biophys.* **41**, 173-178 (2004).
77. Chakrabarty, A., Mallick, A., Haldar, B., Das, P. & Chattopadhyay, N. Binding interaction of a biological photosensitizer with serum albumins: A biophysical study. *Biomacromolecules* **8**, 920-927 (2007).

78. Liu, Y., Hu, Y.J. & Xiao, X.H. Investigation of the interaction between berberine and human serum albumin. *Biomacromolecules* **10**, 517-521 (2009).
79. Kandoth, N., Dutta Choudhury, S., Mohanty, J., Bhasikuttan, A.C. & Pal, H. Inhibiting intramolecular electron transfer in flavin adenine dinucleotide by host−guest interaction: A fluorescence study. *J. Phys. Chem. B* **114**, 2617-2626 (2010).
80. Sugio, S., Kashima, A., Mochizuki, S., Noda, M. & Kobayashi, K. Crystal structure of human serum albumin at 2.5 A resolution. *Protein Eng.* **12**, 439-446 (1999).
81. Robert F, A. Energetics of the one-electron reduction steps of riboflavin, FMN and FAD to their fully reduced forms. *Biochim. Biophys. Acta* **722**, 158-162 (1983).
82. Harriman, A. Further comments on the redox potentials of tryptophan and tyrosine. *J. Phys. Chem.* **91**, 6102-6104 (1987).
83. Laan, W., Gauden, M., Yeremenko, S., van Grondelle, R., Kennis, J.T.M. & Hellingwerf, K.J. On the mechanism of activation of the BLUF domain of AppA. *Biochemistry* **45**, 51-60 (2005).
84. Hazra, P., Inoue, K., Laan, W., Hellingwerf, K.J. & Terazima, M. Energetics and role of the hydrophobic interaction during photoreaction of the BLUF domain of AppA. *J. Phys. Chem. B* **112**, 1494-1501 (2008).
85. Benesi, H.A. & Hildebrand, J.H. A Spectrophotometric investigation of the interaction of iodine with aromatic hydrocarbons. *J. Am. Chem. Soc.* **71**, 2703-2707 (1949).
86. Mataga, N., Chosrowjan, H., Taniguchi, S., Tanaka, F., Kido, N. & Kitamura, M. Femtosecond fluorescence dynamics of flavoproteins: Comparative studies on flavodoxin, its site-directed mutants, and riboflavin binding protein regarding ultrafast electron transfer in protein nanospaces. *J. Phys. Chem. B* **106**, 8917-8920 (2002).
87. Shortle, D. & Ackerman, M.S. Persistence of native-like topology in a denatured protein in 8 M urea. *Science* **293**, 487-489 (2001).
88. Chen, X., Sagle, L.B. & Cremer, P.S. Urea orientation at protein surfaces. *J. Am. Chem. Soc.* **129**, 15104-15105 (2007).
89. Das, A. & Mukhopadhyay, C. Urea-mediated protein denaturation: A consensus view. *J. Phys. Chem. B* **113**, 12816-12824 (2009).
90. Leggio, C., Galantini, L., Konarev, P.V. & Pavel, N.V. Urea-induced denaturation process on sefatted human serum albumin and in the presence of palmitic acid. *J. Phys. Chem. B* **113**, 12590-12602 (2009).
91. Sulkowska, A., Bojko, B., Równicka, J., Pentak, D. & Sulkowski, W. Effect of urea on serum albumin complex with antithyroid drugs: fluorescence study. *J. Mol. Struct.* **651-653**, 237-243 (2003).
92. González-Jiménez, J. & Cortijo, M. Urea-induced denaturation of human serum albumin labeled with acrylodan. *J. Protein Chem.* **21**, 75-79 (2002).
93. Beychok, S. Circular dichroism of biological macromolecules. *Science* **154**, 1288-1299 (1966).
94. Monti, S., Manoli, F., Sortino, S., Morrone, R. & Nicolosi, G. Binding of a chiral drug to a protein: an investigation of the 2-(3-benzoylphenyl)propionic acid/bovine serum

albumin system by circular dichroism and fluorescence. *Phys. Chem. Chem. Phys.* **7**, 4002-4008 (2005).

95. Moriyama, Y. & Takeda, K. Re-formation of the helical structure of human serum albumin by the addition of small amounts of sodium dodecyl sulfate after the disruption of the structure by urea. A comparison with bovine serum albumin. *Langmuir* **15**, 2003-2008 (1999).
96. Bengt Norden, Alison Rodger & Dafforn, T. Linear dichroism and circular dichroism: A textbook on polarized-light spectroscopy (Royal Society of Chemistry, 2010).
97. Parker, W. & Song, P.S. Protein structures in SDS micelle-protein complexes. *Biophys. J.* **61**, 1435-9 (1992).
98. Moriyama, Y. & Takeda, K. Protective effects of small amounts of bis(2-ethylhexyl)sulfosuccinate on the helical structures of human and bovine serum albumins in their thermal denaturations. *Langmuir* **21**, 5524-5528 (2005).
99. Si, Z., Madani, N., Cox, J.M., Chruma, J.J., Klein, J.C., Schön, A., Phan, N., Wang, L., Biorn, A.C., Cocklin, S., Chaiken, I., Freire, E., Smith, A.B. & Sodroski, J.G. Small-molecule inhibitors of HIV-1 entry block receptor-induced conformational changes in the viral envelope glycoproteins. *Proc. Natl. Acad. Sci. U.S.A.* **101**, 5036-5041 (2004).
100. Kiselev, M.A., Gryzunov, Y.A., Dobretsov, G.E. & Komarova, M.N. Size of a human serum albumin molecule in solution. *Biofizika* **46**, 423-427 (2001).
101. Sudhamalla, B., Gokara, M., Ahalawat, N., Amooru, D.G. & Subramanyam, R. Molecular dynamics simulation and binding studies of β-sitosterol with human serum albumin and its biological relevance. *J. Phys.Chem. B* **114**, 9054-9062 (2010).
102. Deeb, O., Rosales-Hernández, M.C., Gómez-Castro, C., Garduño-Juárez, R. & Correa-Basurto, J. Exploration of human serum albumin binding sites by docking and molecular dynamics flexible ligand-protein interactions. *Biopolymers* **93**, 161-170 (2010).
103. Morris, G.M., Huey, R., Lindstrom, W., Sanner, M.F., Belew, R.K., Goodsell, D.S. & Olson, A.J. AutoDock4 and AutoDockTools4: Automated docking with selective receptor flexibility. *J. Comput. Chem.* **30**, 2785-2791 (2009).
104. Pettersen, E.F., Goddard, T.D., Huang, C.C., Couch, G.S., Greenblatt, D.M., Meng, E.C. & Ferrin, T.E. UCSF Chimera-A visualization system for exploratory research and analysis. *J. Comput. Chem.* **25**, 1605-1612 (2004).
105. Tan, W., Donovan, M.J. & Jiang, J. Aptamers from cell-based selection for bioanalytical applications. *Chem. Rev.* **113**, 2842-2862 (2013).
106. Liu, J., Cao, Z. & Lu, Y. Functional Nucleic Acid Sensors. *Chem. Rev.* **109**, 1948-1998 (2009).
107. Famulok, M., Hartig, J.S. & Mayer, G. Functional aptamers and aptazymes in biotechnology, diagnostics, and therapy. *Chem. Rev.* **107**, 3715-3743 (2007).
108. Cheng, C., Chen, Y.H., Lennox, K.A., Behlke, M.A. & Davidson, B.L. In vivo SELEX for identification of brain-penetrating aptamers. *Mol. Ther. Nucleic Acids* **2**, e67 (2013).
109. Chow, C.S. & Bogdan, F.M. A structural basis for RNA-ligand interactions. *Chem. Rev.* **97**, 1489-1514 (1997).

110. Stojanovic, M.N. & Kolpashchikov, D.M. Modular aptameric sensors. *J. Am. Chem. Soc.* **126**, 9266-9270 (2004).
111. Cheng, A.C., Calabro, V. & Frankel, A.D. Design of RNA-binding proteins and ligands. *Curr. Opin. Struct. Biol.* **11**, 478-484 (2001).
112. Schroeder, R., Barta, A. & Semrad, K. Strategies for RNA folding and assembly. *Nat. Rev. Mol. Cell Biol.* **5**, 908-919 (2004).
113. Vicens, Q. & Westhof, E. RNA as a drug target: The case of aminoglycosides. *ChemBioChem* **4**, 1018-1023 (2003).
114. Warui, D.M. & Baranger, A.M. Identification of small molecule inhibitors of the HIV-1 nucleocapsid-stem-loop 3 RNA complex. *J. Med. Chem.* **55**, 4132-4141 (2012).
115. Winkler, W.C. & Breaker, R.R. Genetic control by metabolite-binding riboswitches. *ChemBioChem* **4**, 1024-1032 (2003).
116. Thomas, J.R. & Hergenrother, P.J. Targeting RNA with small molecules. *Chem. Rev.* **108**, 1171-1224 (2008).
117. Burgstaller, P. & Famulok, M. Isolation of RNA aptamers for biological cofactors by in vitro selection. *Angew. Chem. Int. Ed. Engl.* **33**, 1084-1087 (1994).
118. Burgstaller, P. & Famulok, M. Structural characterization of a flavin-specific RNA aptamer by chemical probing. *Bioorg. Med. Chem. Lett.* **6**, 1157-1162 (1996).
119. Fan, P., Suri, A.K., Fiala, R., Live, D. & Patel, D.J. Molecular recognition in the FMN-RNA aptamer complex. *J. Mol. Biol.* **258**, 480-500 (1996).
120. Soukup, G.A. & Breaker, R.R. Engineering precision RNA molecular switches. *Proc. Natl. Acad. Sci. U.S.A* **96**, 3584-3589 (1999).
121. Robertson, M.P. & Ellington, A.D. Design and optimization of effector-activated ribozyme ligases. *Nucleic Acids Res.* **28**, 1751-1759 (2000).
122. Lauhon, C.T. & Szostak, J.W. RNA aptamers that bind flavin and nicotinamide redox cofactors. *J. Am. Chem. Soc.* **117**, 1246-1257 (1995).
123. Roychowdhury-Saha, M., Lato, S.M., Shank, E.D. & Burke, D.H. Flavin recognition by an RNA aptamer targeted toward FAD. *Biochemistry* **41**, 2492-2499 (2002).
124. Anderson, P.C. & Mecozzi, S. Identification of a 14mer RNA that recognizes and binds flavin mononucleotide with high affinity. *Nucleic Acids Res.* **33**, 6992-6999 (2005).
125. Draper, D.E. A guide to ions and RNA structure. *RNA* **10**, 335-343 (2004).
126. Leipply, D. & Draper, D.E. Evidence for a thermodynamically distinct Mg^{2+} ion associated with formation of an RNA tertiary structure. *J. Am. Chem. Soc.* **133**, 13397-13405 (2011).
127. Misra, V.K. & Draper, D.E. On the role of magnesium ions in RNA stability. *Biopolymers* **48**, 113-135 (1998).
128. Fiore, J.L., Holmstrom, E.D. & Nesbitt, D.J. Entropic origin of Mg^{2+}-facilitated RNA folding. *Proc. Natl. Acad. Sci. U.S.A* **109**, 2902-2907 (2012).
129. Yagi, K., Ohishi, N., Nishimoto, K., Choi, J.D. & Song, P.-S. Effect of hydrogen bonding on electronic spectra and reactivity of flavins. *Biochemistry* **19**, 1553-1557 (1980).

130. Fukuzumi, S., Miyao, H., Ohkubo, K. & Suenobu, T. Electron-transfer oxidation properties of DNA bases and DNA oligomers. *J. Phys. Chem. A* **109**, 3285-3294 (2005).
131. Crespo-Hernández, C.E., Close, D.M., Gorb, L. & Leszczynski, J. Determination of redox potentials for the Watson-Crick base pairs, DNA nucleosides, and relevant nucleoside analogues. *J. Phys. Chem. B* **111**, 5386-5395 (2007).
132. Jovanovic, S.V. & Simic, M.G. One-electron redox potentials of purines and pyrimidines. *J. Phys. Chem.* **90**, 974-978 (1986).
133. Healy, E.F. Quantitative determination of DNA-ligand binding using fluorescence spectroscopy. *J. Chem. Edu.* **84**, 1304 (2007).
134. Douthart, R.J., Burnett, J.P., Beasley, F.W. & Frank, B.H. Binding of ethidium bromide to double-stranded ribonucleic acid. *Biochemistry* **12**, 214-220 (1973).
135. Loret, E.P., Georgel, P., Johnson, W.C. & Ho, P.S. Circular dichroism and molecular modeling yield a structure for the complex of human immunodeficiency virus type 1 trans-activation response RNA and the binding region of Tat, the trans-acting transcriptional activator. *Proc. Natl. Acad. Sci. U.S.A* **89**, 9734-9738 (1992).
136. Higashi, K., Terui, Y., Inomata, E., Katagiri, D., Nomura, Y., Someya, T., Nishimura, K., Kashiwagi, K., Kawai, G. & Igarashi, K. Selective structural change of bulged-out region of double-stranded RNA containing bulged nucleotides by spermidine. *Biochem. Biophys. Res. Commun.* **370**, 572-577 (2008).
137. Nakano, S.-i., Kanzaki, T. & Sugimoto, N. Influences of ribonucleotide on a duplex conformation and its thermal stability: Study with the chimeric RNA-DNA strands. *J. Am. Chem. Soc.* **126**, 1088-1095 (2004).
138. Jack, K.D., Means, J.A. & Hines, J.V. Characterizing riboswitch function: Identification of Mg^{2+} binding site in T box antiterminator RNA. *Biochem. Biophys. Res. Commun.* **370**, 306-310 (2008).
139. Sokoloski, J.E., Dombrowski, S.E. & Bevilacqua, P.C. Thermodynamics of ligand binding to a heterogeneous RNA population in the malachite green aptamer. *Biochemistry* **51**, 565-572 (2011).
140. Ouyang, W., Okaine, S., McPike, M.P., Lin, Y. & Borer, P.N. Probing the RNA binding surface of the HIV-1 nucleocapsid protein by site-directed mutagenesis. *Biochemistry* **52**, 3358-3368 (2013).
141. Zhang, J., Umemoto, S. & Nakatani, K. Fluorescent indicator displacement assay for ligand-RNA interactions. *J. Am. Chem. Soc.* **132**, 3660-3661 (2010).
142. Sinha, R. & Kumar, G.S. Interaction of Isoquinoline Alkaloids with an RNA Triplex: Structural and Thermodynamic Studies of Berberine, Palmatine, and Coralyne Binding to Poly(U).Poly(A)*Poly(U). *J. Phys. Chem. B* **113**, 13410-13420 (2009).
143. McLaughlin, K.J., Jenkins, J.L. & Kielkopf, C.L. Large favorable enthalpy changes drive specific RNA recognition by RNA recognition motif proteins. *Biochemistry* **50**, 1429-1431 (2011).
144. Bec, G., Meyer, B., Gerard, M.-A., Steger, J., Fauster, K., Wolff, P., Burnouf, D., Micura, R., Dumas, P. & Ennifar, E. Thermodynamics of HIV-1 reverse transcriptase in action elucidates the mechanism of action of non-nucleoside inhibitors. *J. Am. Chem. Soc.* **135**, 9743-9752 (2013).

145. Thomas, J.R., Liu, X. & Hergenrother, P.J. Biochemical and thermodynamic characterization of compounds that bind to RNA hairpin loops: Toward an understanding of selectivity. *Biochemistry* **45**, 10928-10938 (2006).
146. Mukherjee, A. Entropy balance in the intercalation process of an anti-cancer dug daunomycin. *J. Phys. Chem. Lett.* **2**, 3021-3026 (2011).
147. Lustig, B., Baharand, I. & Jernigan, R.L. RNA bulge entropies in the unbound state correlate with peptide binding strengths for HIV-1 and BIV TAR RNA because of improved conformational access. *Nucleic Acids Res.* **26**, 5212-5217 (1998).
148. Lin, P.-H., Yen, S.-L., Lin, M.-S., Chang, Y., Louis, S.R., Higuchi, A. & Chen, W.-Y. Microcalorimetrics studies of the thermodynamics and binding mechanism between l-tyrosinamide and aptamer. *J. Phys. Chem. B* **112**, 6665-6673 (2008).

4.3. Appendix

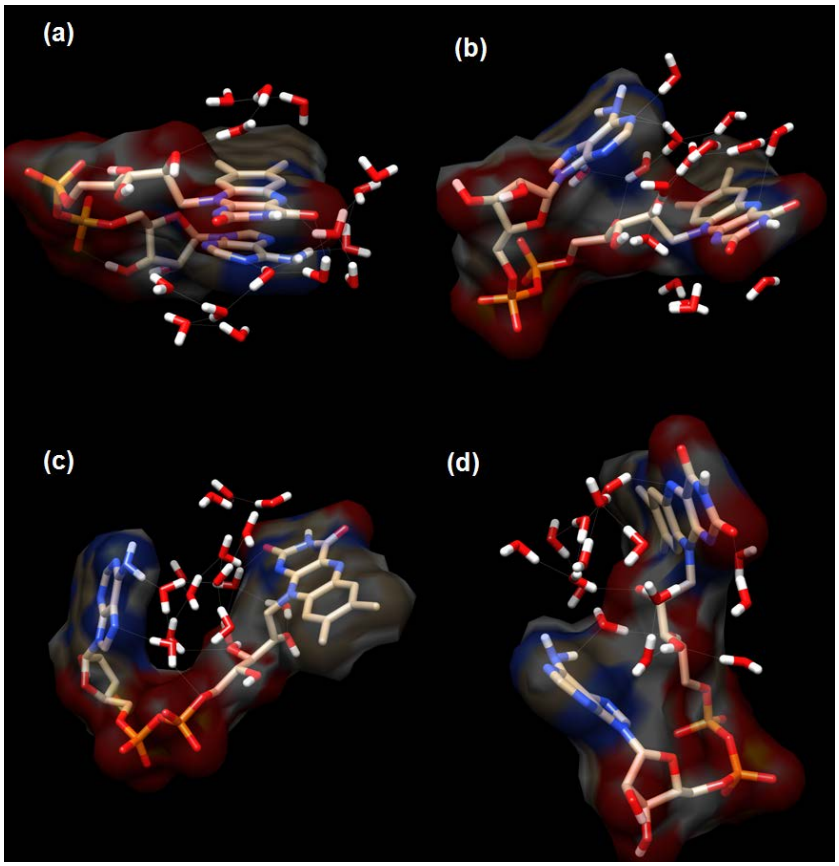

Appendix 4b.1. *Orientations of water molecules around adenine and isoalloxazine rings of FAD at different time points in the trajectory.*

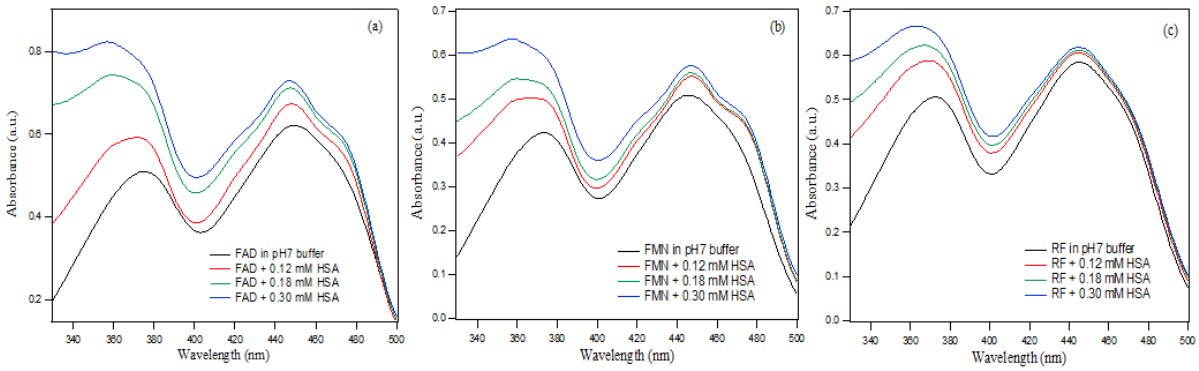

Appendix 4c.1. *Absorption Spectra of (a) FAD, (b) FMN and (c) RF at different HSA concentration*

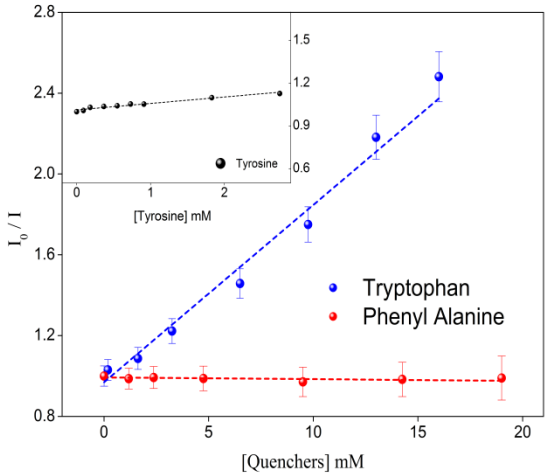

Appendix 4c.2. *Comparative quenching of FMN by tryptophan, phenylalanine and tyrosine in bulk.*

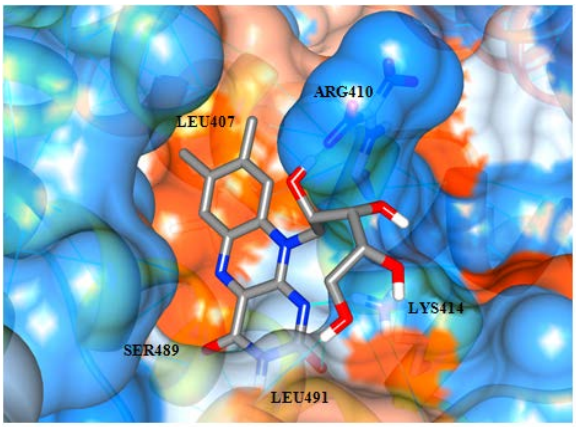

Appendix 4c.3. *RF bound to SS2 after docking. RF is given element-based color. The amino acids are colored according to hydrophobicity. The picture is plotted using chimera.*

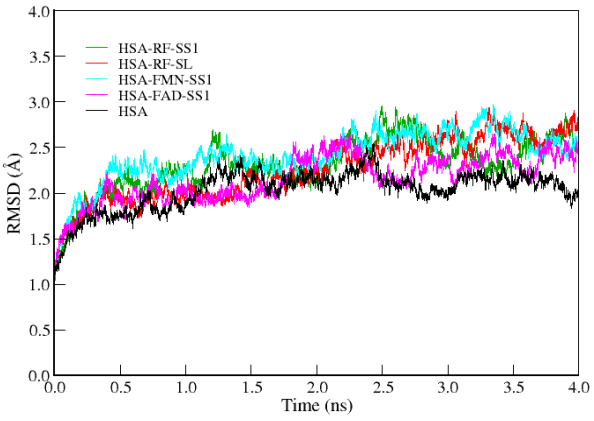

Appendix 4c.4. *Root Means Square Deviation of HSA chain in HSA, HSA-RF, HSA-FMN and HSA-FAD systems.*

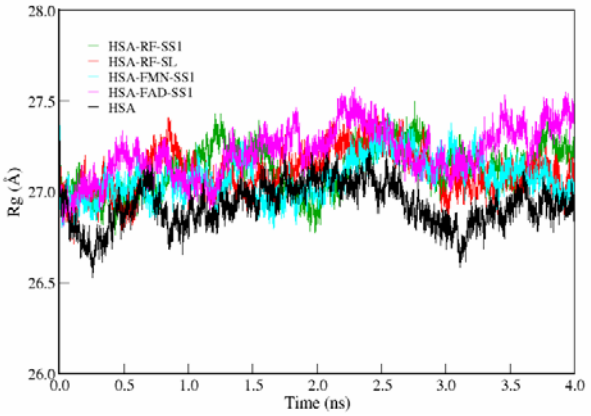

Appendix 4c.5. *Radius of Gyration of HSA chain in HSA, HSA-RF, HSA-FMN and HSA-FAD systems.*

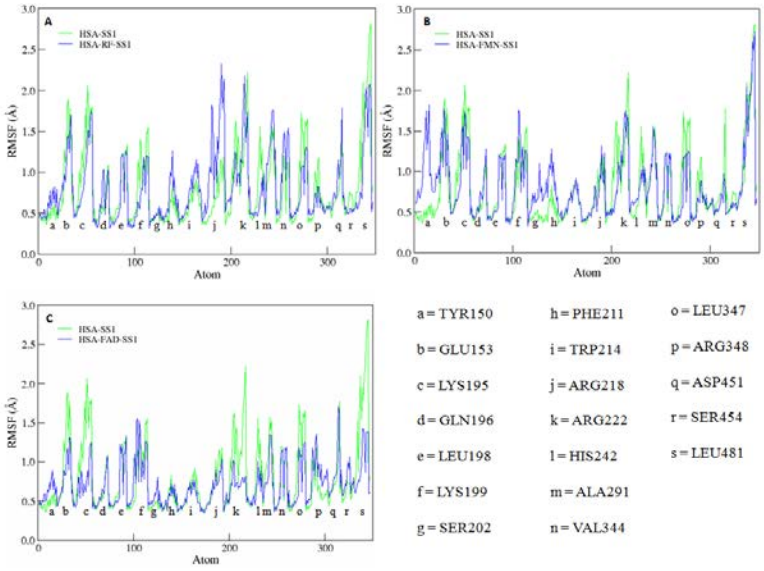

Appendix 4c.6. *RMSF of amino acids of active site SS1 in A) HSA-RF, B) HSA-FMN and C) HSA-FAD systems in comparison with RMSF of amino acids of SS1 in HSA only. Amino acids present in the SS1 binding pockets are also mentioned.*

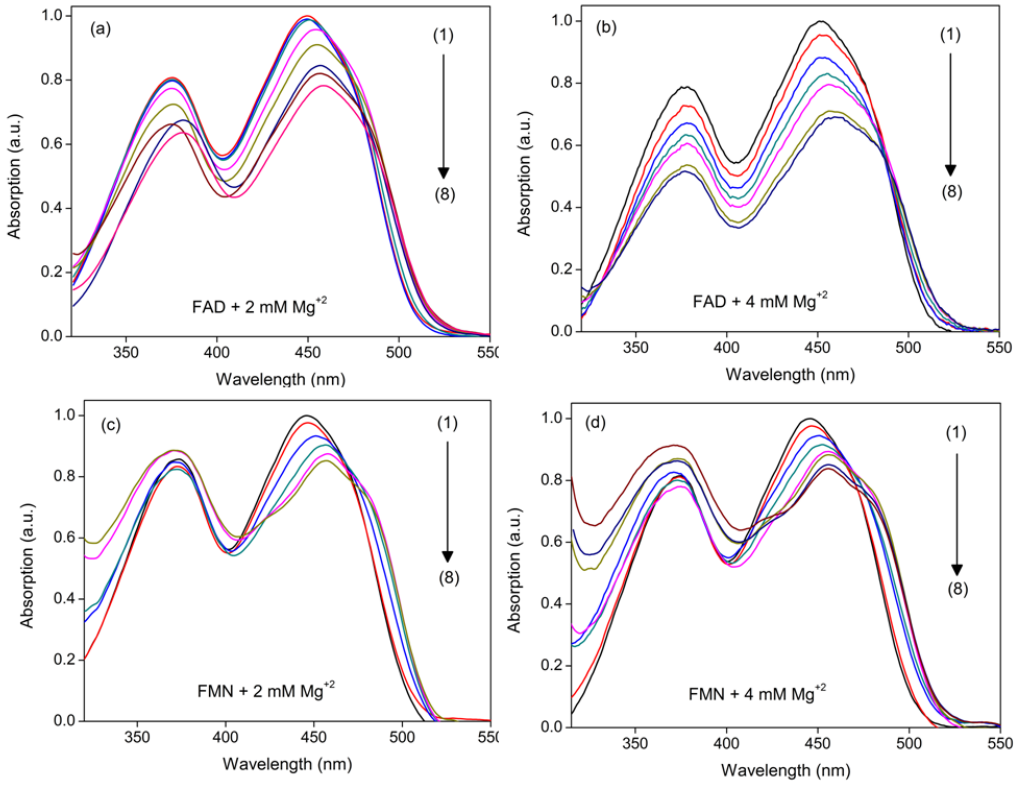

Appendix 4d.1. *Absorption spectra of FAD (a, b) and FMN (c, d) in presence of 2 mM and 4 mM Mg^{+2} ion concentration with increasing RNA aptamer concentrations; where 1→8 represents RNA concentration 0, 1, 3, 5, 10, 20, 30 and 50 µM, respectively.*

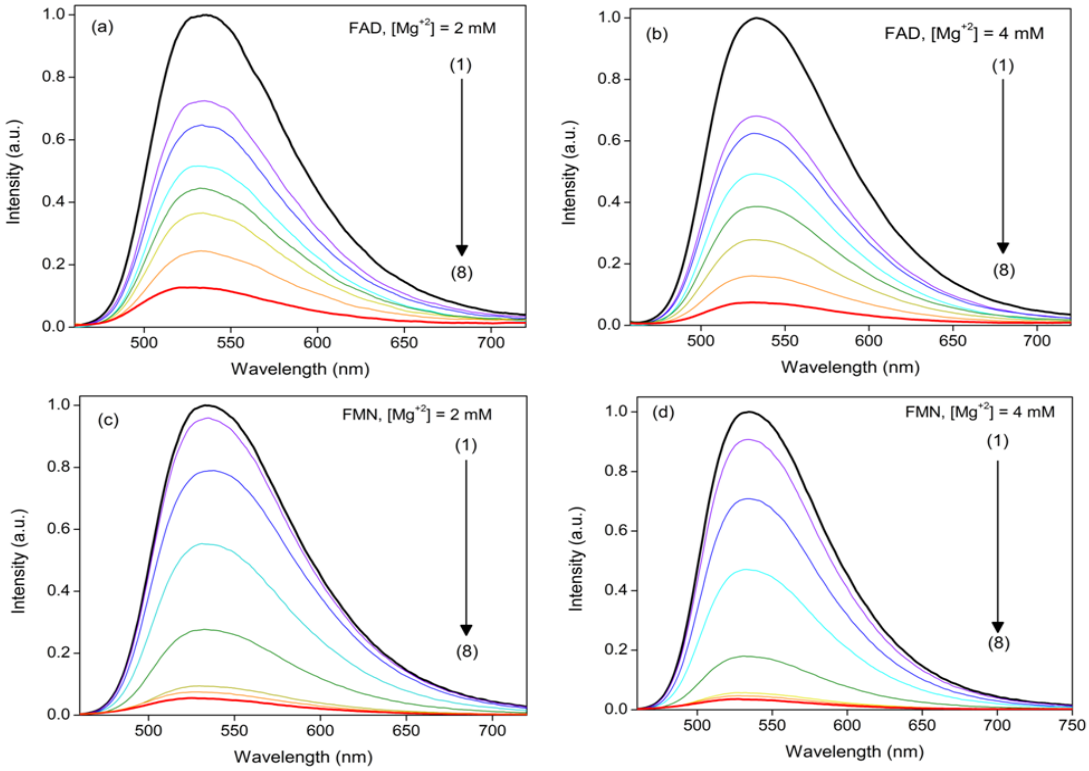

Appendix 4d.2. *Fluorescence spectra of FAD (a, b) and FMN (c, d) in presence of 2 mM and 4 mM Mg^{+2} ion concentration with increasing RNA aptamer concentrations; 1→8 represents RNA concentration 0, 1, 3, 5, 10, 20, 30 and 50 µM, respectively.*

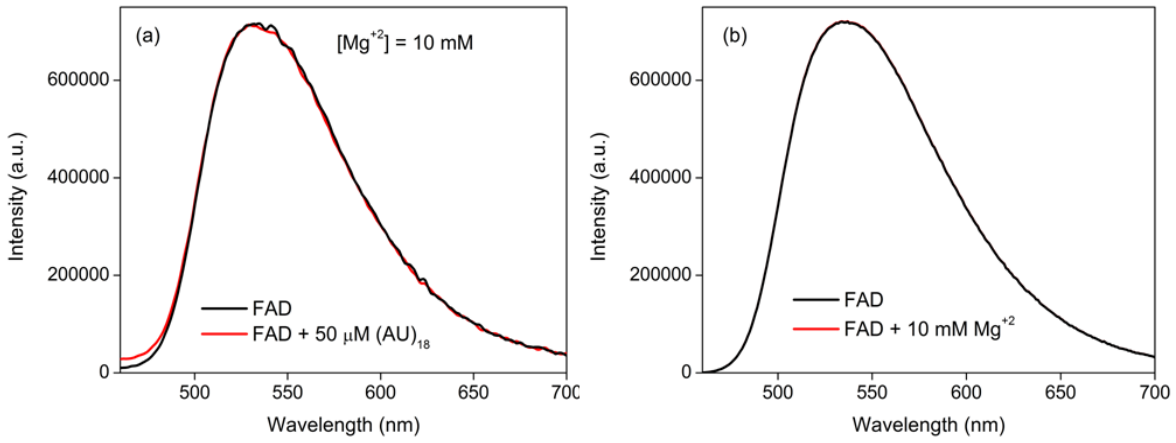

Appendix 4d.3. *(a) Emission spectra of FAD with 50 µM $(AU)_{18}$ RNA in presence of 10 mM Mg^{+2}. (b) Emission spectra of FAD in absence and presence of maximum Mg^{+2} ion concentration (10 mM).*

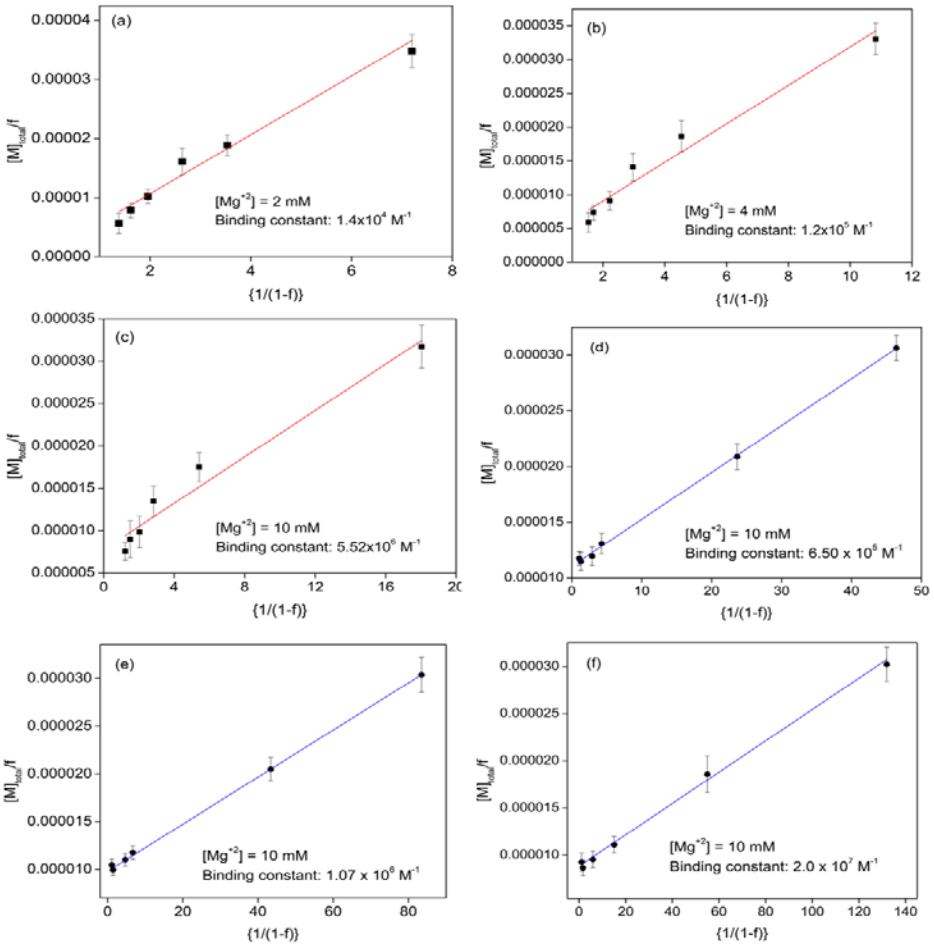

Appendix 4d.4. *Modified Scatchard plot for FAD with increasing RNA concentrations and variable Mg^{+2} ion concentrations (a) 2 mM, (b) 4 mM and (c) 10 mM, and FMN with increasing RNA concentrations in presence of variable Mg^{+2} ion concentrations (d) 2 mM, (e) 4 mM and (f) 10 mM.*

Table 4d.t1. *Fluorescence Decay components of FAD and FMN in buffer and with RNA*

	τ_1 (ns)	a_1	τ_2 (ns)	a_2	τ_3 (ns)	a_3	τ_{av} (ns)	χ^2
FMN	4.3	1					4.3	1.0
FMN + RNA 50 μM	4.3	0.96	0.2	0.04			4.1	1.1
FAD	4.0	0.55	2.2	0.45			3.2	1.02
FAD + RNA 50 μM	4.0	0.51	2.2	0.455	0.2	0.035	3.00	1.1

End of Chapter 4

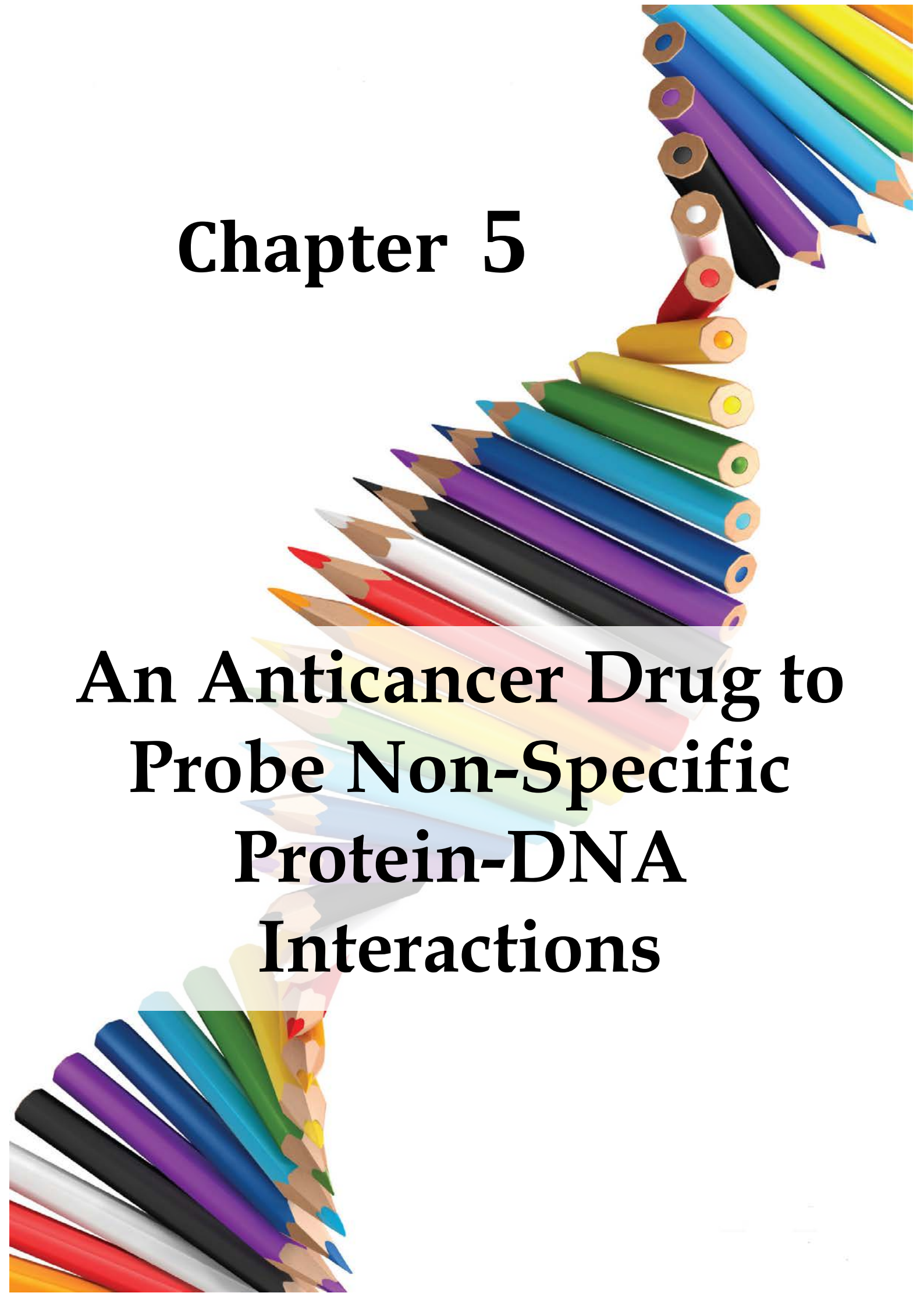

Chapter 5

An Anticancer Drug to Probe Non-Specific Protein-DNA Interactions

5.1. Motivation

Molecular switches are receiving up-rising attention from recent past owing to its potential applications in bio-sensors, memory devices, logic gates and in many others.[1-13] Electronic and optical properties of these molecular switches are responsive to diverse environmental stimuli which promotes them as indispensible choice for biophysical and biochemical applications.[1, 4, 6, 14-16] Among others, the fluorescence switching is of special interest owing to its high sensitivity and the easy detection of the signal. Fluorescence switching is governed mainly by two mechanisms, (i) photo-induced electron transfer (PET)[17-19] and (ii) fluorescence resonance energy transfer (FRET).[20-23] In 'PET' a donor molecule transfers electron to the excited state acceptor and reduces the fluorescence, which is designated as "turn off" fluorescence. If the electron donating abilities of the donor is reduced significantly, the fluorescence "turns on".[17-19] Whereas, in 'FRET' a donor and acceptor pair approaches within Förster distance and the emission switches form high energy to low energy photons.[20-23] Although extensively used but their applications in biology have some limitations. Note that efficient 'PET' and 'FRET' requires covalent tagging of donor and acceptor in macromolecules, which appears to be a tough challenge for chemists. Moreover, 'PET' or 'FRET' from weakly bound or freely roaming fluorophore is most likely to be diffusion controlled, which may not serve the purpose properly.[24] If a single fluorophore could execute fluorescence switching, it would facilitate sample labeling, and eliminates the complications of integrating two dyes into desired locations. Such kind of fluorescent dyes are scarcely available, and have limited applications in biology. Therefore, it would be worthy to think about a molecule which is biologically important, exhibits dual fluorescence and switches its emission while assisted by some macromolecules, like natural biopolymers. After an extensive search we discovered ellipticine, an important anticancer drug, exhibits dual

fluorescence in few selective solvents, and, therefore, it can pave a way towards single probe fluorescence switching.

5,11-dimethyl-6H-pyrido[4,3-b]carbazole or trivially known ellipticine (**Scheme 5.1**) is a naturally occurring plant alkaloid, better known as anti carcinogen since 1960s.[25, 26] Ellipticine and its several other derivatives effectively intercalate in DNA and inhibit the activity of DNA topoisomerase II, which ultimately restricts the process of DNA replication and hence transcription of RNA.[25, 27] Although anticancer activity of ellipticine is well known, its mechanism of action is not well explored. To understand whether DNA intercalation of ellipticine is facilitated by topoisomerase II, several studies have been done.[28, 29] In 1995, Thomson group have shown that the anticancer activity of ellipticine occurs

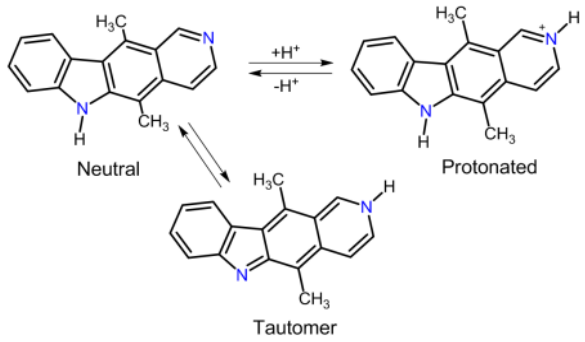

Scheme 5.1. *Different forms of ellipticine in solution.*

through DNA-ellipticine-topoisomerase II ternary complex formation.[29] Till date a few scattered studies related to solvatochromic behavior of ellipticine have been reported in literature.[30-32] In non-polar solvents ellipticine emission is detected around 410 nm, and it is attributed mainly to the neutral form of ellipticine. With increasing solvent polarity, the emission maximum shifts towards red edge (at 520 nm). Moreover, in water ellipticine emits at 520 nm, which is believed to appear from protonated pyridine nitrogen (**Scheme 5.1**). On the other hand in methanol and ethylene glycol it exhibits concomitant dual emission at ~430 nm and ~510 nm.[30-32] Miskolczy *et al.* assigned the red edge emission of ellipticine to excited state protonation of pyridine moiety by solvent proton transfer.[32] Fung *et al.* highlighted high polarity and dipole moments (higher than 12.2 D) of the solvents along with a strong hydrogen bonding ability as the origin of higher wavelength peak.[30] Very recently, Banerjee *et al.* reported solvent mediated excited state intramolecular proton transfer from the pyrrole nitrogen to pyridine nitrogen as origin of fluorescence from protonated ellipticine.[31]

Irrespective of the origin of the dual emission, the vast separation of fluorescence emission of neutral (generally prevails in non-polar environment), and protonated ellipticine (exists in polar-protic environment) indicates that it can be the ideal molecule for fluorescence switching studies.

Protein-DNA interaction plays an important role in all aspect of genetic activity within organism, such as regulation of gene expression, transcription, repair and packaging.[33-37]Therefore, it appears extremely important to get insight about the mechanism as well as dynamics of this process. Literatures about DNA-protein interactions using fluorescence of trivial hydrophobic dyes are available,[36-41] where quantum yield of the dye was monitored to probe the interaction and in most cases the decreasing fluorescence makes the process complicated. Therefore, it would be worth to think about a fluorescent probe, which will shine brighter or shift its emission during binding with a macromolecule.

Herein, we report a non-specific protein (serum albumin)-DNA (calf thymus) interaction monitored through a tuneable emission switch of ellipticine, with the help of steady state, time resolved fluorescence spectroscopy and circular dichroism. Molecular modelling using Autodock has been employed to get detailed insight about drug-protein interaction. We have demonstrated that two different bio-macromolecules can shuffle the emission position so effectively that ellipticine can even be promoted as a molecular sensor for these biopolymers. Moreover, a direct morphological pattern of the protein-DNA self-assembled aggregates have been reported through field emission scanning electron microscopy (FE-SEM). This unique approach offers valuable physical insight about the probable ternary complexation comprising of protein, ellipticine and DNA.

5.2. Results and Discussions

5.2.1 Ellipticine-Serum Protein Interaction

5.2.1a. Steady State Results

Ellipticine (**Scheme 5.1**) in phosphate buffer saline of physiological pH exhibits a single, broad and unstructured emission at 525 nm (**Figure 5.1**) attributed to protonated ellipticine, as the protonation pK_a of quinoline nitrogen in water is 7.4.[28] A dramatic modification of ellipticine emission (**Figure 5.1**) has been observed with increasing concentration of serum albumin (BSA & HSA). At very first addition of BSA (0.25 μM), a new peak starts appearing at ~440 nm. With upraising BSA concentrations the intensity at 440 nm strongly rises, and

finally gets saturated at higher protein additions (maximum 110 μM). It is already reported that when ellipticine resides in hydrophobic environment, the apparent pK_a of quinoline nitrogen drops down to ~6 due to reduced polarity,[28] and facilitates the transformation from protonated to neutral form of ellipticine.[28, 30] Moreover, in low dielectric solvents, ellipticine exhibits high energy emission peak mainly originated from neutral form.[30-32] Therefore, the emission peak at 440 nm is ascribed to the neutral ellipticine molecules bound to serum albumin (BSA/HSA). Relative comparison with previous results shows ellipticine exhibits a peak at ~444 nm in methanol and ethanol having $E_T(30)$ value of 55.4 and 51.90,[42] respectively. Hence, neutral ellipticine experiences a polarity value close to ~53.5 in E_T (30) scale inside the protein binding pocket. Ellipticine constituted by extended aromatic rings is highly hydrophobic and the hydrophobic-hydrophobic interaction between protein and drug drags the drug molecule inside protein pocket away from high polarity environment of water (63.1 in E_T (30) scale). With every addition of serum albumin (SA) more hydrophobic

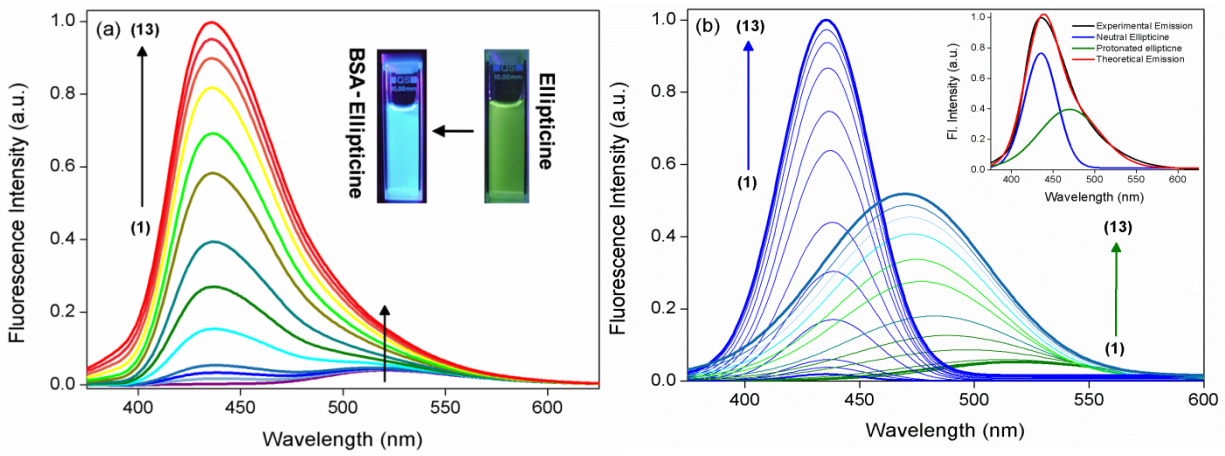

Figure 5.1. *(a) Fluorescence emission intensity of ellipticine with increasing BSA concentrations where 1→13 represents 0, 0.25, 0.50, 1, 3, 6, 10, 20, 30, 50, 70, 90 and 110 μM BSA. Inset shows the colour switch by BSA addition. (b) Deconvoluted emission intensity of ellipticine with variable BSA concentrations, where 1→13 caries the same meaning of (a).*

vicinity has been created around the drug molecules, which modulates the emission behaviour of ellipticine, and plays a crucial role for the fluorescence switching from 525 nm to 440 nm. Unlike 440 nm, emission at 525 nm does not shoot up drastically but an apparent enhancement of fluorescence intensity is observed with increasing SA concentrations (**Figure 5.1a**). Deconvoluted spectra show prominent intensity rise at 525 nm along with a dominant blue shift (**Figure 5.1b**), which infers that a fraction of protonated ellipticine molecules are

also moving inside the binding pocket of serum protein. The reduced polarity at binding pockets might be responsible for the blue shift of the protonated peak.

A quantitative estimation of drug-protein interaction is always important since the interaction efficiency and influence of the drug on protein structure governs the therapeutic importance of the drug. Ellipticine-BSA binding constant was elucidated using modified Scatchard plot[43, 44] (described in **Chapter 3**) which offers association constant (K_a) of $(2.75 \pm 0.138)\times10^5$ M^{-1} for 440 nm emission using modified Scatchard plot (**Appendix 5.1**). The association constant along with high free energy change (ΔG^0 = -7.41 kcal.mol^{-1} at 298 K) implies that the binding interaction between neutral ellipticine and BSA is energetically favored. The binding constant $(2.50 \pm 0.126) \times 10^5$ M^{-1} measured at 525 nm and free energy change (-7.30 kcal.mol^{-1}) for the complexation, clearly implies that the protonated ellipticine also has strong binding affinity towards BSA. The K_a and ΔG^0 values are found to be in good accordance with literature reports for several other probe-protein interaction studies.[45-48] On basis of steady state emission results we anticipate that domain I characterized by net negative charge[49, 50] and can serve as a suitable binding site for protonated ellipticine (as it contains one unit positive charge). Whereas domain II or III, being dominantly hydrophobic[49, 50] is the most probable location for neutral ellipticine. To extend the applicability of our work, we have also monitored interaction of ellipticine with human serum albumin (HSA) under similar experimental conditions (**Appendix 5.2**).

5.2.1b. Steady State Anisotropy

Anisotropy measurement can offer a vivid perception about the bound and an unbound state of the molecule.[24] The difference of anisotropy between free and bound drug molecules can be utilized extensively to evaluate the location of the probe in macro structures.[45, 51] **Figure 5.2** depicts the change of steady state anisotropy for both neutral and protonated ellipticine with the increasing concentrations of protein. In both the cases, a steep rise followed by saturation in anisotropy value is observed **(Figure 5.2)**. The steep rise in the anisotropy indicates increasing restriction of rotational motion of drug, and the attainment of plateau implies the saturation in the binding interaction between the drug and protein. The applicability of anisotropy measurements has been extended by determining the association constant (K_a) for drug-protein interaction (**Appendix 5.n1**). The association constant (K_a) (from the plot in inset of **Figure 5.2**) determined for neutral and protonated ellipticine are 1.27×10^5 M^{-1} and 1.15×10^5 M^{-1} respectively. These values are in close agreement with the

results obtained from steady state emission measurements. Therefore, anisotropy data also supports our steady state emission results where we have seen that both protonated and neural ellipticine molecules strongly interact with protein.

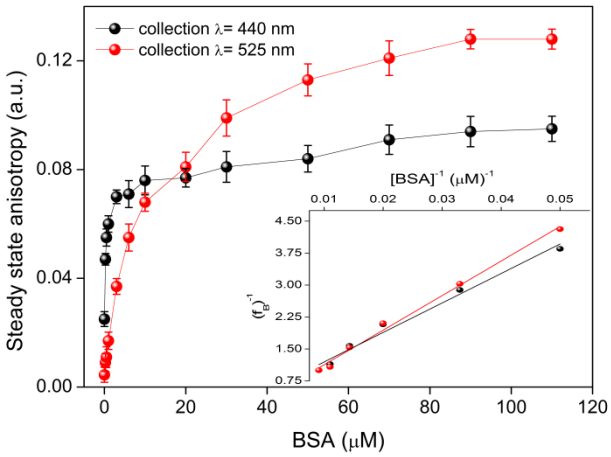

Figure 5.2. *Steady state anisotropy of ellipticine with increasing BSA concentration, inset shows the binding curve generated from anisotropy data.*

5.2.1c. Time Resolved Lifetime Measurements

The fluorescence lifetime data can significantly contribute in realizing the interaction behavior between ellipticine and BSA.[24, 45] The typical time-resolved fluorescence decay profiles are displayed in **Figure 5.3** and the fitting parameters are summarized in **Table 5.1**. The decay profile of free drug (PBS, pH7) monitored at 525 nm (**Table 5.1**) is found to exhibit bi-exponential feature with the lifetime component of 2 ns (92%) and 5.38 ns (8%). In aqueous buffer ellipticine mainly exists in protonated form,[28-30, 32] hence, we believe the dominant contribution (92%) of 2 ns component corresponds to the lifetime of protonated ellipticine. The 5.38 ns component is unlikely to appear from neutral ellipticine, as neutral form of the drug does not show any emission at 525 nm. However, tautomeric form (**Scheme 5.1**) of ellipticine can contribute towards the 525 nm emission intensity, though the quantum yield is very low in water (**Figure 5.1**). Therefore, we anticipate that 5.38 ns component reflects the lifetime of tautomeric form of ellipticine, which has minute population in water. In presence of protein, the contribution from the protonated form of ellipticine (~2 ns) decreases sharply, whereas a long component of ~16 ns to ~19 ns appears in place of 5.38 ns component (**Table 5.1**). The newly appeared long component is believed to be an outcome of protonated (or tautomeric) ellipticine bound to the protein binding pocket, and it corroborates

well with the steady state results where we have observed that protonated ellipticine also participates in BSA binding. At higher protein concentration a fast component of ~500 ps appears in addition to other two components. We believe that due to the increased crowdedness at higher protein concentration, the drug molecules cannot easily access the binding pocket of protein. However, due to the Brownian motion as well as electrostatic attraction drug molecules can easily repose on protein surface. The short lifetime might be outcome of the strong electrostatic attraction between the protonated ellipticine and negatively charged side chains of amino acid at the protein surface, by which electronic structure of protonated ellipticine is getting perturbed.

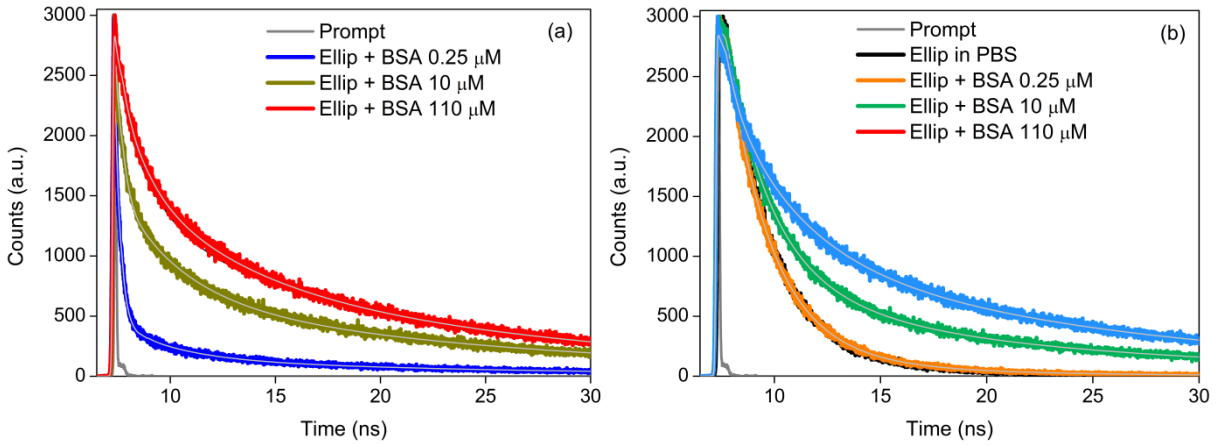

Figure 5.3. *Lifetime decay profile of ellipticine in PBS (λ_{ex}=375 nm) and with increasing BSA concentrations collected at (a) 440 nm and (b) 525 nm, respectively.*

To get insight about the dynamics of neutral ellipticine generated in presence of protein, we have also collected lifetime at 440 nm in presence of protein (**Figure 5.3, Table 5.1**). At 0.25 μM of protein concentration, a tri-exponential decay shows lifetime components of 220 ps (90%), 2.67 ns (7%) and a long lifetime 17 ns (3%). It is reported that ellipticine in non-polar solvents (like dioxane, cyclohexane, hexane etc.) exhibits very long lifetime,[30] and in these non-polar media ellipticine is likely to exist exclusively in neutral form due to the reduced pK_a of protonation in non-polar environment.[28, 30] Hence, 17 ns lifetime is attributed to neutral ellipticine inside the protein nano-cavity, where it experiences a relatively higher hydrophobicity. A glance at **Table 5.1** reveals that the contribution of this long component increases with rising BSA concentration, which proves that a dominant fraction of neutral ellipticine enters inside the protein binding pocket and it is in well agreement with the steady

state results where we have observed that the intensity of neutral ellipticine (**Figure 5.1**) is progressively enhanced in presence of BSA. The appearance of ~2.5 ns component (which is matching with the lifetime of protonated ellipticine) seems unusual as neutral ellipticine molecules mostly contribute at 440 nm. Moreover, the contribution of this component increases as protein concentration increases. It is already observed from deconvoluted emission profiles that protonated form of ellipticine has significant intensity contribution

Table 5.1. *Lifetime results of ellipticine in buffer and in presence of BSA. Drug molecules are excited at 375 nm and decay profiles are collected at (a) 525 nm and (b) 440 nm.*

Sample	τ_1 (ns)	τ_2 (ns)	τ_3 (ns)	R_1	R_2	R_3	τ_{av}(ns)[#]	χ^2
(a) $\lambda_{collection}$ = 525 nm								
Ellip in PBS (pH 7)		2	5.38		0.92	0.08	2.31	1.00
Ellip + BSA 3 μM		2.24	15.0		0.91	0.09	3.35	1.01
Ellip + BSA 10 μM		2.30	16.0		0.57	0.43	8.15	1.00
Ellip + BSA 50 μM	0.464	3.09	17.0	0.25	0.42	0.33	7.01	0.96
Ellip + BSA 110 μM	0.510	2.89	16.7	0.32	0.29	0.39	7.50	0.99
(b) $\lambda_{collection}$ = 440 nm								
Ellip + BSA 0.25 μM	0.220	2.67	17.00	0.90	0.07	0.03	0.900	1.02
Ellip + BSA 3 μM	0.273	2.80	17.82	0.58	0.24	0.18	3.98	1.03
Ellip + BSA 10 μM	0.501	3.31	18.47	0.42	0.31	0.27	6.35	0.98
Ellip + BSA 50 μM	0.717	4.08	19.05	0.38	0.30	0.32	7.58	1.06
Ellip + BSA 110 μM	0.661	4.53	19.40	0.41	0.31	0.27	6.96	1.02

[#] $\tau_{av} = (\tau_1 \times R_1) + (\tau_2 \times R_2) + (\tau_3 \times R_3)$

even at 440 nm, and its contribution increases sharply, as the protein concentration increases. Hence, ~2.5 ns component appeared in the decay profile of 440 nm is attributed to the protonated ellipticine molecules those are free or unbound. The existence of relatively shorter lifetime (200-700 ps) in presence of protein environment is more interesting. At low BSA concentration the 220 ps component has a very high contribution of ~90%, and with increasing BSA concentration the component lifetime slightly increases but the contribution decreases sharply. We anticipate that the fastest component (~200-700 ps) reflects the dynamics of neutral ellipticine attached to the surface of protein by strong hydrogen bond

with the side chains of amino acids. The reduced lifetime value can probably be attributed to energy dissipation via the vibrations associated with the intermolecular hydrogen bonding between N-H of the pyrrole ring and -OH/O^-/-NH_2/-S/-SH group of amino acid side chains.[32]

5.2.1d. Time Resolved Anisotropy Measurements

We have also performed time resolved anisotropy measurement, which provides notion about the rotational relaxation of the drug, when it binds to the protein.[24, 52, 53] The typical anisotropy decay profile of ellipticine in aqueous buffer as well as protein environment is shown in **Figure 5.4**. The drug exhibits a single exponential decay in aqueous buffer with rotational relaxation time of ~130 ps (**Table 5.2a**). As in aqueous buffer ellipticine exists

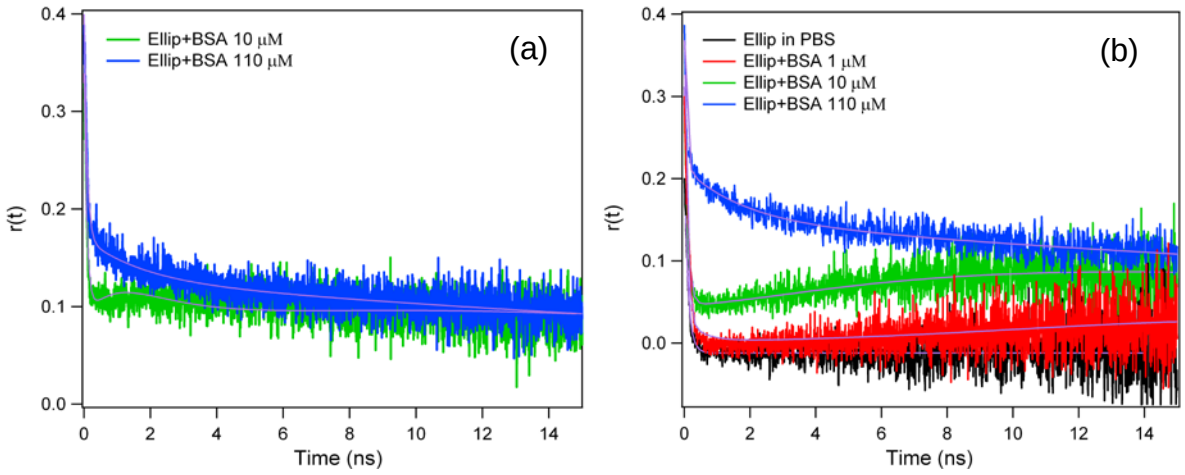

Figure 5.4. *Anisotropy decay profile of ellipticine at different BSA concentrations (shown in legends). Ellipticine was excited (λ_{ex}) 375 nm and anisotropy was collected (λ_{em}) at (a) 440 nm and (b) 525 nm.*

mainly in protonated form, the anisotropy decay in water only provides idea about the rotational relaxation of protonated ellipticine molecules. However, we believe that if neutral ellipticine could exist in water, it would have shown similar relaxation time, as both forms differ only with respect to single proton. In presence of protein environment, anisotropy decay time for both neutral and protonated ellipticine slows down, implying protein induced confinement for both of the forms (**Figure 5.4**). Interestingly at lower concentration of protein (1 μM and 10 μM) a growth component is observed which leads to unusual 'dip-rise' feature in the anisotropy decay (**Figure 5.4)**. This kind of not-so-common time-resolved anisotropy arises due to the presence of multiple species, each characterized by its own

lifetime and anisotropy decay.[54-58] However, at higher protein concentration, the 'dip-rise' feature is absent, and the decay exhibits some residual anisotropy, which does not decay within our experimental time window. This is because at higher protein concentration, the population of short lifetime component reduces down significantly compared to long component population.

The detail fitting analysis of 'dip-rise' profile has been described here under. In case of "dip-rise" nature of anisotropy decay, we have to consider time dependence of weighing factor $x_i(t)$, where $x_i(t)$ depends on the a_i, τ_i, and the total intensity decay $I(t)$ by the following equation as suggested by Ludescher *et al*.[57]

$$x_i(t) = \frac{a_i[exp\left(-\frac{t}{\tau_i}\right)]}{I(t)} \quad \ldots 5.1$$

Where, a_i is the percentage contribution of lifetime component τ_i, and $I(t)$ is the total decay. The final equation for dip-rise anisotropy appears to be;

$$r(t) = r_0 \times \frac{[\{R_1 exp\,(-\frac{t}{\tau_1}) \times f_1 exp\,(-\frac{t}{\tau_{r1}})\} + \{R_2 exp\,(-\frac{t}{\tau_2}) \times f_2 exp\,(-\frac{t}{\tau_{r2}})\} + \{R_3\, exp\,(-\frac{t}{\tau_3}) \times f_3 exp\,(-\frac{t}{\tau_{r3}})\}]}{[R_1 exp\left(-\frac{t}{\tau_1}\right) + R_2 exp\left(-\frac{t}{\tau_2}\right) + R_3 exp\,(-\frac{t}{\tau_3})]} \quad \ldots 5.2$$

where, r_0 known as residual anisotropy, τ_1, τ_2, τ_3, are the lifetime components of the corresponding decays having a relative contribution of each component as R_1, R_2, and R_3 respectively. During 'dip-rise' anisotropy fit the lifetime components and its relative contribution were kept fixed. The rotational decay time of i^{th} component has been represented by 'τ_{ri}', and its corresponding contribution has been designated as 'f_i'. All the "dip-rise" results are shown in **Table 5.2a**.

The anisotropy decays of protonated ellipticine (collected at 525 nm) at higher protein concentrations are devoid of any 'dip-rise' features, and hence fitted by trivial equation of fitting for anisotropy data which is described in **Chapter 3**. It is found that anisotropy decays of protonated ellipticine (monitored at 525 nm) in presence of 110 μM protein consists of three components, with a rotational relaxation times of ~130 ps, ~2 ns, and ~47 ns (**Table 5.2b**). The fast rotational relaxation component corresponds to the unbound protonated ellipticine. Slower component (2 ns) might reflect either the segmental motion of protein or

surface bound protonated ellipticine, while the slowest component of ~47 ns is assigned to be global tumbling motion of the protein. The anisotropy decay of neutral ellipticine monitored at 440 nm in presence of 110 μM protein concentration also consists of three components having similar rotational time constants as that of protonated one (**Table 5.2b**). However, the percentage contribution of each component is slightly different. Here it is necessary to mention that protonated ellipticine also contributes to the anisotropy decay profile monitored at 440 nm, as it has some reasonable intensity at 440 nm. Therefore, the decay characteristics at 440 nm may not reflect the true anisotropy decay of neutral ellipticine. However, it provides conclusive evidence for the strong interaction between the neutral form of drug and protein.

Table 5.2a. *Fitting parameters of 'dip-rise' anisotropy decay features of ellipticine-BSA.*

Sample	τ_{r1} (ns)	τ_{r2} (ns)	τ_{r3} (ns)	f_1	f_2	f_3	r_0
Ellip + BSA (1 μM) at 440 nm	0.075	1.32	37.34	0.92	1.36	0.31	0.40
Ellip + BSA (10 μM) at 440 nm	0.091	3	45	2.08	0.40	0.50	0.27
Ellip + BSA (1 μM) at 525 nm	0.08	1	48	2.0	0.13	0.15	0.30
Ellip + BSA (10 μM) at 525 nm	0.1	2.38	45	1.61	0.32	0.45	0.30

Table 5.2b. *Anisotropy results of ellipticine in buffer and in presence of BSA (no dip-rise feature).*

Sample	τ_{r1} (ns)	τ_{r2} (ns)	τ_{r3} (ns)	a_1	a_2	a_3	r_0
Ellip in PBS 525 nm	0.13	-	-	0.39	-	-	0.39
Ellip + BSA (110 μM) at 440 nm	0.08	1.86	45	0.23	0.04	0.12	0.39
Ellip + BSA (110 μM) at 525 nm	0.13	2.0	47	0.18	0.06	0.15	0.39

5.2.1e. Molecular Modelling

Insight about the location of drug inside the protein binding pocket is always important in order to judge the carriage and therapeutic efficiency of the drug. To evaluate the molecular interaction and accurate binding locations of ellipticine, we have utilized molecular docking study (protocol is described in chapter 3). As it is already evident from experimental results that both the forms of the drug interact with serum protein, hence we have chosen both the

forms of the drug for docking study. Before docking these two forms of ellipticine have been energy minimized using Gaussian 98[59]. The most probable binding site for protonated

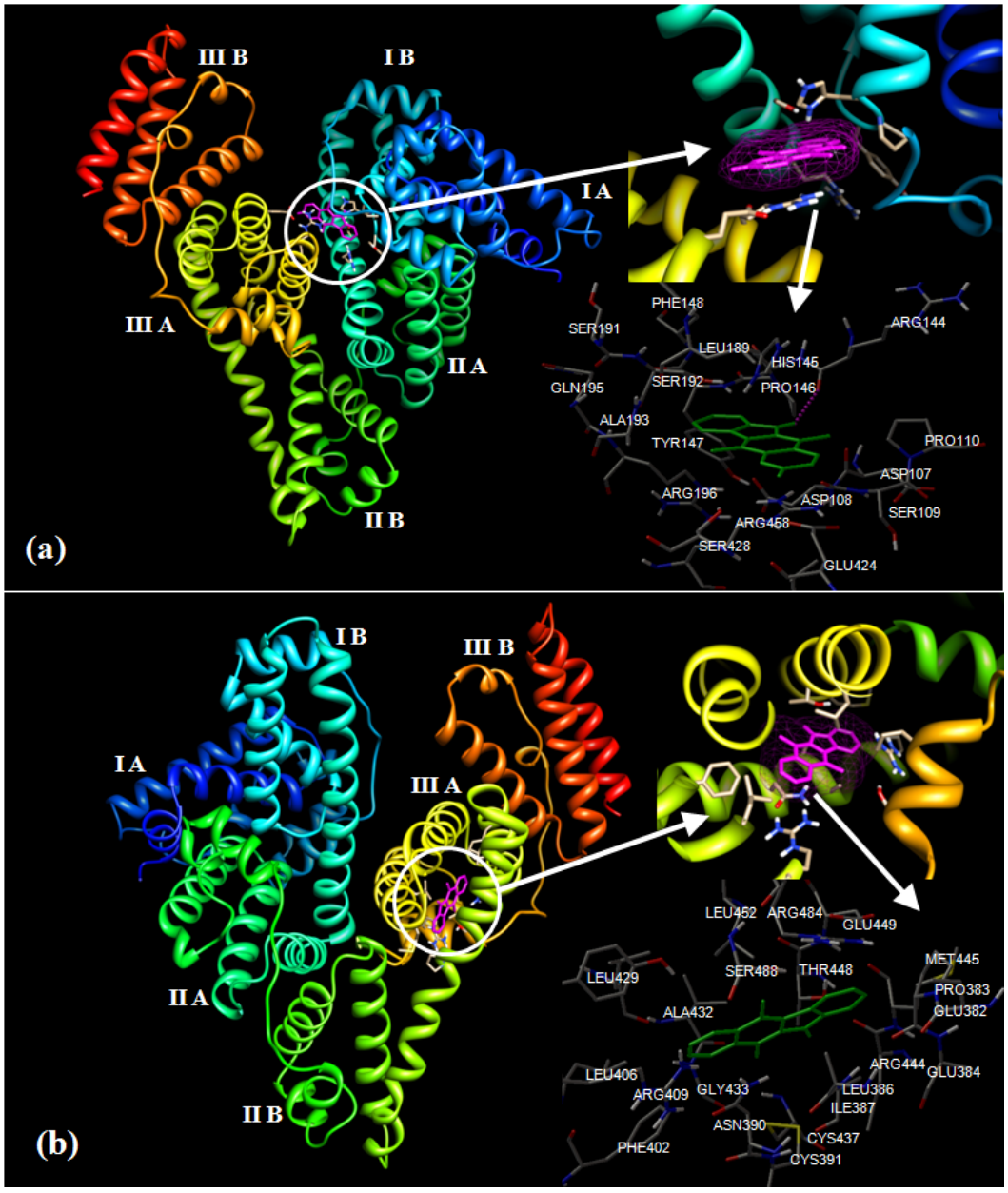

Figure 5.5. *Docked conformation of ellipticine with BSA. (a) Protonated ellipticine bound to domain IB, where inset shows the magnified view of binding site along with hydrogen bonding interaction. (b) Neutral ellipticine bound to domain IIIA, where inset shows the magnified view of binding along with surrounding amino acids.*

ellipticine is found to be domain IB (**Figure 5.5a**). The domain I is surrounded by ASP107, ASP108, SER109, PRO110, ARG144, HIS145, PRO146, TYR147, SER191, SER192, ALA193, ARG196 and ARG458 amino acids.[49, 50] Hence, the protonated ellipticine feels a

strong electrostatic drag towards this domain, and offers a very high binding free energy change ~ -9.03 kcal/mol. Protonated ellipticine forms a hydrogen bonding interaction with HIS145 with reasonably high energy (-0.227 kcal/mol, and interaction distance 2.112 Å), which offers stability of the drug in this domain. On the other hand the docking study reveals that neutral form is found to reside at domain IIIA (**Figure 5.5b**), surrounded by the amino acids GLU382, PRO383, LEU386, ILE387, ASN390, CYS391, PHE402, LEU406, ASG409, LEU429, ALA432, GLY433, CYS437, MET445, THR448, GLU449, LEU452 and ARG484. This finding also seems logical as domain III A is characterized as hydrophobic domain,[45, 49] which is more likely to favour neutral instead charged structure of ellipticine. Moreover, in case of neutral ellipticine no hydrogen bonding interaction between drug and above mentioned amino acids is observed. Neutral ellipticine also shows a quite high binding free energy change, -7.8 Kcal.mol^{-1} and a binding constant (K_a) of 5.0 ×10^5 M^{-1}. In summary, the docking results validate well the experimental observations, where we have found enough evidence for the binding of both the forms of ellipticine with serum albumin.

5.2.2. Ellipticine CT-DNA Interaction

Although the interaction behavior of ellipticine with DNA is well explored in the literature,[28, 29] in order to compare with protein, we have probed the interaction characteristics between ellipticine and CT-DNA mainly through fluorescence measurements. A dramatic enhancement of the intensity at 525 nm peak (attributed to protonated ellipticine) is observed with the hike in DNA concentration (**Figure 5.6**). The huge enhancement of emission is an outcome of the intercalation of protonated ellipticine to DNA[28, 60-62]. Unlike protein environment, ellipticine does not bind to DNA in its neutral form, because of apparent increase of protonation pK_a due to the enhanced proton activity at the anionic interface.[28] Intensity at peak maximum has been utilized to calculate the binding constant of ellipticine and DNA. The binding constant is estimated from Scatchard plot (detail description in **Chapter 3**) determined to be K_a=5.04×10^5 M^{-1}, which is very close to the value obtained from chromatin bound ellipticine case.[28] The higher binding affinity is also supported by steady state anisotropy measurement, where it is observed that with gradual addition of DNA anisotropy value of ellipticine rises up and gets saturated at ~70 μM DNA (**Figure 5.6b**). Above 70 μM the anisotropy value reaches to a plateau region, which infers the saturation in the binding interaction between the drug and DNA.

Fluorescence decay profiles of the drug in absence and presence of CT-DNA are shown in **Figure 5.6c** and the results are tabulated in **Table 5.3**. With the gradual addition of DNA, the percentage contribution of short lifetime component (~2 ns) progressively decreases, whereas a longer lifetime component of ~12 ns generates in the decay profile, and ultimately reaches to 96% at maximum DNA concentration. The increased lifetime of ellipticine in presence of DNA might be attributed to the enhanced stability of the drug by the stacking interaction with DNA. The interaction between ellipticine and DNA is also probed

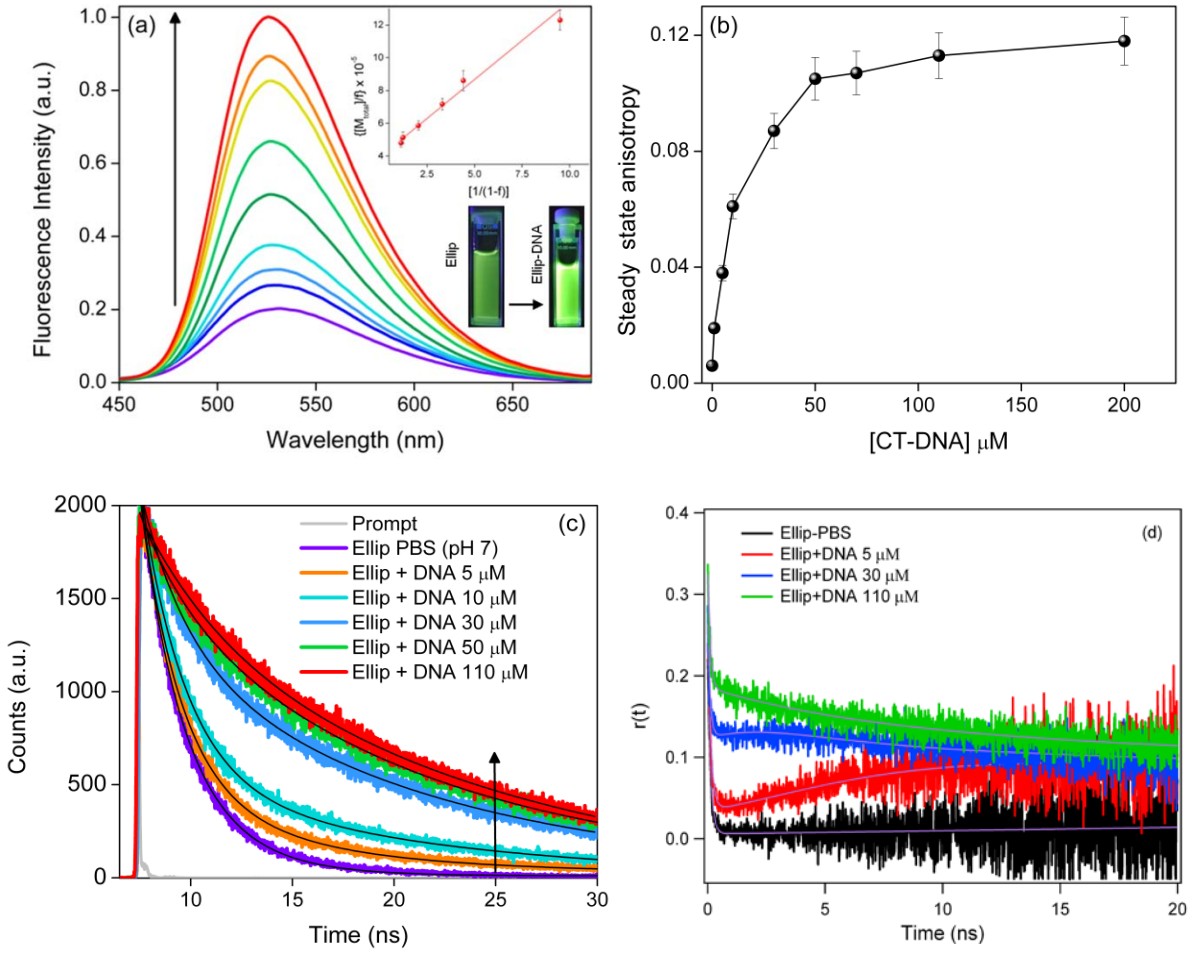

Figure 5.6. *(a) Fluorescence emission spectra of ellipticine in PBS and with increasing DNA concentration ([DNA] = 1, 5, 10, 20, 30, 50, 70, 110 μM, respectively). Inset shows the Scatchard plot constructed from emission intensities. (b) Steady state anisotropy change of ellipticine at various DNA concentrations. (c) Lifetime decay profiles of ellipticine with various DNA concentrations. (d) Anisotropy decay profiles of ellipticine with various DNA concentrations.*

from time-resolved anisotropy measurements (**Figure 5.6d**). Like protein, initial addition of DNA leads to 'dip-rise' feature of anisotropy decay profile (**Table 5.4a**). However, at higher DNA concentration the 'dip-rise' feature is totally vanished (**Figure 5.6d, Table 5.4b**). The analysis of anisotropy decay profiles clearly implies that the rotational relaxation of the drug is significantly retarded in presence of DNA (**Table 5.4**). A very slow rotational relaxation time together with the existence of residual anisotropy reflects the intercalation is preferred binding mode of the drug to DNA.

Table 5.3. *Lifetime results of ellipticine in buffer and with CT-DNA where samples were excited (λ_{ex}) at 375 nm and emission decays were (λ_{em}) collected at 525 nm.*

Sample	τ_1 (ns)	τ_2 (ns)	R_1	R_2	τ_{av} (ns)[#]	χ^2
Ellip in PBS (pH 7)	2	5.38	0.92	0.08	2.31	1.00
Ellip + DNA 5 μM	2.06	11.70	0.49	0.51	3.54	1.05
Ellip + DNA 10 μM	2.05	12.75	0.32	0.68	4.75	1.03
Ellip + DNA 50 μM	2.00	13.8	0.06	0.94	10.6	1.03
Ellip + DNA 110 μM	2.82	14.43	0.04	0.96	12.32	1.02

[#] $\tau_{av} = (\tau_1 \times R_1) + (\tau_2 \times R_2)$

Table 5.4a. *Fitting parameters of 'dip-rise' anisotropy decay features of ellipticine-DNA system.*

Sample	τ_{r1} (ns)	τ_{r2} (ns)	τ_{r3} (ns)	f_1	f_2	f_3	r_0
Ellip + DNA (5 μM) at 525 nm	0.1	5	100	2.09	0.24	0.47	0.25
Ellip + DNA (30 μM) at 525 nm	0.1	8.0	100	1.45	1.74	0.44	0.27

Table 5.4b. *Anisotropy results of ellipticine in buffer and in presence of DNA (no dip-rise feature).*

Sample	τ_{r1} (ns)	τ_{r2} (ns)	τ_{r3} (ns)	a_1	a_2	a_3	r_0
Ellip + DNA (50 μM) at 525 nm	0.09	6.82	100	0.24	0.03	0.13	0.40
Ellip + DNA (70 μM) at 525 nm	0.09	5.82	110	0.17	0.05	0.14	0.36
Ellip + DNA (110 μM) at 525 nm	0.09	4.87	93	0.14	0.05	0.14	0.33

5.2.3. Serum Protein-Ellipticine-DNA Interaction

5.2.3a. Steady State Results

As mentioned earlier, serum protein (BSA)-bound ellipticine mainly emits blue fluorescence at 440 nm, and is attributed to the neutral ellipticine molecules residing at domain IIIA

(Figure 5.1). With gradual addition of calf-thymus DNA (CT-DNA), the intensity of blue emission (440 nm) decreases sharply and a new peak appears in the green region at ~512 nm (**Figure 5.7**). A strong intensity decrease at 440 nm along with a freshly appearing green emission at 512 nm infers DNA mediated withdrawal of neutral ellipticine molecules from ellipticine-BSA complex. The increasing ellipticity of BSA in circular dichroism (CD) (**Appendix 5.3**) spectra with raising DNA concentration suggests that secondary structure of

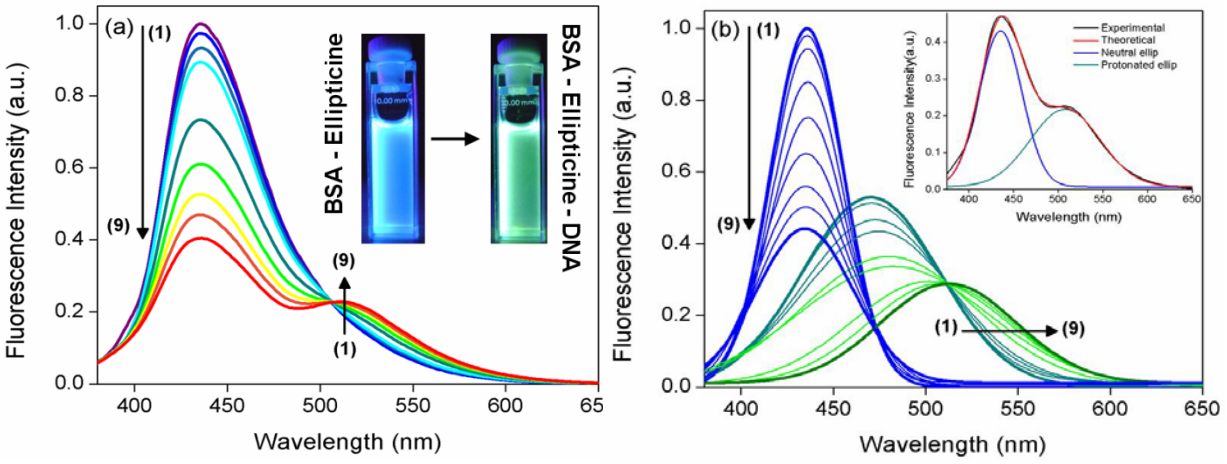

Figure 5.7. *(a) Fluorescence emission spectra of BSA (110 μM) bound ellipticine with increasing DNA concentration (1→9 represents [DNA] = 0, 1, 6, 10, 30, 50, 70, 90 and 110 μM). Inset shows colour transition due to ternary complexation. (b) Deconvoluted emission intensity of ellipticine-BSA with variable DNA concentration, where 1→9 caries the same meaning as that of (a). Inset represents a sample of deconvolution.*

BSA is not perturbed; rather CT-DNA stabilizes the secondary structure of the protein. This substantiates well with the previous reports about structural stabilization of HSA by CT-DNA.[63] Henceforth, DNA assisted perturbation of the tertiary structure of BSA may be the possible reason for the displacements of drug molecules from protein binding cavity. It is also noticeable from **Figure 5.7b** that the intensity at 440 nm does not vanish completely even at highest concentration of CT-DNA, indicating a small fraction of neutral ellipticine molecules are still left inside the binding pocket of BSA. The DNA driven dissociation constant; K_d = (2.70 ±0.2)×10^5 M^{-1} calculated from the intensity decrement at 440 nm (**Appendix 5.4**) is very close to that of ellipticine-BSA binding constant (K_a=1.27×10^5 M^{-1}) which infers about the possibility of DNA induced removal of drug molecules from protein pocket.

Although in BSA the main emitting specie is neutral ellipticine, the deconvoluted emission spectra (**Figure 5.7b**) clearly indicates the presence of protonated ellipticine in

BSA. The deconvoluted emission spectra (**Figure 5.7b**) show that BSA bound protonated ellipticine peak appears at ~475 nm and gradually shifts to red region along with progressive decrease of emission intensity. Moreover, a clear iso-emissive point observed at 507 nm in presence of DNA. The red shift along with iso-emissive point is indicative towards the existence of ternary complex comprising DNA, protein and protonated ellipticine. Using the emission intensities at respective peak maximum, the binding constant for ternary complexation is calculated to be $(2.20\pm0.18)\times10^4$ M^{-1}, which infers the process is highly energy favoured and spontaneous (ΔG^0=-5.90 kcal.mol^{-1}). It is intriguing to observe that HSA and salmon sperm DNA (**Appendix 5.5**) also offers similar trends in emission and changes in binding free energies like BSA-DNA system, inferring the wide applicability of present work for wild DNA and globular proteins. Previously, IR studies revealed that the interaction between CT-DNA and HSA (a homologous protein of BSA) takes place via polypeptide C=O, C-N and N-H groups.[63] Moreover, IR studies showed that two major binding sites were located at G-C bases and the backbone phosphate group of DNA.[63] Considering the fact that protonated ellipticine will be attracted by the phosphate backbone of DNA; we believe that electrostatically formed tertiary complex might be favoured in our case. It is also noticeable that at higher concentration of DNA (~110 μM), protonated ellipticine emits at ~512 nm (**Figure 5.7b**) which is ~13 nm blue shifted from DNA-intercalated protonated ellipticine emission at ~525 nm (**Figure 5.6a**). This suggests ellipticine does not intercalate, rather it is involved in ternary complex formation with BSA and DNA. A more clear insight about the formation of ternary complex is described through lifetime traces and time-resolved anisotropy results described afterwards.

5.2.3b. Time Resolved Lifetime Results

We have monitored the fluorescence lifetime of protein bound ellipticine with raising concentration of DNA to get insight into the protein-DNA interaction scenario. The typical time-resolved decay profiles are depicted in **Figure 5.8** and the results are summarized in **Table 5.5**. The drug molecules show a multi-exponential decay profile, which is obvious for the case of micro-heterogeneous environment comprising both protein and DNA. In such a case, it appears to be difficult to assign individual decay components. Therefore, it is rational to consider the average fluorescence lifetimes of the drug instead of emphasizing on individual decay components. It is noticeable from the results shown in **Table 5.5** that the average lifetime of BSA-bound protonated ellipticine (~7 ns) progressively increases with the

gradual addition of DNA, and this is certainly an outcome of the interaction between protein bound drug and DNA. Steady state results have already provided a notion that protonated

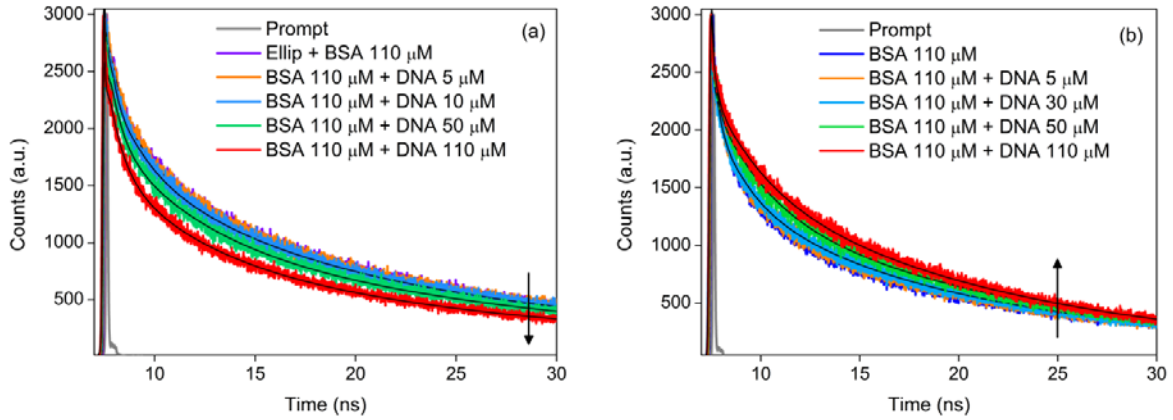

Figure 5.8. *Lifetime decay profile of ellipticine-BSA (λ_{ex}=375 nm) with increasing DNA concentrations (shown in legend) collected at (a) 440 nm and (b) 525 nm respectively.*

form of drug molecule involves in ternary complex formation. We believe that the increase in average lifetime of drug from 6-9 ns is an outcome of the same. Therefore, lifetime results pave a way for assessing the existence of ternary complex comprising of protein, DNA and

Table 5.5. *Lifetime results of ellipticine-BSA with increasing concentration of DNA. Ellipticine is excited (λ_{ex}) at 375 nm and emission collected (λ_{em}) at (a) 440 nm and (b) 525 nm.*

Sample	τ_1 (ns)	τ_2 (ns)	τ_3 (ns)	R_1	R_2	R_3	τ_{av} (ns)[#]	χ^2
(a) $\lambda_{collection}$ = 440 nm								
Ellip-BSA + DNA 5 μM	0.461	4.15	21.16	0.36	0.26	0.36	8.97	1.01
Ellip-BSA + DNA 10 μM	0.454	3.94	21.40	0.38	0.26	0.35	8.77	1.03
Ellip-BSA + DNA 50 μM	0.221	3.30	20.72	0.46	0.25	0.29	6.91	1.10
Ellip-BSA + DNA 100 μM	0.176	2.88	20.22	0.54	0.23	0.23	5.42	1.06
(b) $\lambda_{collection}$ = 525 nm								
Ellip-BSA + DNA 5 μM	0.530	3.00	16.34	0.32	0.28	0.41	7.73	1.02
Ellip-BSA + DNA 30 μM	0.535	3.10	16.13	0.28	0.28	0.44	8.10	1.01
Ellip-BSA + DNA 50 μM	0.610	3.40	15.60	0.29	0.24	0.47	8.40	1.02
Ellip-BSA + DNA 100 μM	0.535	3.13	15.00	0.23	0.23	0.54	8.96	1.01

[#] $\tau_{av} = (\tau_1 \times R_1) + (\tau_2 \times R_2) + (\tau_3 \times R_3)$

protonated ellipticine. The average fluorescence lifetime of protein bound neutral ellipticine monitored at 440 nm (**Table 5.5**) progressively decreases with increasing DNA concentration, indicating the expulsion of neutral ellipticine from its stronger binding sites to the proximity of bulk water. Hence, lifetime results corroborate the steady state results, where we have also noticed that the quantum yield of neutral ellipticine progressively decreases with increase in DNA concentration.

5.2.3c. Time Resolved Anisotropy Results

We have further exploited fluorescence anisotropy technique to establish the interaction behaviour of ellipticine in presence of both protein and DNA. **Figure 5.9** depicts the typical anisotropy decays of protonated ellipticine (monitored at 525 nm) containing 110 μM of protein with increasing DNA concentration and the results are tabulated in **Table 5.6**. Anisotropy decay of protonated ellipticine in 110 μM protein concentrations consists of three components, which are ~130 ps and ~2 ns, along with a long component of 47 ns (**Table 5.6**).

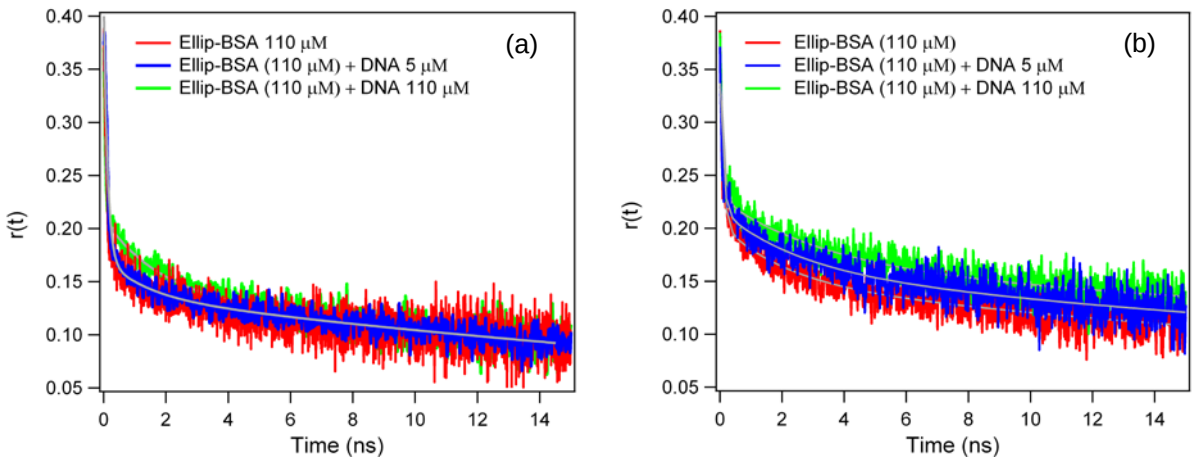

Figure 5.9. *(a) Anisotropy decay profile of ellipticine-BSA (λ_{ex}=375 nm)at various DNA concentrations (shown in legend) collected at (a) 440 nm and (b) 525 nm respectively.*

The fast rotational relaxation component corresponds to the unbound ellipticine. Relatively slower component (2 ns) might reflect either the segmental motion of the protein or the surface bound protonated ellipticine, while the major contribution of the slowest component of ~47 ns is assigned as global tumbling motion of the protein. With varying concentration of DNA, the time constant for slower component increases indicating retarded global tumbling

motion due to the interaction with DNA (**Figure 5.9, Table 5.6**). The slowing down of global tumbling time-scale in presence of DNA actually supports the existence of ternary complex, by which the net hydrodynamic radius of the BSA-DNA complex increases and rotational relaxation becomes sluggish. Moreover, as the increment is not abruptly high, it is logical to anticipate that only a segment of DNA is involved in the ternary complex formation. It is already revealed from FTIR studies that CT-DNA interacts with serum albumin either through G-C rich region or through the phosphate backbone interaction of DNA.[63] If the whole DNA was involved in the ternary complex formation, then it would have shown highly sluggish global tumbling motion along with a higher value of residual anisotropy.

Rotational relaxation data obtained from the time-resolved anisotropy data are employed to calculate hydrodynamic radius of protein-bound ellipticine and ternary complex consists of protein-drug-DNA (a detailed description of calculation method is given in chapter 3). Note that, we have found ~22.5 percent increase of hydrodynamic radius from BSA-ellipticine (r=35.6 Å) to BSA-ellipticine-DNA system (r=43.3 Å). Interestingly, the change in hydrodynamic radius of BSA bound DNA (~8 Å) is closely matching with the width of DNA base pair (~9 Å), which infers that BSA predominantly interacts with major groove region of DNA. This corroborates well with the proposed concept of ternary complexation as phosphates in DNA attract serum proteins to a great extent to bind to the

Table 5.6. *Anisotropy data of ellipticine-BSA with increasing DNA concentration (no dip-rise feature).*

Sample	τ_{r1} (ns)	τ_{r2} (ns)	τ_{r3} (ns)	a_1	a_2	a_3	r_0
Ellip-BSA + DNA 5 μM (440 nm)	0.12	1.83	50	0.21	0.05	0.13	0.39
Ellip-BSA + DNA 50 μM (440 nm)	0.12	2.48	50	0.19	0.04	0.13	0.36
Ellip-BSA + DNA 110 μM (440 nm)	0.12	2.93	48	0.14	0.07	0.13	0.34
Ellip-BSA + DNA 5 μM (525 nm)	0.10	2.64	54	0.12	0.06	0.16	0.34
Ellip-BSA + DNA 50 μM (525 nm)	0.10	3.08	60	0.12	0.08	0.14	0.34
Ellip-BSA + DNA 110 μM (525 nm)	0.10	3.50	83	0.14	0.07	0.16	0.37

G-C rich major groove of CT-DNA.We can rule out the possibility of ternary complex formation with neutral ellipticine as 440 nm peaks does not exhibit any red shift (**Figure 5.7**). Moreover, the anisotropy decay feature of the neutral (λ_{em}=440 nm) ellipticine molecules bound to protein binding pocket are not getting affected by the presence of CT-DNA (**Figure 5.9**), though the population of neutral ellipticine significantly decreases by the addition of

DNA. Combining all these facts a formation of ternary complex can be speculated.

5.2.3d. Field Emission Scanning Electron Microscopy (FE-SEM) Images

To visualize the morphology of protein-DNA aggregates a mixture of serum protein (HSA)

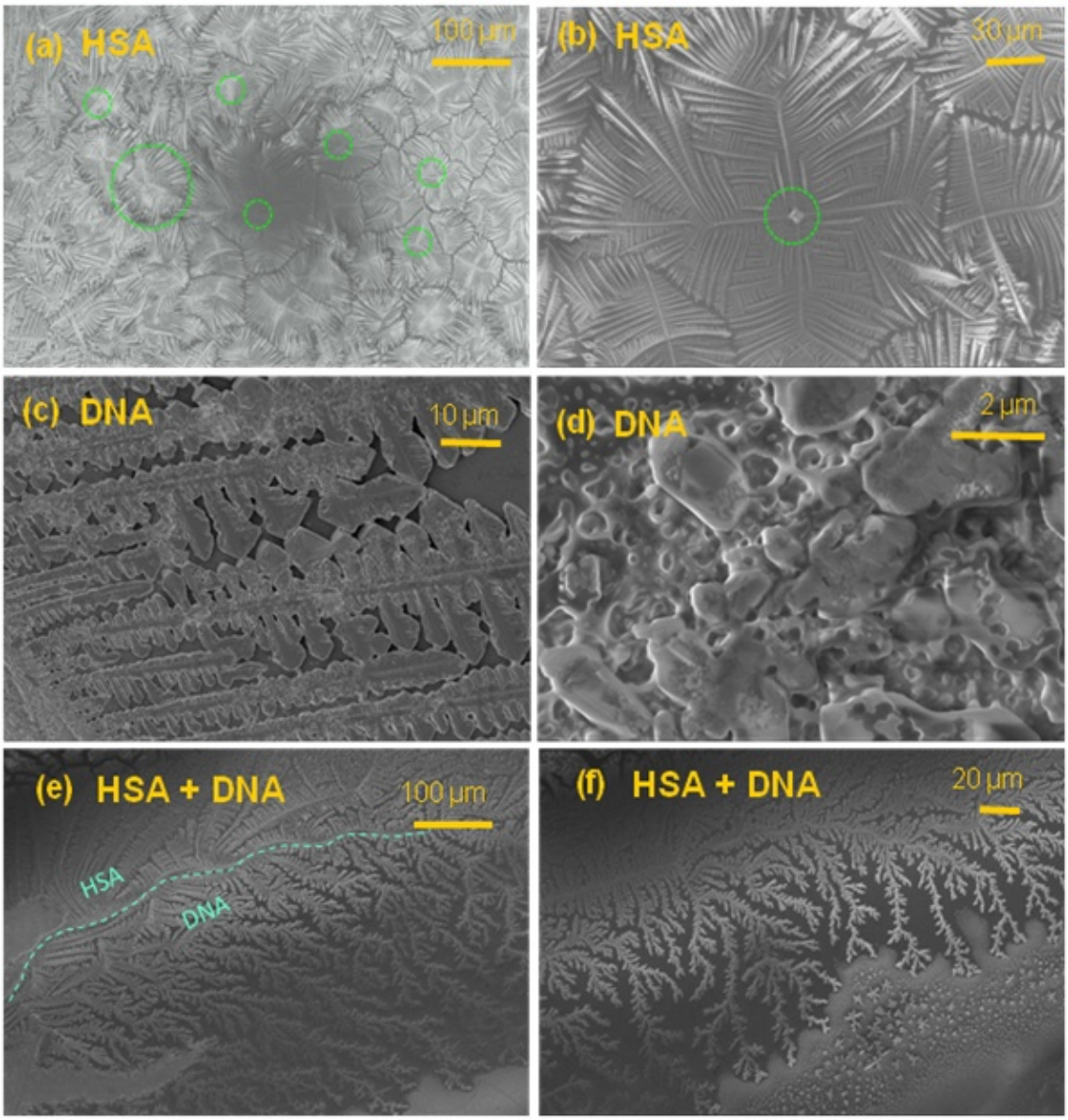

Figure 5.10. *Field Emission Scanning Electron Microscopic (FE-SEM) images of (a) HSA 100 µM, where the green circles show the protein nucleation centres, (b) zoomed view of HSA .(c) Salmon sperm DNA 100 µM, (d) is the respective zoomed view of salmon sperm DNA. (e) Interaction of HSA and salmon sperm DNA (1:1) mixture where the dotted cyan line shows the nucleation barrier between protein and DNA; (f) zoomed view of serum albumin and DNA system*

and salmon sperm DNA (concentration ratio 1:1) has been subjected to field emission scanning electron microscopy (FE-SEM) (**Figure 5.10**). For relative comparison, we have also recorded the FE-SEM images of HSA and salmon sperm DNA under identical experimental conditions. A flowery distribution of aggregated HSA is visible with a singlenucleation centre for each aggregate (marked by green circles). A closer look shows each arm of the flowery structure is extended in a typical fashion on 2D plane and resembles to 'fern leaf' structure. As protein is solubilised in PBS, evaporation of water gives a rapid aggregation, where hydrophobic interaction drives protein molecules together and forms this kind of 'fern leaf' structure. A more distinctive self-assembled structure has been retrieved when equimolar DNA has been added to serum protein. Additional nucleation centre at the tip of 'fern leaf' is found in presence of DNA, which extends randomly and results a dendriticdistribution. These radially branched dendritic architectures are best described by diffusion limited aggregation model (DLA)[64], in which DNA nucleation at the tip of 'fern leaf' structure of protein is an outcome of diffusion limited process. The results have close resemblance with the recently reported morphology of silk proteins of Bombyx mori and Wako sericin.[65, 66] This kind of unidirectional dendritic growth of DNA as detected in SEM images, together with the estimated hydrodynamic radius of the BSA-DNA system, infers that DNA is involved in ternary complex formation with protein and ellipticine, which is believed to be the key point of ellipticine anticancer activity. However, the possibility of partial wrapping by DNA cannot be excluded. To best of our knowledge, this type of self-assembled aggregates from two different bio-macromolecules is unique, and it might provide a deep insight towards the development of novel hybrid biomaterials for therapeutic applications.

5.3. Conclusion

In summary, the present work illustrates the interaction scenario of wild DNA and serum protein probed by fluorescence switch of an anti cancer drug, ellipticine. In protein (Serum Albumins) it dramatically shifts the equilibrium from protonated (~525 nm in water) to the neutral (~440 nm) (**Scheme 5.2**) which reflects through a ~85 nm blue shift in emission. In DNA, only protonated form of ellipticine intercalates due to strong electrostatic interaction between the drug and negatively charged phosphate backbone of DNA, reflected by tremendous hike in intensity at 525 nm. The very different fluorescence feature of ellipticine with serum albumin and DNA, offers a notion about monitoring the protein-DNA interaction

with the help of fluorescence switch of this drug from green (in water) to blue (in presence of protein) to sea green (in protein-DNA) (**Scheme 5.2**). We found DNA does not disturb but stabilizes the secondary structure of protein through complexation comprising protein and DNA. SEM images depict the formation of radially branched dendritic architecture for

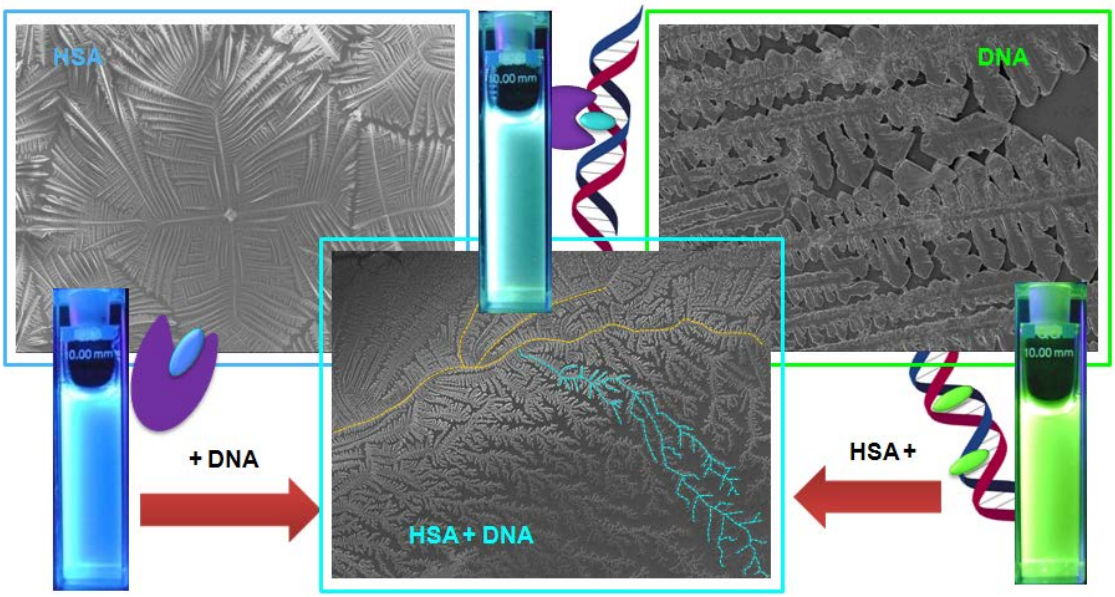

Scheme 5.2. *Schematic representation of ellipticine colour switch used for detection of non-specific protein-DNA interaction, where the SEM images are shown for protein, DNA and protein-DNA complex.*

protein-DNA interaction, driven by the above mentioned self assembled structure. This kind of fluorescence switch of a biologically important drug molecule provides a new strategy to monitor protein-DNA interaction. Moreover, in near future this approach can be effectively used to probe different kind of bio-macromolecular interactions *in vivo* and *in vitro*.

5.4. Reference

1. Tian, Z., Wu, W., Wan, W. & Li, A.D.Q. Single-chromophore-based photoswitchable nanoparticles enable dual-alternating-color fluorescence for unambiguous live cell imaging. *J. Am. Chem. Soc.* **131**, 4245-4252 (2009).
2. Bruchez, M., Moronne, M., Gin, P., Weiss, S. & Alivisatos, A.P. Semiconductor nanocrystals as fluorescent biological labels. *Science* **281**, 2013-2016 (1998).
3. Chan, W.C.W. & Nie, S. Quantum dot bioconjugates for ultrasensitive nonisotopic detection. *Science* **281**, 2016-2018 (1998).
4. Dubertret, B., Skourides, P., Norris, D.J., Noireaux, V., Brivanlou, A.H. & Libchaber, A. In vivo imaging of quantum dots encapsulated in phospholipid micelles. *Science* **298**, 1759-1762 (2002).
5. Åkerman, M.E., Chan, W.C.W., Laakkonen, P., Bhatia, S.N. & Ruoslahti, E. Nanocrystal targeting in vivo. *Proc. Natl. Acad. Sci. U. S. A.* **99**, 12617-12621 (2002).
6. Michalet, X., Pinaud, F.F., Bentolila, L.A., Tsay, J.M., Doose, S., Li, J.J., Sundaresan, G., Wu, A.M., Gambhir, S.S. & Weiss, S. Quantum dots for live cells, in vivo imaging, and diagnostics. *Science* **307**, 538-544 (2005).
7. Jisha, V.S., Arun, K.T., Hariharan, M. & Ramaiah, D. Site-selective binding and dual mode recognition of serum albumin by a squaraine dye. *J. Am. Chem. Soc.* **128**, 6024-6025 (2006).
8. Zadmard, R. & Schrader, T. Nanomolar protein sensing with embedded receptor molecules. *J. Am. Chem. Soc.* **127**, 904-915 (2004).
9. Babendure, J.R., Adams, S.R. & Tsien, R.Y. Aptamers switch on fluorescence of triphenylmethane dyes. *J. Am. Chem. Soc.* **125**, 14716-14717 (2003).
10. Li, Y.-P., Yang, H.-R., Zhao, Q., Song, W.-C., Han, J. & Bu, X.-H. Ratiometric and selective fluorescent sensor for Zn^{2+} as an "off–on–off" switch and logic gate. *Inorg. Chem.* **51**, 9642-9648 (2012).
11. Elstner, M., Weisshart, K., Müllen, K. & Schiller, A. Molecular logic with a saccharide probe on the few-molecules level. *J. Am. Chem. Soc.* **134**, 8098-8100 (2012).
12. Prokup, A., Hemphill, J. & Deiters, A. DNA computation: A photochemically controlled AND gate. *J. Am. Chem. Soc.* **134**, 3810-3815 (2012).
13. Shin, J.-S. & Pierce, N.A. Rewritable memory by controllable nanopatterning of DNA. *Nano Lett.* **4**, 905-909 (2004).
14. Paul, B.K., Samanta, A. & Guchhait, N. Implication toward a simple strategy to generate efficiency-tunable fluorescence resonance energy transfer emission: Intertwining medium-polarity-sensitive intramolecular charge transfer emission to fluorescence resonance energy transfer. *J. Chem. Phys. A* **114**, 6097-6102 (2010).
15. Shaikh, M., Mohanty, J., Singh, P.K., Bhasikuttan, A.C., Rajule, R.N., Satam, V.S., Bendre, S.R., Kanetkar, V.R. & Pal, H. Contrasting solvent polarity effect on the photophysical properties of two newly synthesized aminostyryl dyes in the lower and in the higher solvent polarity regions. *J. Chem. Phys. A* **114**, 4507-4519 (2010).

16. di Nunzio, M.R., Wang, Y. & Douhal, A. Structural spectroscopy and dynamics of inter- and intramolecular H-bonding interactions of topotecan, a potent anticancer drug, in organic solvents and in aqueous solution. *J. Chem. Phys. B* **116**, 7522-7530 (2012).
17. Monnereau, C., Gomez, J., Blart, E., Odobel, F., Wallin, S., Fallberg, A. & Hammarström, L. Photoinduced electron transfer in platinum(II) terpyridinyl acetylide complexes connected to a porphyrin unit. *Inorg. Chem.* **44**, 4806-4817 (2005).
18. Hub, W., Schneider, S., Doerr, F., Oxman, J.D. & Lewis, F.D. trans-Stilbene-amine exciplexes. Behavior of the exciplex, solvent-separated radical ion pair, and free radical ions. *J. Am. Chem. Soc.* **106**, 708-715 (1984).
19. Nakanishi, T., Ohkubo, K., Kojima, T. & Fukuzumi, S. Reorganization energies of diprotonated and saddle-distorted porphyrins in photoinduced electron-transfer reduction controlled by conformational distortion. *J. Am. Chem. Soc.* **131**, 577-584 (2008).
20. Erbse, A.H., Berlinberg, A.J., Cheung, C.-Y., Leung, W.-Y. & Falke, J.J. OS-FRET: A new one-sample method for improved FRET measurements. *Biochemistry* **50**, 451-457 (2010).
21. Allain, C., Monchaud, D. & Teulade-Fichou, M.-P. FRET templated by G-quadruplex DNA: A specific ternary interaction using an original pair of donor/acceptor partners. *J. Am. Chem. Soc.* **128**, 11890-11893 (2006).
22. Biju, V., Anas, A., Akita, H., Shibu, E.S., Itoh, T., Harashima, H. & Ishikawa, M. FRET from quantum dots to photodecompose undesired acceptors and report the condensation and decondensation of plasmid DNA. *ACS Nano* **6**, 3776-3788 (2012).
23. Kienzler, A., Flehr, R., Kramer, R.A., Gehne, S.r., Kumke, M.U. & Bannwarth, W. Novel three-color FRET tool box for advanced protein and DNA analysis. *Bioconjugate Chem.* **22**, 1852-1863 (2011).
24. R.Lakowicz, J. Principles of fluorescence spectroscopy (Springer Science, New York, USA, 2006).
25. Le Pecq, J.-B., Nguyen Dat, X., Gosse, C. & Paoletti, C. A new antitumoral agent: 9-hydroxyellipticine. Possibility of a rational design of anticancerous drugs in the series of DNA intercalating drugs. *Proc. Natl. Acad. Sci. U. S. A.* **71**, 5078-5082 (1974).
26. Ohashi, M. & Oki, T. Overview Oncologic, Endocrine & Metabolic: Oncologic, Endocrine & Metabolic :Ellipticine and related anticancer agents. *Expert Opin. Ther. Pat.* **6**, 1285-1294 (1996).
27. Arteaga, C.L., Kisner, D.L., Goodman, A. & Von Hoff, D.D. Elliptinium, a DNA intercalating agent with broad antitumor activity in a human tumor cloning system. *Eur. J. Cancer Clin. Oncol.* **23**, 1621-1626 (1987).
28. Sureau, F., Moreau, F., Millot, J.M., Manfait, M., Allard, B., Aubard, J. & Schwaller, M.A. Microspectrofluorometry of the protonation state of ellipticine, an antitumor alkaloid, in single cells. *Biophys. J.* **65**, 1767-1774 (1993).
29. Froelich-Ammon, S.J., Patchan, M.W., Osheroff, N. & Thompson, R.B. Topoisomerase II Binds to Ellipticine in the Absence or Presence of DNA. *J. Biol. Chem.* **270**, 14998-15004 (1995).

30. Fung, S.Y., Duhamel, J. & Chen, P. Solvent effect on the photophysical properties of the anticancer agent ellipticine. *J. Chem. Phys. A* **110**, 11446-11454 (2006).
31. Banerjee, S., Pabbathi, A., Sekhar, M.C. & Samanta, A. Dual fluorescence of ellipticine: Excited state proton transfer from solvent versus solvent mediated intramolecular proton transfer. *J. Chem. Phys. A* **115**, 9217-9225 (2011).
32. Miskolczy, Z., Biczók, L. & Jablonkai, I. Effect of hydroxylic compounds on the photophysical properties of ellipticine and its 6-methyl derivative: The origin of dual fluorescence. *Chem. Phys. Lett.* **427**, 76-81 (2006).
33. Xian, J., Harrington, M.G. & Davidson, E.H. DNA-protein binding assays from a single sea urchin egg: a high-sensitivity capillary electrophoresis method. *Proc. Natl. Acad. Sci. U. S. A.* **93**, 86-90 (1996).
34. Wang, Y.-T., Wright, J.D., Doudeva, L.G., Jhang, H.-C., Lim, C. & Yuan, H.S. Redesign of high-affinity nonspecific nucleases with altered sequence preference. *J. Am. Chem. Soc.* **131**, 17345-17353 (2009).
35. Xia, S., Christian, T.D., Wang, J. & Konigsberg, W.H. Probing minor groove hydrogen bonding interactions between RB69 DNA polymerase and DNA. *Biochemistry* **51**, 4343-4353 (2012).
36. Zhong, D., Pal, S.K. & Zewail, A.H. Femtosecond studies of protein-DNA binding and dynamics: Histone I. *ChemPhysChem* **2**, 219-227 (2001).
37. Narayanan, S.S. & Pal, S.K. Nonspecific protein-DNA interactions: Complexation of α-chymotrypsin with a genomic DNA. *Langmuir* **23**, 6712-6718 (2007).
38. Xu, X., Zhao, Z., Qin, L., Wei, W., Levine, J.E. & Mirkin, C.A. Fluorescence recovery assay for the detection of protein-DNA binding. *Anal. Chem.* **80**, 5616-5621 (2008).
39. Moreno, A., Knee, J. & Mukerji, I. Applying 6-methylisoxanthopterin-enhanced fluorescence to examine protein-DNA interactions in the picomolar range. *Biochemistry* **51**, 6847-6859 (2012).
40. Hariharan, C. & Reha-Krantz, L.J. Using 2-aminopurine fluorescence to detect bacteriophage T4 DNA polymerase−DNA complexes that are important for primer extension and proofreading Reactions. *Biochemistry* **44**, 15674-15684 (2005).
41. Tleugabulova, D. & Reha-Krantz, L.J. Probing DNA polymerase−DNA interactions: Examining the template strand in exonuclease complexes using 2-aminopurine fluorescence and acrylamide Quenching. *Biochemistry* **46**, 6559-6569 (2007).
42. Matyushov, D.V., Schmid, R. & Ladanyi, B.M. A Thermodynamic Analysis of the π* and ET(30) Polarity Scales. *J. Chem. Phys. B* **101**, 1035-1050 (1997).
43. Healy, E.F. Quantitative determination of DNA-ligand binding using fluorescence spectroscopy. *J. Chem. Educ.* **84**, 1304 (2007).
44. Silverstein, T.P. Quantitative determination of DNA-ligand binding: Improved data analysis. *J. Chem. Educ.* **85**, 1192 (2008).
45. Paul, B.K. & Guchhait, N. Modulation of prototropic activity and rotational relaxation dynamics of a cationic biological photosensitizer within the motionally constrained bio-environment of a protein. *J. Chem. Phys. B* **115**, 10322-10334 (2011).

46. Bolli, A., Marino, M., Rimbach, G., Fanali, G., Fasano, M. & Ascenzi, P. Flavonoid binding to human serum albumin. *Biochem. Biophys. Res. Commun.* **398**, 444-449 (2010).
47. Chi, Z., Liu, R., Teng, Y., Fang, X. & Gao, C. Binding of oxytetracycline to bovine serum albumin: Spectroscopic and molecular modeling investigations. *J. Agric. Food. Chem.* **58**, 10262-10269 (2010).
48. Chakrabarty, A., Mallick, A., Haldar, B., Das, P. & Chattopadhyay, N. Binding interaction of a biological photosensitizer with serum albumins: A biophysical study. *Biomacromolecules* **8**, 920-927 (2007).
49. Carter, D.C. & Ho, J.X. in Adv. Protein Chem. (eds. C.B. Anfinsen, J.T.E.F.M.R. & David, S.E.) 153-203 (Academic Press, 1994).
50. He, X.M. & Carter, D.C. Atomic structure and chemistry of human serum albumin. *Nature* **358**, 209-215 (1992).
51. Ghosh, S., Jana, S. & Guchhait, N. Domain specific association of small fluorescent probe trans-3-(4-monomethylaminophenyl)-acrylonitrile (MMAPA) with bovine serum albumin (BSA) and its dissociation from protein binding sites by Ag nanoparticles: Spectroscopic and molecular docking study. *J. Chem. Phys. B* **116**, 1155-1163 (2011).
52. Deprez, E., Tauc, P., Leh, H., Mouscadet, J.-F., Auclair, C., Hawkins, M.E. & Brochon, J.-C. DNA binding induces dissociation of the multimeric form of HIV-1 integrase: A time-resolved fluorescence anisotropy study. *Proc. Natl. Acad. Sci. U.S.A.* **98**, 10090-10095 (2001).
53. Chang, K.-S., Luo, L., Chang, C.-W., Huang, Y.-C., Cheng, C.-Y., Hung, C.-S., Diau, E.W.-G. & Li, Y.-K. Novel steroid-sensing model and characterization of protein interactions based on fluorescence anisotropy decay. *J. Chem. Phys. B* **114**, 4327-4334 (2010).
54. Sinha, S.S., Mitra, R.K. & Pal, S.K. Temperature-dependent simultaneous ligand binding in human serum albumin. *J. Chem. Phys. B* **112**, 4884-4891 (2008).
55. Guest, C.R., Hochstrasser, R.A., Allen, D.J., Benkovic, S.J., Millar, D.P. & Dupuy, C.G. Interaction of DNA with the Klenow fragment of DNA polymerase I studied by time-resolved fluorescence spectroscopy. *Biochemistry* **30**, 8759-8770 (1991).
56. Kanti Das, T. & Mazumdar, S. Effect of Adriamycin on the boundary lipid structure of cytochrome c oxidase: pico-second time-resolved fluorescence depolarization studies. *Biophys. Chem.* **86**, 15-28 (2000).
57. Ludescher, R.D., Peting, L., Hudson, S. & Hudson, B. Time-resolved fluorescence anisotropy for systems with lifetime and dynamic heterogeneity. *Biophys. Chem.* **28**, 59-75 (1987).
58. Bhattacharya, B., Nakka, S., Guruprasad, L. & Samanta, A. Interaction of bovine serum albumin with dipolar molecules: Fluorescence and molecular docking studies. *J. Chem. Phys. B* **113**, 2143-2150 (2009).
59. M. J. Frisch, G.W.T., H. B. Schlegel, G. E. Scuseria, M. A. Robb, J. R. Cheeseman, G. Scalmani, V. Barone, B. Mennucci, G. A. Petersson, H. Nakatsuji, M. Caricato, X. Li, H. P. Hratchian, A. F. Izmaylov, J. Bloino, G. Zheng, J. L. Sonnenberg, M. Hada, M. Ehara, K. Toyota, R. Fukuda, J. Hasegawa, M. Ishida, T. Nakajima, Y. Honda, O.

Kitao, H. Nakai, T. Vreven, J. A. Montgomery, Jr., J. E. Peralta, F. Ogliaro, M. Bearpark, J. J. Heyd, E. Brothers, K. N. Kudin, V. N. Staroverov, R. Kobayashi, J. Normand, K. Raghavachari, A. Rendell, J. C. Burant, S. S. Iyengar, J. Tomasi, M. Cossi, N. Rega, J. M. Millam, M. Klene, J. E. Knox, J. B. Cross, V. Bakken, C. Adamo, J. Jaramillo, R. Gomperts, R. E. Stratmann, O. Yazyev, A. J. Austin, R. Cammi, C. Pomelli, J. W. Ochterski, R. L. Martin, K. Morokuma, V. G. Zakrzewski, G. A. Voth, P. Salvador, J. J. Dannenberg, S. Dapprich, A. D. Daniels, Ö. Farkas, J. B. Foresman, J. V. Ortiz, J. Cioslowski, and D. J. Fox,. (Gaussian, Inc., Wallingford CT, 2009).

60. Kolář, M., Kubař, T.s. & Hobza, P. Sequence-dependent configurational entropy change of DNA upon intercalation. *J. Chem. Phys. B* **114**, 13446-13454 (2010).
61. Das, A., Thakur, R. & Chakraborty, A. A steady-state and time-resolved fluorescence study on liposome-calf thymus DNA interaction: Probed by an anticancer drug ellipticine. *RSC Adv.* **3**, 19572-19581 (2013).
62. Ryvolova, M., Adam, V., Eckschlager, T., Stiborova, M. & Kizek, R. Study of DNA–ellipticine interaction by capillary electrophoresis with laser-induced fluorescence detection. *Electrophoresis* **33**, 1545-1549 (2012).
63. Malonga, H., Neault, J.F., Arakawa, H. & Tajmir-Riahi, H.A. DNA Interaction with human serum albumin studied by affinity capillary electrophoresis and FTIR spectroscopy. *DNA and Cell Biol.* **25**, 63-68 (2006).
64. Witten, T.A. & Sander, L.M. Diffusion-limited aggregation, a kinetic critical phenomenon. *Phys. Rev. Lett.* **47**, 1400-1403 (1981).
65. Khire, T.S., Kundu, J., Kundu, S.C. & Yadavalli, V.K. The fractal self-assembly of the silk protein sericin. *Soft Matter* **6**, 2066-2071 (2010).
66. Kurland, N.E., Kundu, J., Pal, S., Kundu, S.C. & Yadavalli, V.K. Self-assembly mechanisms of silk protein nanostructures on two-dimensional surfaces. *Soft Matter* **8**, 4952-4959 (2012).

5.5. Appendix

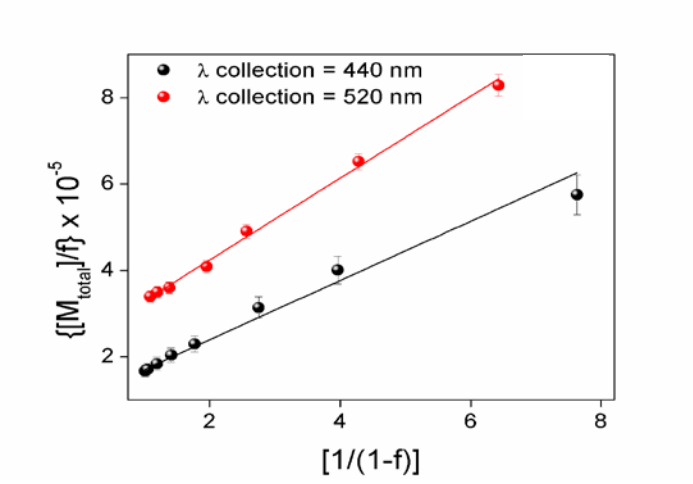

Appendix 5.1. *Modified Scatchard plot of Ellipticine-BSA system, where legends carry the respective meanings. A detailed method of modified Scatchard in described in* ***Chapter 3.***

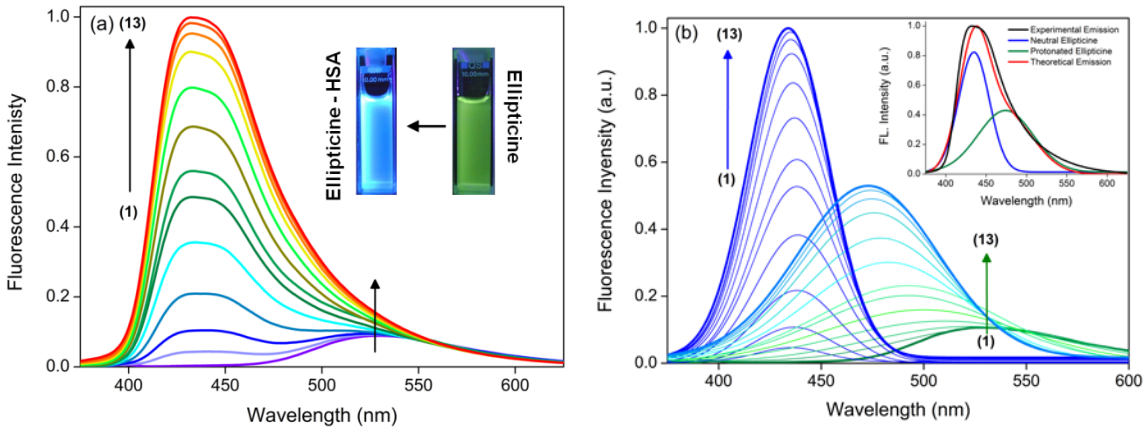

Appendix 5.2. *(a) Fluorescence emission intensity of ellipticine with variable HSA ([HSA] = 0, 0.25, 0.50, 1, 3, 6, 10, 20, 30, 50, 70, 90 and 110 μM respectively (1→13)). Inset shows the color switch by HSA addition. (b) Deconvoluted emission intensity of ellipticine with variable HSA concentrations, where inset stand for a sample deconvolutioon.*

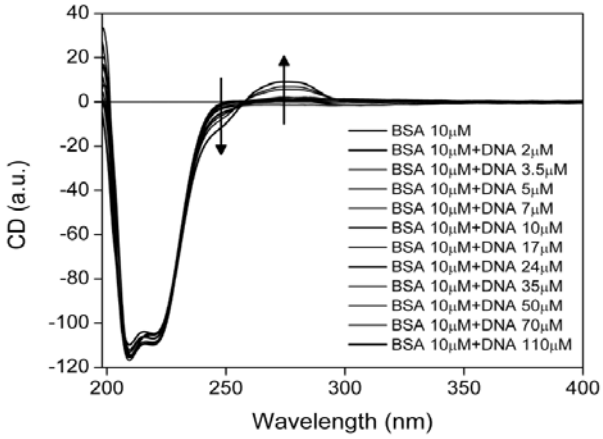

Appendix 5.3. *Circular dichroism spectra of BSA and DNA interaction. BSA (10 μM) is titrated with increasing DNA concentrations (legend carries the respective meaning).*

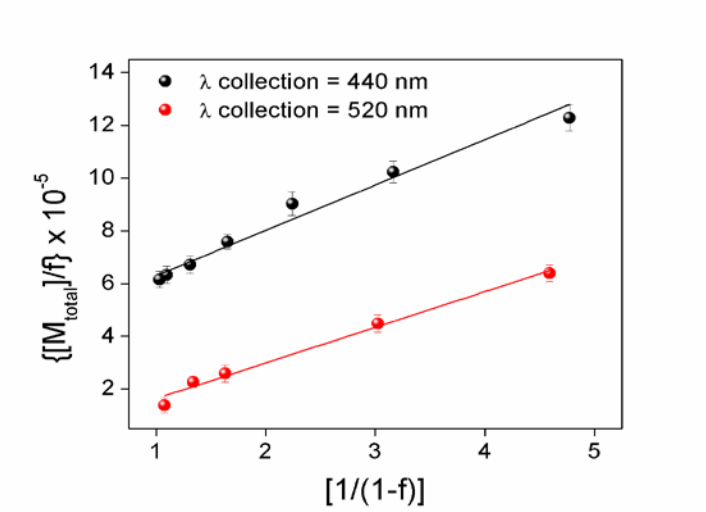

Appendix 5.4. *Binding constants determined for BSA-ellipticine-DNA system considering emission intensities at 440 nm and 520 nm using modified Scatchard plot.*

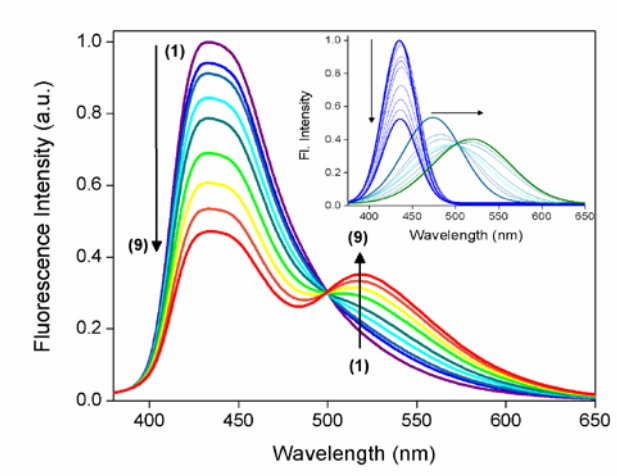

Appendix 5.5. *Fluorescence spectra of HSA-bound ellipticine with increasing concentration salmon sperm (SS DNA) DNA, where the inset shows deconvoluted emission spectra for the same.*

Appendix 5.n1. Binding Constant Determination from Steady State Anisotropy Data

The applicability of anisotropy measurements has been extended by determining the association constant for drug-protein interaction. Binding constant (K) is determined using the following equations[24]

$$\frac{1}{f_B} = 1 + \frac{1}{K_f[Protein]} \quad \ldots n1.1$$

in above equation …n1.1 the term f_B can be defined as;

$$f_B = \frac{(r - r_F)}{R(r_B - r) + (r - r_F)} \quad \ldots n1.2$$

where, f_B is fraction of drug molecules bound to protein, and r_F, r_B are the anisotropy of free and bound drug, respectively. R is the correction factor (ratio of bound/free drug intensities measured under same experimental conditions). The binding plot is constructed by $1/f_B$ vs 1/[protein], and binding constant is evaluated from the slope.

End of Chapter 5

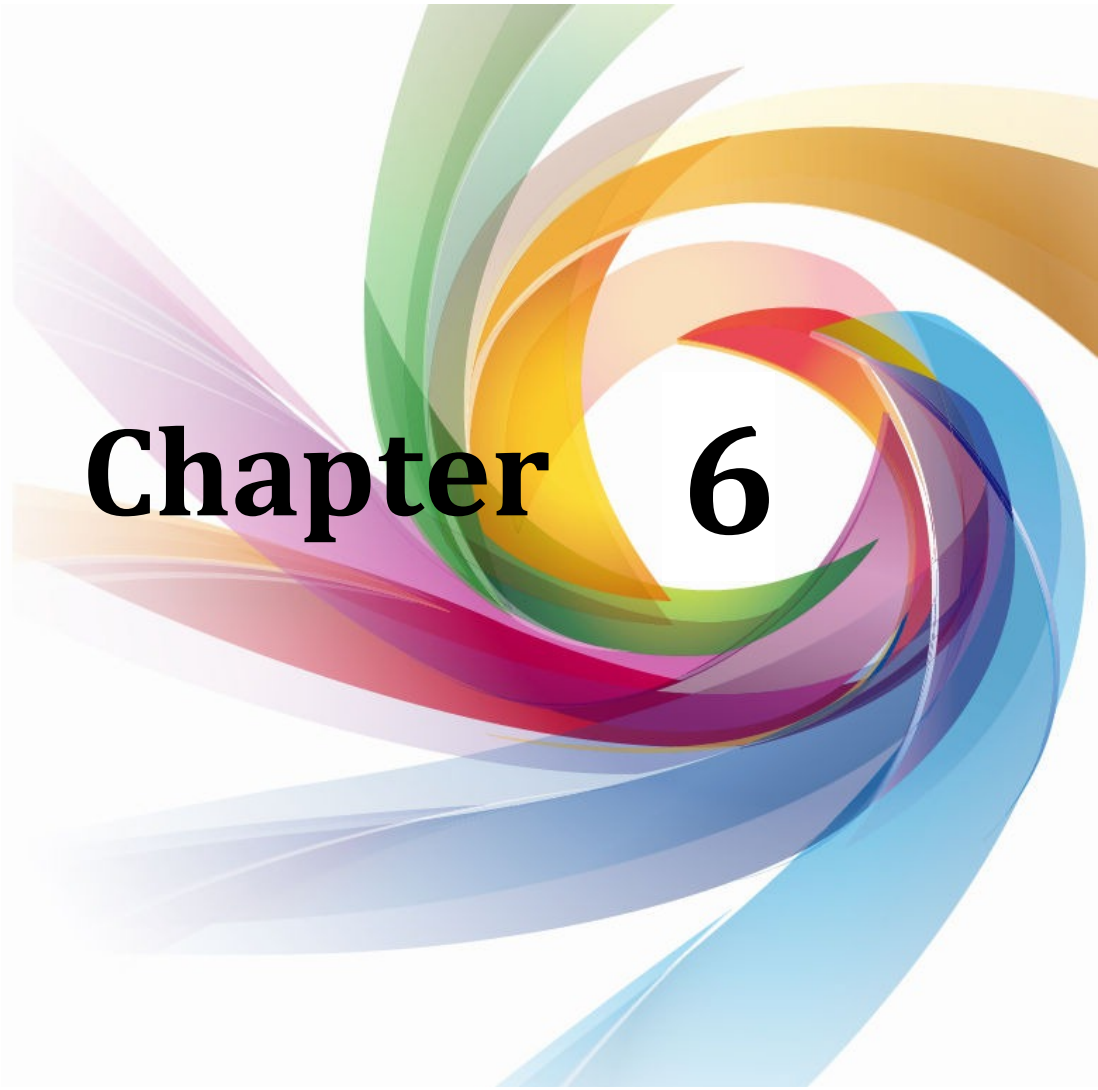

Chapter 6

Solvation Dynamics in Heterogeneous and Confined Media

6.1. Introduction

Water, the origin of life on earth is an indispensible solvent for all nature mediated reactions. Due to the ubiquitous existence of water as reaction matrix, it's celebrated as the universal solvent and hence researchers are always interested about the dynamics and kinetic behaviour of water in its liquid state. Water dynamics is known to have a direct correlation with different biological phenomena, like protein folding-unfolding dynamics,[1-14] DNA dynamics,[15-21] protein-ligand,[5, 11, 22-25] DNA-ligand[26-30] and protein-DNA[31-34] interaction processes. As described in **Chapter 1**, the reorientation dynamics of water around a fluorophore followed by photo-excitation is known as solvation dynamics. Dynamics of water molecules around an excited molecule is a venerable concept and is applied to explore the dynamics of water in a diverse kind of systems.[16, 35-39] The solvation dynamics of water over a hydrophobic surface is one of the topics of interest of the present chapter and we have explored the behaviour of water molecules on the surface or carbon nanotubes. Not only water, but the reorientation dynamics of different other solvents around an excited molecule carries immense importance to explain the photophysical and photo-chemical behaviour of the matrix itself. As for example, the dynamics of hydrogen bonded network is well correlated to protein denaturation[40]. Therefore, the other part of the present chapter deals with the solvation dynamics of hydrogen bonded urea network confined inside reverse micellar cavity. Hence this chapter is subdivided in two parts as follows;

6a. Solvation Dynamics of Coumarin 153 in SDS Dispersed Single Walled Carbon Nanotubes (SWNTs) and

6b. How Does the Urea Dynamics Differ from Water Dynamics Inside the Reverse Micelle?

6a. Solvation Dynamics of Coumarin 153 in SDS Dispersed Single Walled Carbon Nanotubes (SWNTs)

6a.1. Motivation

Confined water within restricted spaces deserves special attention because it behaves differently compared to normal water. For example, water at the surface of protein is called 'biological water' and is different from bulk water. The knowledge about the physical properties of confined water is rather limited. Many experimental and computational studies have done to explore the physical properties of this confined water.[1, 36, 41-43] However, it needs more systematic study and more confined environments. Discovery of carbon nanotube (CNT) provides such restricted environments for water molecules. CNT provides quasi one dimensional cavity with a diameter of few nanometers. CNTs are categorized as single-walled nanotubes (SWNTs) and multi-walled nanotubes (MWNTs). The detail description of SWNTs and MWNTs are provided in **Chapter 1.** It is seen that water molecules entering the nano-tube lose an average two out of four hydrogen bonds.[44] **Considering** this loss of hydrogen bonding and the weak attraction of water to the nano-tube C-atoms, hydration of the nano-tube interior seem surprising. But experimental and simulation studies confirmed the adsorption of water into the nano-tube.[45-48] It has been observed that heat treated single walled carbon nanotubes (SWNTs) with an average diameter of 13.6 Å can absorb water molecules inside the SWNTs and that adsorbed water exhibits liquid-solid phase transition at 235 K.[46] It has also been observed that ordered water inside SWNTs form pentagonal ice nanotubes at 300 K and octagonal ice-nanotubes at 190 K[45] (**Scheme 6a.1**). Simulations of water encapsulated in CNT suggest a new ice phase not seen in bulk ice[47] (**Scheme 6a.1**). NMR study of the water adsorption isotherms in SWNTs suggests that hydrophilic-hydrophobic transition inside surface of SWNT takes place upon cooling from 295 K to 281 K.[48] Moreover, NMR study revealed that the correlation time of water orientation in SWNTs is on the order of 10 to 100 ns.[48] This means dynamics of water reorientation inside the cavity of CNT is hindered compared with bulk water.

Although numerous experimental and theoretical studies have focused on the physical properties of water inside the cavity of CNT, a very few studies are reported about the water adsorbed on the external walls of CNT. Molecular dynamics simulations of water on the outer surface of a bundle of CNTs proposed two interesting surface phases of water.[49] The

first of them is characterized by the presence of water in one groove of the tube bundle (Phase I). For increasing density, a first-order phase transition occur leading to a second phase of the system. This second phase is characterized by the presence of water molecules

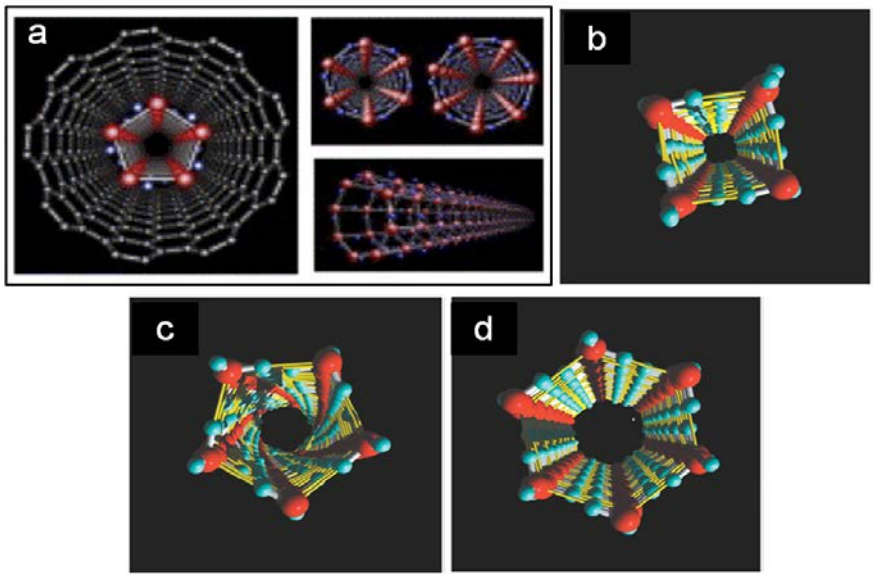

Scheme 6a.1. *Illustration of ice-nanotube structures given by Maniwa et al.[45] (a) The left is a pentagonal ice-nanotube formed inside a (9,9) SWNT. The right shows n = 6, 7 and 8 ice-nanotubes. The largest red and small blue spheres are oxygen and hydrogen atoms, respectively. The white spheres in the left figure are carbon atoms of SWNT. Koga et al.[47] reported (b) Square; (c), pentagonal; (d), hexagonal ice nanotubes in (14,14), (15,15) and (16,16) SWNTs.*

filling the whole outer surface of the nanotube bundle (Phase II). Moreover, molecular dynamics simulation study of water adsorbed in the external walls of a carbon nanotube bundles has been reported, paying special attention to the hydrogen bond structure and dynamic aspects such as diffusion and vibrations.[50] Experimental study indicates that water could wet the outer surface of CNT, since its surface tension of 72 mN/m is well below the upper limit for the surface tension of the liquid (~180 mN/m) beyond which wetting of multi-shell nanotubes is no longer favorable.[51] The first is covalent functionalization of SWNTs. However, such covalent approaches have been shown to disrupt the π-networks of the SWNT, leading to possible losses in their mechanical and electrical properties. The second strategy is the use of polymers or surfactants in a water to assist in the dispersion of SWNTs.[52] Both get adsorbed onto nanotube surface, rendering them soluble in aqueous and organic solvents. Nonetheless, dispersion of nanotubes in polymer matrices may not be a

proper choice for electronic device applications, as polymer itself can participate in electrical events.[52] Dispersion using surfactants diminishes such anomalies, as they can be removed easily by washing.[52] To date, a wide variety of surfactants have been investigated for dispersion of carbon nanotubes, such as sodium dodecyl benzenesulfonate (SDBS),[53] dodecyltrimethylammonium bromide (DTAB),[54] hexadecyltrimethylammonium bromide (CTAB),[55] octyl phenol ethoxylate (Triton X-100),[56] and sodium dodecyl sulfate (SDS),[57, 58] Among them SDS is commonly used to disperse SWNTs, however, the dispersion mechanism is a debatable issue. Richard *et al.* shown the TEM images of CNT (both SWNT and MWNT) dispersed in 1% SDS[56] which clearly indicate to a SDS formed supramolecular structures made of rolled-up half-cylinders on the nanotube surface[57] (**Scheme 6a.2**). On the other hand, small angle neutron scattering (SANS) study suggests that structure less random adsorption with no preferential arrangement of the head and tail of surfactants is responsible for the stabilization of the dispersions[58] (**Scheme 6a.2**). Adsorption studies of sodium dodecylbenzenesulfonate (NaDDBS) on SWNT revealed that at high NaDDBS concentration (above CMC), each nanotube is covered by a monolayer of surfactant.[59]

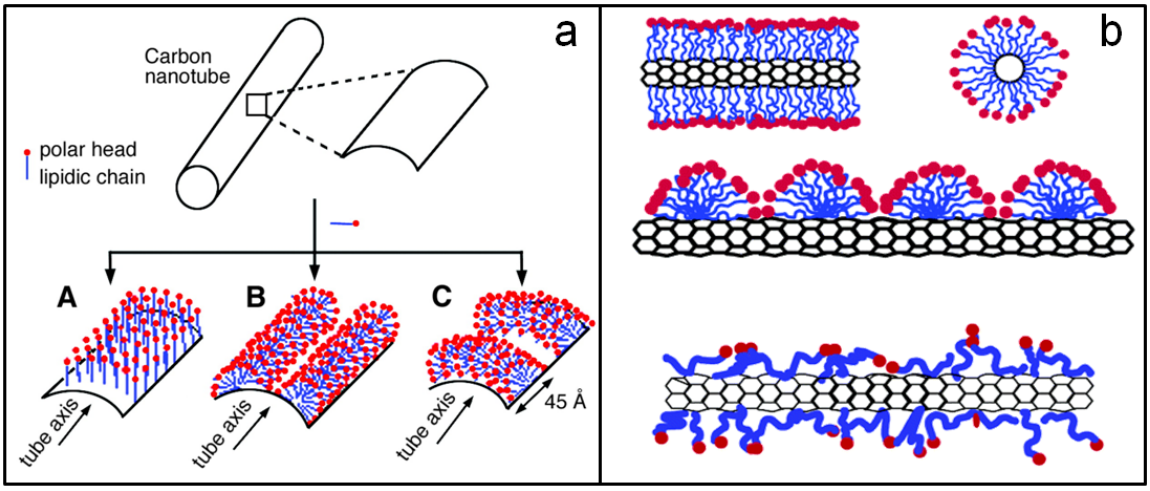

Scheme 6a.2. *Illustration of surfactant dispersed carbon nanotube given by (a) Richard et al.[57] and (b) Yurekli et al.[58]*

The buoyant density of SWNTs in aqueous solution will subtly depend on electrostatically adsorbed hydration layer. To gain insight into the hydration layer adsorbed on SWNT, it is necessary to study dynamic properties of those adsorbed water molecules. In this chapter, we report dynamics of water molecules absorbed on the surface of SWNTs

dispersed in 1% SDS solution. We have taken two different types of SWNTs, namely, semiconducting and metallic. To probe the water dynamics, we have monitored the time resolved fluorescence spectra of Coumarin 153 (**Scheme 6a.3**) in SWNTs. The neutral probe

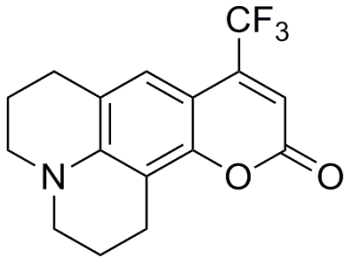

Scheme 6a.3. *Structure of Coumarin 153 (C-153).*

Coumarin 153 (C-153) offers outstanding sensitivity to environmental polarity[60] and C-153 is used as a nearly ideal solvation probe for solvation dynamics measurements[61]. Another reason for choosing C-153 is that solvation dynamics data using C-153 are available in pure solvents, organized assembly and it will be helpful for us to compare our solvation data with that of pure solvents and of other organized environments.

6a.2. Results and Discussions

The emission maximum of C-153 in water appears at ~558 nm. The emission maxima of C-153 in SWNTs appeared at ~543 nm (**Figure 6a.1a**). In this context, it should be mentioned that at our excitation wavelength (λ_{ex}=402 nm), both the SWNTs give fluorescence with an emission maxima situated around 478 nm (**Figure 6a.1b**). The spikes appear around 467 nm due to Raman scattering from water. Now, when we add C-153 in the SWNTs solutions, fluorescence intensity of C-153 becomes almost 100 times more than that of SWNTs using the same excitation and emission slit (**Figure 6a.1b**). Moreover, the peak of C-153 is now appearing at ~543 nm and at this wavelength both the SWNTs have almost negligibly small fluorescence (inset in **Figure 6a.1b**). Hence, the fluorescence spectral profiles of C-153 in presence of SWNTs are almost unaffected by the fluorescence of SWNTs. The blue shift of emission maxima of C-153 in presence of SWNTs compared to water clearly indicates that C-153 molecules are sensing hydrophobic environment in SWNTs. Now, one obvious question may arise that, whether the hydrophobic environment experienced by C-153 is due to the surface of SWNT or it is an effect of the Stern layer of SDS micelle. Because SWNTs

are dispersed in 1% SDS, corresponds to SDS concentration of ~34 mM, which is quite higher than the CMC (8 mM) of SDS. So, it is expected that SDS can form micelle at this concentration. In order to clarify the origin of the observed blue shift, emission spectra of C-153 in 1% SDS micellar solution is separately recorded. We have observed that emission

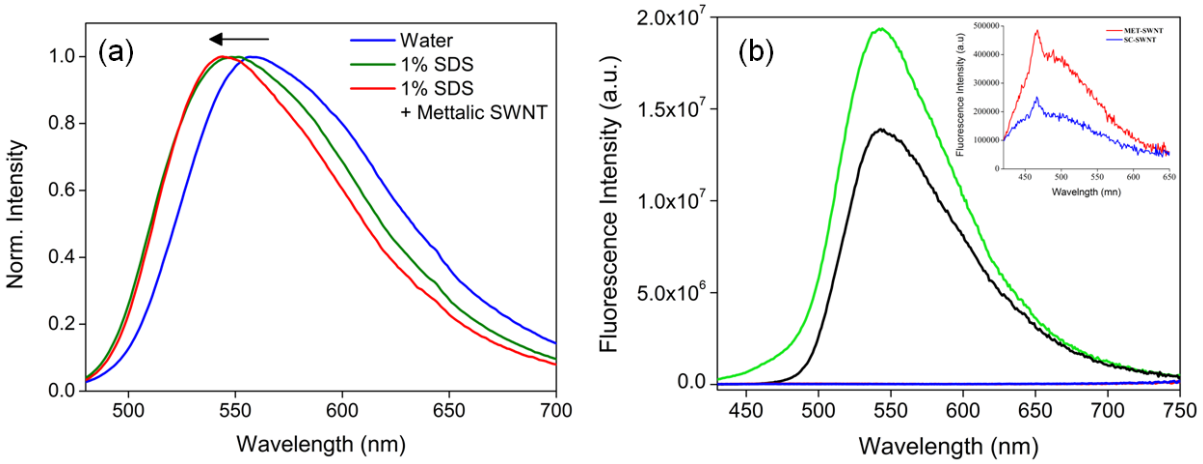

Figure 6a.1. *(a) Steady state emission spectra of C-153 in water, 1% SDS and SDS dispersed SWNT. All Legends carry respective meaning. (b) Steady state emission spectra of SWNTs and C-153 containing SWNTs. Red, blue, black and green lines indicate Met-SWNT, SC-SWNT, (SC-SWNT + C-153) and (Met-SWNT + C-153) respectively. Inset is shown for the better clarification of emission spectra of SWNTs.*

maximum of C-153 in 1% SDS is at ~547 nm, which is 4 nm red shifted than that of C-153 in SWNTs. This indicates that C-153 is experiencing slightly more hydrophobic environment in SWNTs compared to SDS micelles. As SWNTs are micro-heterogeneous, one should also consider the microenvironment around the C-153. Heterogeneous distribution of the probe could be verified by the excitation wavelength dependence on the steady state fluorescence spectra of the fluorescence probe. We have found that emission spectra of C-153 in SWNTs depend on the excitation wavelength (**Figure 6a.2a**). However, this dependence is not at all observed in 1% SDS, which is consistent with the previously reported results by Shirota *et al.*[62] This means that all the coumarin molecules are not in the similar microenvironment in SWNTs; whereas in SDS micelle, coumarin molecules experience similar microenvironment. In next section, we will further discuss the microenvironment of the probe in SWNTs.

Although the emission spectra gives a notion about the polarity of the micro-heterogeneous environment sensed by C-153, but it cannot predict the proper location of the

probe. The location of the probe in this micro-heterogeneous environment can be accurately predicted by time resolved fluorescence anisotropy measurements. The time resolved fluorescence anisotropy (r(t)) is measured using the method described in Chapter 3. Anisotropy decays are shown in **Figure 6a.2b** and the results are tabulated in **Table 6a.1**.

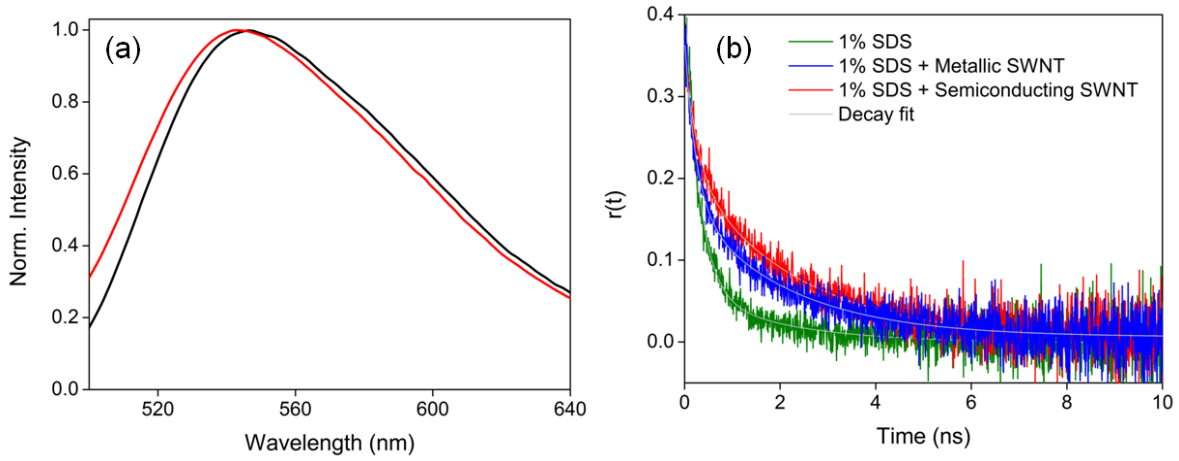

Figure 6a.2. (a) *Steady state emission spectra of C-153 in metallic SWNT at different excitation wavelengths. Solid lines for 385 nm excitation and dot line for 480 nm excitation. (b) Decay of fluorescence anisotropy of C-153 in 1% SDS micelle (black lines), in metallic SWNT (red lines) and in semiconducting SWNT (blue lines). The solid grey lines denote the best fit.*

It is clear from the results that rotational relaxation of the probe in 1% SDS micelle as well as in SWNTs occurs at a much slower rate compared to pure water. Moreover, the average rotational relaxation times of C-153 in both the SWNT are in nanosecond time scale, whereas the same occurs in sub-nanosecond time scale in 1% SDS micelle. Hence, C-153 is sensing more rigid micro-environment in SWNT compared to SDS micelle. In order to understand the origin of this hindered rotation, it is necessary to know the adsorption mechanism of SDS on SWNT. We have already mentioned that there are mainly two different adsorption mechanisms of SDS on SWNT surface. TEM studies suggest that half-cylindrical SDS micelles wrap around the CNT surface[57], whereas SANS study infers that structureless random adsorption of SDS monomer with no particular arrangement of the head and tail of the surfactants[58]. Moreover, SANS study confirmed the existence of free SDS micelle even in presence of SWNT.[58] We explain our results using both the above mentioned observations.

We have observed bi-exponential feature of anisotropy decay in which the fast component of rotational relaxation time (238 ps) of C-153 in SWNTs is very close to the relaxation

Table 6a.1. *Rotational relaxation parameters of C-153 in 1% SDS, Semiconducting (SC) and Metallic (Met) SWNTs.*

Sample Name	r_0	a_{1r}	τ_{1r} (ns)	a_{2r}	τ_{2r} (ns)	$<\tau_r>^{\#}$ (ns)
C-153 in water	0.40	0.40	0.100	-	-	-
C-153 in 1% SDS	0.40	0.06	1.970	0.34	0.295	0.546
C-153 in SC	0.36	0.21	2.220	0.15	0.238	1.394
C-153 in Met	0.36	0.16	2.127	0.20	0.238	1.078

$^{\#}<\tau_r> = \tau_{1r} \times [a_{1r}/(a_{1r} + a_{2r})] + \tau_{2r} \times [a_{2r}/(a_{1r} + a_{2r})]$

component observed in SDS micelle (**Table 6a.1**). Therefore, we ascribe this fast component to the rotational relaxation of C-153 molecules residing to the Stern layer of either free SDS micelle in SWNT solution (according to SANS study[58]) or SDS half-cylindrical micelle (according to TEM study[57]) adsorbed on SWNT surface (**Scheme 6a.4**). Moreover, both the studies confirm that SDS is adsorbed on the CNT surface either in the form of monomer or in the form of half-cylindrical micelle. Therefore, the slower component of rotational relaxation (~2 ns) of C-153 in both the SWNTs suggests that probe molecules are located on SWNT surface, where the rotational movement of the probe molecule is more restricted compared to the SDS micelle due to the restriction imposed by SWNT surface as well as surrounding SDS monomers or half-cylindrical micelles adsorbed on SWNT (**Scheme 6a.4**). We have observed that the fluorescence decays of C-153 in SWNTs as well as 1% SDS depend on the emission wavelength (**Figure 6a.3)**. At the short edge of the emission spectra faster decay is observed whereas at the long edge the decay profile consists of a clear rise followed by decay. In this context, it should be mentioned that we have used a 495 nm long pass filter before the emission chamber (mentioned in the Experimental Section) to avoid the interference of SWNT's fluorescence during the lifetime measurements of C-153. Moreover, collecting wavelengths for C-153 were varied from 505 nm to 615 nm, where SWNTs have negligibly small fluorescence.

We have observed a dynamic Stokes' shift in the emission spectra. The time-resolved emission spectra (TRES) (**Figure 6a.4a**) have been constructed following the procedure given by Fleming and Maroncelli[63] mentioned in detail in the **Chapter 3**. The decay of

solvent correlation function (C(t), described in **Chapter 3**) was fitted to a bi-exponential function (**Figure 6a.4b**). The average solvation time of C-153 in SC-SWNT and Met-SWNT are ~595 ps and ~540 ps, respectively (**Table 6a.2**). Here it is necessary to mention that the solvation time of pure water is ~310 fs using Coumarin 480 as a probe, similar in structure to C-153.[64] Thus, the water dynamics is significantly retarded at the SWNTs surface. Now, one obvious argument may arise here that the observed solvation dynamics may reflect the solvation in SDS micelle, as both of the SWNTs are dispersed in 1% SDS, which higher than

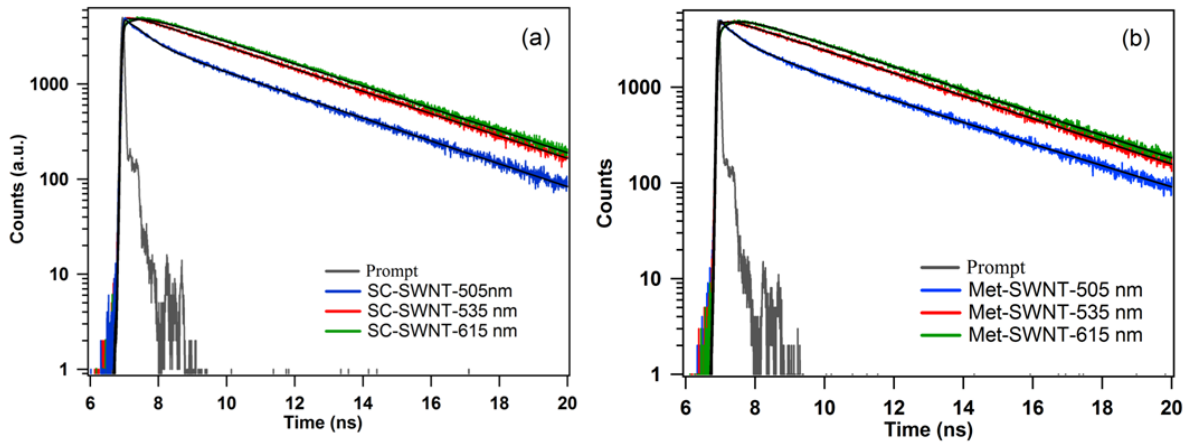

Figure 6a.3. *Wavelength dependent decay profiles of C-153 in SDS dispersed (a) semiconducting and (b) metallic SWNT. All the collection wavelengths are mentioned in the inset.*

the CMC. To verify that we have also measured solvation dynamics of C-153 in 1% SDS and we found that the average solvation time in SDS is ~155 ps (**Table 6a.2**). The dynamics that we observed in SWNTs are significantly slower than that observed in 1% SDS micelle. It infers that that the observed solvation dynamics in SWNTs does not reflect the solvation dynamics in SDS micelles alone, instead it may correspond to new dynamics of water. Moreover, we have observed a bimodal solvation dynamics: one is fast component with time constant of 350-445 ps, another is slow component with a time constant of 740-860 ps. It has been observed that the relaxation of water molecules present in the Stern layer of micelle takes place in the range of 180-550 ps time-scale.[65] Hence, the observed ~350-445 ps dynamics reflects the dynamics of water molecules at the Stern layer of either half-cylindrical SDS micelles adsorbed on the SWNT surface[57] or free SDS micelles in the SWNT solution.[58] This is consistent with our rotational relaxation results, where we have found that few C-153 molecules may reside at the Stern layer of either free SDS micelles in SWNT solution or SDS

half-cylindrical micelles adsorbed on SWNT. The prediction of second component (which is almost 738 ps in case of Met and 860 ps in case of SC), is not straight forward. However, this component is absent in case of 1% SDS micelle. Hence, it does not correspond to water dynamics at the Stern layer of SDS micelle. Recently, Rezus and Bakker reported the existence of the immobilized water molecules in the hydration layer of hydrophobes with the help of femtosecond mid-infrared spectroscopy and a slow orientational dynamics of water with a time constant >10 ps was observed.[66] Moreover, it is reported that hydrophobic surface can modify the water dynamics significantly because it can induce a structure in the

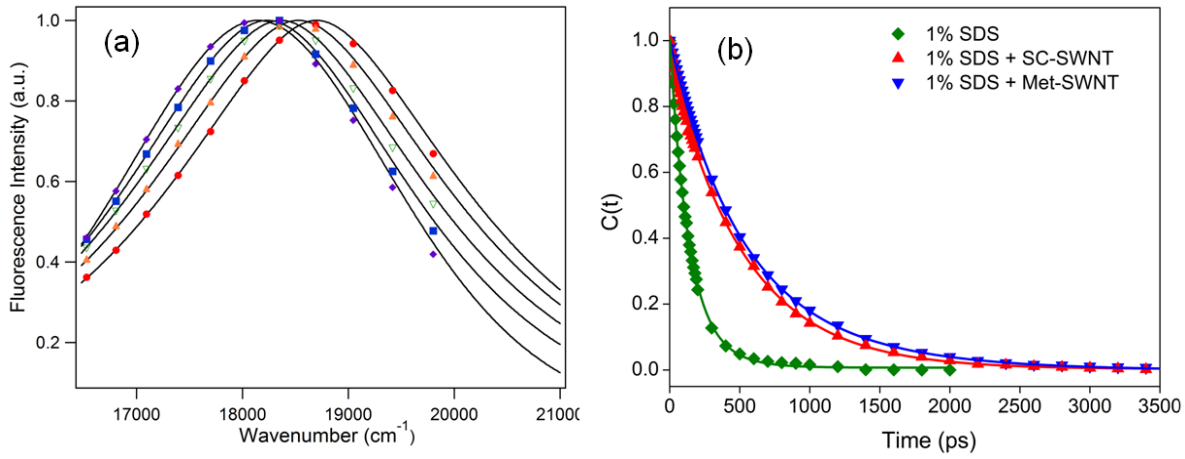

Figure 6a.4. *(a) Time-resolved emission spectra of C-153 in metallic SWNT at 0 ps (●), 200 ps (▲), 500 ps (▽), 1000 ps (■) and 3000 ps (♦).(b) Decay of solvent correlation function (C(t)) of C-153 in 1% SDS micelle and SWNTs. The points denote the actual values of C(t), and the solid lines denote the best fit.*

surrounding water layer.[67] Xu and Berne showed that hydrogen bonds among water molecules become stronger in the solvation shell of nonpolar groups.[68] Therefore, we initially anticipated the second slow component observed in SWNTs is appearing due to the hydrophobic effect of SWNT surface and corresponds to the water molecules adsorbed at SWNT surface. However, the water dynamics is predicted to be slower near hydrophilic surface compared to hydrophobic surface due to the possibility of hydrogen bond formation with hydrophilic surface.[67] Moreover, it is reported that the residence time of water in a hydrophobic surface is ~150 ps.[69] Hence, the observed 740-860 ps dynamics cannot be solely due to the water molecules adsorbed at the hydrophobic surface of SWNTs. Moreover, our rotational relaxation results suggest that C-153 molecules are located on SWNT surface (**Scheme 6a.2**), where the probe molecule can sense the hydrophobic effect of SWNT and

hydrophilic effect of surrounding head groups of SDS monomers[58] or half-cylindrical SDS micelles.[57] Therefore, we believe that hydrophobic water molecules at the surface of SWNT

Table 6a.2. *The fitting parameters of solvent correlation function (C(t)) of C-153 in 1% SDS, Semiconducting (SC) and Metallic (Met) SWNTs.*

Sample	$\Delta\upsilon^a$ (cm^{-1})	a_1	τ_1 (ps)	a_2	τ_2 (ps)	$<\tau_{av}>^b$ (ps)
C-153 in 1% SDS	400	0.063	450	0.937	135	155
C-153 in SC	565	0.36	860	0.64	445	594
C-153 in Met	474	0.48	738	0.52	353	538

[a] $\Delta\upsilon=(\upsilon_0-\upsilon_\infty)$
[b] $<\tau_{av}>=(\tau_1\times a_1)+(\tau_2\times a_2)$

and hydrophilic water molecules of nearby head groups of SDS contribute jointly to the observed slow solvation dynamics. This is justified as water dynamics at the protein surface takes place in nano-second time scale, where both hydrophobic and hydrophilic effects exist simultaneously.[41-43]

In the present study, using the TCSPC setup, we are missing the fast component of the solvation dynamics, which is below 40 ps, due to limited time resolution of our set-up. We have applied method proposed by Fee and Maroncelli[70] (**Appendix 6.n1**) to calculate

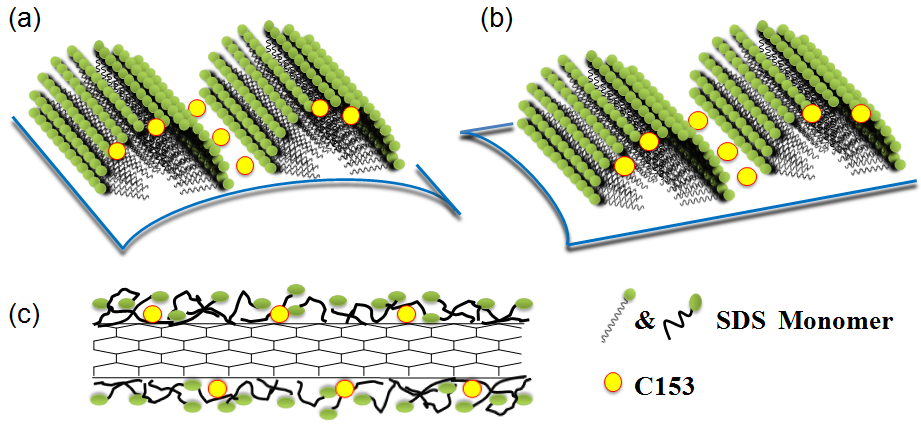

Scheme 6a.4. *Schematic representation for the probable arrangements of the SDS molecules on the surface of SWNT as well as locations of C-153 on SWNT surface. (a) arrangement of half-cylinder SDS micelles parallel to the tube axis[57]; (b) arrangement of half-cylinder SDS micelles perpendicular to the tube axis[57]; (c) random arrangement of SDS monomers on SWNT[58].*

that missing part of solvation dynamics and we have found that the missing component is almost 66% and 67% of the total dynamics for SC and Met, respectively. Vajda *et al.* pointed out that the contribution of the slow relaxation is expected to be ≤10%.[71] However, the missing components observed in many other organized assemblies are more than 20%.[72, 73] According to Fee and Maroncelli, if the absorption spectrum of probe in nonpolar solvent is not structureless, the reliability of the missing component is questionable.[70]

6a.3. Conclusion

In this work, we have observed that C-153 molecule exhibits time dependent Stokes' shift in SDS dispersed single walled carbon nanotubes (SWNTs). The location of the probe is predicted from the excitation wavelength dependence emission spectra and time resolved anisotropy study and thesestudies indicate that most of the C-153 molecules reside at the surface of SWNTs. We have also observed retardation of solvation time of C-153 in SWNTs compared to pure water as well as SDS micelle. Moreover, we have observed biexponential decay of solvent correlation function in which the time span for the fast component ranges from 350 ps to 445 ps, whereas time span for the slow component ranges from 740 ps to 860 ps. It has been reported that the relaxation of water molecules present in the stern layer (**Scheme 6a.4**) of micelle takes place in the range of 180-550 ps time-scale.[65] Hence, the observed ~350-445 ps dynamics may reflect the dynamics of water molecules in the Stern layer of either SDS free micelles in SWNT solution[58] or SDS half cylindrical micelles, which wrap around the SWNT surface[57]. The observed 740-860 ps dynamics cannot be solely due to the water molecules adsorbed at the hydrophobic surface of SWNTs, as it is shown that residence time of hydrophobic water molecules is ~150 ps.[69] Therefore, the slow component may arise due to combined effect of water molecules adsorbed on hydrophobic surface of SWNT and water molecules surrounding the head groups of either SDS monomer on SWNT or SDS half cylindrical micelles adsorbed on SWNT (**Scheme 6a.4**).

6b. How Does the Urea Dynamics Differ from Water Dynamics Inside the Reverse Micelle?

6b.1. Motivation

For preceding few decades aqueous urea solution has been pervasively used as protein denaturant, which emerged burgeoning interest in the past and still is an attractive topic for enduring research. However, the mechanism of protein denaturation by urea is still a debatable topic. Two distinct mechanisms are offered regarding urea induced denaturation of protein.[74-82] In one case, it is considered that urea wanes the hydrophobic interaction and in other, it is proposed that urea weakens the intramolecular proteinous hydrogen bonds while directly binds to proteins.[74-82] Now an important question arises, at what extent the hydrogen-bond network of water is perturbed by the addition of urea in water? To understand the properties of urea-water system, a great deal of research has been carried out by using a variety of experimental and theoretical techniques. However, no common consensus has been reached among these studies. Some work suggests that urea breaks water structure and is termed as a 'structure breaker' or 'chaotrope'.[83, 84] Others find urea to enhance the water structure and it is termed as 'structure maker' or 'kosmotrope'.[85, 86] However, a number of recent studies also suggest a combination of both the effects result the denaturation.[75, 87, 88]

Dielectric relaxations, NMR and optical Kerr effect (OKE) techniques have been used to get dynamical information of water in urea-water solution.[89-91] Although dielectric relaxation and OKE techniques offer dynamical information in picosecond time scale, these techniques monitor the dynamics of both urea and water in the solution, and make it difficult to strike out urea response from the observed dynamics.[89, 90] NMR study could selectively probe the water dynamics. However, it cannot distinguish water in the urea solvation shell from the bulk.[91] Very recently, infrared pump-probe spectroscopy has been employed to study the effect of urea on the structure and dynamics of water and it was found that even at high concentrations of urea (8M), the orientation dynamics of most of the water molecules are same as in pure liquid water.[92] This infers that urea has negligible effect on the hydrogen bond dynamics of the water molecules.[92] However, a small fraction of the water molecules displays orientational dynamics, which is more than six times slower than bulk water.[92] It was suggested that these water molecules are tightly associated with urea, forming a specific urea-water complex.[92] The short time dynamics of the water-urea mixture is also studied by

molecular dynamics (MD) simulation and the results indicate that the addition of urea leads to an overall isotropy and stiffening of the short time dynamics of both the species.[93] Both the experimental and simulation studies showed that diffusion of urea decreases with the increase in urea concentration in water.[94-96] Moreover, increasing urea concentration retards water diffusion. [95, 96] Most of these studies have been focused to probe the dynamics of water in urea-water mixtures, so that it could predict whether water is strongly or loosely hydrogen bonded in presence of urea.[89-93] There are few reports where the dynamics of urea has been monitored as a function of urea concentration in water. [94-96] Experimentally it is very difficult to monitor the dynamics of urea alone as urea has to be dissolved in water and in that case the observed dynamics will embrace the combinatorial effect of both water as well as urea. Recently, the solubilization property of urea in dry AOT reverse micelle (RM) has been investigated with the help of small angle neutron scattering (SANS) (**Scheme 6b.1a**) and FT-IR studies, and it is confirmed that urea is encapsulated in the micellar core as molecular clusters.[97, 98] These studies pave a way to elucidate urea dynamics without intervention of water inside the reverse micelle.

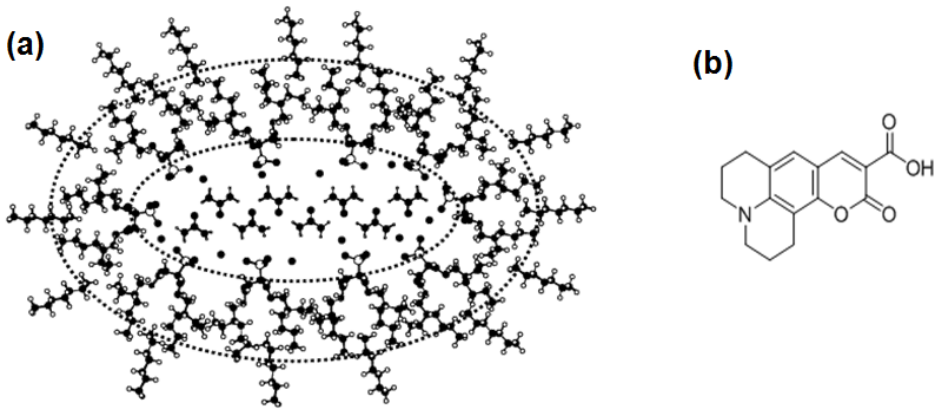

Scheme 6b.1. *(a) Schematic presentation of urea-AOT reverse micelle proposed by Caponetti[98] et al. from SANS study. (b) Chemical structure of Coumarin-343 (C-343)*

In this work, we have investigated urea dynamics inside the RM as a function of urea concentration with the help of time-resolved stokes shift and we believe that this is the first experimental attempt to unravel the dynamics of urea without intermediation of water. For comparison, water dynamics inside the RM has also been explored at various concentrations of water. Furthermore, we have studied urea-water mixture at various concentrations of urea inside the RM to estimate the effect urea on overall dynamics. Here, Coumarin-343 (**Scheme**

6b.1b) has been chosen as a solvation probe because it's extensive use in solvation dynamics studies.[73, 99, 100] Moreover, due to low solubility of Coumarin 343 (C-343) in hydrocarbon solvents it prefers to reside at the RM interface or interior avoiding problems of partitioning between organic bulk solvents and RM, and makes it possible to interpret the observed results without any ambiguity. We anticipate that our results furnish a comprehensive picture of urea dynamics, which will be helpful in understanding the dynamic behavior of molecular clusters.

6b.2. Results and Discussions

6b.2a. Steady State Absorption Spectra

The steady state absorption spectra of C-343 in urea/water containing RMs are shown in **Figure 6b.1** and results are summarized in **Table 6b.1**. In this context, it is pertinent to mention that C-343 has very low solubility in *n*-heptane and because of low solubility it forms aggregates in non-polar solvents like *n*-heptane.[101] The observed peak at ~402 nm is ascribed to the monomer, whereas ~428 nm peak reflects the aggregated state of C-343 in *n*-heptane (**Figure 6b.1**).[101] The solubility of C-343 increases in presence of 0.38 M AOT and it displays absorption maximum at 402 nm, which confirms that C-343 exists as monomer in presence of AOT. As the monomer peak doesn't show any bathochromic shift in going from pure *n*-heptane to 0.38 M AOT, hence, it intimates that the ground state of monomer is less

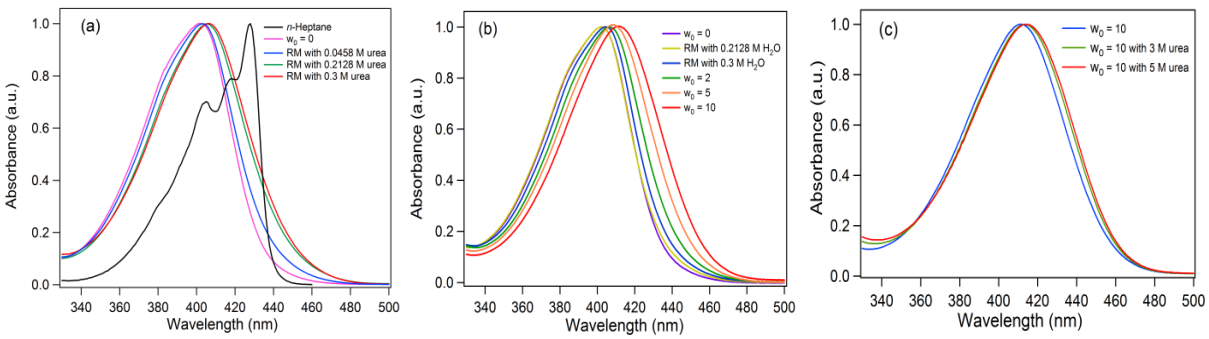

Figure 6b.1. *Absorption spectra of C-343 (a) in n-heptane, and different concentrations of urea in AOT RM, (b) at different concentrations of water in AOT RM, (c) at w_0 = 10 and two different concentrations of urea in RM at w_0 = 10.*

sensitive to polarity. On addition of urea to the 0.38 M AOT solution, a slight red shift is perceived (**Table 6b.1, Figure 6b.1**). However, the concentration of urea cannot go beyond

0.3 M due to the limited solubility of urea in the RM.[97, 98] The red shift of absorption spectra with the addition of urea infers that the dye is experiencing slightly more polar milieu in presence of urea in the reverse micellar core. For water RM, we extended our measurement until water concentration of ~3.8 M, corresponding to w_0 = 10. The absorption spectral features of C-343 in *n*-heptane/AOT/water system are almost similar to that of literature reports.[99] It is noticeable that the absorption maximum of C-343 at w_0 = 10 is blue shifted compared to bulk water (**Table 6b.1**). This indicates that the environment sampled by the dye inside the RM differ from that of bulk water.

Table 6b.1. *Absorption and steady state emission maxima of C-343 in (a) dry AOT RM, Urea containing AOT RM and water containing AOT RM, and (b) pure solvents.*

(a) Sample	w_0	λ_{abs} (max) / nm	λ_{em} (max) / nm
AOT RM	0	402	443
RM + Urea 0.0458 M	0.12	403	454
RM + Urea 0.2128 M	0.56	405	460
RM + Urea 0.30 M	0.79	406	461
RM + Water 0.0458 M	0.12	403	443
RM + Water 0.2128 M	0.56	403	446
RM + Water 0.30 M	0.79	404	448
RM + Water 0.76 M	2.0	408	460
RM + Water 1.89 M	5.0	409	478
RM + Water 2.85 M	7.5	411	483
RM + Water 3.80 M	10.0	412	484
RM + Water 5.70 M	15.0	413	486
Water RM + Urea 3M	10.0	414	484
Water RM + Urea 5M	10.0	414	484

(b) Solvents	λ_{abs} (max) / nm	λ_{em} (max) / nm
n-heptane	428	436
Water	432	490
MeOH	435	488
EtOH	435	488
MeCN	436	462

To verify the combined effect of urea and water towards the absorption spectra, we have collected the same for C-343 in RM at w_0 = 10 containing various concentrations of urea

dissolved in water. The results are shown in **Figure 6b.1c** and tabulated in **Table 6b.1**. The results clearly infer that absorption spectra of the dye display small red shift in presence of urea in water RM compared to water RM. Recently, it has been reported that urea increases bulk dielectric constant of the medium.[102] Hence, we ascribe the observed shift to the urea induced increase in the local dielectric constant inside the reverse micelle.

6b.2b. Steady State Emission Spectra

The emission maximum of C-343 is monitored to characterize the environment experienced by the dye inside the RM, as the emission spectrum of the dye largely depends on the polarity of its surroundings.[101] The spectral features of C-343 in urea or (and) water containing RM are shown in **Figure 6b.2** and results are summarized in **Table 6b.1**. The emission maximum of C-343 in *n*-heptane appears at 436 nm. However, in presence of 0.38 M AOT the spectrum displays a peak at ~443 nm. On successive addition of urea, the emission peak is gradually red shifted and there is almost ~17 nm bathochromic shift while switching from dry to 0.3 M urea containing RM (**Figure 6b.2(a)** and **Table 6b.1**). The spectral shift indicates that the

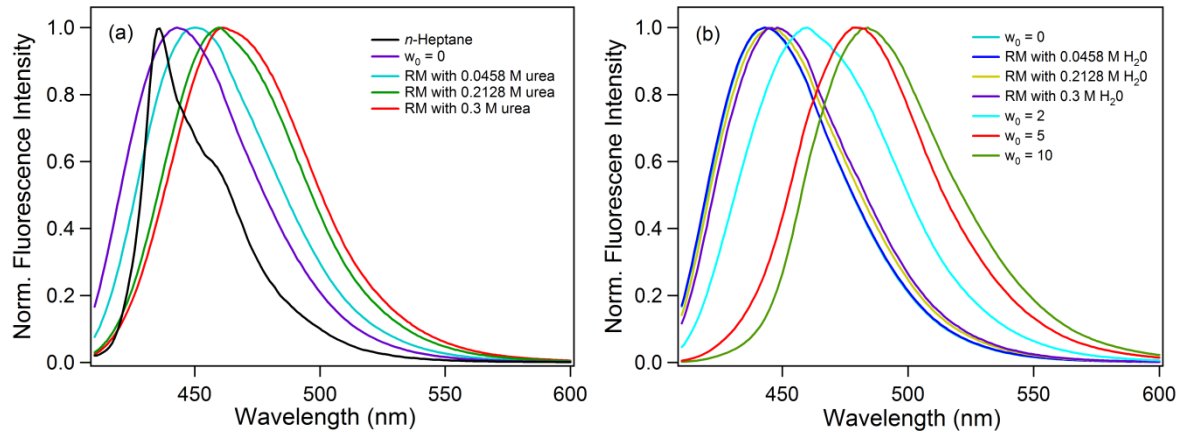

Figure 6b.2. *Steady state fluorescence emission spectra of C-343 (a) in n-heptane, and different concentrations of urea in AOT RM, (b) at different concentrations of water in AOT RM. All legends carry respective meaning.*

fluorescent dye is sensing more polar environment with the gradual addition of urea in the RM. Interestingly, when the shift of emission spectra is compared to water RM, it suggests that the dye is more sensitive to urea compared to water, e.g., the emission maximum of C-343 in 0.3 M urea containing RM is located at 461 nm, whereas the same in 0.3 M water

containing RM is situated at ~448 nm (**Figure 6b.2b** and **Table 6b.1**). Comparison with the emission peak of C-343 in various solvents suggests that the polarity of 0.3 M urea containing RM is close to acetonitrile (**Table 6b.1b**). The immense shift in emission spectra in presence of urea offers a clear hint about the presence of 'urea pool' inside the RM even at very low concentration of urea (0.3 M). However, this is not the case for water RM, where 'water pool' starts forming after w_0 = 2,[103] corresponds to water concentration of 0.76 M. Moreover, C-343 exhibits an emission peak at 460 nm in 0.76 M water concentration (w_0 = 2) inside RM. Although *n*-heptane/AOT/water system is well studied, in order to compare the results with urea RMs, we have extended our study up to w_0 = 10. The emission characteristics of C-343 in *n*-heptane/AOT/water system are almost similar to that of literature report,[101] and as expected the emission peak is gradually red shifted with respect to water concentration of the RM **(Figure 6b.2b)**. However, even at w_0 = 10, the peak maximum does not resemble to that of bulk water. This infers that at this w_0 the dye molecule senses water environment, which is quite different from bulk water.

We have also monitored the emission spectra of C-343 in AOT RM at w_0 = 10 with increasing urea concentration in water (**Appendix 6b.1**) to verify the combined effect of urea and water towards the emission spectra of C-343. However, we have noticed that the emission spectrum is almost unchanged with respect to urea concentration in water (**Table 6b.1a)**. This suggests that in the excited state dye senses almost similar polarity of urea-water mixture as that of water alone inside the RM.

6b.2c. Time-resolved Studies

6b.2c.1. Time Resolved Anisotropy

Although steady state measurements provide a qualitative idea about the location of C-343 inside AOT-RM, to ascertain the location of the probe we have employed time resolved fluorescence anisotropy study. The time-resolved anisotropy measurements provide information about the local viscosity as well as the rigidity of the milieu sensed by the dye and provide a notion about the location of the probe in the RM. The anisotropy decays are shown in **Figure 6b.3** and the results are tabulated in **Table 6b.2**. The anisotropy decay of the dye in water can be well fitted by a single exponential decay function with time constant of ~130 ps (**Figure 6b.3**). In contrast, the rotational time constants of the dye in the RM are few orders larger in magnitude compared to bulk water. These results clearly suggest that the

dye molecules are experiencing a rigid milieu inside the RM than bulk water, irrespective of the nature/composition of loading solvents or molecules. Moreover, the anisotropy decay profiles of C-343 in water containing RM are non-exponential in nature, which is consistent with literature reports.[99] The anisotropy results conspicuously indicate that the dye molecule is sensing more hindered environment in urea containing RM compared to water containing RM (**Table 6b.2**), even though the concentration of urea inside the RM is reasonably lower than water. Recently, SANS studies of urea containing AOT RM revealed that urea is encapsulated as small sized ellipsoidal hydrogen-bonded clusters within the hydrophilic micellar core of the AOT RM.[98] This is reflected in our anisotropy decay profile of the dye in urea containing RM, where we have noticed that the rotational motion of the dye is not at all

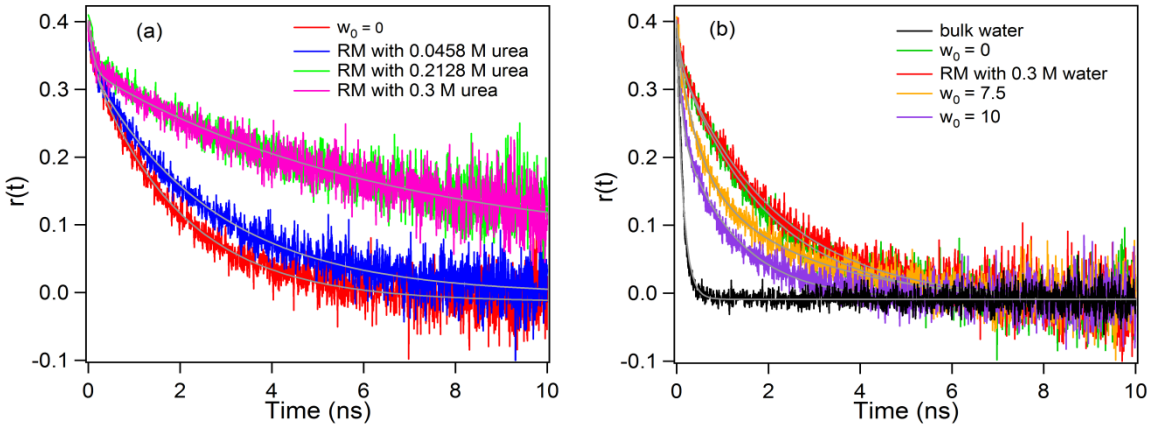

Figure 6b.3. *Fluorescence anisotropy decay profile of C-343 (a) different concentrations of urea in RM, (b) at different concentrations of water in AOT RM and bulk water. All legends carry respective meaning.*

completed within our observation time scale even after the urea concentration of >0.0458 M (**Figure 6b.3a**), and this may be ascribed to the rigidity of the urea cluster around the dye molecule. Moreover, the anisotropy decay profiles clearly reveal that the environment of AOT-RM in presence of urea is more hindered than that of dry AOT-RM. But this is not true for water RMs, where it has been observed that rotational motion of the probe becomes faster as the water content of the RM increases (**Figure 6b.3b, Table 6b.2**). This demonstrates that urea encapsulation to RM increases the rigidity of the environment inside the RM.

At w_0 = 0, the dye molecules exclusively located at the micellar interface near the AOT head groups, as 'water pool' does not exist at w_0 = 0. This is confirmed by the anisotropy decay profile of the dye, where the rotational motion of dye takes place in 1.9 ns

time scale. Previously, the rotational relaxation time for dry AOT RM has been shown via electron spin resonance (ESR) to be ~1.2 ns.[103] Thus, the rotational relaxation of dye in nano-second time scale implies that the dye molecules interact strongly with the reverse micellar interface. In case of urea RM, dye molecules are located at the micellar interface at very low urea concentration (<0.2128 M), as the anisotropy decay profile is very close to that of dry AOT RM (**Figure 6b.3a**). After the urea concentration of ≥ 0.2128 M in RM, most of the dye molecules move from micellar interface to the core of AOT RM as urea starts forming chain

Table 6b.2. *Anisotropy decay characteristics of C-343 in dry AOT RM, Urea containing AOT RM, water containing AOT RM and urea-water mixture containing RM.*

Sample	w_0	r_0	a_{1r} (%)	τ_{1r} (ns)	a_{2r} (%)	τ_{2r} (ns)	a_{3r} (%)	τ_{3r} (ns)
AOT RM	0	0.40	10	0.100	90	1.97	-	-
RM + Urea 0.0458 M	0.12	0.39	12	0.090	88	2.64	-	-
RM + Urea 0.2128 M	0.56	0.38	13	0.060	24	1.60	63	8.4
RM + Urea 0.30 M	0.79	0.37	14	0.065	23	1.76	63	9.2
RM + Water 0.30 M	0.79	0.40	13	0.090	87	2.17	-	-
RM + Water 3.80 M	10.0	0.38	47	0.260	53	1.54	-	-
Water RM + Urea 3M	10.0	0.39	49	0.390	51	2.12	-	-
Water RM + Urea 5M	10.0	0.37	35	0.220	65	1.68	-	-

like aggregates (or molecular clusters) at the reverse micellar core.[97, 98] For water-RM, C-343 molecules might have distribution in between micellar interface as well as 'water pool' after w_0 = 2. Multiple time constants for the anisotropy decays support our conjecture. Additionally, the magnitude of the picosecond component increases and the relative contribution of nanosecond component decreases as w_0 increases. This observation infers that the dye molecules are experiencing a decreasingly restrictive milieu with increasing RM size. Interestingly, even at w_0 = 10, the dye molecules do not sample a bulk like environment. To check the effect of urea towards the rigidity of water structure, we have collected the anisotropy decay profiles of C-343 in AOT RM at a particular w_0 with varying urea concentration in water (**Appendix 6b.2**). We have observed that urea has almost negligible effect on the rotational motion of C-343 (**Appendix 6b.2**). This means that rigidity of the surrounding environment of C-343 in water is not changing in the presence of urea. This is consistent with the observations that there are no major disruptions of the hydrogen bond

network of water in presence of urea.[92, 104] The slight change in anisotropy decay might arise due to increased viscosity inside the RM by the addition of urea.

Although the dye molecules have negligible solubility in *n*-heptane, we cannot rule out the possibility of residing very few dye molecules in *n*-heptane. To get a quantitative idea of the dye partition between the n-heptane/water system, we have estimated the partition coefficient of the dye using UV-visible absorption spectroscopy. The partition coefficient for the n-heptane/ water system is 0.06 (±0.01). This suggests that the solubility of C-343 in n-heptane is much less. The 60-100 ps component might reflect the rotational relaxation of the dye molecules those are situated in *n*-heptane (**Table 6b.2**). Interestingly, this 100 ps component exists in dry, urea and low-water containing RM. However, this dynamics is no

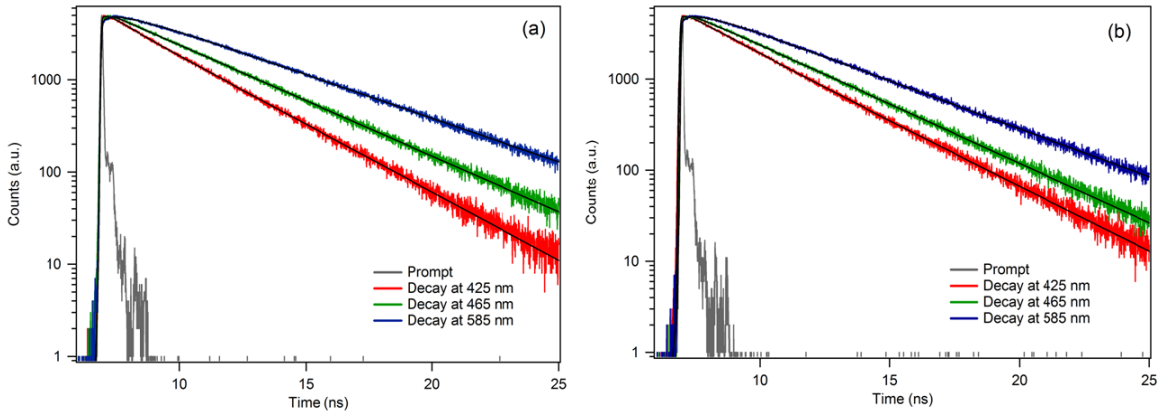

Figure 6b.4. *Wavelength dependent decay profiles of C-343 in (a)* RM + urea 0.30 M *and (b)* RM + water 0.30 M. *All the collection wavelengths are mentioned in the inset.*

longer observed in water or urea-water RM after a certain water concentration. This observation is tempting us to anticipate that the incorporation of water or urea-water mixture favors the transfer of more dye molecules from *n*-heptane to the reverse micellar core. One possible reason may be the size of the RM, which increases with the addition of polar solvent. Larger size of RM accommodates a higher number of dye molecules, and hence the dye molecules cannot be found in *n*-heptane at higher concentration of water or urea-water mixture of the RM.

6b.2c.2. Dynamic Fluorescence Stokes Shift

To probe the alteration of the dynamical properties of urea inside the reverse micelle, we

have examined pico-second resolved solvation dynamics of the dye (C-343) in AOT RM. For the purpose of comparison, the dynamic properties of water as well as urea-water mixture inside the RM have also been investigated using the same dye molecule. The fluorescence transients of C-343 in urea containing RM at different wavelengths ranging from 415 nm to 585 nm (10 nm successive intervals from 415 nm to 445 nm and consecutive 20 nm interval from 465 nm to 585 nm) have been collected and it was found that the red end side of the transient displays prominent growth (**Figure 6b.4**), indicating the dye molecule is gradually solvated with time. The fluorescence decays of C-343 at different wavelengths of other RMs, for example, water and urea-water containing RMs have a similar type of features. In this context, it is relevant to mention that the decays at the short and long wavelengths of C-343 are identical in the pure solvents, e.g., in *n*-heptane, water as well as in the urea-water mixture. The time-resolved emission spectra (TRES) have been constructed from the fluorescence decays at different wavelengths adopting the procedure given by Fleming and Maroncelli[63] (described in **Chapter 3**). Representative TRES of C-343 in RM is shown in **Figure 6b.5**.

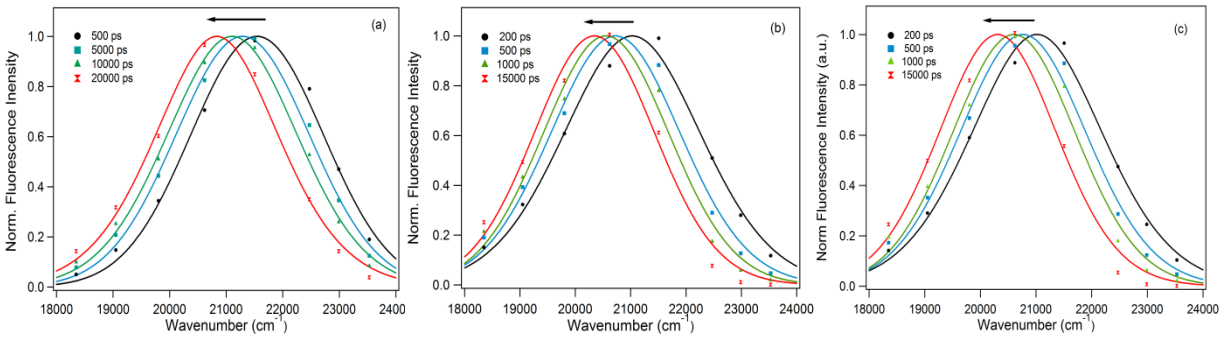

Figure 6b.5. *Time-resolved emission spectra (TRES) of C-343 (a) in 0.3 M urea containing RM, (b) at w_0 = 10, and (c) at 5 M urea containing RM at w_0 = 10.*

The decay properties of solvent correlation function (C(t)) are shown in **Figure 6b.6** and the results are tabulated in **Table 6b.3**. Interestingly, the decay of C(t) starts from a value lesser than unity. This is because the ultrafast dynamics in these systems cannot be captured by our TCSPC set-up (<40 ps). Here, it should be mentioned that although the decays are not starting from unity, but in order to make comparison we have provided average solvation time based on the percentage of the dynamics detected by our set-up (**Table 6b.3**). In

heterogeneous environment like RM, the interpretation of solvation dynamics results depends on the location of the probe, as the dye might have a distribution between non-polar solvent

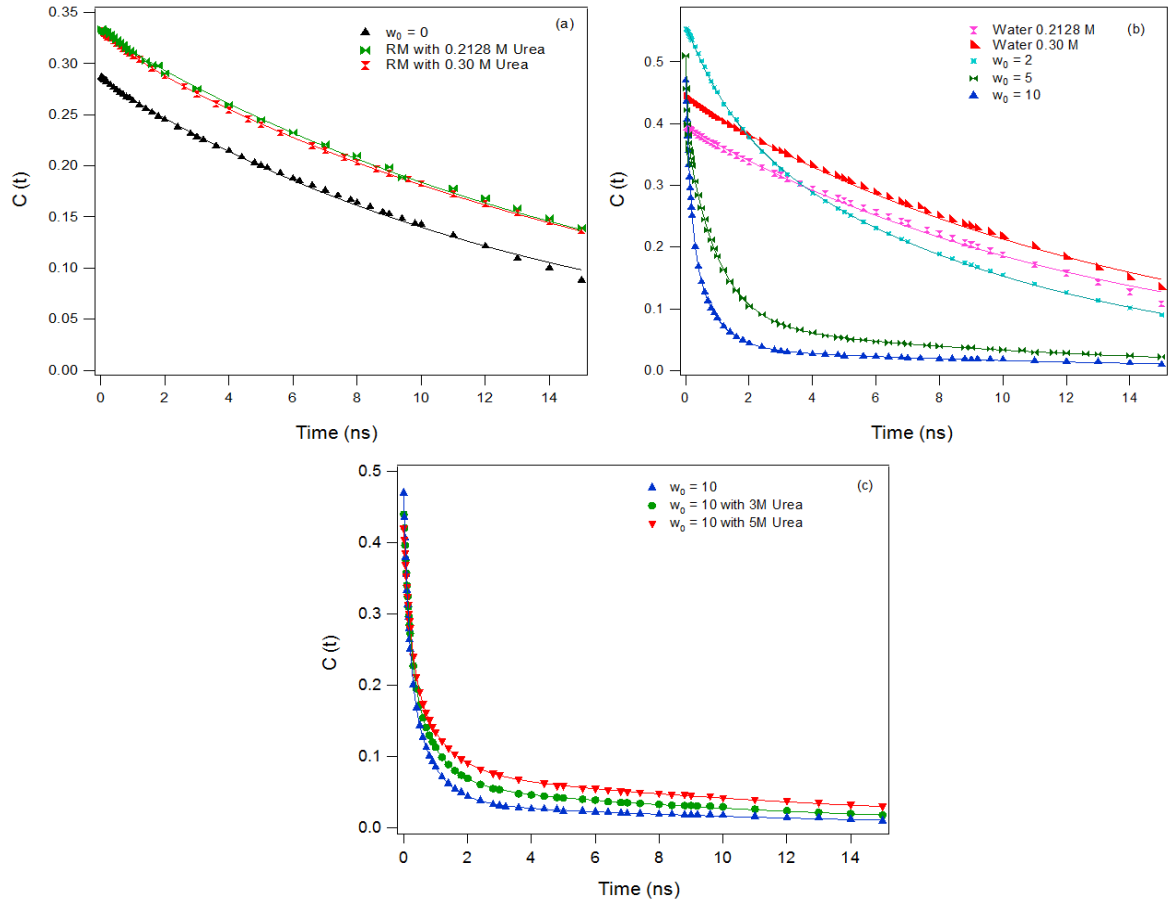

Figure 6b.6. *Decay of solvent correlation function (C(t)) of C-343 (a) in dry AOT and different urea containing RM, (b) in dry AOT and different water containing RM, (c) at w_0 = 10 and two different concentrations of urea in RM at w_0 = 10.*

and reverse micellar core. Moreover, even inside the RM, the dye might have a distribution between the interface and central 'water pool' of the RM. Most importantly, the distribution of the probe depends on the nature of the probe. If the dye is neutral in nature, then it will be partitioning between non-polar solvent and reverse micellar core. On the other hand if the dye is ionic in nature, then it prefers to stay inside the RM. As our monitoring dye (C-343) is anionic in nature (as the pK_a of C-343 is ~4.6[105]), hence, almost all the dye molecules prefer to reside at the core of the RM. Moreover, our steady state (absorption and fluorescence) as well as time resolved fluorescence anisotropy results also suggest that almost all of the dye molecules stay inside the RM. However, as we already discussed (in time-resolved anisotropy

section) that almost 10% of the dye molecules remain in the bulk *n*-heptane in case of dry, urea and low water containing RM due to the smaller sizes of these RMs. It is conspicuous from **Table 6b.3** that the solvation dynamics of the dye is very slow for dry AOT RM and it

Table 6b.3. *Decay characteristics of solvent correlation function (C(t)) of C-343 in AOT-RM, urea containing AOT-RM and water containing AOT-RM.*

Sample	w_0	a_1 (%)	τ_1 (ns)	a_2 (%)	τ_2 (ns)	a_3 (%)	τ_3 (ns)	$<\tau_{av}>$ (ns)
RM	0	2.0	0.20	98.0	14.12	-	-	13.84
RM + Urea 0.0458 M	0.12	1.0	0.20	99.0	14.55	-	-	14.40
RM + Urea 0.2128 M	0.56	2.0	0.60	98.0	17.16	-	-	16.83
RM + Urea 0.30 M	0.79	4.0	1.11	96.0	17.52	-	-	16.86
RM + Water 0.2128	0.56	1.0	0.40	99.0	13.80	-	-	13.67
RM + Water 0.30 M	0.79	1.8	0.40	98.2	13.75	-	-	13.51
RM + Water 0.76 M	2.0	22	1.28	78.0	9.32	-	-	7.55
RM + Water 1.89 M	5.0	22	0.12	63.0	1.00	15	11.52	2.38
RM + Water 3.80 M	10.0	51	0.16	40.0	0.74	09	12.16	1.47
Water RM + Urea 3M	10.0	45	0.19	40.0	0.82	15	12.00	2.21
Water RM + Urea 5M	10.0	42	0.20	38.0	0.90	20	13.70	3.16

occurs in ~14 ns time scale. The slow solvation time in dry RM might arise due to solvation by Na^+ ions, as it is already transpired that ionic solvation crops up slowly.[106, 107] The long lifetime of ~14.1 ns corresponds to ionic solvation. The fast component of ~200 ps is attributed to the presence of a trace amount of water in AOT, which is very difficult to remove. In literature, the solvation dynamics results in pure AOT RM is scarce. Only result that we are able to find out is the results published by Sarkar *et al.* using Coumarin 152 as a solvation probe.[108] The solvation time that they reported in dry AOT RM using C-152 is ~12.22 ns. However, we have observed a solvation time of ~14 ns in dry AOT RM. The relative difference in solvation time in our case and Sarkar *et al.* may turn up due to the use of a different type of solvation probe.

The results in **Table 6b.3** demonstrate that the solvation time of C-343 is escalating with the increase in urea concentration inside the AOT RM, e.g., the average time of solvation for C-343 in dry AOT RM is ~14 ns, whereas the same in 0.3 M urea containing RM is ~17 ns. However, the solvation time in RM containing 0.3 M water is very close to that of dry AOT RM (**Figure 6b.6a**, **Table 6b.3**). This is reasonable as the 'water pool' of

RM doesn't exists at this water concentration and all the water molecules are likely to be located at the interface of AOT RM.[109] It was already perceived that hydrodynamic radius of the water RM at $w_o \leq 2$ is minuscule,[109] which suggests that this water concentration (0.3 M) has a trifling effect on the size and shape of the RM. On the other hand, 0.3 M urea has colossal influence on the size of AOT RM. SANS study indicates that the radius of quite spherical urea-AOT aggregate increases with urea, and falls within the range of 15-25 Å,[97, 98] which is equivalent to the variation of 'water pool' size of RM from w_0 = 1 to w_0 = 6.[110] Moreover, SANS study infers that urea molecules are molecularly dispersed among the AOT hydrophilic head groups at lower concentration (<0.2128 M); and at higher concentration they form molecular clusters surrounded by appropriately oriented AOT molecules.[97, 98]These urea clusters are very rigid as they are strongly hydrogen bonded, and hence, their movements are extremely restricted. Therefore, the observed slow component (17 ns) in urea RM is attributed to the slow dynamics of urea clusters. The fast component (0.60-1.11 ns), with a negligible contribution of ~2-4% might be attributed to the dynamics of waters and (or) urea molecules at the interfacial region of the RM. It would be interesting if we could be able to monitor the urea dynamics at higher concentration of urea, but due to the limited solubility of urea in AOT RM, we are unable to detect urea dynamics at higher urea concentrations (>0.3 M). It is noteworthy to mention here that formamide (FA), has a close structural resemblance to urea, also displays hindered solvation dynamics inside the reverse micellar core, and the dynamics becomes faster as the FA concentration increases.[99, 111] The solvation dynamics of FA inside the reverse micellar core decreases from 9.45 to 6.2 ns with the increase in FA concentration, [111] whereas the same for urea increases from ~14.4 to ~17 ns as the concentration of urea inside the RM increases. The different solvation dynamics features between urea and FA arises due to different kinds of interactions inside the RM. The concentration dependence of FA dynamics inside the RM is attributed to the complex hydrogen bonding interactions between FA and AOT or FA and FA in the polar solvent pool of the RM.[111] For urea RMs, concentration dependence of solvation dynamics inside the RM is ascribed to the formation of molecular cluster at higher urea concentration (≥0.2128 M).

The solvation dynamics of water inside AOT RM is non-exponential in nature after $w_0 \geq 2$ (**Table 6b.3, Figure 6b.6**). The non-exponential feature of solvation dynamics signifies the existence of different kinds of water molecules inside the reverse micellar core. Here, it is relevant to mention that FT-IR and ultrafast infrared studies revealed the existence of three diverse types of water molecules in the AOT RM and they are termed as 'bound

water', 'trapped water' and 'free water'.[110, 112] 'Free water' forms water cluster after a certain concentration and this is designated as 'water pool' of the RM. Considering the FT-IR results, we anticipate that tri-exponential feature of solvation dynamics reflects the dynamics of three distinct kinds of water inside the reverse micelle. The fast component of solvation dynamics (120-160 ps) might reflect the dynamics of water cluster in the 'water pool' of the RM (**Table 6b.3**). This infers that the dynamics of water cluster is quite faster than urea cluster as the water clusters inside the reverse micellar core are not rigid like urea cluster. The slower component of ~1.00 ns might be attributed to the 'trapped' water molecules in between neighboring surfactant head groups and the slowest component (~11.5-12.2 ns) might be ascribed to the dynamics of 'bound' water molecules those are strongly hydrogen bonded to the wall of the RM through the Na^+ ions.[42] Surprisingly, at w_0 = 2, the solvation dynamics consists of only two components having solvation time of 1.28 ns and ~9 ns (**Table 6b.3**). In analogy to our prophecies about solvation dynamics components at higher w_0, we believe that 1.28 ns and ~9 ns components are featured by the 'trapped' and 'bound' water molecules, respectively. This insinuates the solvation dynamics of C-343 at w_0 = 2 is devoid of the 'free water' dynamics, which allude to the non-existence of 'water pool' at w_0 = 2. This conjecture is supported by literature, where it has been reported that at this w_0 essentially all the water molecules are associated with sulfonate head groups of AOT.[112] Unless noted otherwise, the dynamics of 'water pool' water is almost 100 times slower than that of bulk water as the relaxation dynamics of bulk water around C-343 takes place in <1 ps time scale.[99] It is believed that chemical exchange between interfacial water ('trapped' and 'bound' water) and the 'water pool' water would result in apparently sluggish solvation time of 'water pool' water than that of bulk water.[67]

Here, it is worth mentioning that most of the previous studies have detected only two kinds of water dynamics inside the AOT RM.[108, 113] However, in this study we have perceived three different dynamics corresponds to three different types of water molecules inside the reverse micellar core. Riter *et al.* also reported the dynamics of three different kinds of water molecules based on the ultrafast components of C-343 in AOT RM.[99] Although we have missed such ultrafast components in our study due to our limited instrument resolution (IRF ~ 80 ps), still the dynamics of all the three kinds of water molecules inside the reverse micellar core are efficiently perceived. The use of highly water soluble solvation probe like C-343 might be the apparent reason for effective detection of three distinct kinds of water dynamics inside the RM. In the case of C-343 in RM, the majority of the dye molecules reside at the

interface of the micelle. However, a fraction of dye molecules also dwell in between the interface and water pool, and there is a finite probability that during the excited state lifetime dye molecules may diffuse toward the water pool of the RM. Therefore, C-343 molecules can probe the dynamics of three different kinds of water molecules present inside the RM. The biexponential feature of solvation dynamics reported by other groups results from the use of neutral solvation probe, the solubility of which in water is very low.[108, 113] Hence, the probability of finding this neutral solvation probe in 'water pool' of the RM is very less; instead they are more probable to subsist at the interface of the RM. Although it is reported that nanosecond component of solvation dynamics corresponds to 'free water' in the 'water pool' of the RM[108, 113], we believe that nanosecond component does not reflect the dynamics of 'free water' of the RM, rather it displays the dynamics of the 'trapped water' inside the reverse micellar core. This can be vindicated from the fact that 'free water' in the water pool of the RM generally comprises a dynamics of 120-160 ps (**Table 6b.3**). These observations lead us to reckon that heterogeneity of water environment could be detected by the solvation dynamics technique with the help of proper choice of solvation probe.

We have also monitored the dynamics of urea-water mixtures inside the AOT RM with increasing urea concentration to get insight about the effect of urea on the overall solvation dynamics feature. The characteristics of solvation dynamics feature is shown in **Figure 6b.6** and the results are tabulated in **Table 6b.3**. It is unequivocal from the results that solvation dynamics is slowing down with increasing urea concentration in water RM. Small angle x-ray scattering (SAXS) study indicates that urea cannot modify the RM structure with respect to its shape and size.[114] Hence, the observed slow solvation dynamics is not arising due to the size of the RM. The dielectric spectroscopic study of urea-water liquid structure proposed that there are two types of hydrated water molecules in urea solution, which are strongly and weakly associated to the urea molecule.[115] Moreover, polarization-resolved pump-probe spectroscopy elucidated the effect of urea on the structure and dynamics of water.[92] It was found that a small fraction of the water molecules are strongly associated with urea and those water molecules flaunts an orientational dynamics that are more than six times slower than in bulk water.[92] Therefore, the observed slow dynamics in presence of urea might be attributed to the dynamics of those strongly associated water molecules with urea. This is also reflected in our solvation dynamics results, where it is seen that the time constant as well as amplitude of the slow component is increasing in going from water RM to urea-water containing RM. However, we cannot rule out the possibility that the observed slow dynamics

might reflect the dynamics of few urea molecules those are strongly hydrogen bonded with surroundings urea and (or) water molecules.

Table 6b.4. *Calculated time-zero fluorescence maxima, observed time-zero fluorescence maxima and missing components.*

Sample	$\nu_0{}^{a}{}_{(cal)}$ (cm^{-1})	$\nu_{0(obs)}$ (cm^{-1})	$\Delta\nu^{b}{}_{cal}$ (cm^{-1})	$\Delta\nu^{c}{}_{obs}$ (cm^{-1})	% MC[d]
RM	23864	22508	1903	547	71
RM + Urea 0.0458 M	23830	22054	2539	763	69
RM + Urea 0.2128 M	23781	21637	3221	1077	67
RM + Urea 0.30 M	23732	21591	3213	1072	66
RM + Water 0.0458 M	23802	22517	1798	513	71
RM + Water 0.2128 M	23743	22462	2117	836	61
RM + Water 0.30 M	23681	22404	2295	1018	56
$W_0 = 2$	23428	22161	2850	1583	45
$W_0 = 5$	23230	21850	2813	1433	49
$W_0 = 10$	23158	21638	2844	1324	53
$W_0 = 10$ + Urea 3 M	23082	21509	2820	1247	56
$W_0 = 10$ + Urea 5 M	23063	21427	2840	1204	58

[a] $\Delta\nu_{cal}$ *determined using Fee-Maroncelli method*[70]
[b] $\Delta\nu_{cal} = \nu_{0\,(cal)} - \nu_{\infty}$
[c] $\Delta\nu_{obs} = \nu_{0\,(obs)} - \nu_{\infty}$
[d] *MC: Missing Component*

We have already mentioned that in our experimental set-up we miss ultrafast components of solvation dynamics due to limited instrumental resolution, and we have estimated the missing component with the help of the procedure developed by Fee and Maroncelli[70] (**Appendix 6.n1**). It is noticeable that dry, urea and lower water content RMs have larger percentage of missing component than higher concentration of water as well as urea-water containing RMs (**Table 6b.4**). This is probably due to the fact that in these systems a small percentage of dye molecules (~10%) reside outside the reverse micellar core, and they are also excited along with the dye molecules staying inside the reverse micellar core. The solvation dynamics of the dye molecules, those are residing outside the reverse micellar core, might be taking place in several pico-second time scale. Therefore, the overall solvation component detected in these systems is significantly lower than other water and urea-water containing RMs. The missing component trend in case of water RMs shows a good agreement with the previous report.[116] According to Fee and Maroncelli, if the absorption spectrum of the dye in nonpolar solvent is not structure-less, the reliability of the

missing component is questionable.[70] The absorption spectrum of the dye in non-polar solvent in our case is structured, and, hence, the calculated missing component may not be precise.

6b.3. Conclusion

In this work, we have observed that C-343 in 0.3 M urea containing RM exhibits a huge bathochromic shift in emission spectra compared to 0.3 M water containing RM. Comparing the peak maximum of C-343 in pure solvents, it is found that 0.3 M urea in the RM conceives a polarity which is closer to acetonitrile. The dynamics of urea in the RM has been also monitored using time resolved Stokes shift method. It has been observed that after a certain

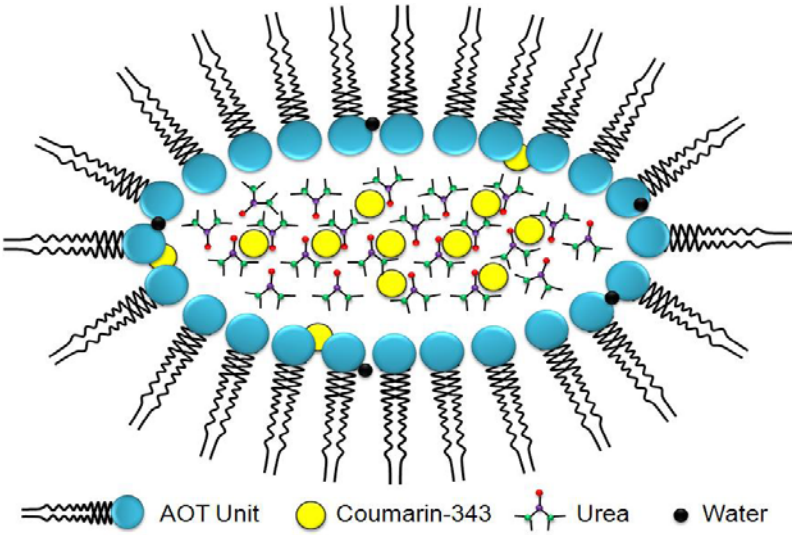

Scheme 6b.2. *Illustration of urea loaded RM containing Coumarin 343.*

concentration, urea exhibits highly retarded dynamics compared to dry as well as water RM, and this is ascribed to the highly hydrogen bonded network of urea molecules inside the RM. Time resolved anisotropy study also supports the existence of highly networked urea cluster inside the reverse micellar core (**Scheme 6b.2**). Moreover, to get an idea about the perturbation of urea on the overall solvation dynamics feature, we have also probed the dynamics of urea-water mixtures inside the AOT RM with increasing urea concentration. It has been observed that with the increase in urea concentration, the overall dynamics becomes

slower and it might be attributed to the presence of few water or urea molecules those are strongly associated with surroundings urea and (or) water by hydrogen bonds.

6.2. Reference

1. Pal, S.K., Peon, J. & Zewail, A.H. Biological water at the protein surface: Dynamical solvation probed directly with femtosecond resolution. *Proc. Natl. Acad. Sci. U.S.A.* **99**, 1763-1768 (2002).
2. Othon, C.M., Kwon, O.-H., Lin, M.M. & Zewail, A.H. Solvation in protein (un)folding of melittin tetramer–monomer transition. *Proc. Natl. Acad. Sci. U.S.A.* **106**, 12593-12598 (2009).
3. Zhong, D., Pal, S.K., Zhang, D., Chan, S.I. & Zewail, A.H. Femtosecond dynamics of rubredoxin: Tryptophan solvation and resonance energy transfer in the protein. *Proc. Natl. Acad. Sci. U.S.A.* **99**, 13-18 (2002).
4. Johansson, A.C.V. & Lindahl, E. Protein contents in biological membranes can explain abnormal solvation of charged and polar residues. *Proc. Natl. Acad. Sci. U.S.A.* **106**, 15684-15689 (2009).
5. Warncke, K. & Dutton, P.L. Experimental resolution of the free energies of aqueous solvation contributions to ligand-protein binding: quinone-QA site interactions in the photosynthetic reaction center protein. *Proc. Natl. Acad. Sci. U.S.A.* **90**, 2920-2924 (1993).
6. Fernández-Escamilla, A.M., Cheung, M.S., Vega, M.C., Wilmanns, M., Onuchic, J.N. & Serrano, L. Solvation in protein folding analysis: Combination of theoretical and experimental approaches. *Proc. Natl. Acad. Sci. U.S.A.* **101**, 2834-2839 (2004).
7. Mallick, P., Weiss, R. & Eisenberg, D. The directional atomic solvation energy: An atom-based potential for the assignment of protein sequences to known folds. *Proc. Natl. Acad. Sci. U.S.A.* **99**, 16041-16046 (2002).
8. Chiche, L., Gregoret, L.M., Cohen, F.E. & Kollman, P.A. Protein model structure evaluation using the solvation free energy of folding. *Proc. Natl. Acad. Sci. U.S.A.* **87**, 3240-3243 (1990).
9. Rodriguez-Larrea, D., Minning, S., Borchert, T.V. & Sanchez-Ruiz, J.M. Role of solvation barriers in protein kinetic stability. *J. Mol. Biol.* **360**, 715-724 (2006).
10. Meister, K., Ebbinghaus, S., Xu, Y., Duman, J.G., DeVries, A., Gruebele, M., Leitner, D.M. & Havenith, M. Long-range protein–water dynamics in hyperactive insect antifreeze proteins. *Proc. Natl. Acad. Sci. U.S.A.* **110**, 1617-1622 (2013).
11. Eisenberg, D. & McLachlan, A.D. Solvation energy in protein folding and binding. *Nature* **319**, 199-203 (1986).
12. Bandyopadhyay, S., Chakraborty, S. & Bagchi, B. Exploration of the secondary structure specific differential solvation dynamics between the native and molten globule states of the protein HP-36. *J. Phys. Chem. B* **110**, 20629-20634 (2006).
13. Sen, P., Mukherjee, S., Dutta, P., Halder, A., Mandal, D., Banerjee, R., Roy, S. & Bhattacharyya, K. Solvation dynamics in the molten globule state of a protein. *J. Phys. Chem. B* **107**, 14563-14568 (2003).
14. Zhang, L., Kao, Y.-T., Qiu, W., Wang, L. & Zhong, D. Femtosecond studies of tryptophan fluorescence dynamics in proteins: Local solvation and electronic quenching. *J. Phys. Chem. B* **110**, 18097-18103 (2006).

15. Jayaram, B. & Beveridge, D.L. Modeling DNA in aqueous solutions: Theoretical and computer simulation studies on the ion atmosphere of DNA. *Annu. Rev. Biophys. Biomol. Struct.* **25**, 367-394 (1996).
16. Furse, K.E. & Corcelli, S.A. Molecular Dynamics Simulations of DNA Solvation Dynamics. *J. Phys. Chem. Lett.* **1**, 1813-1820 (2010).
17. Pal, S., Maiti, P.K., Bagchi, B. & Hynes, J.T. Multiple time scales in solvation dynamics of DNA in aqueous solution: The role of water, counterions, and cross-correlations. *J. Phys. Chem. B* **110**, 26396-26402 (2006).
18. Andreatta, D., Pérez Lustres, J.L., Kovalenko, S.A., Ernsting, N.P., Murphy, C.J., Coleman, R.S. & Berg, M.A. Power-law solvation dynamics in DNA over six decades in time. *J. Am. Chem. Soc.* **127**, 7270-7271 (2005).
19. Balasubramanian, S. & Bagchi, B. Slow solvation dynamics near an aqueous micellar surface. *J. Phys. Chem. B* **105**, 12529-12533 (2001).
20. DeMille, R.C., Cheatham, T.E. & Molinero, V. A coarse-grained model of DNA with explicit solvation by water and ions. *J. Phys. Chem. B* **115**, 132-142 (2010).
21. Banerjee, D. & Pal, S.K. Direct observation of essential DNA dynamics: Melting and reformation of the DNA minor groove. *J. Phys. Chem. B* **111**, 10833-10838 (2007).
22. Mandal, D., Sen, S., Sukul, D., Bhattacharyya, K., Mandal, A.K., Banerjee, R. & Roy, S. Solvation dynamics of a probe covalently bound to a protein and in an AOT microemulsion: 4-(N-bromoacetylamino)-phthalimide. *J. Phys. Chem. B* **106**, 10741-10747 (2002).
23. Bandyopadhyay, S., Chakraborty, S., Balasubramanian, S. & Bagchi, B. Sensitivity of polar solvation dynamics to the secondary structures of aqueous proteins and the role of surface exposure of the probe. *J. Am. Chem. Soc.* **127**, 4071-4075 (2005).
24. Levy, Y. & Onuchic, J.N. Water mediation of protein folding and molecular recognition. *Annu. Rev. Biophys. Biomol. Struct.* **35**, 389-415 (2006).
25. Schatz, G.C. DNA Structures and Excited States. *J. Phys. Chem. Lett.* **1**, 2054-2054 (2010).
26. Banerjee, D. & Pal, S.K. Excited-state solvation and proton transfer dynamics of DAPI in biomimetics and genomic DNA. *J. Phys. Chem. A* **112**, 7314-7320 (2008).
27. Pal, N., Verma, S.D. & Sen, S. Probe position dependence of DNA dynamics: Comparison of the time-resolved stokes shift of groove-bound to base-stacked probes. *J. Am. Chem. Soc.* **132**, 9277-9279 (2010).
28. Verma, S.D., Pal, N., Singh, M.K. & Sen, S. Probe position-dependent counterion dynamics in DNA: Comparison of time-resolved Stokes shift of groove-bound to base-stacked probes in the presence of different monovalent counterions. *J. Phys. Chem. Lett.* **3**, 2621-2626 (2012).
29. Dupradeau, F.-Y., Case, D.A., Yu, C., Jimenez, R. & Romesberg, F.E. Differential solvation and tautomer stability of a model base pair within the minor and major grooves of DNA. *J. Am. Chem. Soc.* **127**, 15612-15617 (2005).
30. Parker, J.B. & Stivers, J.T. Dynamics of uracil and 5-fluorouracil in DNA. *Biochemistry* **50**, 612-617 (2010).
31. Jayaram, B. & Jain, T. The role of water in protein-DNA recognition. *Annu. Rev. Biophys. Biomol. Struct.* **33**, 343-361 (2004).

32. Batabyal, S., Mondol, T., Choudhury, S., Mazumder, A. & Pal, S.K. Ultrafast interfacial solvation dynamics in specific protein DNA recognition. *Biochimie* **95**, 2168-2176 (2013).
33. Zhou, P., Tian, F., Ren, Y. & Shang, Z. Systematic classification and analysis of themes in protein-DNA recognition. *J. Chem. Inf. Model.* **50**, 1476-1488 (2010).
34. Reddy, C.K., Das, A. & Jayaram, B. Do water molecules mediate protein-DNA recognition? *J. Mol. Biol.* **314**, 619-632 (2001).
35. Bose, S., Adhikary, R., Mukherjee, P., Song, X. & Petrich, J.W. Considerations for the construction of the solvation correlation function and implications for the interpretation of dielectric relaxation in proteins. *J. Phys. Chem. B* **113**, 11061-11068 (2009).
36. Nandi, N. & Bagchi, B. Dielectric relaxation of biological water. *J. Phys. Chem. B* **101**, 10954-10961 (1997).
37. Bhattacharyya, K. & Bagchi, B. Slow dynamics of constrained water in complex geometries. *J. Phys. Chem. A* **104**, 10603-10613 (2000).
38. Samanta, A. Solvation dynamics in ionic liquids: What we have learned from the dynamic fluorescence stokes shift studies. *J. Phys. Chem. Lett.* **1**, 1557-1562 (2010).
39. Moilanen, D.E., Spry, D.B. & Fayer, M.D. Water dynamics and proton transfer in nafion fuel cell membranes. *Langmuir* **24**, 3690-3698 (2008).
40. England, J.L. & Haran, G. Role of solvation effects in protein denaturation: From thermodynamics to single molecules and back. *Annu. Rev. Phys. Chem.* **62**, 257-277 (2011).
41. Pal, S.K., Mandal, D., Sukul, D., Sen, S. & Bhattacharyya, K. Solvation dynamics of DCM in human serum albumin. *J. Phys. Chem. B* **105**, 1438-1441 (2001).
42. Pal, S.K., Peon, J., Bagchi, B. & Zewail, A.H. Biological Water: Femtosecond dynamics of macromolecular hydration. *J. Phys. Chem. B* **106**, 12376-12395 (2002).
43. Jordanides, X.J., Lang, M.J., Song, X. & Fleming, G.R. Solvation dynamics in protein environments studied by photon echo spectroscopy. *J. Phys. Chem. B* **103**, 7995-8005 (1999).
44. G. Hummer, J. C. Rasaiah & Noworyta, J.P. Water conduction through the hydrophobic channel of a carbon nanotube. *Nature* **414**, 188-190 (2001).
45. Maniwa, Y., Kataura, H., Abe, M., Udaka, A., Suzuki, S., Achiba, Y., Kira, H., Matsuda, K., Kadowaki, H. & Okabe, Y. Ordered water inside carbon nanotubes: formation of pentagonal to octagonal ice-nanotubes. *Chem. Phys. Lett.* **401**, 534-538 (2005).
46. Maniwa, Y., Kumazawa, Y., Saito, Y., Tou, H., Kataura, H., Ishii, H., Suzuki, S., Achiba, Y., Fujiwara, A. & Suematsu, H. Anomaly of X-ray diffraction profile in single-walled carbon nanotube. *J. J. App. Phys.* **38**, L668-L670 (1999).
47. Koga, K., Gao, G.T., Tanaka, H. & Zeng, X.C. Formation of ordered ice nanotubes inside carbon nanotubes. *Nature* **412**, 802-805 (2001).
48. Wang, H.-J., Xi, X.-K., Kleinhammes, A. & Wu, Y. Temperature-induced hydrophobic-hydrophilic transition observed by water adsorption. *Science* **322**, 80-83 (2008).

49. Martí, J. & Gordillo, M.C. Structure and dynamics of liquid water adsorbed on the external walls of carbon nanotubes. *J. Chem. Phys.* **119**, 12540-12546 (2003).
50. Gordillo, M.C. & Martí, J. Water on the outside of carbon nanotube bundles. *Phys. Rev. B* **67**, 205425 (2003).
51. Dujardin, E., Ebbesen, T.W., Krishnan, A. & Treacy, M.M.J. Wetting of single shell carbon nanotubes. *Adv. Mater.* **10**, 1472-1475 (1998).
52. Vaisman, L., Wagner, H.D. & Marom, G. The role of surfactants in dispersion of carbon nanotubes. *Adv. Colloid Interface Sci.* **128–130**, 37-46 (2006).
53. Islam, M.F., Rojas, E., Bergey, D.M., Johnson, A.T. & Yodh, A.G. High weight fraction surfactant solubilization of single-wall carbon nanotubes in water. *Nano Lett.* **3**, 269-273 (2003).
54. Wang, Q., Han, Y., Wang, Y., Qin, Y. & Guo, Z.-X. Effect of surfactant structure on the stability of carbon nanotubes in aqueous solution. *J. Phys. Chem. B* **112**, 7227-7233 (2008).
55. Ryabenko, A.G., Dorofeeva, T.V. & Zvereva, G.I. UV–VIS–NIR spectroscopy study of sensitivity of single-wall carbon nanotubes to chemical processing and Van-der-Waals SWNT/SWNT interaction. Verification of the SWNT content measurements by absorption spectroscopy. *Carbon* **42**, 1523-1535 (2004).
56. Wang, H., Zhou, W., Ho, D.L., Winey, K.I., Fischer, J.E., Glinka, C.J. & Hobbie, E.K. Dispersing single-walled carbon nanotubes with surfactants: A small angle neutron scattering study. *Nano Lett.* **4**, 1789-1793 (2004).
57. Richard, C., Balavoine, F., Schultz, P., Ebbesen, T.W. & Mioskowski, C. Supramolecular self-assembly of lipid derivatives on carbon nanotubes. *Science* **300**, 775-778 (2003).
58. Yurekli, K., Mitchell, C.A. & Krishnamoorti, R. Small-angle neutron scattering from surfactant-assisted aqueous dispersions of carbon nanotubes. *J. Am. Chem. Soc.* **126**, 9902-9903 (2004).
59. Matarredona, O., Rhoads, H., Li, Z., Harwell, J.H., Balzano, L. & Resasco, D.E. Dispersion of single-walled carbon nanotubes in aqueous solutions of the anionic surfactant NaDDBS. *J. Phys. Chem. B* **107**, 13357-13367 (2003).
60. Hazra, P., Chakrabarty, D., Chakraborty, A. & Sarkar, N. Probing protein-surfactant interaction by steady state and time-resolved fluorescence spectroscopy. *Biochem. Biophys. Res. Commun.* **314**, 543-549 (2004).
61. Barbara, P.F. & Jarzeba, W. in Ultrafast photochemical intramolecular charge and excited state solvation: Advances in Photochemistry 1-68 (John Wiley & Sons, Inc., 1990).
62. Shirota, H., Tamoto, Y. & Segawa, H. Dynamic fluorescence probing of the microenvironment of sodium dodecyl sulfate micelle solutions: Surfactant concentration dependence and solvent isotope effect. *J. Phys. Chem. A* **108**, 3244-3252 (2004).
63. Maroncelli, M. & Fleming, G.R. Picosecond solvation dynamics of coumarin 153: The importance of molecular aspects of solvation. *J. Chem. Phys.* **86**, 6221-6239 (1987).

64. Vajda, S., Jimenez, R., Rosenthal, S.J., Fidler, V., Fleming, G.R. & Castner, E.W. Femtosecond to nanosecond solvation dynamics in pure water and inside the [gamma]-cyclodextrin cavity. *J. Chem. Soc., Faraday Trans.* **91**, 867-873 (1995).
65. Sarkar, N., Datta, A., Das, S. & Bhattacharyya, K. Solvation dynamics of coumarin 480 in micelles. *J. Phys. Chem.* **100**, 15483-15486 (1996).
66. Rezus, Y.L.A. & Bakker, H.J. Observation of immobilized water molecules around hydrophobic groups. *Phys. Rev. Lett.* **99**, 148301 (2007).
67. Bagchi, B. Water dynamics in the hydration layer around proteins and micelles. *Chem. Rev.* **105**, 3197-3219 (2005).
68. Xu, H. & Berne, B.J. Hydrogen-bond kinetics in the solvation shell of a polypeptide. *J. Phys. Chem. B* **105**, 11929-11932 (2001).
69. Lee, S.H. & Rossky, P.J. A comparison of the structure and dynamics of liquid water at hydrophobic and hydrophilic surfaces-a molecular dynamics simulation study. *J. Chem. Phys.* **100**, 3334-3345 (1994).
70. Fee, R.S. & Maroncelli, M. Estimating the time-zero spectrum in time-resolved emmsion measurements of solvation dynamics. *Chem. Phys.* **183**, 235-247 (1994).
71. Siano, D.B. & Metzler, D.E. Band shapes of the electronic spectra of complex molecules. *J. Chem. Phys.* **51**, 1856-1861 (1969).
72. Chakrabarty, D., Hazra, P. & Sarkar, N. Solvation dynamics of coumarin 480 in tritonX-100 (TX-100) and bile salt mixed micelles. *J. Phys. Chem. A* **107**, 5887-5893 (2003).
73. Shirota, H. & Horie, K. Solvation dynamics in nonaqueous reverse micelles. *J. Phys. Chem. B* **103**, 1437-1443 (1999).
74. Yamazaki, T., Kovalenko, A., Murashov, V.V. & Patey, G.N. Ion solvation in a water-urea mixture. *J. Phys. Chem. B* **114**, 613-619 (2009).
75. Das, A. & Mukhopadhyay, C. Urea-mediated protein denaturation: A consensus view. *J. Phys. Chem. B* **113**, 12816-12824 (2009).
76. Stumpe, M.C. & Grubmüller, H. Aqueous urea solutions: Structure, energetics, and urea aggregation. *J. Phys. Chem. B* **111**, 6220-6228 (2007).
77. van der Vegt, N.F.A., Trzesniak, D., Kasumaj, B. & van Gunsteren, W.F. Energy-entropy compensation in the transfer of nonpolar solutes from water to cosolvent/water mixtures. *ChemPhysChem* **5**, 144-147 (2004).
78. Trzesniak, D., van der Vegt, N.F.A. & van Gunsteren, W.F. Computer simulation studies on the solvation of aliphatic hydrocarbons in 6.9 M aqueous urea solution. *Phys. Chem. Chem. Phys.* **6**, 697-702 (2004).
79. Wallqvist, A., Covell, D.G. & Thirumalai, D. Hydrophobic interactions in aqueous urea solutions with implications for the mechanism of protein denaturation. *J. Am. Chem. Soc.* **120**, 427-428 (1998).
80. Ikeguchi, M., Nakamura, S. & Shimizu, K. Molecular dynamics study on hydrophobic effects in aqueous urea solutions. *J. Am. Chem. Soc.* **123**, 677-682 (2001).
81. Tobi, D., Elber, R. & Thirumalai, D. The dominant interaction between peptide and urea is electrostatic in nature: A molecular dynamics simulation study. *Biopolymers* **68**, 359-369 (2003).

82. Graziano, G. On the solubility of aliphatic hydrocarbons in 7 M aqueous urea. *J. Phys. Chem. B* **105**, 2632-2637 (2001).
83. Finer, E.G., Franks, F. & Tait, M.J. Nuclear magnetic resonance studies of aqueous urea solutions. *J. Am. Chem. Soc.* **94**, 4424-4429 (1972).
84. Hoccart, X. & Turrell, G. Raman spectroscopic investigation of the dynamics of urea–water complexes. *J. Chem. Phys.* **99**, 8498-8503 (1993).
85. Vanzi, F., Madan, B. & Sharp, K. Effect of the protein denaturants urea and guanidinium on water structure: A structural and thermodynamic study. *J. Am. Chem. Soc.* **120**, 10748-10753 (1998).
86. Chitra, R. & Smith, P.E. Molecular dynamics simulations of the properties of cosolvent solutions. *J. Phys. Chem. B* **104**, 5854-5864 (2000).
87. Bennion, B.J. & Daggett, V. The molecular basis for the chemical denaturation of proteins by urea. *Proc. Natl. Acad. Sci. U.S.A.* **100**, 5142-5147 (2003).
88. Caflisch, A. & Karplus, M. Structural details of urea binding to barnase: a molecular dynamics analysis. *Structure* **7**, 477-S2 (1999).
89. Kaatze, U., Gerke, H. & Pottel, R. Dielectric relaxation in aqueous solutions of urea and some of its derivatives. *J. Phys. Chem.* **90**, 5464-5469 (1986).
90. Idrissi, A., Bartolini, P., Ricci, M. & Righini, R. Time resolved optical Kerr effect analysis of urea–water system. *J. Chem. Phys.* **114**, 6774-6780 (2001).
91. Shimizu, A., Fumino, K., Yukiyasu, K. & Taniguchi, Y. NMR studies on dynamic behavior of water molecule in aqueous denaturant solutions at 25°C: Effects of guanidine hydrochloride, urea and alkylated ureas. *J. Mol. Liq.* **85**, 269-278 (2000).
92. Rezus, Y.L.A. & Bakker, H.J. Effect of urea on the structural dynamics of water. *Proc. Natl. Acad. Sci. U.S.A.* **103**, 18417-18420 (2006).
93. Idrissi, A., Sokolić, F. & Perera, A. A molecular dynamics study of the urea/water mixture. *J. Chem. Phys.* **112**, 9479-9488 (2000).
94. Tsai, J., Gerstein, M. & Levitt, M. Keeping the shape but changing the charges: A simulation study of urea and its iso-steric analogs. *J. Chem. Phys.* **104**, 9417-9430 (1996).
95. Reimers, J.R., Watts, R.O. & Klein, M.L. Intermolecular potential functions and the properties of water. *Chem. Phys.* **64**, 95-114 (1982).
96. Gosting, L.J. & Akeley, D.F. A study of the diffusion of urea in water at 25° with the gouy interference method 1. *J. Am. Chem. Soc.* **74**, 2058-2060 (1952).
97. Calvaruso, G., Minore, A. & Liveri, V.T. FT-IR investigation of the urea state in AOT reversed micelles. *J. Colloid Interface Sci.* **243**, 227-232 (2001).
98. Caponetti, E., Chillura-Martino, D., Ferrante, F., Pedone, L., Ruggirello, A. & Turco Liveri, V. Structure of urea clusters confined in AOT reversed micelles. *Langmuir* **19**, 4913-4922 (2003).
99. Riter, R.E., Willard, D.M. & Levinger, N.E. Water immobilization at surfactant interfaces in reverse micelles. *J. Phys. Chem. B* **102**, 2705-2714 (1998).
100. Willard, D.M., Riter, R.E. & Levinger, N.E. Dynamics of polar solvation in lecithin/water/cyclohexane reverse micelles. *J. Am. Chem. Soc.* **120**, 4151-4160 (1998).
101. Correa, N.M. & Levinger, N.E. What can you learn from a molecular probe? New insights on the behavior of C343 in homogeneous solutions and AOT reverse micelles. *J. Phys. Chem. B* **110**, 13050-13061 (2006).

102. Dias, L.G., Florenzano, F.H., Reed, W.F., Baptista, M.S., Souza, S.M.B., Alvarez, E.B., Chaimovich, H., Cuccovia, I.M., Amaral, C.L.C., Brasil, C.R., Romsted, L.S. & Politi, M.J. Effect of urea on biomimetic systems: Neither water 3-D structure rupture nor direct mechanism, simply a more "polar water". *Langmuir* **18**, 319-324 (2001).
103. Krishnakumar, S. & Somasundaran, P. Aggregation behavior of aerosol OT in nonaqueous solvents and its desorption-an ESR study. *J. Colloid Interface Sci.* **162**, 425-430 (1994).
104. Panuszko, A., Bruździak, P., Zielkiewicz, J., Wyrzykowski, D. & Stangret, J. Effects of urea and trimethylamine-N-oxide on the properties of water and the secondary structure of hen egg white lysozyme. *J. Phys. Chem. B* **113**, 14797-14809 (2009).
105. Riter, R.E., Undiks, E.P. & Levinger, N.E. Impact of counterion on water motion in aerosol OT reverse micelles. *J. Am. Chem. Soc.* **120**, 6062-6067 (1998).
106. Bart, E. & Huppert, D. Dynamic salt effect on excited large dipole solvation. *Chem. Phys. Lett.* **195**, 37-44 (1992).
107. Chapman, C.F. & Maroncelli, M. Fluorescence studies of solvation and solvation dynamics in ionic solutions. *J. Phys. Chem.* **95**, 9095-9114 (1991).
108. Hazra, P., Chakrabarty, D. & Sarkar, N. Intramolecular charge transfer and solvation dynamics of coumarin 152 in aerosol-OT, water-solubilizing reverse micelles, and polar organic solvent solubilizing reverse micelles. *Langmuir* **18**, 7872-7879 (2002).
109. Maitra, A. Determination of size parameters of water-aerosol OT-oil reverse micelles from their nuclear magnetic resonance data. *J. Phys. Chem.* **88**, 5122-5125 (1984).
110. Jain, T.K., Varshney, M. & Maitra, A. Structural studies of aerosol OT reverse micellar aggregates by FT-IR spectroscopy. *J. Phys. Chem.* **93**, 7409-7416 (1989).
111. Shirota, H. & Segawa, H. Solvation dynamics of formamide and N,N-dimethylformamide in aerosol OT reverse micelles. *Langmuir* **20**, 329-335 (2003).
112. Moilanen, D.E., Levinger, N.E., Spry, D.B. & Fayer, M.D. Confinement or the nature of the interface? Dynamics of nanoscopic water. *J. Am. Chem. Soc.* **129**, 14311-14318 (2007).
113. Sarkar, N., Das, K., Datta, A., Das, S. & Bhattacharyya, K. Solvation dynamics of coumarin 480 in reverse micelles. Slow relaxation of water molecules. *J. Phys. Chem.* **100**, 10523-10527 (1996).
114. Itri, R., Amaral, C.L.C. & Politi, M.J. Interactive forces on aerosol-OT/n-hexane/water/urea reversed micelles by small angle x-ray scattering. *J. Chem. Phys.* **111**, 7668-7674 (1999).
115. Hayashi, Y., Katsumoto, Y., Omori, S., Kishii, N. & Yasuda, A. Liquid structure of the urea-water system studied by dielectric spectroscopy. *J. Phys. Chem. B* **111**, 1076-1080 (2007).
116. Hazra, P., Chakrabarty, D. & Sarkar, N. Solvation dynamics of coumarin 153 in aqueous and non-aqueous reverse micelles. *Chem. Phys. Lett.* **371**, 553-562 (2003).

6.3 Appendix

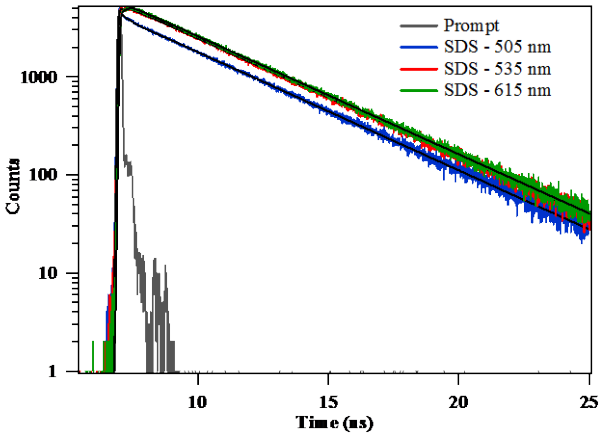

Appendix 6a.1. *Wavelength dependent Decay profiles of C-153 in 1% SDS. The wavelengths are mentioned in the inset.*

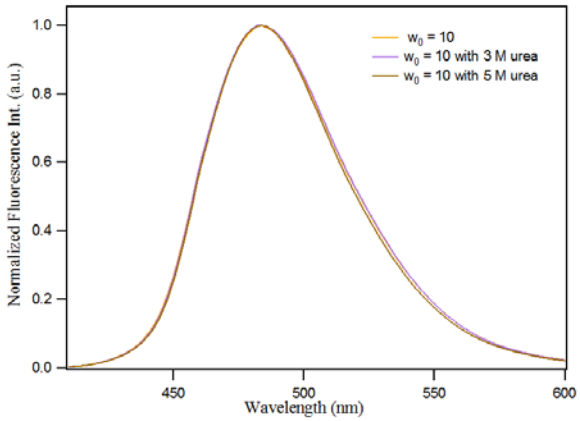

Appendix 6b.1. *Steady state fluorescence emission spectra of C-343 at w_0 = 10 and two different concentrations of urea in RM at w_0 = 10.*

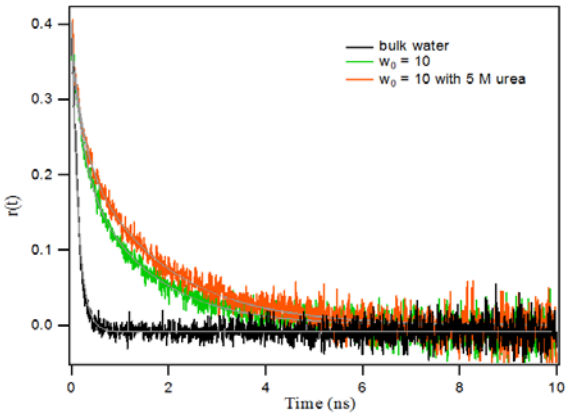

Appendix 6b.2. *Fluorescence anisotropy decay profile of C-343 at w_0 = 10, two different concentrations of urea in RM at w_0 = 10 and bulk water.*

Appendix 6.n1. Percentage missing componant calculation

The percentage missing component (MC) for solvation dynamics is calculated by the following formula;

$$MC = \frac{[\nu_{cal}(0) - \nu(0)]}{[\nu_{cal}(0) - \nu(\infty)]} \quad \ldots 6.a1$$

where, the calculated time zero frequency can be estimated using the following relation from absorption and fluorescence spectra;

$$\nu_p(t = 0) = \nu_p(abs) - [\nu_{np}(abs) - \nu_{np}(emi) \quad \ldots 6.a2$$

Where, the subscripts ‘p’ and ‘np’ refer to the polar and nonpolar spectrum, whereas ‘abs’ and ‘emi’ stands for absorption and emission spectrum respectively.

End of Chapter 6

- **List of Publication**

No.	Publications (Included in Thesis)	Year
01.	Influence of Mg^{+2} ions over flavin recognition by RNA aptamer: A spectroscopic and thermodynamic glimpse. **Abhigyan Sengupta**, K. Gavvala, R. K. Koninti, P. Hazra*. ***Journal of Photochemistry and Photobiology B: Biology***, 140, 240-248.	**2014**
02.	Urea induced unfolding dynamics of flavin adenine dinucleotide (FAD): Spectroscopic and molecular dynamics simulation studies from femto-second to Nano-second regime **Abhigyan Sengupta**, R. K. Singh, K. Gavvala, R. K. Koninti, A. Mukherjee*, P. Hazra*. ***The Journal of Physical Chemistry B***, 118, 1881-1890.	**2014**
03.	An anticancer drug to probe non-specific protein-DNA interactions **Abhigyan Sengupta**, R. Koninti, K. Gavvala, N. Ballav, P. Hazra*. ***Physical Chemistry Chemical Physics (Communication)***, 16, 3914-3917.	**2014**
04.	Comparative study of flavins binding with human serum albumin: A fluorometric, thermodynamic, and molecular dynamics approach. **Abhigyan Sengupta**, W. D. Sasikala, A. Mukherjee*, P Hazra*. ***ChemPhysChem***, 13, 2142-2153.	**2012**
05.	How does the urea dynamics differ from water dynamics inside the reverse micelle? **Abhigyan Sengupta**, R.V. Khade, P. Hazra*. ***The Journal of Physical Chemistry A***, 115, 10398-10407.	**2011**
06.	pH dependent dynamic behavior of flavin mononucleotide (FMN) and flavin adenine dinucleotide (FAD) in femtosecond to nanosecond time scale. **Abhigyan Sengupta**, R.V. Khade, P. Hazra*. ***Journal of Photochemistry and Photobiology A: Chemistry***, 221, 105-112.	**2011**
07.	Solvation dynamics of Coumarin 153 in SDS dispersed single walled carbon nanotubes (SWNTs) **Abhigyan Sengupta**, P. Hazra*. ***Chemical Physics Letters***, 501, 33-38.	**2010**

No.	Publications (Not Included in Thesis)	Year
08.	Proflavine Stabilizes Human Telomeric G-Quadruplex DNA: An Additional Mode of Action for Anticancer Agent. V. Kumar[†], **Abhigyan Sengupta**[†], R. K. Koninti, K. Gavvala, P. Hazra*. ***The Journal of Physical Chemistry B***, 118, 11090-11099.	**2014**
09.	Excited state proton transfer dynamics of topotecan, a potential anti-cancer drug, inside bio-mimicking nano-cavity. R. K. Koninti, K. Gavvala, **Abhigyan Sengupta**, P. Hazra*. ***The Journal of Physical Chemistry B***, **DOI**: 10.1021/jp5066902 (just accepted).	**2014**
10.	Blue emission in proteins. S Sarkar, **Abhigyan Sengupta**, P. Hazra*, P. Mandal*. ***arXiv*** preprint arXiv:1404.6859	**2014**
11.	*In vitro* Sensing of Cu^{+} through a Green Fluorescence Rise of Pyranine. T.Saha, **Abhigyan Sengupta**, P. Hazra and P. Talukdar*. ***Photochemical Photobiological Sciences***, 13, 1427-1433.	**2014**
12.	Excited state proton transfer dynamics of an eminent anticancer drug, ellipticine, in octyl glucoside (OBG) micelle. K. Gavvala, Raj K. Koninti, **Abhigyan Sengupta**, Partha Hazra*. ***Physical Chemistry Chemical Physics***, 16, 14953-14960.	**2014**
13.	Folding dynamics of flavin adenine dinucleotide (FAD) inside non-aqueous and aqueous reverse micelles. **Abhigyan Sengupta***, K. Gavvala, R. K. Koninti, H. Chaudhuri, P. Hazra*. ***Chemical Physics Letters***, 584, 67-70.	**2014**
14.	Loading of an anti-cancer drug onto graphene oxide and subsequent release to DNA/RNA: a direct optical detection. R. K. Koninti, **Abhigyan Sengupta**, K. Gavvala, N. Ballav, P. Hazra*. ***Nanoscale***, 6, 2937-2944.	**2014**
15.	Cucurbit [7] uril assisted ultraviolet to visible fluorescence switch of a heart medicine. K. Gavvala, R. K. Koninti, **Abhigyan Sengupta**, P. Hazra*. ***Physical Chemistry Chemical Physics Communication***, 16, 2823-2826.	**2014**
16.	Unraveling the mode of binding of the anticancer drug topotecan with ds-DNA. H. Joshi, **Abhigyan Sengupta**, K. Gavvala, P. Hazra*. ***RSC Advances***, 4, 1015-1024.	**2014**

17. Prototropical and photophysical properties of ellipticine inside the nanocavities of molecular containers. **2013**
K. Gavvala, **Abhigyan Sengupta**, R. K. Koninti, P. Hazra*.
The Journal of Physical Chemistry B, 117, 14099-14107.

18. Femtosecond to nanosecond dynamics of 2, 2′-bipyridine-3, 3′-diol inside the nano-cavities of molecular containers. **2013**
K. Gavvala, **Abhigyan Sengupta**, R. K. Koninti, P. Hazra*.
Physical Chemistry Chemical Physics, 16, 933-939.

19. Supramolecular host-inhibited excited state proton transfer and fluorescence switching of the anti-cancer drug, topotecan. **2013**
K. Gavvala, **Abhigyan Sengupta**, R. K. Koninti, P. Hazra*.
ChemPhysChem, 14, 3375-3383.

20. Modulation of excimer formation of 9-(dicyano-vinyl) julolidine by the macrocyclic hosts. **2013**
K. Gavvala, W. D. Sasikala, **Abhigyan Sengupta**, S. A. Dalvi, A. Mukherjee, P. Hazra*.
Physical Chemistry Chemical Physics, 15, 330-340.

21. Modulation of photophysics and pKa shift of the anti-cancer drug camptothecin in the nanocavities of supramolecular hosts. **2013**
K. Gavvala, **Abhigyan Sengupta**, P. Hazra*.
ChemPhysChem, 14, 532-542.

"If I have seen so far, it is only because I have stood on the shoulder of giants."

..... Sir Issac Newton

THE END